Extending the reach of crushed-rock fertilizers to Africa: Alternative potassium fertiliser using nepheline syenites from Malawi

Annock Gabriel Chiwona

A thesis submitted in fulfilment of the requirements for the degree of Doctor of Philosophy, University of Newcastle upon Tyne.

School of Natural and Environmental Sciences, University of Newcastle upon Tyne,

United Kingdom

January 2020

Abstract

Africa has one of the most disadvantaged agricultural sectors in the world due to high poverty levels and high fertiliser import costs from the northern hemisphere. This study was conducted to assess the potential of nepheline syenites from Malawi, representing others from the rift tectonic settings of Africa, for their potential as potash sources. This was a multidisciplinary study which used a combination of remote sensing, airborne and field gamma-ray geophysics, and petro-geochemical techniques to assess the potential of nepheline syenite as fertiliser. Petrological and geochemical analyses of rock samples and soil samples were conducted for determination of K content and to confirm the presence of nepheline and other associated minerals within the rock and soil samples.

Petro-geochemical results show the presence of nepheline in most of the samples and this agrees well with expectations from the geophysical and remote sensing digital terrain model results. The study has also discovered the presence of davidsmithite ($((\mathrm{Ca},\square)_2\mathrm{Na}_6\mathrm{Al}_8\mathrm{Si}_8\mathrm{O}_{32})$ an uncommon silicate mineral of the nepheline group, associated with the heterovalent replacement of Ca^{2+} for K^{+}. Plant growth trials using this study's nepheline syenite and crushed-rock from other parts of the world have shown that Malawi's nepheline syenite is able to release K for plant growth. Although different intrusive complexes are not homogenous, the results show that, generally, nepheline syenites from Malawi have similar geochemistry to those in other parts of the world, some of which have been used as crushed-rock fertilisers. This thesis, therefore, provides an initial reference material on how geophysical and remote sensing techniques can be used to delineate nepheline syenite occurrences in the East African Rift System as a potassium source. This thesis further shows Malawi's potential as a source of crushed-rock potash fertilisers. It also provides pilot information for further research in this area because agro-geology is a new discipline in both Malawi and Africa as a whole.

Key words: potash, nepheline syenite, gamma-ray, rift tectonics, Malawi, crushed-rock, silica

Acknowledgements

Firstly, I owe my thanks to the Lord God Almighty, for the precious gift of life, health and the privilege to undertake this study. I am so grateful to my supervisors, Prof David Manning, Dr Rachel Gaulton and Dr Joaquin Cortés for their patience, encouragement and mentoring throughout the time of my study. No words would be enough to describe their guidance, encouragement and motivation from Prof David Manning and Dr Rachel Gaulton who believed in me even when I could not. So grateful to Dr Joaquin Cortés, sacrificing his time and taking me through the petrological and XRF sample preparation and analyses even when some schedules were not convenient for him.

I am greatly indebted in thanks to Newcastle University Faculty of Science's Doctoral Training Award (DTA); and Ingo Wender and Terrativa Inc. without whose support this study would have been been difficult to undertake. I also thank the Geological Survey of Malawi for the airborne survey geophysical data, satellite imagery and some software packages and field equipment, which were provided at no cost. The Society of Economic Geologists (SEG) is appreciated for additional funding for the fieldwork in Malawi, I am also grateful to the University of Edinburgh for the X-ray fluorescence (XRF) and Scanning Electron Microscopy with Energy Dispersive Spectroscopy (SEM-EDS) analyses. I am very grateful to Phil Green, Alex Charlton, Maggie White, David Earley, Stuart Patterson and Jane Davis for their technical support with sample analyses at various times. The NEOLab, Geosciences and Biogeochemistry Research Groups friends, I owe you so much appreciation for the fruitful discussions and encouragement throughout my study.

It would be incomplete not to mention special friends who never stopped encouraging me: Capt. Dr Mphatso Boti-Phiri (Rtd.) and Dr Rachel Chimbwetete-Phiri, I really salute you; Lisa and Ike Igbinogun you are the best; Luella Khonje, Chifundo and Eric Chiotha, your support, encouragement and prayers were never in vain. Pastors David and Fumi Odumade, and the RCCG Solution Assembly, the Living Waters Church Malawi, the Lighthouse Christian Church, Australia, Pastors Mathew Phiri, Late Geoffrey Idana, Dzimbiri, Olalekan Aladesanmi, James and many more who stood with me in prayers I salute you. Dr Martin Cooke, Dr Ces van der Land, Dr Geoffrey Abbott, Dr Blackwell Manda, Dr Annie Chizengo-Thawani, Prof. Peter Clarke, Ass. Prof. Leonard Kalindekafe, Prof. Bryne Ngwenya, Abigail and Chikondi Chisenga, Caroline Mkandawire, Osward Theu, Charles Missi, Kondwani Dombola, Harrison Mtumbuka, my family and friends all over the world, you made this journey worthwhile.

Dedication

To my late parents, my elder brother Chawupi, Benjamin and Abigail, for all the love, encouragement and support.

Table of Contents

List of tables

List of Figures

List of Abbreviations

ADMARC	:Agriculture development and marketing cooperation
ASD	: Analytical spectral device
ASTER	:Advanced spaceborne thermal emission and reflection radiometer
CIA	:Chemical index of alteration
CIPW	: Cross, Iddings, Pirsson and. Washington classification of igneous rocks
DEM	:Digital elevation models
DTM	:Digital terrain models
EARS	:East African rift system
EDS	:Energy dispersive spectrometer
ENVI	:Environment for visualizing images
FISP	:Farm input fertiliser subsidy programme
FLAASH	:Fast line-of-sight atmospheric analysis of spectral hypercubes
GDEM	:Global Digital Elevation Model
GIS	:Geographical information systems
IUGS	:International Union of Geological Sciences
LDA	:Linear discriminant analysis
LiDAR	:Light detection and ranging.
MODIS	:Moderate resolution imaging spectroradiometer
PCA	:.Principal component analysis
PIA	:Plagioclase index of alteration
REE	: Rare earth elements
REEs	:Rare earth elements
SEM	: Scanning electron microscope
SRTM	:Shuttle radar topography mission
SWIR	:Short wave infrared radiation
TAS	:Total silica-alkali
TIR	: Thermal infra-red radiation
VNIR	: Visible near infrared spectroscopy
XRD	: X-ray powder diffraction
XRF	: X-ray fluorescence analysis

Chapter 1: General introduction

1. Introduction

The global community faces several crucial challenges including food security. It is undeniable that the world greatly needs to grow more food and to offer relief to the global population. One of doing this is through intensification of food production by among others increasing the use of fertilisers for the crops. In spite of the different policies and advocacy to increase food production, it is noted that the high prices of commercial fertilisers negatively impact on poor farmers especially, in Africa and Latin America as they cannot afford these exorbitant prices. It is for this reason that there is need for alternative fertiliser sources which could help farmers to remineralise their soils. Malawi is not left alone in this problem because there is low fertiliser use especially potassium fertilisers, a problem which is further aggravated by the country's location, inland away from the major sea ports. This is a serious problem to other African countries which are also disadvantaged by high purchasing prices and transport costs of the fertilisers. For example, Africa's three staple crops: rice, maize and wheat, jointly, annually remove 100Kg ha^{-1}, 140Kg ha^{-1} and 104Kg ha-^{1} of N, P and K, respectively, and these nutrients need to be replenished (Sheldrick and Lingard, 2004).

Among the soil macro-nutrients (namely nitrogen (N), phosphorus (P) and potassium (K)), the most critical need in many countries is K. Globally, potassium demand for agricultural use is on the increase by about 3-3.5% annually (Jena et al., 2014) but only about 1-2% of the natural potassium in the soil is available for plant uptake and soil enrichment (S Mohammed et al., 2014; Öborn et al., 2010; Priyono and Gilkes, 2008). Due to the alarming K depletion rates, which are mainly due to *soil mining* by plants, global production of potash fertilisers needs to double to compensate for K removed from soils by food crops (Sheldrick and Lingard, 2004). This needs to be done as soon as possible because both the K demand and human global population keep on increasing.

Manning (2015) adds that the situation is most critical in Africa, where 15% of the global population use just 1.5% of the world's fertiliser production yet Africa's population is expected to double by 2050. Between 1961 and 1998, the potassium (K) deficit in Africa rose from 1.6 million tonnes (10.6 kg ha $^{-1}$ yr^{-1}) to 4.1 million tonnes (20.0 kg ha $^{-1}$ yr^{-1}) according to Sheldrick and Lingard (2004) As such, extraction of K from various indigenous sources to replenish the soil is greatly needed. Studies elsewhere, notably in Brazil, have shown that nepheline-bearing rocks are a potential source of K as a direct application fertiliser (Bakken et al., 2000; Tavares et al., 2018). Assuming there is no increase in fertilizer use and amidst increased crop production, resulting into soil potassium (K) nutrient deficiency, the annual depletion rates are projected to increase to 36 kg ha^{-1} for K in Africa by 2020 (Sheldrick et al., 2002). Soil nutrient audits by Sheldrick et al., (2002), showed that by 2004, all but only four African countries (namely: Botswana, Namibia, Somalia and Niger) were K deficient, as shown in Appendix 1.1.

While plant uptake had nearly doubled between 1961 and 1998, to about 30 kg K ha^{-1} year^{-1}, the K fertiliser input into the soil remained as low as 2.1 kg K ha^{-1} year^{-1} even as recently as of 2009 (Manning, 2010). However, alternatives from rock fertilisers, such as K-rich silicate rocks, which may help farmers to replenish K removed through *soil mining* by crops (Goldschmidt, 1922; Jena et al., 2014; Manning, 2015, 2017) are locally available in many parts of the world. Several works including the use of crushed-rock in Brazil (Theodoro and Leonardos, 2006) and studies by Manning (2010), Bakken et al. (2000) and Mohammed et al. (2014) have shown that silicate rocks especially alkaline rocks, which have high K content, have great potential as alternative potassium silicate sources. Nepheline syenite is one of the rock types but it has not been tested, specifically, in Africa where K fertiliser is most scarce.

This study, therefore, aimed to identify novel potassium sources for alternative agricultural fertilisers using nepheline syenites. The study is the first work on the potential use of nepheline in Malawi, which, being on the East African Rift, contains many localities with nepheline-bearing rocks. Remote sensing, gamma ray radiometric survey, digital terrain models (DTM), and ASTER / field spectroscopy were tested to identify favourable nepheline syenite areas. In Malawi many of the localities are well known and so it is a good field laboratory to test techniques for application in Malawi and elsewhere in Africa.

1.1. Context of the study

1.1.1. Potassium fertiliser global requirements, supply and use

The nepheline syenites of Malawi have been recognised as potential sources and are being explored for Rare Earth Elements (REEs) and dimension stone (BGS, 2009). Successful evaluation of potential of these rocks as alternative potash sources by this study, will therefore, provide an additional advantage for potential investors like Mkango Resources Ltd, whose primary interest in their Songwe-Mauze Rare Earth Elements (REE) prospect lies in carbonatites (Swinden and Hall, 2012). Most carbonatites in Malawi and much of the entire East African Rift System (EARS) occur together with nepheline syenites (Woolley, 2001). Instead of being a waste, disposed of as unwanted tailings, nepheline-bearing products of processing could then be used as a second economic resource, alongside REEs concentrates, in such carbonatite-nepheline syenite complexes.

1.1.2. Potassium fertiliser use in Africa

An agricultural growth rate in Africa of 2.5% or more is required to meet food needs over the two decades from 2000 to 2020 (Sheldrick et al., 2002; Sheldrick and Lingard, 2004), based on levels of inputs known at the time of these studies. However, this cannot be achieved without a large increase in soil nutrient input and it is also not sustainable now. As will be shown in Chapter 3, in most African countries, nutrient depletion is increasing and is estimated at around 100-140kg ha^{-1} plant removal of major soil nutrients (N, P, K) from soil (Sheldrick et al., 2002; Sheldrick and Lingard, 2004). For instance, Sheldrick and Lingard (2004) note that Africa's three main staple crops: rice, maize and wheat, jointly, remove 100kg ha^{-1}, 140kg ha^{-1} and 104kg ha^{-1} of N, P and K, respectively. In addition, land area used for food production per capita is ever declining with reports showing a reduction from 0.42 to 0.21 ha per capita between 1961 and 2007 (Gregory and George, 2011) while human population continues to increase. It is, therefore, not surprising then that soil productivity at these depletion rates makes it impossible to maintain the required annual agricultural growth rate of 2.5% (Sheldrick et al., 2002; Sheldrick and Lingard, 2004).

Most of the K_2O fertilisers are imported from the Northern Hemisphere. Therefore, costs are largely determined by import and transport costs. Other additional costs are also associated with fertiliser distribution within the importing countries (e.g. Malawi), as well as the trader and agro-dealer profit margins. The situation has further worsened in the last decade due to the global economic recession, fertiliser price adjustments and the increasing poverty levels in Africa. On average, African farmers pay between 30-50% more than their counterparts in Europe and North America to purchase K fertilizer (Roberts and Vilakazi, 2014) because the 1st World has large fertilizer producers, better transport infrastructure and distribution networks. Most African economies also have less capacity for sustainable agriculture.

The use of potash from alternative fertiliser rock sources is one of the factors which have led to the growth of Brazil's agricultural sector driven by the *Rochagem* movement. The *Rochagem* movement is an approach whose goal is to replenish soil nutrients in nutrient-poor or degraded soils in agrarian reform communities using crushed-rock fertilizers (Theodoro and Leonardos, 2006). This study, therefore, builds on successes of the work carried out by Terrativa (www.terrativa.com.br/) and Embrapa (www.embrapa.br/en/international) in Brazil as benchmarks, because the identified potash sources in Brazil occur in similar geological settings to Malawi, and have been shown to function in tropical soils.

Malawi is not an exception to the problem of acute fertiliser inadequacy. For a long time, Malawi's perceived major fertiliser challenge has been nitrogen nutrient deficiency (Brown, 1966; Snapp, 1998); because it is the only major nutrient that was considered deficient in most soils of Malawi. Previous studies, therefore, largely ignored studies on K deficiency in soils. However, by the end of the 1990s, 84,000 tonnes of K were reported to be depleted annually from the soil in Malawi, through crop production. Only less than a third of that amount was replaced from all fertiliser sources including compost, crop residue, manure and conventional fertiliser (Sheldrick and Lingard, 2004). Furthermore, contrary to past perceptions that K was not a major requirement in these soils, the fertiliser requirements for Malawi soils show that the soils are depleted in K and need replenishment (Lakudzala, 2013; Snapp, 2008).

The Malawi Government introduced a targeted farm input fertiliser subsidy programme (FISP) in the early 2000s to help vulnerable farmers. However, this initiative faces challenges including corruption, over-dependency on donor funding (Vinet and Zhedanov, 2010), a long fertiliser supply chain (Figure 1.1) and uncertainty over its sustainability. Fertiliser is supplied to rural areas mainly through the state-owned Agriculture and Marketing Cooperation (ADMARC), the Smallholder Farmers Fertiliser Revolving Fund of Malawi SFFRM) and other private traders.

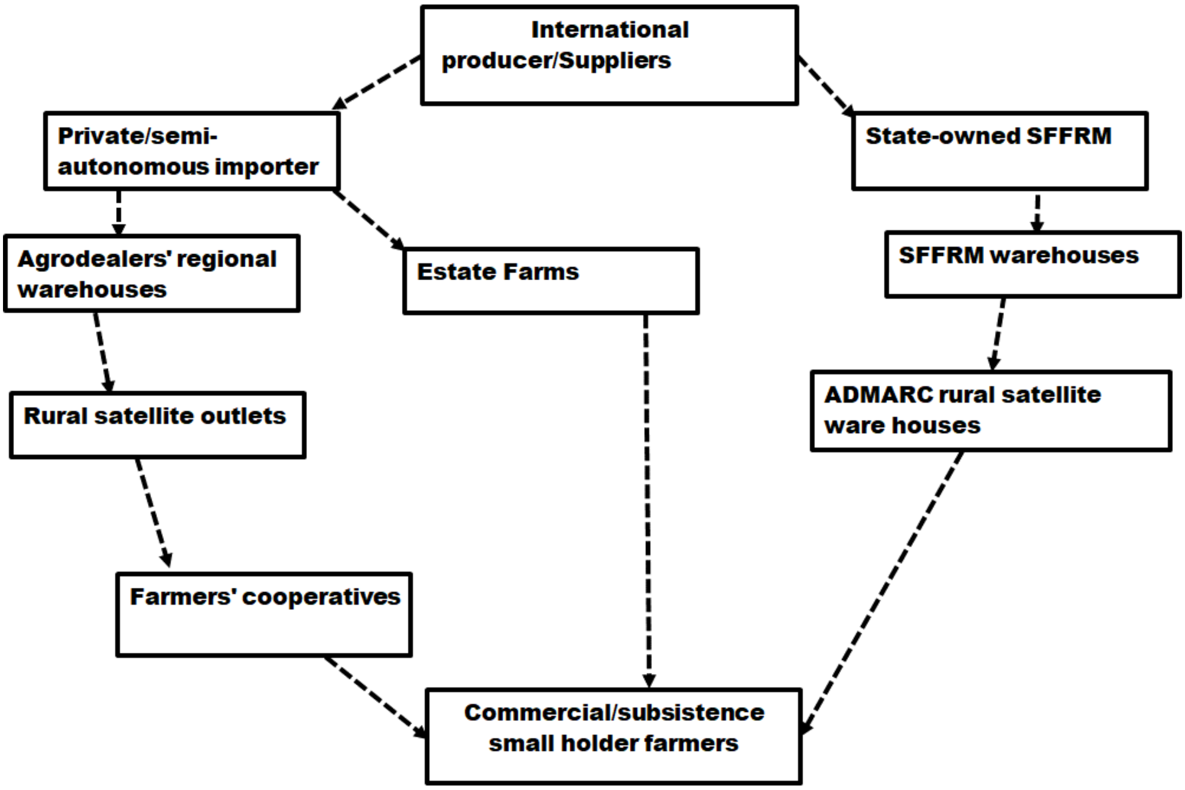

Figure 1.1: Malawi's fertilizer supply chain showing long route to smallholder farmers hence high farm-gate fertilizer prices (using data from Fuentes (2013)).

Malawi's geographic location as a land-locked country, generally, further contributes to higher fertilizer costs than in neighbouring countries such as Tanzania and Mozambique. Malawi relies on three major seaports namely Nacala and Beira (Mozambique), Dar es Salaam (Tanzania) and to some extent Durban (South Africa). Therefore, additional costs apart from the purchasing prices also originate from importation through neighbouring countries' ports. Transport costs from the port to Malawi's capital, Lilongwe, where the fertiliser is delivered, blended and redistributed countrywide, are \$50 to >\$200 (Figure 1.2).

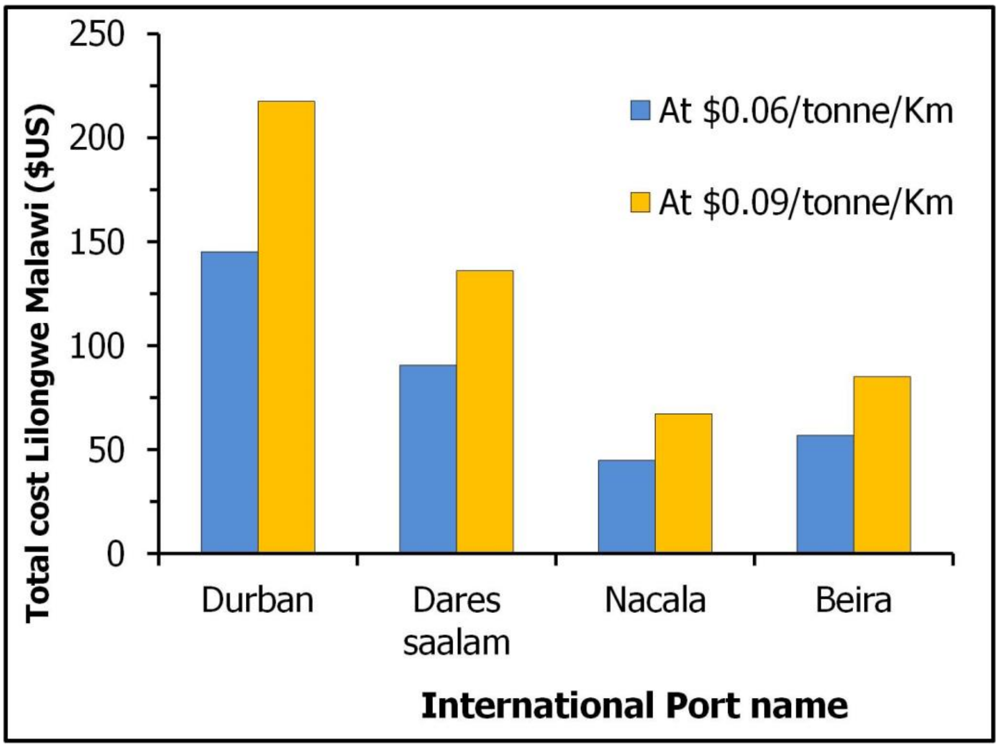

Figure 1.2: Transport costs of fertilizer from the port to Lilongwe Malawi as calculated using the average transport costs for Malawi imports.

Soil audits have further shown that over 60% of Malawi's land area is K-deficient (Chilimba and Liwimbi, 2008; Lakudzala, 2013). In Malawi, 96% of the arable land is occupied by small-holder farmers whose average cereal production is 1.9 tonnes/ha, compared to large estate farmers whose cereal yield is about 3.2 tonnes/ha (Fuentes, 2013). This shows that small-holder farmers are much more negatively affected by soil nutrient deficiency not only for K but other macro nutrients as well (Vinet and Zhedanov, 2010) than large scale affluent farmers. This could be due to prolonged soil mining and inadequate fertilizer usage by the poor smallholder farmers.

Different studies have been conducted to assess the use of various agro-minerals by direct application as reported by van Straaten (2002). The most known and researched agro-minerals are phosphates. These include field trials in Malawi by researchers on using the P from the apatite-rich rock and apatite soevite from Tundulu carbonatite. Other minor phosphate occurrences are reported at Kangankunde and the Chilwa Island carbonatites, Chingale meta-pyroxenite, Mlindi residual soils. Some studies have also been conducted to assess the K resources of which large concentrations have been reported to for Chilwa Island carbonatite's K-feldspar and Tundulu feldspathic breccia with their K_2O contents range between 4.3-13% (van Straaten, 2002). Some areas also contain dolomite and limestone which van Straaten (2002) recommend for use as source of agricultural lime.

While local farmers plant crops in the Mlindi residual soils, which contain some K minerals mainly biotite, and in soils developed on the Chingale meta-pyroxenite, there is no use of crushed rock or direct application of the agrominerals as fertilisers in Malawi (van Straaten, 2007). Trials using maize showed higher yields using for plots with phosphate rock treatment, with yield of plot to 1,396 kg ha^{-1} compared to the control plot which had a yield of 683 kg ha^{-1} (Phiri et al., 2010). However, as rightly noted by van Straaten, (2002) less costly small-scale operations with intermediate crushing and grinding technologies are feasible so that the various agrominerals can be used in Malawi.

1.1.3. Remote sensing and airborne radiometric geophysics application in geology

Remote sensing has been applied extensively in geological mapping and mineral assessments. Remote sensing is concerned with accessing information about an object or phenomenon using electromagnetic energy without physical contact between the sensor and the observed phenomena or material (Eismann, 2012; Khorram et al., 2012). Remote sensing is based on natural energy expressed as a function of transmitted, absorbed or scattered light from a feature of interest. Geologic remote sensing combines principles of remote sensing techniques with the understanding of geological concepts and theories. Various features/materials show different diagnostic spectral response curves based on these features' reflectance or absorption capacity of the electromagnetic energy. Different minerals and rocks have different physical and chemical properties; hence, they also exhibit different spectral patterns. Silicate minerals and rocks show key diagnostic features in some parts of the electromagnetic spectrum which are usually different from those of carbonate minerals (Corrie et al., 2010). Although remote sensing has played a great role in previous geological mapping and mineral exploration projects (as shown in Chapter 4), prior to this study, no research had used remote sensing techniques to specifically delineate nepheline syenites, especially in rift tectonic settings.

On the other hand, airborne gamma-ray spectrometry has also been used widely in geological research involving the determination of surface abundances of radioactive elements (Dickson, 2004; Wilford, 2012; Youssef and Elkhodary, 2013). This is because radiometric data make it easy to delineate the apparent surface concentrations of key naturally occurring radioactive elements. Geophysical spectrometry operates on the principle of measurement of gamma-rays emitted by the decay of naturally occurring radioactive elements, principally from potassium (K), thorium (Th) and uranium (U), in the shallow soil/rock profile. This technique is applied to determine the spatial abundance and characteristics of geological units and lithology on the

Earth's surface (Wemegah et al., 2015; Youssef and Elkhodary, 2013). The absolute concentrations of U, K and Th are closely associated with different lithologies.

In addition, different plants can also be used as pathfinders for certain minerals or rock types due to these plants' tolerance to various minerals. For example, *Cassia auriculata*'s lack of flowering shows that it is associated with chromite mineralisation. *Gymnosporia falconeriis* could be associated with Au, Ba or Sr depending on variations of its abundance (Prasad, 1987). Plant tolerance to potassium may be promoted by rhizospheric micro-organisms in the soils, referred to as the potassium solubilizing micro-organisms (KSMs; Meena et al., 2014). These can help transform insoluble potassium in the soil into soluble forms make its uptake by plants easier. Therefore, on a preliminary basis, this study attempted to assess K tolerance with the vegetation types in nepheline syenite areas of Malawi.

1.2. Overview of the geology of Malawi

Malawi lies at the southern end of the East African Rift System which is characterised by peralkaline igneous rocks. Geologically, Malawi mainly lies within the Mozambican Mobile Orogenic Belt that is associated with reworked meta-igneous and meta-sedimentary rocks of Late Precambrian to Early Palaeozoic age, which is locally known as the Malawi Basement Complex (Carter and Bennet, 1973; Mshali, 2009). These rocks are overlain by Karroo sediments and Mesozoic igneous intrusive events, characterised by a suite of carbonatite centres and nepheline syenites assigned to the Chilwa Alkaline Province (Carter and Bennet, 1973). The alkaline rocks of Malawi are distributed all over the country (Figure 1.3), although most of them occur largely in the Chilwa Alkaline Province of Early Jurassic to Late Cretaceous age. Figure 1.3 shows an overview of the simplified geology of Malawi and the the study areas with their ages.

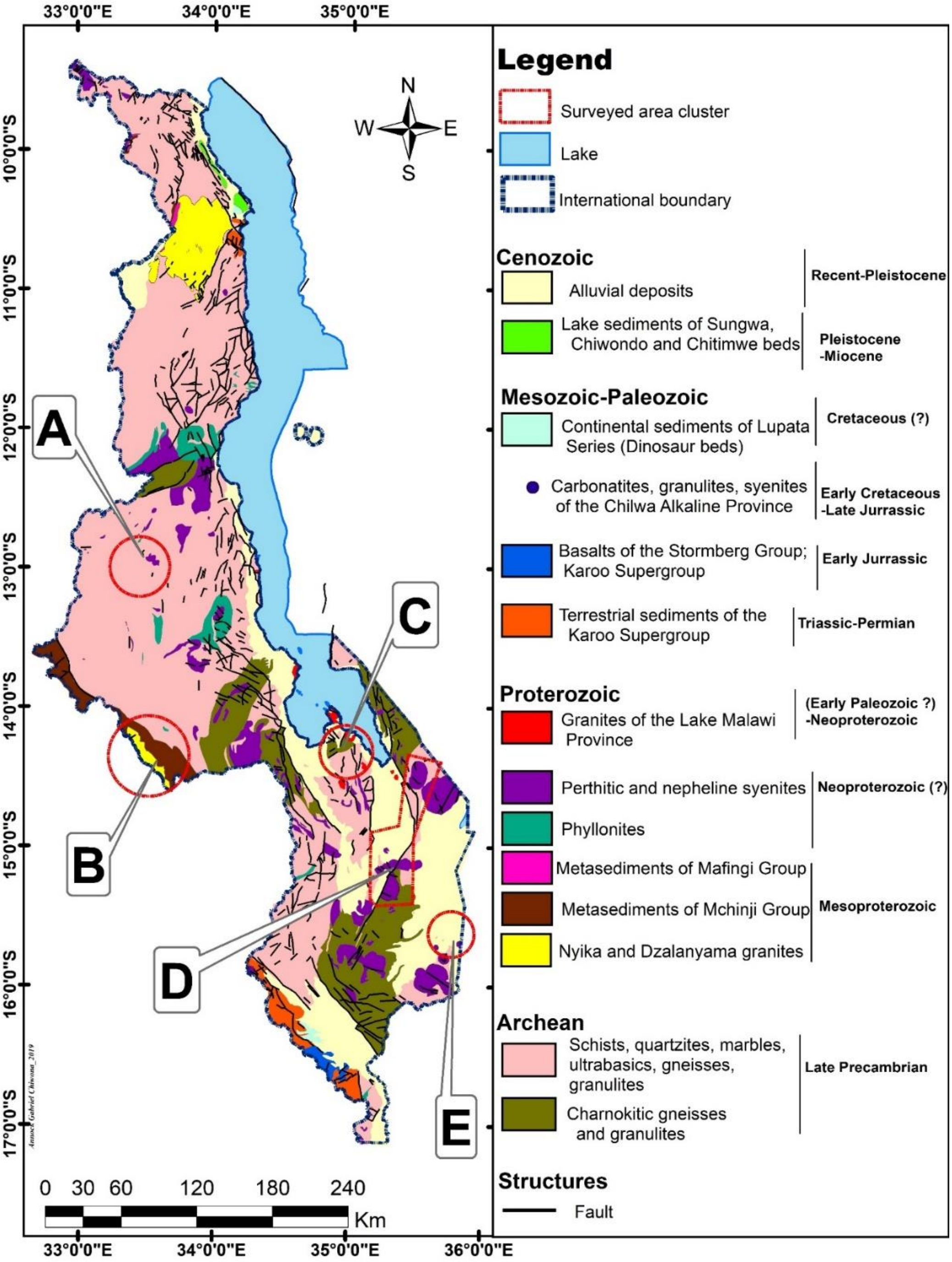

Figure 1.3: Simplified geology of Malawi showing location of areas which were identified for fieldwork (revised after Bloomfield, 1966). These areas are clustered as (A) central Malawi nepheline syenites; (B) central Malawi alkaline granites; (C) S.E Malawi quartz syenites; (D) S. Malawi nepheline syenites and syenites; (E) Carbonatite-associated nepheline syenites.

As shown in the Figure 1.4, some of the areas are known for nepheline syenites while a few others have occurrences of nepheline syenites and carbonatites. There is little published information about the petrology and geochemistry of these nepheline syenites. Therefore, this study is important because it provides much-needed information on the distribution of Malawi's nepheline syenites, permitting assessment of their potential as a K silicate fertilizer.

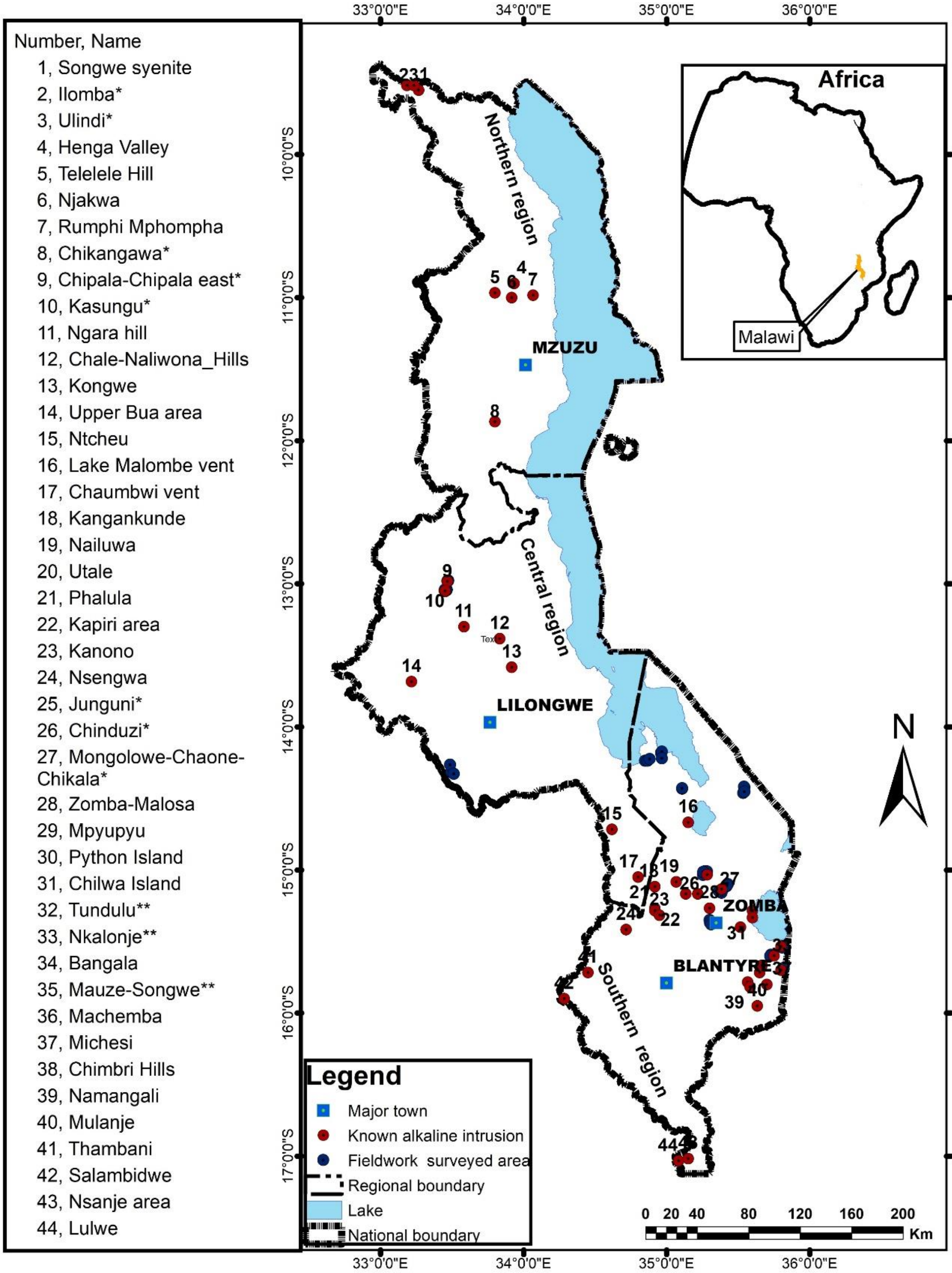

Figure 1.4: Map of Malawi showing known alkaline rock intrusions across the country (data extracted from Woolley (2001)). The intrusions indicated with asterisk (*) are known nepheline syenites while those indicated with double asterix (**) comprise carbonatite and nepheline syenites.

1.3. Rationale and significance of the study

The suitability of silicate rocks as alternative K sources does not depend on the absolute K content but rather on the dissolution rates of the minerals (Manning, 2010). This is why although some feldspars have more absolute K content than nepheline, their suitability as alternative potash sources is still not sufficiently effective (Priyono and Gilkes, 2008). Nepheline is mainly found in nepheline syenite (coarse-grained) and phonolite (fine grained) rocks. Not many crop trials have been conducted using nepheline syenite compared to K feldspar (Manning, 2010). This study is, therefore, important because it is the first of its kind in Africa's East African rift system. The available literature has shown that, prior to this study, the potential of nepheline syenites and other alkaline rocks as K silicate sources had not been tested both in Malawi and Africa as a whole. In addition, most geological mapping is done using field mapping or geophysical surveys which are expensive and more time consuming. However, remote sensing is faster, and some satellite imagery has global coverage. No previous study has applied remote sensing to exclusively map nepheline syenites in Africa and Malawi. This study provides a new approach for mapping these rocks using ASTER imagery.

Furthermore, Malawi does not have any accredited geochemical or petrological laboratories. As a result, geochemical and petrological analyses are usually conducted in South Africa's laboratories such as MINTEK (www.mintek.co.za/technical-divisions/analytical-services-asd/) and the Council for Geosciences (www.geoscience.org.za/index.php), which is costly and time consuming. If the rocks and minerals can be classified using remote sensing and geophysical techniques, it could save funds used for geochemical analyses in external laboratories and provide faster interpretation of the rocks for geological researchers. On the basis of the experience gained for Malawi, this study will provide an important framework for the identification and mapping nepheline syenites in other areas with similar geology globally.

1.4. Hypotheses and research questions

While some studies have previously used digital terrain models (DTM) to identify lineaments and ring structures (Ruzickova, 2012; Ruzickova et al., 2013) and radiometric data for geology mapping (Isioye and Jobin, 2012; Ruzickova et al., 2013; Wilford, 2012; Xiaoye Liu, 2008), no research had been done using ASTER imagery even though ASTER sensor has a global coverage. Previous studies have shown remarkable successes of geologic remote sensing using ASTER data, especially in Africa and Asia (Gomez et al., 2005; Guha and Vinod, 2016; Kumar et al., 2015; Lucas, 2013; Qari et al., 2008). This study, therefore, considered using ASTER satellite data to identify the occurrence of K-rich silicates, especially nepheline syenites. The motivation of this research assumed that airborne geophysics, digital terrain models and satellite remote sensing coupled with ground truthing can identify significant alternative potash fertiliser sources in Malawi, as part of Africa's

EARS region. This was done by delineating suitable nepheline syenite intrusions, in a rift tectonic setting. This study sought to answer the research questions outlined in Table 1.1:

Table 1.1: Four key guiding hypothetical statements and research questions for this study.

Hypothesis 1	***Hypothesis 2:***
Potash fertiliser is in high demand but with inadequate supply chain and impact (addressed by objective 1). -What are the current potash demand and supply dynamics and main potash producing countries? -What are the challenges/factors facing the K fertiliser production and supply in Africa?	*ASTER satellite remote sensing and gamma-ray radiometry can depict nepheline syenites, syenites and phonolites (addressed by objectives 2-5),* -Can ASTER imagery and DTMs locate K-rich nepheline syenites, phonolites and syenites? -Which bands, band ratios and spectral indices correspond with K enriched geological units? -Does gamma-ray radiometry discriminate nepheline syenites from other syenites?
Hypothesis 3:	***Hypothesis 4:***
Nepheline syenites of Malawi have enough nepheline and other K minerals needed for potassium silicate fertilisers (addressed by objectives 5-6). -What is the potassium content and mineral composition of the nepheline syenite samples? -What are petrophysical characteristics of K-rich nepheline syenites, syenites etc?	*Nepheline syenites are suitable alternative potash sources (addressed by objectives 7-8).* -How do plants respond in plant growth experiments to potassium extracted from the Malawi nepheline syenites? -How can this alternative fertiliser be accessed more easily by farmers in remote areas? -Can K be easily extracted at low cost?

1.5. Aims and Objectives

1.5.1. Main goal

To assess the potential of nepheline syenites of the East African rift tectonic setting, with focus on Malawi, for alternative potash silicate agricultural fertilisers.

1.5.2. Specific Objectives

The study sought to:

1) Review the geology and geochemistry of nepheline syenites (Chapter 2).
2) Review the potential of nepheline syenites as potash fertiliser (Chapter 3).
3) Review applications of satellite remote sensing and airborne geophysics in identification of alternative potash sources (Chapter 4).
4) Map the composition of surface rocks (by specifically interpreting K, U and Th data) using airborne geophysical gamma radiometry, and digital terrain models for delineation of nepheline syenite targets (Chapter 5).

5) Conduct ground-truthing to validate remote sensing and airborne geophysical results and identification scheme/model for potential K anomaly zones (Chapter 5).
6) Conduct petrological and geochemical analyses to determine K release (Chapter 6).
7) Use field spectroscopy to guide satellite remote sensing processing and data analysis to delineate nepheline syenite targets (Chapter 7).
8) Assess suitability of Malawi nepheline syenites as fertiliser through plant growth trials (Chapter 8).
9) Discuss the potential of use of nepheline syenites of Malawi, as alternative potash fertiliser sources, given their location and the distance to agricultural communities (Chapter 9).

1.6. Structure of this thesis

This thesis has nine Chapters which are arranged as follows:

- Chapter 1 provides the general introduction of the study including the objectives and rationale for conducting the research.
- Chapter 2 reviews the occurrence and geochemistry of nepheline syenites, alkaline rocks and related rocks (Objective 1).
- Chapter 3 reviews use of nepheline syenites and other alkaline rocks as K fertilisers (Objective 2).
- Chapter 4 reviews use of remote sensing and radiometric data in geology (Objective 3).
- Chapter 5 is based on a fieldwork assessment of nepheline syenites as alternative sources of K fertiliser (Objective 4 and Objective 5).
- Chapter 6 presents the geochemistry and petrology of Malawi's nepheline syenites (Objective 6).
- Chapter 7 shows how field spectroscopy and ASTER satellite imagery can be used to identify and map nepheline syenites and the related silicate rocks (Objective 7).
- Chapter 8 provides an assessment of Malawi soils' geochemistry and suitability of Malawi nepheline syenites as potash fertiliser (Objective 8).
- Chapter 9 provides a general discussion of the results, lessons and conclusion of the study (Objective 9).

1.7. Summary of the methodology used

The study integrated various methods to achieve the goal of the study. Figure 1.5 summarises the tasks and methodology as well as the specific objectives and chapters related to each task.

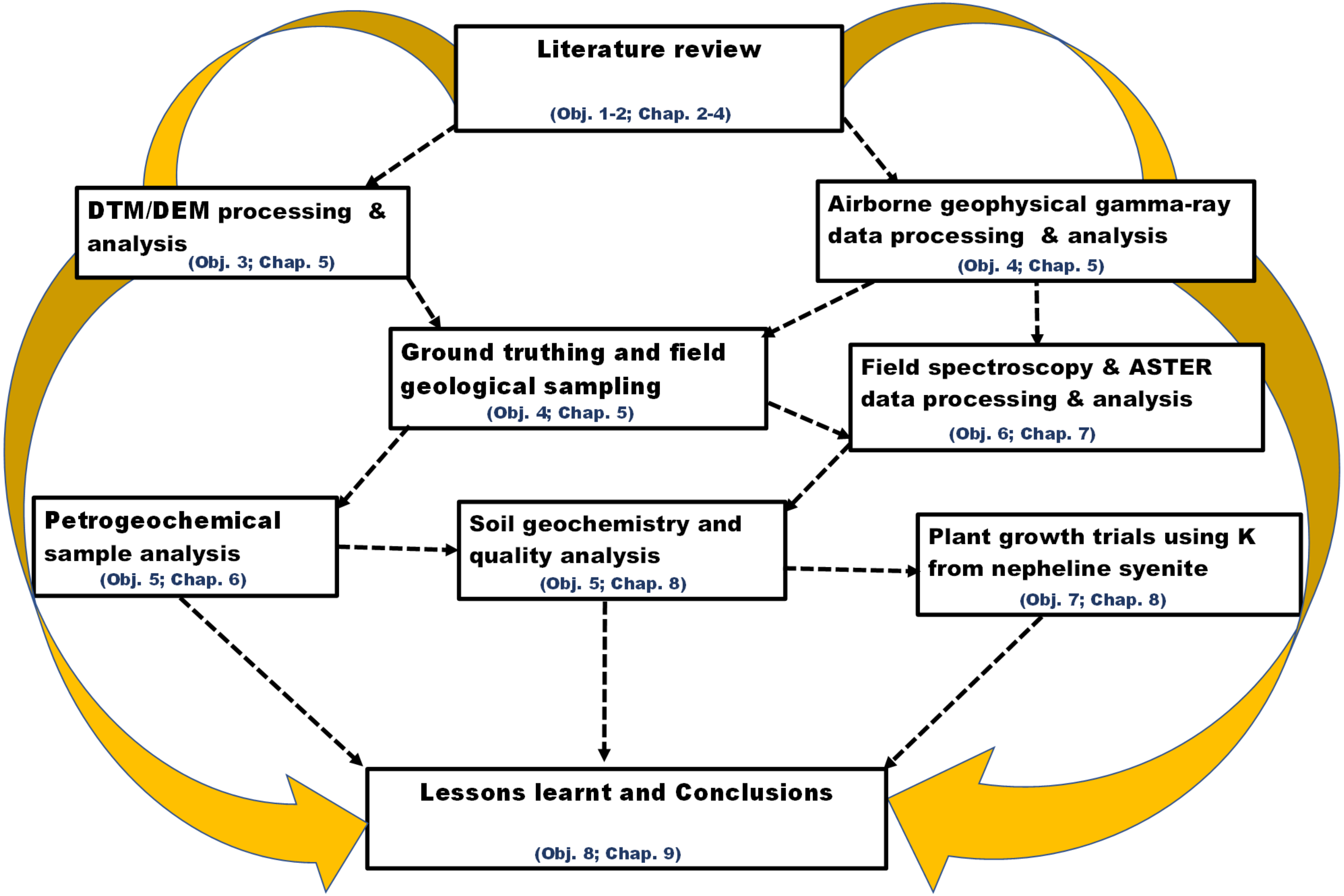

Figure 1.5: Summary of the approach used in this study to achieve each specific objective (Obj.) and as reflected in each respective Chapter (Chap.).

Chapter 2: Occurrence and geochemistry of nepheline syenites and related alkaline rocks

2. Introduction

Nepheline syenites and related alkaline rocks occur in various areas of the world. In Africa, most of them occur within the East African rift system. This chapter addresses this study's Objective 1 by providing a review of alkaline rocks, mainly nepheline syenites and to a lesser extent other related alkaline rocks, such as syenites and quartz syenites. Carbonatites are also discussed because they usually occur together with nepheline syenites, especially in rift tectonic settings. The chapter also highlights the nomenclature and classification systems for magmatic rocks, their petrogenesis, and mode of occurrence of alkaline rocks and carbonatites as well as alkaline metasomatism in relation to fenitisation. Lastly, some examples of nepheline syenite intrusions from different parts of the world are reviewed in terms of their geology, petro-geochemistry and their use as potash fertiliser.

The term "alkaline" has largely been considered ambiguous, due to its lack of a precise definition. Sørensen (1997) describes key characteristics of alkaline rocks; firstly, alkaline rocks include all silica undersaturated rocks. This also includes rocks which are alumina undersaturated, and they usually contain nepheline and/or acmite in their norms (Fitton and Upton, 1987)This description, however, applies to other igneous rocks which are silica-deficient but without necessarily being rich in alkalis. Therefore, Viana and Battilani (2014) and (Fitton and Upton, 2014), propose that alkaline plutonic rocks should be defined as those rocks which are rich in alkalis, relative to silica and alumina. Examples of such alkaline rocks include nepheline syenite, phonolite, nephelinite, ijolite, and lamproite. Some workers have concluded that the term 'alkaline' should be used for those rocks which have excess levels of K_2O+Na_2O (alkalis), above what could be accommodated in the feldspars alone (Fitton and Upton, 1987). Alkaline intrusions such as nepheline syenites are some of the most important rocks in economic geology due to the various economic minerals they host, especially the rare earths. Therefore, understanding the geo-tectonic environment of occurrence of alkaline rocks like nepheline syenites is very important.

2.1 International Union of Geological Sciences (IUGS) nomenclature and classification

The IUGS classification of igneous rocks is based on ten principles which include the use of conventional descriptive features, modal mineralogy, use of natural mineralogical phase relations, and the geochemical characterisation in cases where modal classification is limited (Le Maitre et al., 2002). The modal classification is determined by estimating the distribution and volume percent of minerals within a rock's thin section as observed under the petrological microscope. One of the key IUGS recommendations is for a rock's chemical composition to be determined and classified using variation diagrams such as binary and ternary plots. This means the chemical compositions of rocks and minerals are presented graphically and named in various ways mostly based on their oxide and/or elemental concentrations (Winter, 2014; Gill 2010).

Different discrimination and presentation techniques are used to classify the igneous rocks in geology. These include variation diagrams/plots (Wright, 1974), such as the Harker diagrams, the Total Silica-Alkali (TAS) plots (Le Bas et al., 1986, 1992), the alkali-lime index, spider diagrams, assimilation and fractionation crystallisation plots and phase diagrams (Blatt and Tracy 1996), all of which show trends or patterns in the geochemical and modal data. For example, the quartz-alkali feldspar-plagioclase-feldspathoid (QAPF) diagram classifies rocks on a double triangular diagram with its vertices occupied by quartz, alkali feldspar, plagioclase and feldspathoid.on the QAPF diagram in Figure 2.1,the silica deficient rocks such as alkali feldspar-rich rocks with almost no quartz (feldspathoids), would plot toward the “foids" vertex (F). However, quartz is highest at the apex of the quartz field (Q) and zero along the alkali feldspar (A)-plagioclase (P) line.

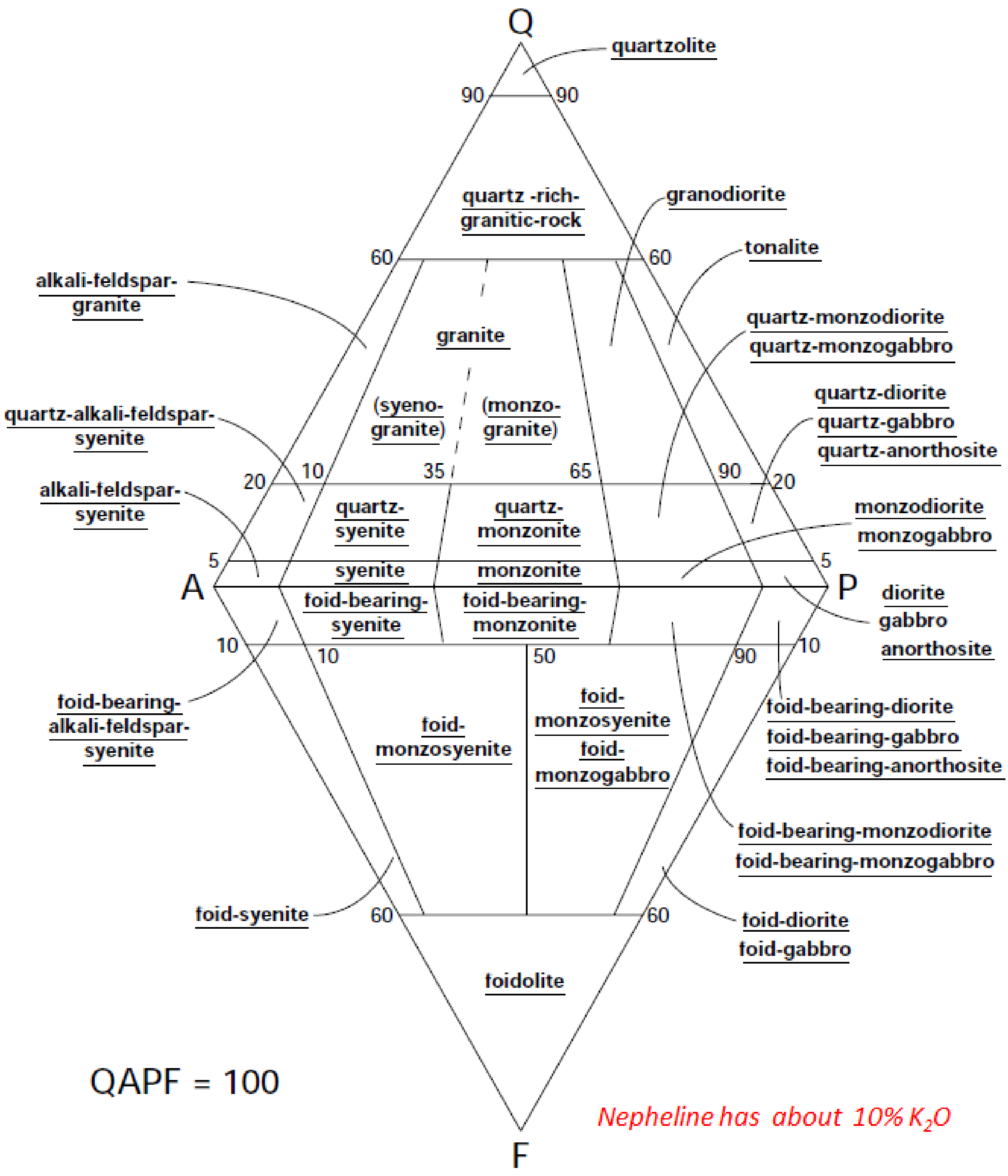

Figure 2.1: The classification and nomenclature of coarse-grained crystalline rocks according to their modal mineral contents using the QAPF diagram, adapted based on the BGS classification as presented by Gillespie and Styles (1999). The corners of the diagram show Q=quartz, A=alkali=P=plagioclase and F=feldspathoids

2.2 Tectono-geological settings of alkaline magmatism

Alkaline rocks occur in a wide range of geological settings globally. However, they are usually associated with intraplate rift tectonic settings and some anorogenic plate margins, also occurring in association with subduction zones (Skirrow et al., 2013). These rocks are not voluminous compared to other magmatic rocks, and only account for 10% of the world’s igneous rocks (Fitton and Upton, 1987). Three types of tectono-geological environments have been identified for the emplacement of alkaline rocks. These include the continental rift-tectonic-induced volcanism, oceanic and lithospheric intraplate magmatism (without tectonic activity), and subduction-related-derived alkaline igneous rocks (Fitton and Upton, 1987). In particular, continental extensional tectonism has played a vital role in the formation of numerous alkaline rocks and some of the most important alkaline-related mineral deposits come from these rocks as noted in the East African Rift System (Fitton and Upton, 1987). The tectonic rifting processes that divide continental plates are usually associated with crustal thinning and formation of rift valleys. The crustal thinning further induces faulting and magmatism, which are in most cases associated with alkaline magmas and volcanism (Skirrow et al., 2013).

2.2.1 Petrogenesis of alkaline rocks and carbonatites

Several studies have explained the evolution of alkaline and carbonatite intrusions (e.g. Andersen et al., 2010; Andersen and Sorensen, 1993; Beccaluva et al., 1992; Burke et al., 2003; Eby, 2004; El-Sayed et al., 2004; Ilbeyli, 2004; Lowell and Villas, 2007; Woolley, 1982; Worley et al., 1995; Worley and Cooper, 1995). Many of these studies show that there is a close spatial-temporal relationship between alkaline rocks and carbonatites (Best, 2003; Robb, 2005; Skirrow et al., 2013), mainly in rift tectonic environments (Woolley, 1982). Emplacement of alkaline rocks, especially nepheline syenites and nephelinites/ijolites, usually precedes carbonatite intrusion. Some igneous petrologists believe that nepheline syenite-carbonatite magmas are derived deep from within the mantle (Best, 2003; Robb, 2005). They argue that the alkaline magma must have a deeper mantle source because partial melting of the near-surface crustal rocks cannot produce such carbon-rich and silica-depleted rocks (Harris et al., 1983; Harris and Grantham, 1993). Best (2003) explains that in some cases carbonatite emplacement is preceded by nepheline syenite volcanism and characterised by fenitisation which is the metasomatic alteration of the country rock by an intrusion. Both primary and secondary fenitisation are common in the East African Rift System (EARS). Recent studies by (Broom-Fendley et al., 2017)tend to support this view by further arguing that the Songwe carbonatite complex formed in this manner in which the Songwe carbonatite magma was emplaced later and fenitised the pre-existing nepheline syenites. Broom-Fendley et al. (2017) have found that the Songwe carbonatites (132.9 ± 6.7 Ma) intruded the Mauze nepheline syenites (aged 134.6 ± 4.4 Ma).

However, other petrologists believe that some alkaline intrusions and carbonatites also form through liquid immiscibility of the parental magma, and so have the same age (e.g. Fitton and Upton, 1987a; Manzines and Murthy, 1980; Robb, 2005). As the melt rises and interacts with crustal rocks, the immiscible magma is segregated in a process which results in the carbonate-rich portion crystallising into a carbonatite while the carbonate-deficient melt forms a silicate-alkali melt. This is thought to be particularly common in subduction-related alkaline environments, where carbonatites and their associated alkaline intrusions, such as nephelinites and nepheline syenites, are produced. This occurs by means of liquid immiscible mantle-derived and mantle-metasomatised melts enriched in alkali elements and volatile elements (Robb, 2005). Robb (2005) also believes that separation of the carbonate liquid from its parental magma leads to strong fractionation among the carbonate liquid, silicate and oxide solid phases.

In other investigations, some radiogenic and stable isotopic studies have also suggested that alkaline magmas and carbonatites originate from low degrees of partial melting of metasomatised or crustally-contaminated mantle (Fitton and Upton, 1987; Manzines and Murthy, 1980). The fractionating melts then become deficient in elements such as Ta, Zr, Nb, and Sr and they tend to be more enriched in light Rare-Earth Elements and other elements like U, Th, and Pb. The world's only active carbonatitic volcano (Wiedenmann et al., 2010), the Oldoinyo Lengai Complex (a natro-carbonatite in Tanzania) is one key example of carbonatite-silicate liquid immiscibility within the EARS. Studies of the Oldoinyo Lengai Complex (Mitchell, 2009; Potter et al., 2017; Sekisova et al., 2015; Wiedenmann et al., 2010) have established that it formed through liquid immiscibility involving two key phases, namely (a) a carbonate-silicate immiscibility (b) a carbonate-halide immiscibility (Potter et al., 2017). This is supported by evidence of inclusions of nephelinite and crystallites of nephelinites and/or different silicates within carbonate and as well as of carbonates within silicate samples analysed from this Complex.

In addition, the alkaline magma ascending through the lithospheric mantle can also become trapped before it intrudes into the crust. Skirrow et al. (2013) further explain that factors which can stop the ascent of magma include heat loss, an increase in the solidus temperature with a decrease in pressure, decrease in density and increase in strength of the wall rocks. More commonly, the carbonatite magma ascent can also be halted by reaction of the ascending magma with wall rocks to form Ca and Mg silicates plus CO_2 (Skirrow et al., 2013). Under reducing conditions, carbonate melt can be reduced to elemental carbon (graphite or diamond) or to methane.

All these processes have the potential to deplete volatiles, like dissolved CO_2, from the magma, thereby facilitating fractional crystallisation of the carbon-rich magma. A typical alkaline and carbonatite mineralisation is the product of the emplacement of volatile-rich (CO_2, F and/or water) alkaline magmas which occur as subsurface intrusions. When a magmatic-hydrothermal fluid is released from the alkaline melt, there may be depressurisation and metasomatism through the magmatic fluid and wall-rock interaction or between two or more melts themselves (Robb, 2005; Skirrow et al., 2013).

From the review of the literature, there is still much debate about the actual mode of petrogenesis of these rocks. The role of carbonatite–nepheline syenite segregation and subsequent emplacement in rift tectonics needs more detailed studies. The melt is derived from a silica-depleted, volatile-rich, deeper mantle parental magma which would then form carbonatites and nepheline syenites occurring close to each other. This is common in some carbonatite–nepheline syenite intrusions including those in Malawi, where this close occurrence is noted in areas such as the Tundulu, Songwe-Mauze and Nkalonje complexes.

2.2.2 Role of alkaline fenitisation

Fenitisation is the metasomatic alteration of the country rocks through contact metamorphism with nepheline syenites and carbonatites (Robb, 2005). Fenitisation is common within the continental alkaline complexes, where potassic and/or sodic fluids of the crystallising alkaline melt alter the country rocks, through contact metasomatism, to produce new rock units known as *fenites.* The fenites have a close resemblance to the metasomatising rocks such that they may sometimes be indistinguishable from their igneous protoliths.

The main effects of fenitisation include the development of sodic and ferromagnesian minerals (mainly aegirine and arfvedsonite), the substitution of quartz by alkali feldspars, whereas the original feldspars become substituted by nepheline (Harlov and Hakon Austrheim, 2013). This shows that fenitisation be could potentially helpful for potassium resource exploration because it makes the nepheline syenites more potassic as sodium exsolves from the nepheline syenites to the fenites during metasomatism. Mineralisation is commonly restricted to carbonatite dykes, sills, breccias, sheets, veins, and large masses, but may also occur in other rocks associated with the complex rocks. For example, fenitisation is also associated with widespread alkali metasomatism of quartzo-feldspathic rocks. Around the carbonatite contact zones, fenitisation is also associated with reducing alkali feldspar, some aegerine and subordinate alkali-hornblende, accessory titanite and apatite as noted by Broom-Fendley et al. (2016) and Simakin et al. (2010).

2.3 Nepheline syenite occurrence and mineralogy

Nepheline syenite is a leucocratic, coarse to medium-grained, alkaline igneous rock, which is usually silica undersaturated and so contains no quartz. In terms of its mineralogical composition, the key minerals include about 48–54% albite ($NaAlSi_3O_8$); 18–23% microcline ($KAlSi_3O_8$), 20–30% nepheline ($(Na,K)AlSiO_4$) and less than 30% mafic minerals (Gill, 2010). Minor minerals may include pyroxene, biotite, magnetite and hornblende. Accessory minerals may include zircon, titanite, apatite and corundum. Nepheline syenite falls under a syenite sub-category of "*foid-bearing*" group of alkali-feldspar syenites. The major petrographical characteristics of these rocks include a coarse-grained, holocrystalline, hypidiomorphic granular texture. The key mineral in a nepheline syenite is nepheline, $(Na,K)AlSiO_4$, which is unstable in silica saturated environments at high temperatures. Nepheline is a dark grey brittle mineral and with a tridymite derivative structure (Haaker and Ewing, 1981). It has a poor cleavage, and a hardness of 5.5-6 on the Mohr's scale of hardness. In thin sections, nepheline usually shows subhedral grains (Gill, 2010; Winter, 2014).

Nepheline syenite is a rock with high nepheline and potassium content. Therefore, nepheline syenites could be potentially ideal as possible sources of K silicate fertilisers. Ultra-potassic rocks have K_2O/Na_2O values of >3, with K_2O values ranging between 2-19wt%; they also have high concentrations of lithophile elements such as Rb, Ba and Zr (Gupta, 2015). Nepheline syenites are generally classified as either agpaitic or miaskitic (Marks and Markl, 2017; Sørensen, 1974). Agpaitic nepheline syenites are described by Sørensen (1997) as those peralkaline nepheline syenites (and phonolites – the fine grained equivalent) that are characterised by a larger agpaitic coefficient (alkaline/alumina ratio) i.e:

$$\textit{Agpaitic nepheline syenite: } \frac{(Na_2O+K_2O)}{Al_2O_3} = >1.2 \qquad (2.1)$$

They often contain minerals like eudialyte $Na_{15}Ca_6Fe_3Zr_3Si(Si_25O_{73})(O,OH,H_2O)_3(Cl,OH)_2)$ and rinkite $((Ca_3REE)Na(NaCa)Ti(Si_2O7)_2(OF)F_2)$ according to Marks and Markl (2017). The agpaitic rocks exhibit very high concentrations of various elements notably Li, Be, Nb, Ta, REE, Zr, Th, among others plus some volatiles of which F and C1 are key. Some workers attribute the evolution of these rocks to their parental magma and mode of emplacement. For example, Sørensen (1997) postulates that agpaitic nepheline syenites form through amalgamation of oversaturated alkali (especially sodium) enriched magma under high-pressure environments that make it difficult for the volatiles to escape. However, Heifer (1964) does not accept this notion, counter-arguing that alkaline rocks are usually associated with a geological setting characterized by faulting and mobile crustal belts, like the case of the African rift system. Therefore, the argument of these rocks developing under high CO_2 pressure or not is still debatable. Examples of agpaitic nepheline syenites in Malawi are the eudialyte-bearing Junguni nepheline syenite, and the Mauze and Nkalonje intrusions (Marks and Markl, 2017) .

On the other hand, miaskitic nepheline syenites are usually leucocratic and hypersolvus. Sørensen (1997) further elaborates that agpaitic nepheline syenites are distinguished by a smaller agpaitic coefficient i.e:

$$\textit{Miaskitic nepheline syenite: } \frac{(Na_2O+K_2O)}{Al_2O_3} = <1 \qquad (2.2)$$

Miaskatic nepheline syneites are characterised by minerals such as nepheline, perthite, leucite and sodalite as some of principal minerals. Biotite is the major mafic mineral, while ilmenite, zircon and pyrochlore are characteristic accessory constituents. These include nepheline syenites from the Miask, (South Urals, Russia), the Litchfield intrusion (Maine, USA) and the Lujavr/Lovozero intrusions in the Kola Peninsula, north-western Russia. Sodalite-bearing nepheline syenites are known from the Dìtro complexes in Romania (Sorensen, 1997).

2.4 Petro-geochemistry of selected nepheline syenites

The nepheline syenites from different parts of the world, generally, show similar characteristic features. Some notable petrogenetic differences also exist among these rocks. It is vital to understand these petrogenetic features in order to determine their potential as alternative potash sources. The available literature about the geochemistry of nepheline syenites is not detailed in many areas, especially in Africa. The lack of interest shown by researchers in these rocks could suggest that their economic potential has not been recognised, apart from the common role they serve as sources of industrial minerals (especially as raw materials for glass and ceramics manufacture). Examples of occurrence of these rocks, globally, include the nepheline syenites, carbonatites and associated rocks of the South Nyanza complexes, Kenya (Chorowicz, 2005), the nepheline syenite pegmatites of the Oslo Rift, Norway (Andersen et al., 2010), the Monte Santo (Viana and Battilani, 2014), and the Poços de Caldas (Schumann, 1993) syenite and nepheline syenite complexes in Brazil (Schorscher and Shea, 1992; Shea, 1992), the nepheline syenites of North Cape and Stjernøy, North Norway (Heier, 1963) as well as the carbonatites and nepheline syenites of the British

Columbia (Pell, 1994). The following section discusses the different nepheline complexes grouped in accordance with their geographical locations.

2.4.1 The Stjernøy, Oslo Rift and Lassefjordfjell nepheline syenites from Oslo, Norway

Previous petrological and geochemical studies have shown that nepheline syenites of Norway, especially the Stjernøy complex, are characterized by substantial silica-deficiency and excess alumina. For instance, comparative representative samples of biotite-nepheline syenites and pyroxene-nepheline syenites from these areas show contents of SiO_2 (52.37-52.73 wt.%), Al_2O_3 (23.22-23.71 wt.%), Na_2O (6.87-7.78 wt.%), K_2O (8.30-8.8% wt.%), (Heier, 1963). Furthermore, comparison between these two Norwegian igneous provinces shows that the Oslo area largely comprises nepheline syenites which have lower silica and alumina, especially in the Lardalite area. Geochemical characterization has also shown a close association between the nepheline syenites of Stjernøy and neighbouring carbonatites. However, in both Oslo and Stjernøy, metasomatically altered rocks show similar minerals to the ones observed in the unaltered nepheline syenites. For example, both metasomatic and unaltered rocks show that nepheline is gradually replaced by other minerals such as sericite, calcite and albite (Andersen and Sørensen, 1993).

In addition, the Oslo Rift nepheline syenites also show low TiO_2, MnO and MgO concentrations (Figure 2.1). The data from both the Stjernøy and Lassefjordfjell nepheline complexes also show that the nepheline syenites contain low Th and U concentration although the Stjernøy nepheline syenites are more depleted in U and Th relative to K (Heier, 1963). These low U values are an important diagnostic feature for the geochemical discrimination of nepheline syenites from granites (Dickson, 2004; Dickson and Scott, 1997; Wilford, 2012). Heier (1963) also noted that contents of major elements in the Stjernøy nepheline syenites are much closer to the mean geochemical elemental concentration for the Oslo Rift nepheline syenites, which suggests that they could be from a similar parental magma or may have a similar petrogenetic history.

The nepheline syenites within the Oslo Rift characteristically contain metasomatized xenoliths (Andersen and Sørensen, 1993). The fresh nepheline syenite samples also contain titanite and clinopyroxene, which occur in contact zones with unaltered nephelines plus magnetite and apatite as accessory minerals (Frost and Frost, 2008). Other researchers have argued that the Oslo Rift nepheline syenites possibly formed *in situ* in an environment characterised by degassing (Frost and Frost, 2008). They advance that, in such circumstances, the melt could have been associated with the mixing of crustal rocks with high temperature vapours and energy from beneath the Earth’s surface. However, strong evidence to support such an argument is lacking.

2.4.2 Nepheline syenites from the British Columbia and Ontario

Until 1989, there was no commercial production of nepheline syenite in Western Canada and most of the raw materials were then exported from Ontario (White, 1989). However, by 1994 Canada’s Blue Mountain deposit (in British Columbia) was not only dominating Canada, but also the Western world, in terms of production of nepheline syenite. Like other alkaline rocks and associated carbonatites, metasomatic fenitisation in the nepheline syenites of British Columbia, usually gives fenites more enriched in sodium and ferric iron (Pell, 1994). Thus fenitisation makes the nepheline syenites more potassic as sodium exsolves to the fenites.

While most continental alkaline rocks tend to be structurally controlled having been, mostly, fault-initiated, the Blue Mountain nepheline syenites of British Colombia are different from many known complexes. Pell (1994) highlights that the Blue Mountain nepheline syenites were emplaced within a sedimentary prism of a rifted continental margin, unlike most of the world’s mantle-derived nepheline syenites’ parental magmas, which intrude into areas of long tectonic stability (cratons). Possibly, this is why the Blue Mountains nepheline syenites are more voluminous compared to those in other parts of the world. Some of the key characteristics of the nepheline syenite outcrops in British Columbia include their grey colour, medium-coarse gained texture, and high feldspar content (Pell, 1994). In some areas, the weathered nepheline syenites show abundant K feldspar with some plagioclase intergrowths, which occur with or without nepheline, micas (muscovite and biotite) and amphiboles.

In other parts of the British Columbia, such as the Mount Copeland, nepheline syenite gneissic bodies occur conformably, with the calc-silicate gneiss and marble rocks (Pell, 1994). In the Haliburton-Renfrew area of Ontario, the rims of these intrusions lack nepheline and Jaffer (1990) attributed this to reactions with the surrounding country rocks. . Compositional data for Canadian nepheline syenites are summarised in Figure 2.2, where they are compared with data from Norway.

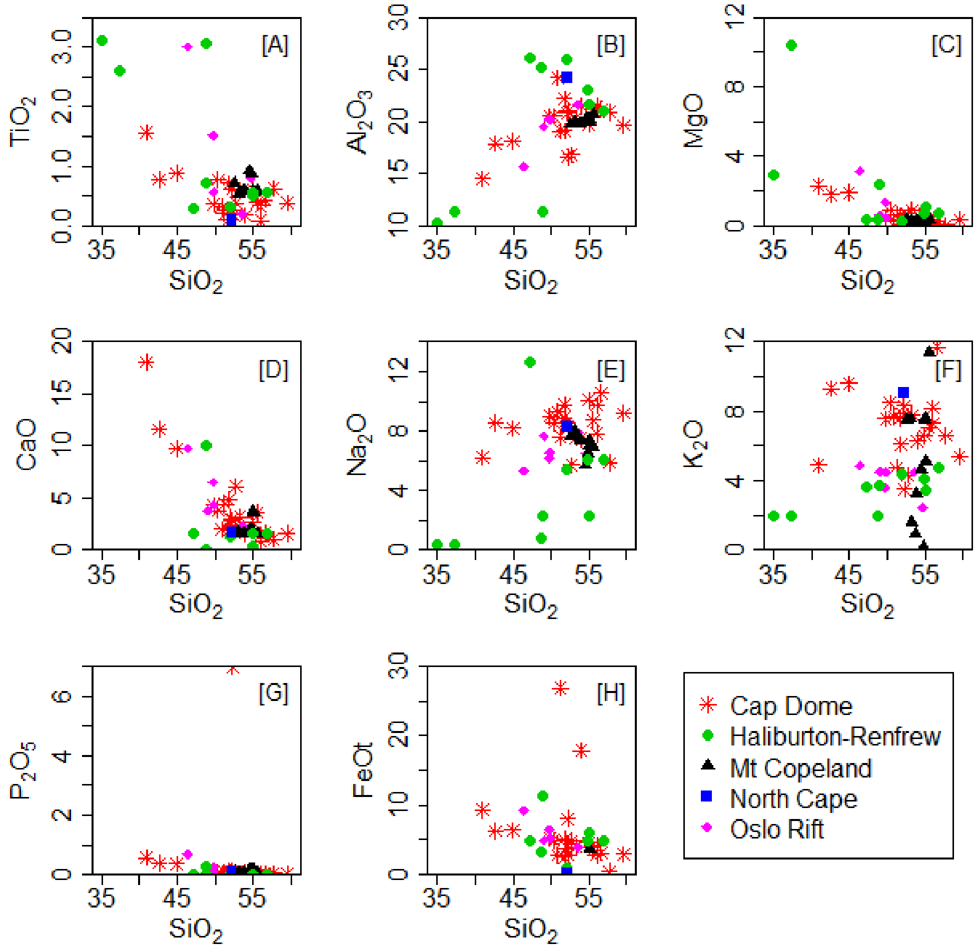

Figure 2.2: Harker diagrams for nepheline syenite from the Oslo Rift and North Cape (Norway), Ontario's Haliburton-Renfrew deposit and Mt Copeland (British Columbia).

2.4.3 The Poços de Caldas, Monte Santo and Magnet Cove nepheline syenites

Brazil's, and probably the world's, largest alkaline ring complex at Poços de Caldas, is another key nepheline syenite complex. Located in southeast of Brazil (21°45'S, 46°25'W), the Poços de Caldas complex shows nepheline syenites, which are weathered to give commercially valuable bauxite deposits (Schumann, 1993). Not much is known about the geological history of this ring complex. However, Schorscher and Shea (1992) and Shea (1992) have hypothesised that the complex evolved from magmatic evolution, which then resulted into the complex being enriched in K to a greater extent than nepheline syenites and phonolites in other areas of the world. The metasomatic alteration in this ring structure is associated with hydrothermal fluids which produce more potassic rocks characterised by low temperature, fine-grained minerals such as microcline, illite, kaolinite, opaque minerals, carbonates and smectites. These minerals replace magmatic K-Na-feldspar, nepheline and some mafic minerals (Schorscher and Shea, 1992). The nepheline syenites of the Poços de Caldas area have low TiO_2, MnO and MgO (Fig 2.3).

The Monte Santo Alkaline Intrusive Suite (MSAIS) is another important intrusion in Brazil (Viana and Battilani, 2014). The area comprises various alkaline rocks including nepheline syenites and syenites which were intruded into the Rio do Coco meta-pelites and meta-volcanic-sedimentary sequences. Comparatively, the rocks from the Monte Santo complex (Viana and Battilani, 2014) contain higher TiO_2, MgO and Na_2O values than those from the Poços de Caldas but lower contents of the other oxides (Figure 2.3). Figure 2.3 also shows data from the Magnet Cove alkaline suite in Hot Spring County, Arkansas, the United States of America (USA). The Magnet Cove intrusion consists of a complex geology made up of different lithological units (Flohr and Ross, 1990). The key rock units in this 12km^2 complex include syenites, phonolites and trachytes, nepheline syenites and ijolites. Most of the rocks are either much weathered or not exposed on the surface. Some of the well-exposed nepheline syenites in the complex have been described as “nepheline syenite pegmatite" because they are uniformly coarse-grained (Flohr and Ross, 1990). These nepheline syenites, especially at the Diamond Jo location, also have high (Na_2O+K_2O) to Al_2O_3 ratios >1, with low MgO and high FeO, and also low contents of some trace elements such as Zr, Nb, U, Th and Zn.

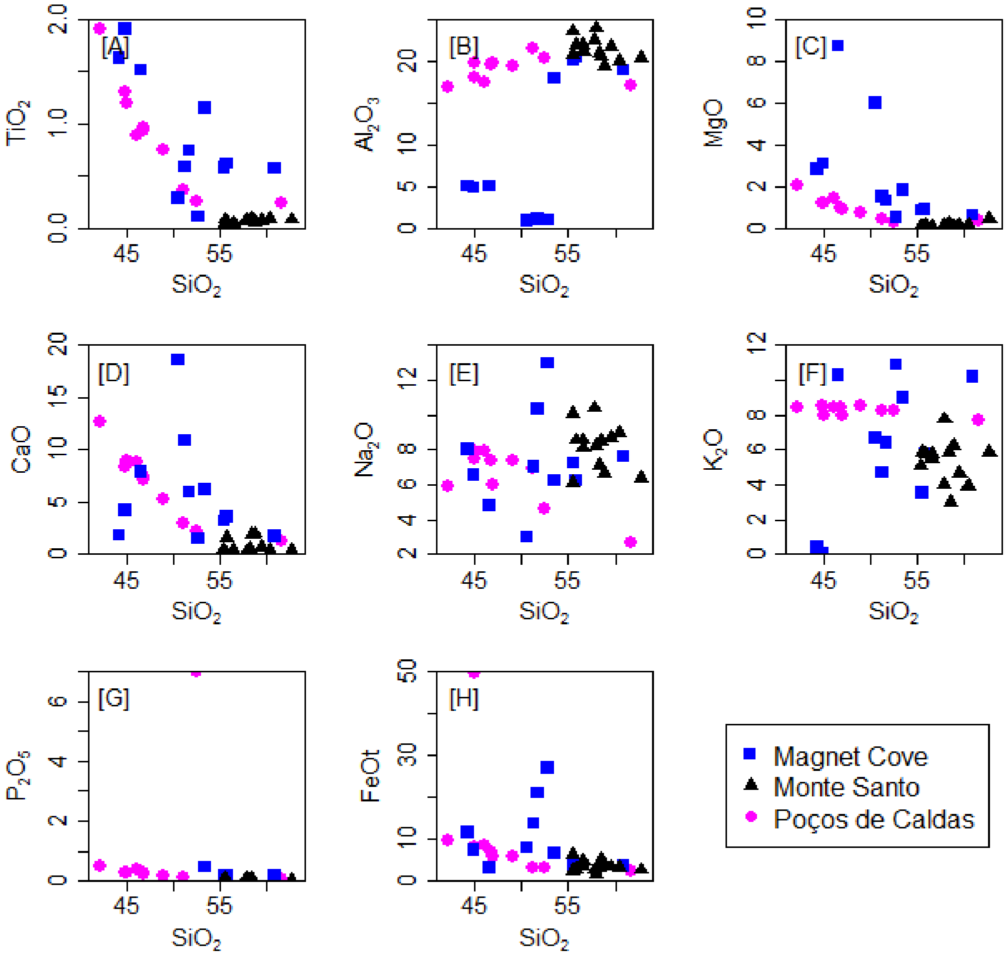

Figure 2.3: Harker diagrams for Magnet Cove alkaline suite (data from Flohr and Ross, 1990) the Poços de Caldas and Monte Santo Brazil (data from Viana and Battilani, 2014).

2.4.4 The Straumsvola nepheline syenite complex, Dronning Maud Land, Antarctica

The Straumsvola nepheline-syenite is a 10km-wide complex on the eastern border of Dronning Maud Land, Antarctica. It is wholly a nepheline syenite intrusion which is dated to the Mesozoic rifting about 170Ma (Harris and Grantham, 1993). The nepheline syenites in the Straumsvola area are classified into two units based on their volumetric and spatial characteristics. One group occurs in the form of a layered inner zone and while the other group occurs as an underlying, relatively structure-less outer zone (Harris and Grantham, 1993). The nepheline syenites in this complex contain more silica than many nepheline syenites in other countries but their geochemical data is scanty.

2.4.5 Nepheline syenites of West and East Africa

In West Africa, the Kpong complex of south-eastern Ghana has nepheline syenites and carbonate-rich rocks which show deformation within the Pan-African Dahomeyide suture zone (Nude et al., 2009). The Dahomeyide orogeny is believed to have formed from oceanic lithospheric subduction (Nude et al., 2009). This suggests that the Kpong complex's nepheline syenites are of a different petrogenetic environment from those of the East African Rift System (EARS), which formed from crustal warping and rift faulting. The Kpong complex nepheline syenites are characterised mainly by feldspars. Biotite, calcite and nepheline are also prominent in both the nepheline syenites and the carbonate rocks. The nepheline syenites in the Kpong complex also contain high TiO_2 and FeO with low MgO, Cr and Ni contents (Figure 2.4). In East Africa, the 6km x 4km Bingo carbonatite-ijolite-nepheline syenite complex, in north-eastern Democratic Republic of Congo (DRC, formerly Zaire), is one of the alkaline complexes close to the margin of the Western arm of the East African Rift System (Woolley et al., 1995). Geochemical data for the nepheline syenites and ijolites in this complex show that the rocks had undergone cycles of fractionation processes. These rocks also show low SiO_2, K_2O, TiO_2 and MgO contents (Figure 2.4). The key minerals in this complex's nepheline syenites include feldspar, nepheline, pyroxene and cancrinite. Accessory minerals include titanite, calcite, biotite, wollastonite, fluorite, zeolite, zircon, eudialyte and amphiboles.

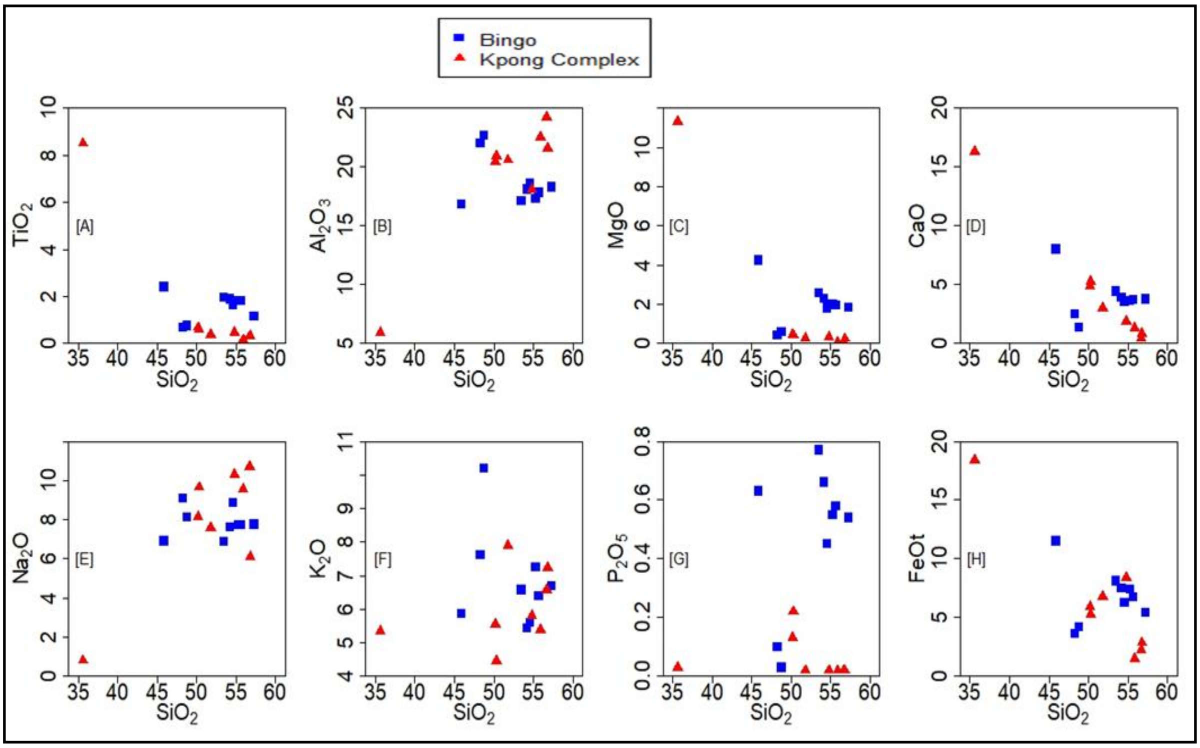

Figure 2.4: Harker diagrams for nepheline syenites of Kpong (Ghana) and Bingo (Zaire) complexes.

Furthermore, Africa’s alkaline ring complexes comprise two groups. On one hand is a group assigned to the Eburnean-Ubendian former mobile domains, which are generally oversaturated in alkalis (Bowden, 1985). Examples of these intrusions occur in Morocco, Mauritania, Ivory Coast, SW Angola, Zambia, Zaire and Tanzania, with their ages ranging between 2000 and 1500 Ma, in the Eburnean-Ubendian former mobile belt. On the hand, is a group of intrusions which are related to the Late Precambrian Pan-African Orogeny (aged ~500 Ma (Kröner and Stern, 2005) and subsequent periods notably the Phanerozoic anorogenic magmatism. These nepheline syenites are slightly silica-saturated unlike the former group, and they include the Palabora carbonatite, the Spitskop and the Pilanesberg complexes of South Africa (Andersen et al., 2016).

2.5 Nepheline syenites of Malawi and relationship with other parts of the world

Information about the geochemistry of many East African alkaline intrusions is limited (Barber, 1974), because not much has been published on the geochemistry of these rocks. Specifically, there has been little research on Malawi’s nepheline syenites until recently, when exploration for Rare Earth Elements in Malawi has attracted interest of some potential investors (BGS, 2009; Broom-Fendley et al., 2017; Onuma et al., 2013). Attention has focused on nepheline syenites occurring mainly in the Chilwa Alkaline Province of Early Jurassic to Late Cretaceous age in southern Malawi, and few intrusions occur outside of this province.

Compared with the nepheline syenites from British Columbia, Brazil and Ontario, the reviewed literature has shown that Malawi's nepheline syenites have higher K_2O and Na_2O content, as observed from geochemical results from the Kasungu-Chipala-Illomba-Ulindi nepheline syenites. Figure 2.5 (A) shows that the rocks from Malawi are much like those from Zaire, Brazil and the British Columbia. Figure 2.5 (B) show that the nepheline syenites from Malawi are similar to the rocks from Zaire, Brazil and the British Columbia.

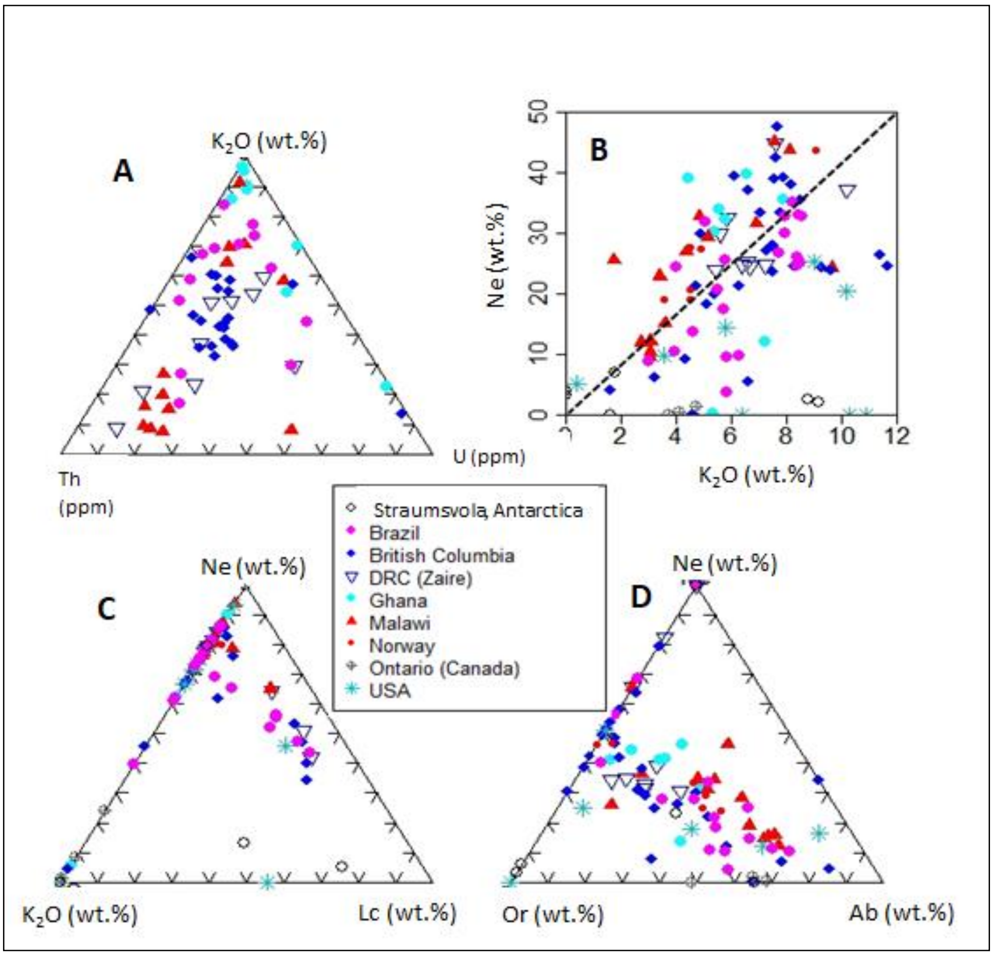

Figure 2.5: Comparison of Malawi nepheline syenites and the rest of the world showing (A) K_2O,U,Th ternary plot, (B). potassium vs normative nepheline binary plots, (C) normative nepheline (Ne)-K_2O-nomative leucite (Lc)ternary plot and (D) normative nepheline (Ne)-normative orthoclase (Or)- normative albite (Ab).

Figure 2.5 (C) and Figure 2.5 (C) also show that the nepheline syenites from Malawi are similar to the rocks from the Coldwell complex, (Ontario, Canada), Brazil and the British Columbia, some of which have been used as potassium sources for agriculture. This suggests that Malawi's rocks could also be suited as potassium fertiliser sources. Malawi's and Zaire's (Democratic Republic of Congo) nepheline syenites appear to be closely related and possibly share a common tectonic environment within the East African Rift System (EARS). However, nepheline syenites from Malawi show higher TiO_2, MgO and MnO contents.

On a global scale, Malawi’s nepheline syenites also compare closely with those from other parts of the world like Norway, British Colombia, and Ontario, the USA, as well as the alkaline rocks which are being used for potash fertiliser in Brazil (Poços de Caldas; Figures 2.6-2.7). Using the North Cape as a model area, show that several areas plot in similar manner like North Cape nepheline syenite. This suggests that these rocks could also be useful as alternative K fertilisers.

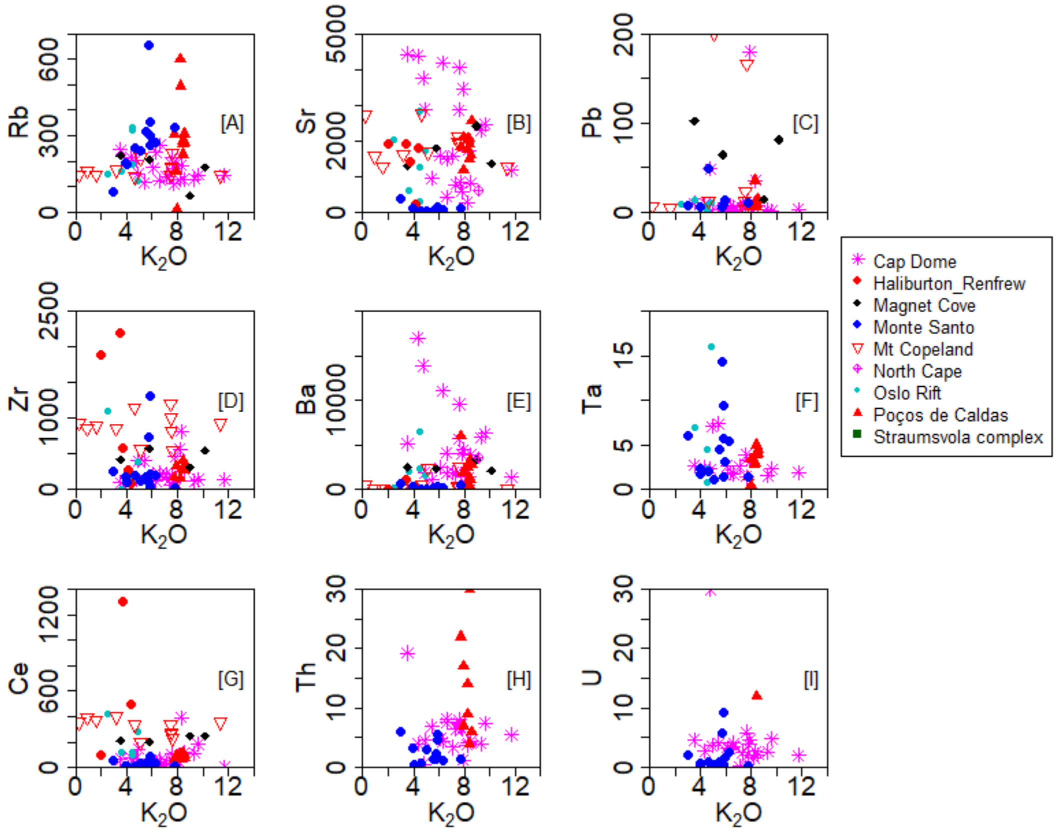

Figure 2.6: K_2O vs selected trace elements for rocks from Europe South and North America in which several areas show geochemical similarities with North Cape Nepheline syenite.

Malawi’s nepheline syenites show U values ranging from 0.12 to 35 ppm and an average of 6.11ppm. Compared to nepheline syenites from other parts of the world, Malawi’s nepheline syenites also have higher average values for K, U and Th than those of most nepheline syenite intrusions from other parts of the world. The values ranged from 1.74 to 9.66 wt % (mean of 4.81 wt %) for K_2O while Th contents ranged from 0.30 to 30.7 ppm (mean 12.59ppm). As shown in Figure 2.5 and Figure 2.6, the nepheline syenites from different parts of the world, as reviewed in this chapter, show values in the range of the ranges of 0 to 11.7 (mean of 5.63 wt %) for K_2O. They, however, show similar ranges of 0.1 to 59.3ppm (average 8.62ppm) for Th and similar ranges of 0.04 to 35ppm (average 4.72ppm) for U. For example, Malawi’s Illomba nepheline syenites and those from the Bingo Complex, British Columbia and some rocks from Brazil all show low U values. In contrast, the Kasungu-Chipala, Ilomba, Ulindi nepheline syenites in Malawi show uranium values which are slightly higher than the reported values for nepheline syenites of Norway and British Columbia. In most reviewed case studies, trace elemental geochemical data have not been adequately presented. Rocks from the Monte Santo Alkaline Suite (Brazil), also show low Th (0.5-4.6%) and U (0.2-1.6%) K values (Viana and Battilani, 2014).

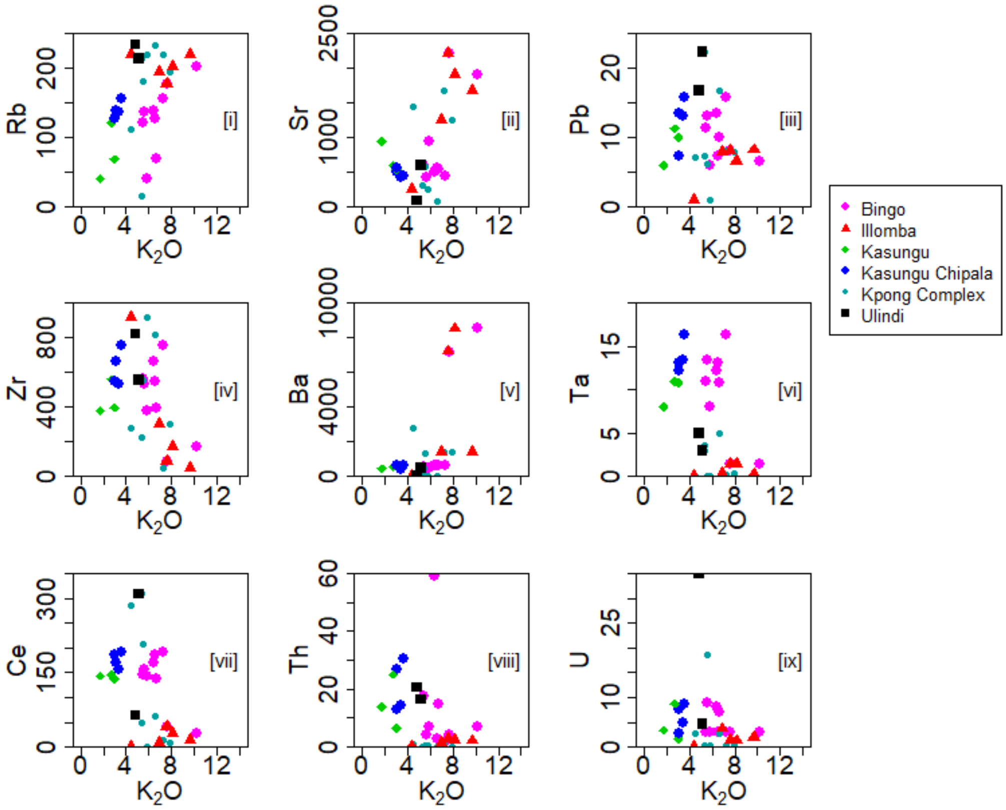

Figure 2.7: K_2O vs selected trace elements for rocks from Malawi and some parts of Africa. There are similarities between data from Malawi and other parts of Africa (namely Bingo and Kpong Complexes).

2.6 Conclusion

This chapter has shown that there is still uncertainty in understanding the origin of the alkaline rocks, especially nepheline syenites and carbonatites. Silicate-carbonate liquid immiscibility may be a key mechanism in the formation and emplacement of some nepheline syenites and carbonatites in rift tectonic settings. Key characteristics of these rocks are that contact metasomatism and fenitisation are common. Nepheline syenites are important rocks in terms of their economic potential as a source of industrial minerals and Rare Earth Elements. Geochemical data from the few areas studied in Malawi is similar to those from other locations whose potential for use as fertilizers has been tested. In addition, it has been noted Th or U data are missing in most of the published literature reviewed so far, which makes detailed comparison of the rocks on basis of Th and U content (essential for airborne gamma surveys) difficult.

Chapter 3. Potential of nepheline syenites as potash fertiliser: literature review

3.0 Introduction

This chapter reviews the potential of nepheline syenite as a possible potash fertiliser. The chapter further builds on chapter 2 by expanding on the Objective 1 of this study. However, unlike chapter 2, this chapter expounds more on the rationale for conducting the research and particularly why Malawi nepheline syenites are potentially suitable candidates for alternative potash sources. chapter 1 has shown the major challenges faced in Malawi and the whole of Sub-Sahara Africa (SSA), where because of lack of fertiliser manufacturing companies and high import costs, fertilisers, especially potassium fertilizer, are expensive and scarce. This has resulted in the failure by subsistence farmers to use these fertilisers. Therefore, the use of geological resources for potassium fertilisers would help such vulnerable agricultural communities and save their farmland from soil nutrient mining. This chapter is, therefore, important as it sets the benchmark on the suitability of nepheline syenites as a viable alternative potash source.

3.1 Alkaline rocks as agricultural fertilizer sources

Potassium concentration in the Earth's crust overall is 2.8% K_2O or 2.3% K (van Straaten, 2007). It is more enriched in silicate minerals such as K feldspar, nepheline, leucite and others (Table 3.1). The use of potash fertiliser was recognised as early as the dawn of the 18th century and has undergone technological advancements since then (Figure 3.1), especially in the First World. Silicate potassium sources were identified as potential K fertiliser sources as early as 1847 but recently, many studies have focussed on using feldspars. Studies have also shown that feldspathoids such as kalsilite and leucite have high K content compared to other silicate minerals (Table 3.1). However, experimental studies have shown that nepheline has the highest dissolution rate compared to other silicates, and dissolves about 10,000,000 times much faster than potassium feldspar (Palandri & Kharaka, 2004). This means that it releases the K needed for plants the fastest. For this reason, nepheline stands out as the most ideal potential alternative K silicate source for agricultural production. Most food crops are seasonal with a short growing period, which, with the faster dissolution rate, then makes nepheline's use more potentially significant in Africa.

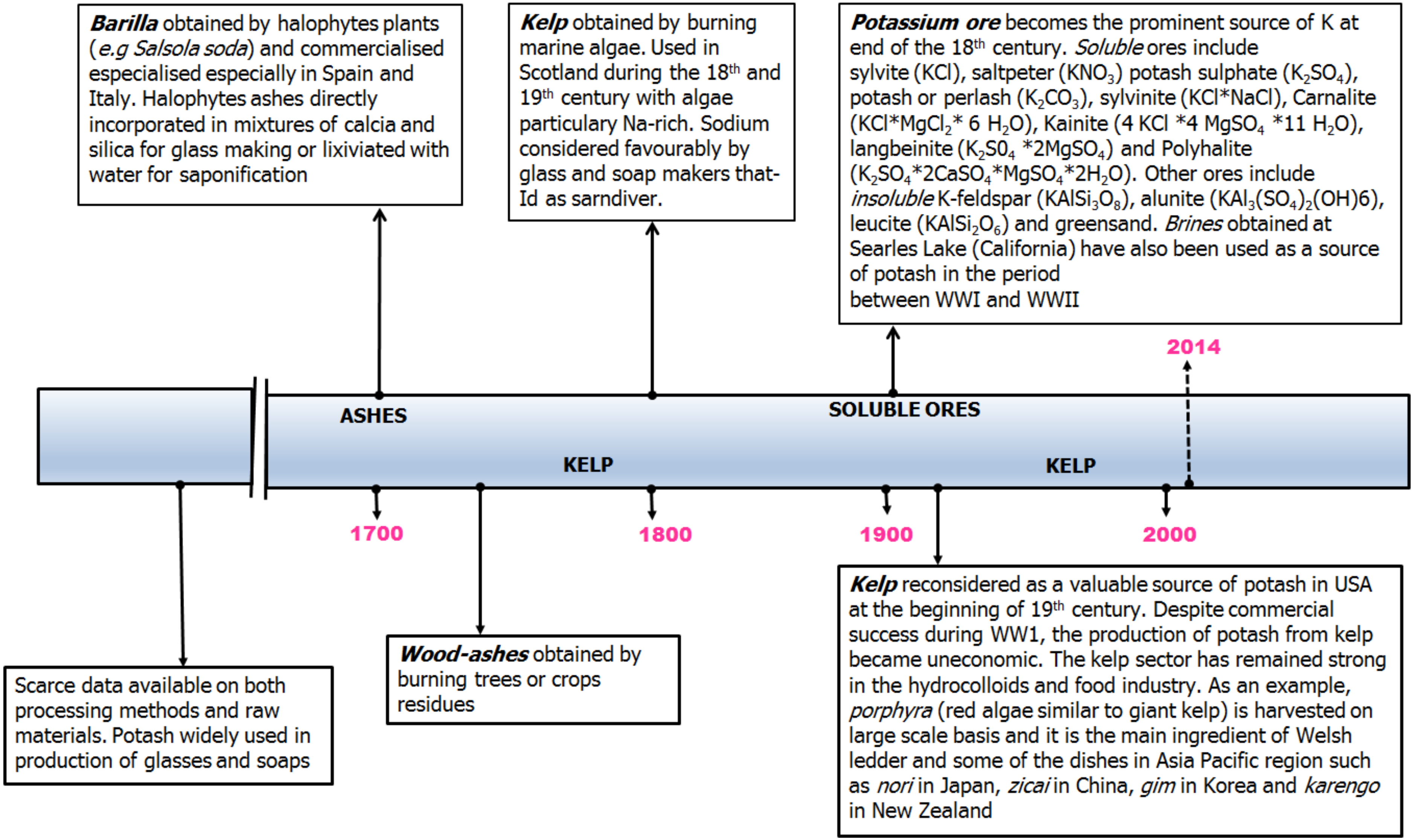

Barilla obtained by halophytes plants (*e.g Salsola soda*) and commercialised especialised especially in Spain and Italy. Halophytes ashes directly incorporated in mixtures of calcia and silica for glass making or lixiviated with water for saponification

Kelp obtained by burning marine algae. Used in Scotland during the 18th and 19th century with algae particulary Na-rich. Sodium considered favourably by glass and soap makers that-Id as sarndiver.

Potassium ore becomes the prominent source of K at end of the 18th century. *Soluble* ores include sylvite (KCl), saltpeter (KNO_3) potash sulphate (K_2SO_4), potash or perlash (K_2CO_3), sylvinite (KCl*NaCl), Carnalite ($KCl*MgCl_2* 6 H_2O$), Kainite ($4 KCl *4 MgSO_4 *11 H_2O$), langbeinite ($K_2S0_4 *2MgSO_4$) and Polyhalite ($K_2SO_4*2CaSO_4*MgSO_4*2H_2O$). Other ores include *insoluble* K-feldspar ($KAlSi_3O_8$), alunite ($KAl_3(SO_4)_2(OH)6$), leucite ($KAlSi_2O_6$) and greensand. *Brines* obtained at Searles Lake (California) have also been used as a source of potash in the period between WWI and WWII

Scarce data available on both processing methods and raw materials. Potash widely used in production of glasses and soaps

Wood-ashes obtained by burning trees or crops residues

Kelp reconsidered as a valuable source of potash in USA at the beginning of 19th century. Despite commercial success during WW1, the production of potash from kelp became uneconomic. The kelp sector has remained strong in the hydrocolloids and food industry. As an example, *porphyra* (red algae similar to giant kelp) is harvested on large scale basis and it is the main ingredient of Welsh ledder and some of the dishes in Asia Pacific region such as *nori* in Japan, *zicai* in China, *gim* in Korea and *karengo* in New Zealand

Figure 2.8: A historical summary of developments in potash use from the 17th century to present (adapted after Ciceri et al., 2015).

Table 3.1 shows that nepheline-bearing syenites and other alkaline rocks are potentially important sources of potassium silicate fertilisers. For example, the nepheline syenite and feldspar mineral deposits of Ontario and British Columbia are reliable K silicate sources for the Western World. In Ontario, ,two companies could produce about 654,000 tonnes in 2014, up from about 646,000 tonnes of nepheline syenite in 2013 (Tanner, 2014). There is need therefore, to map and assess the potential of Malawi's nepheline syenites and other parts of the East African rift system, as potash sources.

Table 3.1: Main K mineral sources with their potassium contents (Source: Manning, 2010).

Mineral	**Formula**	**Weight % K**	**Weight % K_2O**
Potash ore mineral			
Sylvite	KCl	52.35	63.09
Carnalite	$MgCl_2$	14.05	16.94
Kainite	$KMgSO_4Cl.3H_2O$	15.69	18.91
Langbeinite	$2MgSO_4K_2SO_4$	18.84	22.71
Silicate minerals			
Potassium feldspar	$KAlSi_3O_8$	14.03	16.91
Leucite	$KAlSi_2O_6$	17.89	21.56
Nepheline	$(Na, K)AlSiO_4$	13.00	15.67
Kalsilite	$KAlSiO_4$	24.68	29.75
Muscovite	$KAl_3Si_3O_{10}(OH)_2$	9.03	10.88
Biotite	$K_2Fe_6Si_6Al_2O_{20}(OH)_4$	7.62	9.18
Phlogopite	$K_2Mg_6Si_6Al_2O_{20}(OH)_4$	9.38	11.30

Other studies have further shown that nepheline have the highest dissolution rates. For example, the experimentally determined dissolution rates for silicate minerals (collated by Palandri and Kharaka, 2004) found the highest rates in nepheline (Table 3.2).

Table 3.2: Silicate minerals and their dissolution rates (after Palandri & Kharaka, 2004).

Mineral	**Molecular Formula**	**Weight % K**	**Dissolution rate, log mol m^{-2} S^{-1}**	**Relative dissolution rate**
Potassium feldspar	$KAlSi_3O_8$	14.00	-10.06	1
Leucite*	$KAlSiO_6$	17.9	-6.00	10,000
Nepheline*	$(Na, K) AlSiO_4$	8.30	-2.73	20,000,000
Muscovite	$KAl_3Si_3O_{10}(OH)_2$	9.00	-11.85	0.01
Biotite	$K_2Fe_6Si_6Al_2O_{20}(OH)_{24}$	7.60	-9.84	1

* : Feldspar family

Italised: Mica family (release K through cation exchange)

3.2 Case studies of application of crushed-rock fertilizers

Previous studies have shown that crushed rocks offer a viable alternative to chemical fertilisers, especially in highly weathered soils and leaching environments (Ciceri et al., 2015; Gupta, 2015; Harley and Gilkes, 2000; Manning, 2010, 2017; Mohammed et al., 2015; Priyono and Gilkes, 2008; Theodoro and Leonardos, 2006; van Straaten, 2006). Crushed-rocks release nutrients slower than chemical fertilisers (Harley and Gilkes, 2000), which are susceptible to fast removal due to leaching and erosion.

Several studies have shown that rocks containing biotite and nepheline provide K for plant uptake (Bakken et al., 2000; Gautneb and Bakken, 1995; Mohammed et al., 2014). Although K-feldspars are some of the major rock forming minerals, K-nutrient release from these minerals for plant growth, in general, is very slow compared to chemical fertilizers such as KCl (Manning, 2010; Mohammed et al., 2014; Priyono and Gilkes, 2008). This, then, deters their use except where particular soil requirements are favorable for them and where rock powder properties have been improved to required standards (Harley and Gilkes, 2000).

The experiments by Mohammed et al. (2014) showed that biotite released K faster than nepheline. Their study suggests that biotite could be more suited than nepheline. Biotite’s faster K release in studies by Mohammed et al. (2014), was a function of faster combined physical and chemical weathering compared with nepheline syenite. However, studies on the minerals’ stabilities under weathering show that micas and potassium feldspars more stable and more resistant to weathering (Curtis, 1976). Manning (2010), also maintains that nepheline syenite offers a more viable, fast and economical benefit especially, in organic farming. This is the case because, unlike the fast-dissolving chemical fertilisers, which pose environmental concerns due to leaching, nepheline syenite is environmentally friendly. Nepheline syenite may contain both biotite/phlogopite in addition to leucite and this may make it more suited as an alternative potash source. Figure 3.2 shows that nepheline weathers faster and is less stable under surface conditions than biotite and feldspars (Manning, 2012). Using principles of thermodynamics (Manning, 2012), the following is the weathering reaction for nepheline:

	$2NaAlSiO_4$	+	H_2O	+	$2H^+$	$= 2Na^+$	+	$Al_2Si_2O_5(OH)_4$.
	(Nepheline)		*(Water)*					*(Kaolinite)*
ΔGt (kJ/mole)	*-1975.8*		*-237.1*		*- 0*	*-261.5*		*-3797.5*

G= (2*-261.5+-3797.5) - (2*-1975.8+-23.71+0)

G= 131.80kJ/mole

Number of product atoms =17

G/g-atom= -131.80/17 **= - 6.94kJ/g-atom**

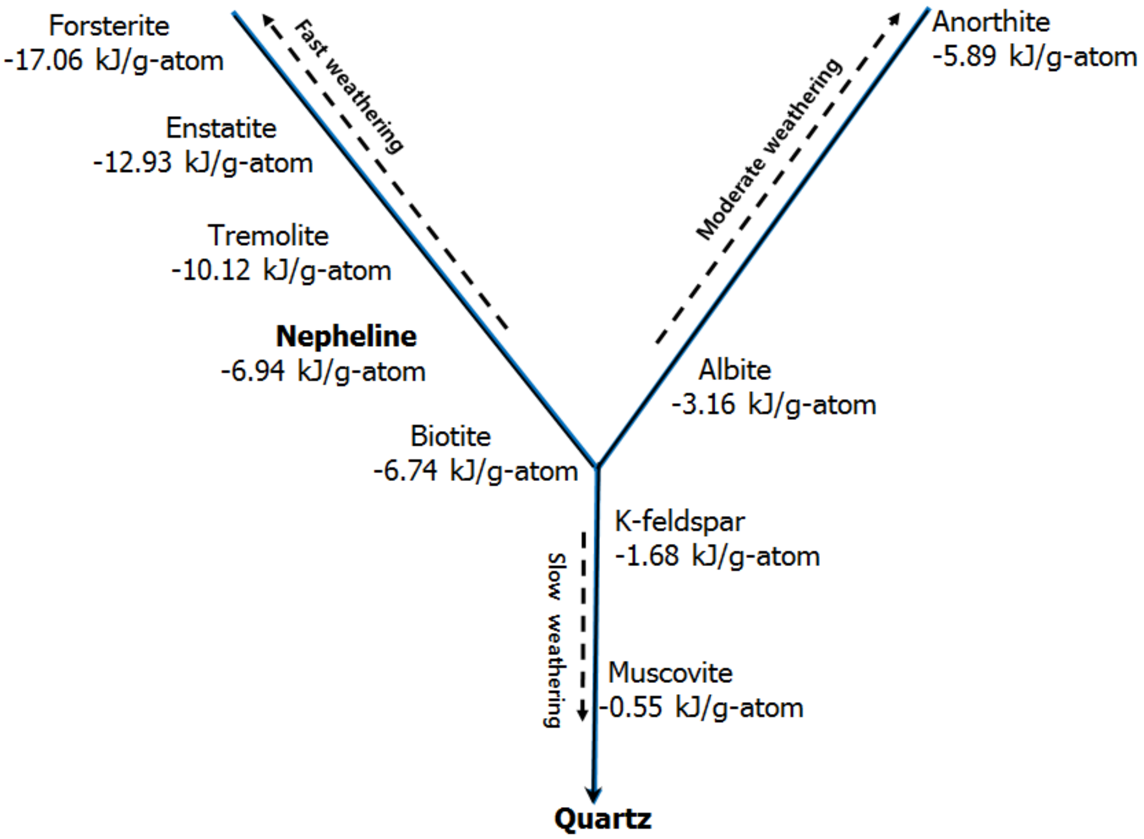

Figure 2.9: The Goldich weathering series with corresponding Gibbs free energy of reaction normalised to the total number reactant atoms calculated using thermodynamic data (after Manning, 2012). Nepheline weathers faster than the feldspars and micas while quartz is the most resistant silicate mineral to weathering

The suitability of silicate rocks as alternative K sources does not depend on their absolute K content but rather, the dissolution rates of their constituent minerals (Manning, 2010). Although some feldspars have greater absolute K contents than nepheline, their suitability for alternative potash sources is still not sufficiently effective (Priyono and Gilkes, 2008), because of their slow dissolution rates. Dissolution rate depends on the minerals' surface area, and these can be enhanced by grinding or milling the rocks, but even so Priyono and Gilkes (2008) found feldspar to be unsuitable.

Few plant growth trials have been conducted using nepheline syenite compared to K feldspar (Manning, 2010). For example, field trials were conducted with crushed rock from different minerals namely K feldspar, nepheline and biotite, and mine tailings from nepheline syenite production at North Cape (Norway), to assess their K release potential to support Italian ryegrass growth (Bakken et al., 1997). The trials involved applying the different K sources to the crop using a six months' growing period. The response in terms of plant growth was highest for nepheline, followed by biotite then K feldspars and mine tailings, suggesting poor

K nutrient supply to the plants from K feldspars and mine tailings. Bakken et al. (1997, 2000) attributed the poor performance of K release from the tailings to strong binding and less carbonate content. This suggests slower mineral dissolution rates, hence the inability of the plants to extract enough K nutrients from these tailings. Some clays are also important sources of K. For example, alteration of Illite to smectite increases K content inn the soil which could be important for plant nutrition. Similarly, K-feldspars such as orthoclase are important sources of K which may also be helpful especially for slow growing plants.

In addition, subsequent studies on fifteen grassland plant growth experiments in the area (Bakken et al., 2000) also supported the combined use of carbonate and biotite minerals. While agreeing that biotite's K release was higher than most soluble K sources, Bakken et al. (1997) reported that there was a slower release for biotite sources compared to nepheline. Pessoa et al. (2015) also assessed the solubility of nepheline syenite using humic and citric acids on coffee husks in Brazil. Their results showed that regardless of K content, when a nepheline syenite-organic mixture is incubated, K solubility was high when extracted with 2% citric acid compared with water. Other experimental studies further suggest that dissolution of silicate minerals, particularly nepheline, is largely influenced by the acidic conditions in the soil (Jena et al., 2014; Priyono and Gilkes, 2008). For example, calculations by Appelo and Postma (2005) show that silicate minerals are stable under typical pH conditions for agricultural soils. Figure 3.3 shows that altering the soil pH, especially below the typical agricultural soil pH levels (between pH 5-7), enhances silicate mineral weathering and dissolution. In addition, the physical properties, notably particle size and surface area of the silicate minerals (Mohammed et al., 2014; Priyono and Gilkes, 2008), play an added role by accelerating their dissolution and suitability as K sources.

The use of nepheline syenites as an alternative to K feldspar-bearing rocks is also supported by studies on Colombian Savanna native grasses (*Brachiaria dyctioneura*) and the legume *Pueraria phaseoloides* (Gautneb and Bakken, 1995; Sanz-Scovino et al., 1992; Sanz Scovino and Rowell, 1988). In their studies of the dry matter yield, Gautneb and Bakken (1995) found that only about 10% of the feldspar's K was absorbed by plants in 14 months, compared to 25-68% of KC1 uptake from the crops in the same period. Since the dissolution rate is also dependent on temperature (Harley and Gilkes, 2000), nepheline syenites would be suited in the Colombian Savanna and other tropical areas where the high temperatures make the environment suitable for higher mineral reaction rates.

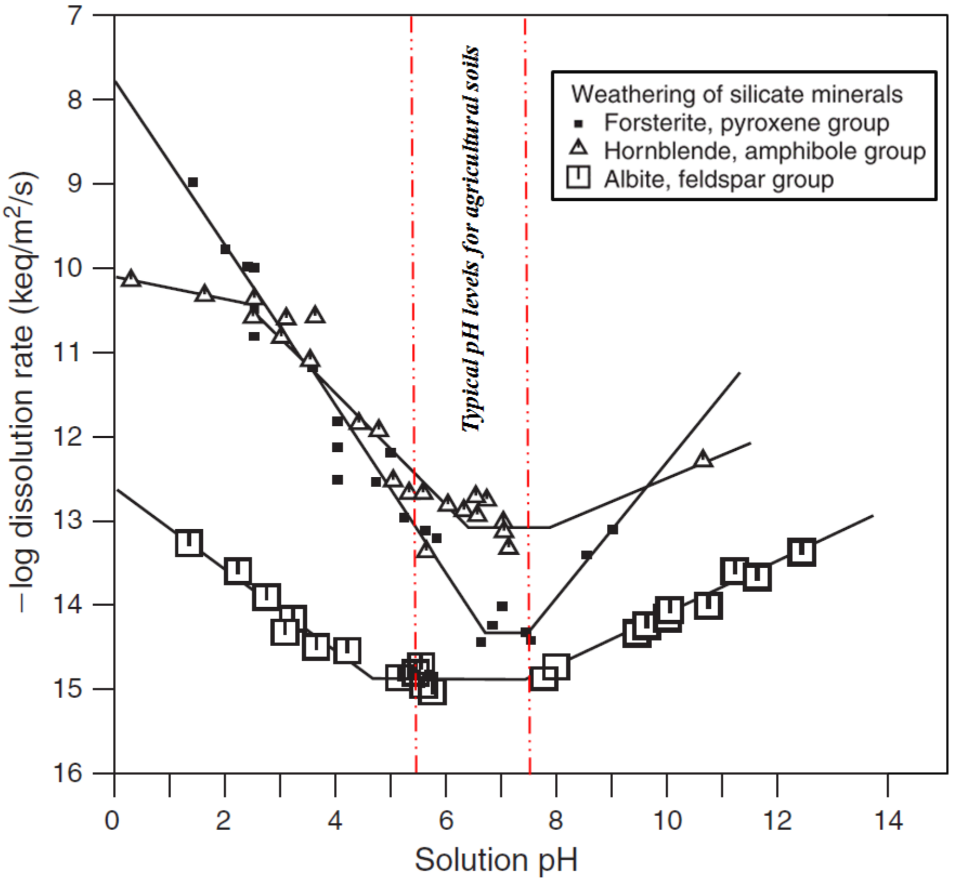

Figure 2.10: Stability and weathering of some silicate mineral groups under different soil pH conditions (modified after Appelo and Postma, (2005).

3.3 Climate conditions and use of nepheline syenite in Malawi

Norway, Ontario and the British Columbia generally have cold climates, with soil temperatures rarely rising above 15°C (www.currentresults.com/Weather/Canada/British-Columbia/temperature-annual-average.php). Comparatively, Malawi falls within the tropics and therefore, associated with Sub-tropical climate. This climate consists of three main seasons, namely, the hot wet season between November and late March, the cold dry season between late April and July and a hot dry season (between August and to October). In general, mean temperatures range between 18°C and 27°C with the mean monthly rainfall of 150mm and 300m in rainfall per month during the wet season (Vincent et al., 2014). On the other hand, Brazil, where crushed-rock remineralisers are currently being used more, has a variable climate from Equatorial in the north to temperate in the south. On average the national mean temperatures range from 15°C and 28°C while the mean annual rainfall is between 1300mm-1700mm (USAID, 2013). While the annual rainfall for Brazil is more than that received in Malawi, both countries have similar high temperatures. Considering that high temperatures and high rainfall contribute to increased weathering rates (Grotzinger and Jordan, 2010), and as noted earlier, in Figure 3.2, the climate of Malawi would offer conducive conditions for the weathering of nepheline syenites to release K silicate fertilisers.

3.4 Conclusion

This Chapter has shown that use of silicate minerals as potash sources was recognised as early as beginning of the 18th century although their use has been overshadowed by use of conventional commercial fertilisers. It has also been demonstrated in this Chapter that nepheline syenites are particularly of great interest as sustainable alternative potash fertiliser sources because of their high dissolution rates and less stability under weathering compared to other K bearing silicates.

Although geochemical information for these rocks is limited for most areas, as shown in Chapter 2, it is appreciated that these deposits occur in economical quantities for use for agriculture. In addition, certain conditions in the soils such as temperature and pH changes, influence the dissolution of the nepheline. The high temperatures and moderately high rainfall for Malawi provide potentially conducive conditions for weathering of the nepheline syenites to provide the much-needed K silicate fertiliser. The high tropical temperatures suggest conducive conditions for nepheline’s K release, mobilisation within the soil and uptake by plants.

Chapter 4: Applied remote sensing and airborne radiometric data in mapping nepheline syenite intrusions

4.0 Introduction

Satellite remote sensing is a very important tool for mineral exploration, geological mapping and many other disciplines such as forestry and agriculture. Remote sensing is concerned with accessing specific features about materials or a phenomenon using electromagnetic energy without physical contact between the sensor and the observed phenomena or material (Eismann, 2012; Khorram et al., 2012). Geologic remote sensing combines remote sensing techniques with the understanding of geological concepts and theories. Various features show different diagnostic spectral features based on their reflectance or absorption of the electromagnetic energy. Airborne geophysics also plays a vital role in modern geological research. This chapter addresses Objective 2 of this project study, by providing a review of the application of remote sensing and airborne geophysical gamma-ray data in mineral exploration and geological research. The review aims to establish a basis for their application in mapping nepheline syenites of the East African rift tectonic setting (EARS).

4.1 Remote sensing applications in geological research and sensor systems

Inferences about mineralisation from satellite imagery are made by combining remote sensing analyses with information about the geological setting, structural control, alteration, drainage systems, lineaments, petrogenetic associations and other parameters. For example, kimberlites associated with diamond occur as discrete circular bodies within stable continental crust, while some deposits such as porphyry copper deposits are usually preferentially emplaced in particular zones of granitoids and intermediate rock types, often associated with specific types of alteration. The understanding that rocks and ore deposits often show strong alteration on the surface (Bhadra et al., 2013; Rajesh, 2004) is important in geological remote sensing. Therefore, geological remote sensing has been used in alteration mapping using multispectral images in various parts of the world (e.g Zhang, Pazner and Duke, 2007; Pour, Hashim and Marghany, 2011; Feizi and Mansuri, 2013; Elsaid *et al.*, 2014; Langford, 2015; Pour and Hashim, 2015).

Remote sensing sensors are classified as either active or passive depending on their energy sources. Passive sensors depend on external sources of energy, and they include the photographic cameras without flashlight and digital scanners. Active sensors such as photographic flashlight cameras, LiDAR and radar sensors have their own energy sources. All these different sensors can be used in geological research and mineral exploration (e.g. Ali et al., 2012; Goodarzi Mehr et al., 2013, 2013; Inzana et al., 2003; Kassou et al., 2012; Mezned et al., 2010; Munyati et al., 2013; Pournamdari et al., 2014a; Qari et al., 2008; Yu and Li, 2010). For example, remote sensing has been used in identifying key minerals that indicate hydrothermal alteration such as kaolinite, alunite, pyrophyllite, illite, muscovite, and sericite, as well as carbonate and other argillic minerals. Table 4.1 shows some of the common applications of remote sensing in geology.

Table 3.1: Examples of some applications of remote sensing data in geological research using different methods

Methodology	***Examples of geologic application***
Band calculation method e.g. Band ratios, spectral indices and relative absorption band-depth.	Lithological mapping of Ophiolite rocks in south Iran using ASTER and Landsat TM bands (Pournamdari et al., 2014b), felsic – mafic complex, in Gujarat , India , using ASTER data (Nair and Mathew, 2012b); Prospecting for new gold-bearing alteration zones at El-Hoteib area, South Eastern Desert, Egypt, using ASTER data (Gabr et al., 2015).
Feature mapping: e.g. derivative analysis, (DA): maximum modulus wavelet transforms (MMW)	Detecting specific absorption features of carbonate on proximal sensed data (Sabins, 1999a) and field lithological mapping and ore mineral identification in Mamandur Polymetal Deposit, India using derivative analysis (Ramakrishnan et al., 2013); Hsu and Researcher (2006) Classification of hyperspectral images using wavelet networks. (200): 1–10.
Spectral derivatives	Mapping Arctic paleo-oceanography (Ortiz, 2011), assessment of soil properties in semi-arid areas (Melendez-Pastor et al., 2008) and lithological mapping (Zhang and Li, 2014).
Spectral Angle Mapper (SAM),	Geologic and lithological mapping of the ultramafic complexes; discriminating granitoids and mineral exploration; Characterization and mapping of kimberlites and related diatremes.
Principal Component Analysis (PCA)	Prospecting for new gold-bearing alteration zones at El-Hoteib area, South Eastern Desert, Egypt, (Gabr et al., 2015). uranium exploration in Mary Kathleen metamorphic-hydrothermal U-REE deposit, Queensland, Australia using hyperspectral data (Salles et al., 2017); extracting structural lineaments from Landsat 7 ETM+ in Central Morocco (Kassou et al., 2012).
Spectral Feature Fitting (SFF) and Matched Filtering (MF) Spectral information divergence (SID)	Geological mapping of the Neoproterozoic Allaqi-Heiani suture, Southern Egypt (Qiu et al., 2006) and mapping of rocks and minerals in the Cuprite, Nevada, and Mountain Pass, California, using ASTER data (Mars and Rowan, 2010). Delineation of alteration zones in the Um Rus region in Egypt (Amer et al., 2012).
Machine learning and statistical -based approaches e.g. Neural networks, support vector machines, self-organizing map, decision trees, random forests	Geological units classification of multispectral images using SVM (Kovacevic et al., 2009); lithological discrimination and mapping using ASTER SWIR data in the Udaipur area, India (Kumar et al., 2015). Geological Units Classification using Landsat multispectral images in Saharan Atlas, southwest of Brezina (Gualtieri and Chettri, 2000).
Minimum Noise Fraction (MNF)	Discrimination of sedimentary units, metamorphic sole, laterite, depleted harzburgite and diabase dikes/sills; Exploration of porphyry copper deposits.

The sensors are also classified into two major categories. These are multispectral and hyperspectral sensors. Both of them may be applied for different purposes in geology.

4.1.1 Multispectral sensors

The multispectral imaging (MSI) sensors are designed to observe only a few spectral bands (usually <20) which cover broad spectral regions (Kruse and Perry, 2007). Common multispectral data systems used in geological remote sensing include Landsat, the Satellite Pour l'Observation de la Terre (SPOT), Sentinel and ASTER systems as well as the Moderate Resolution Imaging Spectroradiometer (MODIS). MODIS data have been applied in areas such as the mapping North African landforms (Ballantine et al., 2005) and quantifying heat flow and hydrothermal changes at Yellowstone National Park (Vaughan et al., 2012). Although results from these projects were generally successful, Mulder et al. (2011), observed that MODIS and Landsat data quality are affected by low spatial and spectral resolutions as they were too coarse to delineate mineral compositions effeciently.

Although the Sentinel sensor is comparatively new and less used in geological mapping, some simulations have shown that Sentinel-2 worked similarly to ASTER's VNIR-SWIR data (Van der Meer et al., 2014), which are the only bands for Sentinel 2. Sentinel-2 has higher spatial resolution bands than ASTER. Therefore, Sentinel-2 data may be ideal for geological mapping, especially where ASTER's VNIR and SWIR data may not be effective due to poor spatial resolution. However, unlike Sentinel 2, the ASTER sensor also has TIR data which gives it an advantage over Sentinel when emissivity and surface temperature data are needed. ASTER data have, therefore, been more widely used in geological mapping and mineral exploration. Examples of these projects include mapping high pressure metamorphic rocks in the As Sifah region, Oman (Rajendran and Nasir, 2015); regional-scale mineral mapping (Jing et al., 2014); geological mapping in Namibia (Gomez et al., 2005) and other examples as shown in Table 4.1. ASTER data are prefered because they have high spectral resolution for VNIR and SWIR, suitable for mineral mapping, and 5 TIR bands at 90 m spatial resolution, suited for delineation of various rock types. Although ASTER data have been the most used in geological mapping, it is important to note that ASTER's SWIR detectors experienced irreparable malfunction in 2008. However, the data acquired before 2008 are still usable for geological and mineral mapping.

4.1.2 Hyperspectral sensors

Hyperspectral imaging sensors (HSI) have numerous narrow bands, which provide higher resolution data than multispectral imaging (MSI) sensors (Kruse and Perry, 2007). Hyperspectral remote sensing provides both imaging and spectrometry functionalities. Due to their many and narrow bands, the hyperspectral sensors can identify minerals and different lithologies more clearly than the lower-resolution multispectral systems. This is because the higher resolution of the HSI makes them capable of depicting subtle spectral features of rocks and minerals. For example, EO-1 Hyperion data have been used to map gold-associated areas and regional lithological mapping in south-eastern Chocolate Mountain, California, USA (Kruse and Perry, 2007; Pour and Hashim, 2014; Zhang and Pazner, 2007).

Although many workers support the use of HSI over MSI instruments, others advocate for combined use of the two datasets or in some cases use of either of the data types. For example, Kruse and Perry (2007) noted that similar results could be obtained by using either ASTER or Hyperion data although the Hyperion data yielded slightly better results. Other workers have proposed combining the use of the Advanced Land Imager (ALI) or Hyperion and ASTER data. This may be done in reconnaissance surveys or where there are fewer chances of field ground survey in mineral exploration (Guha et al., 2012; Pour and Hashim, 2014), for example, due to poor terrain in some areas. However, there are no tangible results to demonstrate where this worked effectively.

4.2 Common data processing techniques for geological remote sensing

Image processing involves various processing and classification approaches. These include techniques that are used in the classification, identification, and extraction of features from an image (Asadzadeh and de Souza Filho, 2016). Geologic remote sensing involves various data screening and cleaning procedures which are performed for effective extraction of geologic features. Some of the key procedures include atmospheric, geometric and radiometric corrections, masking unwanted features and spectral data transformation.

4.3 Principles of geologic remote sensing

Rocks and minerals have different composition and spectral properties. Each mineral or rock material absorbs energy in a different way from other materials, which results in detection and identification of these rocks and minerals. This is what makes the different rocks and minerals give different reflectance patterns, with distinctive spectral signatures for each rock or mineral (Carter, 2008; Clark, 1999; Manchanda et al., 2002; Nair and Mathew, 2012a; Patagonia, 2009; Ramakrishnan and Bharti, 1996; Rowan et al., 2004; Sgavetti et al., 2006; Smith, 2006; Torres, 2007). Different reflectance and absorption features are observed in the visible-near infrared (VNIR) wavelength window of the electromagnetic spectrum between 0.4–1.0µm, the short-wave infrared (SWIR) between 0.35–2.5µm, mid infrared (MIR) between 3–5µm, and/or longwave infrared (LWIR) wavelength region between 8–14µm of the electromagnetic spectrum (Asadzadeh and de Souza Filho, 2016; Sabins, 1999b). Factors such as vibrational overtones, electronic transition, charge transfer and conduction processes result in different diagnostic absorption features for minerals, which are noted between 0.35-11.65µm of the electromagnetic spectrum (Pour and Hashim, 2014; Pournamdari et al., 2014a, 2014b). The differences in spectral response patterns are what make spectral separability of different materials possible. This is important for mapping different minerals and lithological units using geologic remote sensing.

It is the spectral signature for each material which allows discrimination of different rocks and minerals from each other through spectral reflectance, i.e the division of the reflected energy over the incident energy in relation to the wavelength (Smith, 2006). These spectral signatures therefore help in remote sensing interpretation and may also help to ascertain the mineral compositions of different lithologies (Roos and Jong, 2017). Spectral signatures for clay minerals are more diagnostic within the shortwave infrared part of the electromagnetic spectrum, which is why kaolinite shows double absorption features between 1367-1430 nm, 1860-2030 nm and 2130-2230 nm (Roos and Jong, 2017). Band shifts caused by the interaction of Mg and Fe ions with hydroxyls (OH) result in characteristic sharp absorption bands in talc, tremolite and actinolite at wavelengths 1.4µm, 2.3µm and 1.4µm respectively (Clark, 1999). (Clark, 1999) further provides a spectral library of some common minerals and other materials. This helps to distinguish different mineral from each other. In some cases, minerals or lithologies which cannot be directly detected by a sensor are interpreted based on minerals with which the target mineral occurs (Torres, 2007).

Some hydroxylated and hydrated silicate minerals show diagnostic features between wavelengths of 1.0µm to 2.5µm in which absorption features at ~1.40µm but without absorption features at ~1.91µm are usually associated with hydroxylated silicate minerals whereas hydrated phyllosilicates can be identified easily because of their absorption features at ~1.40µm, ~1.91µm, and 2.20µm to 2.40µm (Fan et al., 2012). In addition, Fan et al. (2012) analysed the USGS spectral library for silicate minerals and noted that the minerals which show absorption features at ~1.40µm, ~1.91µm, and 2.20µm to 2.40µm include sillimanite, cordierite, nepheline, microline, orthoclase, albite, oligoclase and anorthite.

In addition, some studies have suggested that most silicate rocks can be distinguished more easily in the Thermal Infrared Radiation (TIR) wavelength region (8µm-12µm) because they display diagnostic properties in this region (Sabins, 1999b). Remote sensing has, therefore, been used to produce mineral base-maps in many mineral exploration projects (e.g Amer et al., 2012; Bhadra et al., 2013; Bishop et al., 2018; Govil et al., 2018; Salles et al., 2017; Wang et al., 2017). Remote sensing is a time and cost-effective system of lithological mapping and mineral exploration, especially in remote areas and unfavourable terrains, which may not be easily accessible for field geological mapping (Azizi et al., 2010; Rajendran and Nasir, 2013).

4.3.1 Radiometric and geometric correction

Satellite data often have geometric and radiometric defects, which need correction. Geometric correction involves image registration to mitigate for shifts in the path of the sensor's orbit, its altitude or speed (Lillesand et al., 2015). This is done by geo-referencing or image registration using ground control points (Lein, 2012) or other spatial reference datasets, such as existing geological and topographic maps from which geographical coordinates can be extracted. Radiometric correction seeks to correct for defects on the image, which may be due to excessive brightness of some features. This can result in anomalous pixels and differences in viewing geometry (Lillesand et al., 2015). Some multispectral data such as ASTER Level 1B and ASTER Level 1T data have their geometric and radiometric correction done at the sensor point. Radiometric correction methods include contrast enhancement and linear stretching (Lein, 2012). The radiometric correction is necessary because it helps to reduce errors in DN values, thereby enhancing classification and the subsequent interpretation of the remote sensing data (Sorzano et al., 2014).

4.3.2 Atmospheric correction

As remote sensing sensors access spectral data of different surface features, atmospheric interference is encountered along the flight path between the Earth's surface and the sensor. This reduces the quality of remotely-sensed data (Ravelo and Abril, 2010). Atmospheric correction methods include subtracting digital number (DN) values of dark pixels from those of bright pixels. The Fast Line-of-sight Atmospheric Analysis of Spectral Hypercubes (FLAASH) tool within ENVI software helps to clear atmospheric effects. The FLAASH algorithm performs the atmospheric correction on the image scenes in the visible-to-shortwave infrared wavelength region, of 0.35µm and 3µm (EXELIS Visual Information Solutions, 2014). The FLAASH model uses a standard equation for spectral radiance at a sensor pixel, L, which is applied to the solar wavelength range, of flat, Lambertian materials. The equation is as follows:

$$L = \left(\frac{A\rho}{1-B\rho_e S}\right) + \left(\frac{B\rho_e}{1-\rho_e S}\right) + L_a \qquad (4.1)$$

where:

ρ is the pixel surface reflectance.

ρ_e is an average surface reflectance for the pixel and surrounding region.

S is the spherical albedo of the atmosphere.

L_a is the radiance back-scattered by the atmosphere.

A and B are coefficients which depend on atmospheric and geometric conditions.

4.3.3 Masking of unwanted features

To enhance image processing and classification, some features may need to be removed to enhance identification of the target features. For example, features like cloud cover, cloud shadow, water bodies and vegetation (Bennett, 2014; Dragut et al., 2014; Guha et al., 2015; Schetselaar and Kemp, 2000) are masked. This can be done by applying band mathematical calculations or by selecting the region of interest and then applying masking procedures.

4.3.4 Spectral data transformation

These are methods used to find linear combinations of features that characterise or separate two or more classes in image processing (Langford, 2015; Yamaguchi and Naito, 2003). The output is a linear classifier or dimensionality reduction for later classification. There are varying ways to implement spectral discrimination including Linear Discriminant Analysis (LDA) and Principal Component Analysis (PCA). LDA is similar to PCA because both methods are used to maximise dimensionality reduction of the remotely-sensed data to minimise data redundancy to only those data that are necessary for classification (Sorzano et al., 2014). However, LDA is a supervised technique which calculates for the data direction and aims to enhance to maximize the separation between multiple classes in image processing. On the other hand, PCA is applied to multispectral and hyperspectral remotely-sensed data (Demšar et al., 2013).

4.4 Remote sensing image classification approaches

Image classification is a process through which image pixels are segmented into different units which represent a given set of surface features or objects (Al-doski et al., 2013). This involves performing various tasks to detect and group related features in an image using rules of logic and other algorithms, which control the feature discrimination process (Lein, 2012). Image classification is categorized into two main methods, namely, supervised and unsupervised classification techniques (Asadzadeh and de Souza Filho, 2016) as shown in Figure 4.1. In supervised classification, the unknown features are delineated by classifying their pixels based on the spectral characteristics of known classes related to the feature being delineated (Enderle and Weih, 2005; Goetz and Rowan, 2016; Hubbard et al., 2007; Keuchel et al., 2003; Mars and Rowan, 2010). The image analyst decides on the thresholds and the number of output classes.

Other workers, notably Asadzadeh and de Souza Filho (2016), have summarised common methods for geologic remote sensing into two major classes, namely knowledge-based and data-driven approaches. The knowledge-based approaches derive their classification from knowledge of the geometric characteristics of geographical/spatial or geological features which represent landforms or spectral features (Asadzadeh and de Souza Filho, 2016; Mwaniki, 2010). On the other hand, data driven approaches require reference data which can be used as reference/training areas.

4.4.1 Band calculation method

This is one of the most commonly used methods of image processing in geological mapping. It estimates the shape or gradient of absorption features in different image bands. Various researchers, including Aboelkhair et al., (2010), Mars and Rowan, (2010), Nair and Mathew, (2012), Qari et al., (2008) and others have used ASTER and LANDSAT band ratios in geological and mineral mapping in different parts of the world. The band ratios are calculated by estimating the differences in reflectance between an absorption band and its shoulder bands (Asadzadeh and de Souza Filho, 2016). Band calculation methods have proven effective for classifying features which have heterogeneous compositions. Such features include rocks and soils; hence, the methods are commonly used in geology (Corrie et al., 2010; Ding et al., 2015). For example, Guha and Vinod (2016) have successfully mapped different rocks units using ASTER TIR band combinations of RGB: bands 14, 13 and 12.

4.4.2 Statistical approaches

These approaches depend on use of statistical parameters of images to identify and classify features in an image. For example, they include using the assumptions of a Gaussian distribution for spectral data to segment an image. Traditional parametric statistical approaches for supervised classification which are commonly used include the maximum likelihood and distance classifiers (Benediktsson et al., 2003; Mirzaie et al., 2014). Simple linear regression can also be used to determine relationships between reflectance and (bio) physical or geological parameters of features.

In addition, based on studies on the properties of different rocks, a number of spectral indices have been developed (Corrie et al., 2010; Ding et al., 2015; Ninomiya and Bihong, 2001;

Ninomiya and Fu, 2016; Yamaguchi and Naito, 2003). Silicate minerals and rocks such as felsic rocks show key emissivity absorption features in the thermal infrared (TIR) region between 8-12µm (Corrie et al., 2010; Wardhana and Wijaya, 2006; Aboelkhair et al., 2010). For example, Ninomiya et al. (2005) and Kalinowski *et al.*, (2004) present a number of important indices based on ASTER sensor bands as shown in equations 4.2 and 4.3. Some of these are potentially useful for mapping nepheline syenites. The Quartz index (QI) is calculated by:

$$\mathrm{QI} = \frac{Band\ 11 * Band\ 11}{Band\ 10 * Band\ 12} \qquad (4.2)$$

where high response suggests high quartz content and low response is associated with K feldspar and sometimes gypsum. Nepheline syenites never contain quartz, and so would be expected to give a low response. Alternatively, quartz-rich rocks may also be mapped using Band 14/Band 12 (Kalinowski et al., 2004) while the mafic index (MI) calculated as:

$$\mathrm{MI} = \frac{Band\ 12}{Band\ 13} \qquad (4.3)$$

where low index values are related to mafic-ultramafic rocks and high values to quartz rich rocks (Ding, et al., 2014). ASTER band ratios of Band4/Band5 for delineating silicate mineral alteration and Band5/Band 6 helps in silicate host-rock discrimination (Kalinowski et al. 2004). On the other hand, carbonate rocks such as dolomitic limestone are associated with low spectral emissivity within the 11.2µm to 11.4µm of the electromagnetic spectrum. Kalinowski et al. (2004) provide a list of other useful mineral and lithological indices for various rock types and minerals and some common band combinations using ASTER data.

4.4.3 Machine learning methods

These are approaches which involve use of computer algorithms that are trained to recognise a model from data so that they can then identify different variables of feature based on the predictive power embedded into them (Gewali et al., 2018). For example, these machine learning algorithms can be trained to detect and map properties of materials for large data sets of information about a material's chemical and physical properties (Gewali et al., 2018). This is the information which is captured by remote sensing sensors mostly,by hundreds of hyperspectral image bands. Machine learning involves a collection of algorithms such as neural networks, support vector machines, self-organizing map, decision trees and random forests, which can be used for multi-variate, nonlinear, nonparametric regression and image classification (Mirzaie et al., 2014). This group of approaches is a subdivision of artificial intelligence methods, and includes algorithms that can retrieve information from machine readable data (Mirzaie et al., 2014; Mountrakis et al., 2011). Usually, comprehensive training datasets need to cover as much of the feature as possible for high quality results (Belgiu et al., 2014; Mirzaie et al., 2014). These approaches are preferred in hyperspectral data analysis because of their ability for automatic pattern recognition and depicting the relationship between the rocks, minerals and the desired information. Examples of machine learning algorithms include Gaussian models, linear and logistic regressions, support vector machines.

4.4.4 Hyperspectral processing techniques

Some classification methods work better specifically for hyperspectral data; derivative analysis is one of these. Derivative analysis has been widely applied in analytical chemistry where peaks in 4th derivatives are related to peaks in absorbing compounds (Owen, 1995; Tsai and Philpot, 1998). Geological applications for the method include in Arctic paleo-oceanography (Ortiz, 2011), assessment of soil properties in semi-arid areas (Melendez-Pastor et al., 2008) and lithological mapping (Zhang and Li, 2014). Spectral derivatives give an indication of rate of change, or slope of the original spectrum. For example, in first derivatives, the increasing reflectance is determined by a positive derivative while decrease is denoted by negative derivatives. Among the different derivatives, Satisvy-Golay derivatives are preferred because they have capacity for data smoothing and differentiation (Asadzadeh and de Souza Filho, 2016). Other approaches for processing these hyperspectral data include machine learning and statistical methods.

4.4.5 *Classification using surface temperature and emissivity separation*

Some minerals and rocks show diagnostic features within in the TIR region (between 8-12um) of the electromagnetic spectrum. For example, most silicate rocks show emissivity minima between 8-11um (Ferrier et al., 2016). Some sensors, such as LANDSAT and ASTER, have bands which can detect the surface temperature and emissivity of rocks and minerals (Danov, 2007; Gillespie et al., 1999). TIR can be used in geological mapping by identifying bands which have diagnostic emissivity minima features of the rocks or minerals (Danov, 2007; Ferrier et al., 2016; Gillespie et al., 1999; Zhang et al., 2017). The TIR bands' irradiance data show the emissivity of different features relative to that of a black body. The bands' irradiance is converted to brightness temperature (T_b) by inversion of the Planck function (Moore and Paine, 2014; Smith, 2003) using the following equation:

$$T_b = \frac{C_2}{\left[\lambda \ln\left(\left(\frac{C_1}{\lambda 5 B\lambda}\right) + 1\right)\right]} \qquad (4.4)$$

where $C_1 = 119.104\text{x}10^{-7}$ ($\text{W/m}^{-3}/\text{sr}^{-1}$); $C_2 = 1438.765\text{K}$; B_λ is for ASTER TIR Band 14 equal to 11.32µm; and ln is the natural log.

The emissivity (ε) of rocks is important because it can be diagnostic of the composition of rocks on the Earth's surface (Gillespie et al., 1999) and can determine the surface heat fluxes of geological units. Therefore, surface temperatures and emissivity data have been used in different areas to study surface processes such as soil erosion and soil development (Danov, 2007; Gillespie et al., 1999). The emissivity spectra of geologic materials can be quite complex; therefore, emissivity studies require many spectral bands in the 8-14 µm TIR window. TIR radiation (8-14µm) is emitted from a surface feature in proportion to its kinetic temperature and emissivity. Each TIR image band provides its own emissivity value and surface temperatures (Gillespie et al., 1999). However, this sometimes offers challenges in estimating temperature and emissivity from remotely sensed data because the data have more unknowns. TIR measurements' primary purpose was to estimate surface kinetic temperatures, which is easier if the emissivity is known *a priori*. Examples of target features that have been distinguished using this approach include oceans, for which the emissivity values have been measured independently (Danov, 2007; Gillespie et al., 1999).

4.5 Summary of geological remote sensing methods

Li et al. (2014) noted that most of the image classification approaches are largely based on the spectral or image pixel as the basic unit of analysis or single feature class. This neglected other aspects of the object/feature because a pixel/feature can be heterogeneous. Rocks have different minerals and some of them, such as silicates, have complex chemistry. Therefore, most of these approaches show limitations to accurately delineate such complex geological units. Hybrid methods which combine techniques of different approaches (Al-doski et al., 2013; Li et al., 2014) have been proposed because no single method can give best results alone. Therefore, using a combination of different approaches could increase the classification capacity of geological remote sensing methods (Amer et al., 2012). However, different methods do not use uniform standards for classification, which also makes combining some of the methods challenging. Table 4.2 shows some advantages and limitations of some common methods which were also introcduced in Table 4.1.

Table 4.4*: Summary of some of the common remote sensing data processing approaches used in geological mapping with some of their successes and limitations.*

	Methodology	***Advantages/successes***	***Limitations***
1.Knowledge-based approach	*Band calculation method e.g. Band ratios, spectral indices and relative absorption band- depth.*	Not affected by variations in the scenes of the images and topography (Asadzadeh and de Souza Filho, 2016). Using the technique different varieties of metavolcanics and varieties of felsic igneous rocks have been delineated from each other (Gabr et al., 2015). allow spectral features of individual bands to be studied and individual rock types to be studied spectrally and helps to remove the shadow and topographic effects and topographic effects, which then makes mapping of difficult terrain (Mwaniki, 2010)	if data not selected properly the outcome is usually ambiguous because a mineral or geological feature could show similar responses in more than one band posing challenges on choice of the best band to use (Gabr et al., 2015).
	Feature mapping: e.g. derivative analysis, (DA): maximum modulus wavelet transforms (MMW)	MMWT is an improvement of DA and it uses second-order derivatives in wavelet domain (Hsu, 2007). Can eliminate background signals which are common in data e.g. lithological spectra Melendez-Pastor et al., 2008.	May be difficult for mapping features/areas with little geological knowledge because processing routine requires prior definition of the absorption features.
	Spectral derivatives	Provides easier way for determining the absorption position of rock and minerals e.g. using derivative analysis The absorption location is shows a positive sign in 3rd derivative and negative sign in 2nd derivative (Asadzadeh and de Souza Filho, 2016).	Assumes sample homogeneity because it is usually used for spectroscopy data collected under standard conditions in laboratory but in reality remote sensing data are usually heterogeneous (Tsai and Philpot, 1998).
2.Data driven approaches	Spectral Angle Mapper (SAM),	-Both SAM and SCM are effective where prior knowledge of geological features is available because they automatically compute spectral similarity between the reference and target spectra to map the most probable targets in the pixel; SCM offers added advantages over SAM because SCM is sensitive to false positive results and directly measures similarity between the shapes of two spectra of geological features (Asadzadeh and de Souza Filho, 2016) . SAM is also capable of reducing the impact shading to enhance thereby enhancing the reflectance of target features (Ma et al., 2016).	-If threshold not well set, it ignores some useful features as features with pixels further away the maximum angle threshold may not be classified. -SAM also only separates positive and negative correlations due to its considerations for only absolute values (Ma et al., 2016).
	Principal Component Analysis (PCA)	Can work both as data transformation and classification method. Transforms original correlated dataset into a substantially smaller set of uncorrelated variables representing most of information present in original dataset (Asadzadeh and de Souza Filho, 2016). Offers image enhancement, noise reduction and highlight specific features on the image (Asadzadeh and de Souza Filho, 2016; Kumar et al., 2015; Salles et al., 2017).	Affected by over-reliance merely upon empirically chosen input bands, and it presents some difficulties in matching PCs to their corresponding target features in an image (Asadzadeh and de Souza Filho, 2016).

	Spectral Feature Fitting (SFF) and Matched Filtering (MF) Spectral information divergence (SID)	-Allows use of spectral signatures from some other sources e.g. Spectral library; -Has shown reduced effect of background materials by projecting pixel vectors that are orthogonal to the background spectra. SID can measure spectral features by using statistical moments; and take count of variations within the spectral with some degree of confidence; Effective in mapping alteration zones(Ma et al., 2016) of mineralised areas (Amer et al., 2012)	Validity of the results may not be guaranteed because the technique can be influenced by physical and the chemical properties of the surface, along with the illumination condition (Mustard and Sunshine, 1999).
	Machine learning and statistical -based approaches e.g. Neural networks, support vector machines, self-organizing map, decision trees, random forests	Neural networks belong to the same class of approaches as automated pattern recognition (Eberle et al., 2015; Krogh, 2008). Do not require assumptions on the probability distribution of the data to be classified because they learn complex patterns which them to perform well even when the feature space is complex, or the source data have different statistical distributions (Hoffbeck and Landgrebe, 1996). SVM is also effective technique for predictive mapping in classification of geological units.	Reliance on underlying assumptions of the model also makes statistical approaches somewhat restrictive. Linear correlation analysis also assumes simple and direct relationships, whether linear or curvilinear, between reflectance and the parameter, or target, which may not always be the case (Im and Jensen, 2005). Requires enough and good quality reference data as training areas.
	Minimum Noise Fraction (MNF)	-Effectively separates noise from the image data hence providing clearer features detection; -Helps to assess image data’s inherent dimensionality.	-Requires that the entire image (not only some bands) be available; -May lead to reduced spatial and spectral resolution of the image.

4.6 Digital terrain models for geological mapping

Remote sensing can be used to extract geological and structural features more clearly than conventional ground-based mapping. For instance, remote sensing data have been used to map lineaments (Badura and Przybylski, 2005). One of the diagnostic features of nepheline syenite intrusions in Malawi and other areas is that they often show up as elevated intrusive bodies on aeromagnetic maps (Isioye and Jobin, 2012; Ruzickova et al., 2013; Wilford, 2012; Xiaoye Liu, 2008) and also occur as ring structures. As such, digital terrain models can be used in mapping these intrusions. Digital terrain models (DTMs) play an important role in classification of landforms including hills or any surface terrain features (Ruzickova, 2012; Ruzickova et al., 2013).

Some of the commonly used data for DTMs include the Shuttle Radar Topography Mission (SRTM) and ASTER Global Digital Elevation Model (GDEM) data. For example, ASTER GDEM was used to produce reconnaissance maps for the geomorphometric analysis of Nisyros volcano in Greece (Zouzias et al., 2011) and for lineaments extraction in the Southern Chitradurga Schist Belt, India. Other studies which have also shown that digital elevation models are useful in mapping geological research include the geological, geomorphological and vegetation community spatial relationships in Quetico Provincial Park, Ontario, Canada (Warner et al., 1991); interpretation of the Klang Valley (Malaysia) geological structure (Manap et al. 2009) and applied geological and geomorphological studies (Badura and Przybylski, 2005). Some lineaments which can be difficult to delineate on topographic and geological maps can be portrayed more easily on DEMs. This makes it easier to interpret even the small-scale features which may not be easily recognisable on the ground due to the scale of the terrain morphology (Badura and Przybylski, 2005).

Several other examples show that remote sensing and DTMs/DEMs can be used in multiple ways to extract geological features. Ruzickova et al (2013) noted that in comparison to SRTM data in lineament extraction, ASTER GDEM offered slightly better-quality results due to its higher resolution (15-30m) compared with SRTM (30m). The Light Detection and Ranging (LIDAR) sensor, an active remote sensing laser sensor, provides higher resolution data at 1-3m and better DTMs than SRTM and GDEM (Gunduz and Kara, 2015). However, the major problem is that open access LIDAR data are not available for some parts of Malawi at the moment (Gunduz and Kara, 2015; Hummel et al., 2011; Wedajo, 2017). In addition, the

LIDAR data are huge in volume which means they require larger data storage platforms, more time and advanced processing skills for more accurate results.

4.7 Remote sensing, mineralisation and plant tolerance to minerals

Lithological extraction in areas covered by dense vegetation is a great challenge for geologic remote sensing. Geo-botanical associations and/or plant tolerance of certain minerals can, however, be very helpful for delineation of the lithology, e.g. in areas with closed-canopy forests. While it is agreed that vegetation impacts on detection of the underlying soils and geology (Warner et al., 1994), it is also appreciated that the underlying soils greatly influence which kind of vegetation will grow in an area. Different plants can be used in mineral exploration due to their tolerance to various minerals. The type, distribution and population of particular plant species in an area are related to the rocks from which the soil formed, especially, where the soils have not been altered by chemical weathering.

Therefore, using remote sensing to delineate plant species associated with particular geological units/minerals would help to understand information about plant tolerance to some minerals, and information about the underlying bedrock or rocks from which the soils have weathered may be extracted. For example, *Cassia auriculata*'s lack of flowering is associated with chromite mineralization whereas *Gymnosporia falconeriis* could be associated with Au, Ba or Sr depending on variations of its (*Gymnosporia falconeriis*) abundance (Prasad, 1987). In addition, *Curatella americana L* has been successfully used as a gold pathfinder in the Mina Santa Clara and other areas of Costa Rica (Miller et al., 1995). Plant tolerance to potassium may also be promoted by rhizospheric microorganisms called the potassium solubilizing microorganisms (KSMs) in the soils (Meena et al., 2014). These can transform the insoluble potassium in the soil into soluble forms so that the K can be used by plants. Miller et al. (1995) observes that the challenge in using information about plant tolerance to minerals is that key pathfinder plants may not be regularly distributed, which could make sampling difficult. On the other hand, potassium is one of the key macro-nutrients and is needed by almost all plants. Therefore, it may not be easy to isolate plant species associated with potassium abundance in the soil using remote sensing techniques.

4.8 Suitability of remote sensing application for nepheline syenites

Nepheline syenite shows high emissivity features between 9.4 µm-10.4 µm wavelength regions (Clark et al., 2007). Nepheline syenite portrays geochemical properties of both felsic and intermediate rocks. For example, the total Fe and Mg content for nepheline syenites is around 3wt% corresponding to other felsic rocks such as granite whereas the silica concentrations (53-63 wt. %) correspond to other intermediate rocks such as andesite and diorite. Therefore, spectral fitting techniques and band calculation methods that can separate quartz or siliceous rocks from felsic rocks could be ideal for mapping nepheline syenites.

Drawing on lessons from the methods applied in different areas, there is strong potential for application of remote sensing approaches to identify nepheline syenites that might be suited for K fertilizers. As noted in this Chapter, there is no agreement of the best method for geological mapping using remote sensing. Some methods are better at discriminating minerals, others at mapping structures while others work better in lithological mapping. The band calculation method appears to serve most of these purposes and to be easier to implement in geological mapping. In addition, some basic band ratios and spectral indices have been developed for geological mapping and these will need to be tested for detection of nepheline-bearing rocks, and revised where necessary. A combination of supervised and unsupervised classification algorithms could also be helpful.

4.9 Use of airborne geophysical techniques in geological research

Airborne geophysical survey combines principles of physics, geochemistry and geology to understand the nature of the rocks on the Earth’s surface (Youssef and Elkhodary, 2013). Three key types of airborne geophysical data sets are usually used in geology namely: magnetic, radiometric and gravity data. Magnetic surveys are concerned with measuring differences in the magnetic susceptibility and intensity of the rocks. Airborne magnetic and aeromagnetic data have played an important role in mineral exploration, geological and structural mapping in many parts of the world (Elezaj, 2016; Grasty et al., 1985; Guimaraes et al., 2013; Tourlière et al., 2003). They help to identify the subsurface geological structures and rocks which may not be delineated by field geological surveys or satellite remote sensing by studying magnetic properties of the rocks. Gravity studies are concerned with measuring the gravimetric field response of the Earth (Barnes and Lumley, 2011; Nabighian et al., 2005; Telford et al., 1990).

4.10 Principles of geophysical gamma-ray surveys

The gamma radiation surveys focus on radioactive elemental abundances in the top layers of the Earth’s surface and atmosphere (Telford et al., 1990). This technique is used to measure the natural radiation emitted by natural and human-induced radioactive processes. Airborne geophysical gamma-ray surveys detect radio-elemental concentrations of uranium (U), potassium (K) and thorium (Th). The radiometric response of the surface materials may be associated with particular lithologies and relate to the mineralogy, moisture content or the geology (Grasty et al., 1985; Minty, 1998; Shives et al., 2000); Telford et al., 1990).

4.11 Airborne geophysical gamma-ray spectrometry and geology mapping

Airborne gamma-ray spectrometry is an advanced geochemical mapping technique in which a gamma-ray spectrometer system is mounted on low flying helicopters or fixed wing aircraft to determine and record the x-ray flux due to terrestrial gamma-ray spectra of surface rocks and soils (Zhang et al., 1998; Bristow, 1983). Airborne surveys use specially designed sensitive spectrometers which mostly contain thallium-activated sodium iodide (NaI) crystals. These have proven to be very effective in absorbing gamma-rays after further processes can be performed to analyse the radioactivity of the rocks (Telford et al., 1990). The measurement is based on the response of the detector to to the total radioactivity and/or the intensity of radioactivity relating to potassium (K), uranium (U) and thorium (Th) concentrations within the rocks and minerals.

In geology, airborne geophysical gamma-ray spectrometry proposes that the radioelement contents of the substrate and overlying rock exposures often reflect the underlying parental bedrock and protoliths from which eroded unconsolidated materials may have been derived. Radiometric studies assume that all rocks contain isotopes, some of which are unstable and so change to reach a stable state by processes which involve emitting ionizing radiation (Wilford and Minty, 2006). Gamma-ray spectrometry is, therefore, an important technique not only for the geological sciences but for a larger part of the geoscientific community. Apart from being vital for baseline geochemical surveys in exploration for radioactive minerals, it also serves other purposes. These include general lithological mapping and investigations for metallic and non-metallic deposits that have affinities or incompatible relationships with radioactive elements (Zhang et al., 1998). Airborne gamma-ray spectrometry calculates specific radioactive spectral peak intensities of radionuclides in the rocks. Such measurements occur within the radiometric channel width of 0.2-0.3 MeV and three characteristic gamma-ray energy peaks (Zhang et al., 1998), from which K, U and Th are calculated.

All rocks have radioactive isotopes which lead to emission of natural gamma-ray radiation when they decay; K, U and Th are considered to emit the greatest amount of gamma-ray radiation (Wilford and Minty, 2006). Isotopes are chemical states related to variations in mass numbers of an atom of an element and they are the result of an element comprising the same atomic numbers (i.e. the same number of protons) but different numbers of neutrons. The role of gamma-ray surveys, therefore, is to identify the spatial distribution and abundance of these elements from the surface of the Earth up to about 30-50cm deep (Raghuwanshi, 1992). The major radioactive isotopes namely: ^{40}K and the ^{232}Th and ^{238}U decay series, are the ones that work best to quantify the respective potassium, thorium and uranium surface abundances (Grasty and Minty, 1995; Wilford and Minty, 2006). Potassium concentration is determined from the 1.46MeV gamma-ray photons emitted when ^{40}K decays to Ar, whereas U and Th are determined using the daughter nuclides in their respective decay chains (Wilford and Minty, 2006). However, gamma-ray spectrometry has in the past years mostly focused on uranium secondary mineralization owing to its greater economic potential, in contrast to Th and K.

4.12 Radiometric data classification and analysis

Gamma-ray spectrometric data analysis involves various classification techniques some of which are related to satellite remote sensing data analyses. These include extracting and analysing information regarding the distribution and concentration of radioactive elements from geophysical sensors. Principal component analysis (PCA) and regression analyses may also be used to model and interpret the geological information (Dickson and Scott, 1997).

4.13 Application of airborne geophysical gamma-ray spectrometry in geology

Gamma-ray spectrometry has been applied in several areas. This section highlights some these applications for geological research. The technology has been used to produce geochemical maps for the surface that show lateral distribution of natural radionuclide elements in some parts of the world, which were used to provide estimates of the apparent surface concentrations of the common naturally occurring radioactive elements (Youssef and Elkhodary, 2013). Airborne radiometric data have also been used for geological mapping even in areas where field mapping is limited by budget and unfavourable terrain (Jaques et al., 1997).

Airborne geophysical radiometric data have also been used in many geological mapping projects, especially in Australia, to provide a basis for both regional and local-scale detailed mineral prospects mapping (Dickson et al., 1996; Dickson and Scott, 1997). However, identification of radiometric spectral features for radioactive minerals needs to consider principles and processes that influence radioactivity for effective interpretations including knowledge of alteration of rocks and soil forming processes (Dickson et al., 1996).
In addition, the technique has also been used, for example, in radon hazard forecast mapping for the Oslofjord region, Norway (Smethurst et al., 2008), digital lithological mapping of the Melville Peninsula, northern Canada (An et al., 1995), and the geological mapping, radioactive mineral exploration and environmental monitoring of south-eastern Aswan city, South Eastern Desert, Egypt, (Youssef and Elkhodary, 2013). Geological mapping in the Carajas Province, Brazil, was also done using gamma-ray data (Paradella et al., 1997). All these case studies show that gamma-ray spectrometry is indeed an important approach for geological mapping.

Furthermore, airborne gamma-ray spectrometry has been used in soil mapping projects. For instance, it has proved very helpful in soil mapping and land degradation processes in the Wagga Wagga area, NSW, Australia (Bierwirth, 1996), and regolith mapping done by integrating Landsat TM imagery and high resolution gamma-ray spectrometry in Cape York Peninsula (Wilford, 1992). Other examples include investigations on the distribution of natural radionuclides in native soils of Southern Saskatchewan, Canada (Kiss et al., 1988); studies on gamma-ray attenuation and soils relationships in SW England (Beamish, 2013); and studies on weathering intensity index in Australia (Wilford, 2012). Potasic signature enrichment in granite rocks has also been mapped based on inferences from the radioactive minerals in the Chitrial area, Nalgonda district, Andhra Pradesh (Rajaraman et al., 2013).

Similarly, Hwang et al. (2014) delineated U mineralized granites in S. Korea using *in situ* gamma-ray spectrometry surveys. Their findings showed lack of substantial K and Th concentrations in the granitic intrusions and a relatively anomalously high U concentration especially in hydrothermally altered granites and pegmatites. This agrees with other studies that have found that granites, *sense stricto*, contain high U values compared to other intermediate intrusions such as nepheline syenites. U, Th and K are all incompatible elements (Wilford and Minty, 2006) and as such their concentrations in common rocks is positively associated with silica content. Therefore, high U levels would be expected in areas underlain by granites and other acidic rocks. This also suggests higher levels of U and Th in granites than nepheline syenites (Wilford and Minty, 2006).

The recent Tellus data's integrated high-resolution airborne geophysical and geochemical survey of Northern Ireland seem to support these results. Results from this survey (Young and Donald 2011), showed that granitoids have high concentrations of both U (>2.6-4.5 mg/kg) and K (2-2.5wt %), although the survey did not show any alkaline rocks from the area. Generally, K has crustal abundance of 2.3%, whereas U and Th have crustal abundances about 3 and 12ppm, respectively. Increased radionuclide remobilization could be influenced by erosion and leaching from high U rocks.

4.14 Gamma-ray spectrometry's potential in delineating nepheline syenite rocks

From the preceding sections, it may be appreciated that airborne gamma-ray spectrometry offers an important application for mineral and geological mapping. This is because with radiometric data it is easy to delineate the apparent surface concentrations of key naturally occurring radioactive elements: K, U and Th. The absolute concentrations of U, K and Th, depict the properties of different lithologies. Therefore, the knowledge of the rocks' response to gamma-ray radiation, provide a viable means of mapping nepheline syenite rocks. Nepheline syenites have the same chemical composition as phonolites. Therefore, in Table 4.3 information for nepheline syenites is interpreted from phonolites because values for nepheline syenites *senso stricto* were not presented by Tye et al. (2017). In Chapter 2, data for the few reviewed nepheline syenites of Malawi showed that their U values ranging from 0.12 to 35.00 ppm and an average of 6.11ppm. The values for K_2O ranged from 1.74 to 9.66 wt% (mean 4.81 wt.%) while Th contents ranged from 0.30 to 30.70 ppm (mean 12.59ppm). This shows that Malawi's nepheline syenites have slightly higher U and K_2O values than the phonolites /nepheline syenites in Table 4.3. In Chapter 2, nepheline syenites from other parts of the world, showed higher K_2O values than those in Table 4.3 ranging from 0 to 11.7 and (mean 5.63 wt%). However, they showed similar ranges of 0.1 to 59.3ppm (mean 8.62ppm) for Th but similar ranges of 0.04 to 35ppm (mean 4.72ppm) for U to the data.

Table 4.5: Summary of radionuclides in common rocks (after Tye et al., 2017)

(a) Global ranges of uranium abundance in common rocks and waters

Igneous Rocks		**Sedimentary Rocks**	
Syenites and phonolites	0.1–26 ppm	Shales, clays, mudrocks	1–5 ppm
Granites and rhyolites	2–50 ppm	Black shales (organic-rich)	2–1250 ppm
Intermediate rocks	1–6 ppm	Phosphorite-black shales	≤700 ppm
Basalts and other mafic rocks	0.1–1 ppm	Sandstones	0.5–4 ppm
Ultramafic	0.001–1 ppm	Limestones, dolomites	<0.1–9 ppm
		Coals, lignites, peats	1–6000 ppm
Metamorphic Rocks		Pure evaporites	<0.1 ppm
Low-grade	<1–5 ppm	**Water**	
Medium-grade	<1–5 ppm	Oceanic seawater	0.3–3 ppb
High-grade	<1–7 ppm	Groundwater	<0.1–460 pp

(b) *Global ranges of thorium abundance in common rocks and waters*

Igneous Rocks		**Sedimentary Rocks**	
Syenites and phonolites	0.7–35 ppm [typically, >10 ppm]	Shales, clays, mudrocks	10–13 ppm
		Pelagic clays and siliceous oozes	2–30 ppm
Granites, rhyolites and intermediate igneous rocks	8–56 ppm	Sandstones	1–7 ppm
Basalts and other mafic rocks	0.1–4 ppm	Phosphorites	1–5 ppm
Ultramafic rocks	<0.1 ppm	Limestones, dolomites	<0.05–3 ppm
		Bauxites	~50 ppm
Metamorphic Rocks		**Waters**	
Highly variable, typically	6–10 ppm	Seawater	0.009 ppb
		River water	<0.26 ppb

(c) Global ranges of potassium abundance in common rocks

Igneous Rocks		**Sedimentary Rocks**	
Syenites and phonolites	3–6%	Shales, clays, mudrocks	<0.01–7.1%
Granites, rhyolites and intermediate igneous rocks	2.5–4.5%	Sandstones	<0.01–5.6%
Basalts and other mafic rocks	1–2%	Evaporites:	variable
		Pure gypsum,	0%
		anhydrite, halite	52.40%
Ultramafic rocks	<10 ppm –1% [av. ~0.6%]	Sylvite (KCl)	
Metamorphic Rocks		**Limestones, Dolomites**	<0.01–5% [av. limestone ~0.3%]
Dependent on parent rock			[av. dolomite ~0.6%]

4.15 Integrating remote sensing and airborne geophysical gamma ray data in geological research

Few studies have attempted to integrate remote sensing and airborne geophysical data. For instance, integrated studies using (ASTER) and Enhanced Thematic Mapper Plus (ETM+) images and airborne magnetic–radiometric data for hydrothermal alteration mapping have been conducted in Sar Cheshmeh porphyry copper deposit, in Central Iran (Ranjbar, et al., 2011). In their study, Ranjbar, et al. (2011) processed and classified ASTER and Landsat ETM$^+$ data using PCA, SAM and band ratio techniques. Gamma-ray radiometric data were also processed used PCA and band ratio techniques. Their results showed that satellite remote sensing was effective for lithological and hydrothermal alteration detection.

Radiometric data were on the other hand more effective in delineating potassic alteration areas (Ranjbar, et al, 2011). In addition, other studies combining ASTER remote sensing data and airborne radiometric survey have also been conducted in Namibia for geological mapping by Gomez et al. (2005). Their study had reported poorer results with supervised classification which the authors attributed to insufficient training areas for remote sensing and low spatial resolution for the radiometric data used in the project.

4.16 Advantages and limitations of combining remote sensing and airborne radiometric data

Remote sensing and airborne geophysics have additional advantages over field-based geological mapping in various ways. For example, some areas may be covered by dense vegetation or extensive sands or may be difficult to access by field geological surveys due to unfavourable terrain. Secondly, funding constraints are major challenges (Eberle et al., 2015) for many developing countries' geological surveys, especially in Africa and Latin America. In addition, some countries are very large which, coupled with inadequate technical capacity in form of enough trained personnel and equipment, poses major challenges for conventional field geological research (Eberle et al., 2015).

In addition, satellite imagery and airborne geophysics data can be re-used for a long time and for different purposes once acquired. Conventional geochemical mapping is more costly than using geophysical and satellite remote sensing techniques. For example, there is now global coverage of some satellite data at little or no cost. Geological structures that extend across international borders can also be easily mapped using remote sensing technology, because it has no political restrictions unlike field geological and geophysical mapping.

However, the spectral response of surface materials including rocks and soil is susceptible to factors such as land cover, soil moisture, solar elevation, surface temperature and other climatic conditions (Yajima, 2014). As these factors greatly affect geologic remote sensing, data collected within the dry season offer reduced negative effects from these factors because some of them mask the geology. For example, vegetation and water bodies interfere with absorption patterns of the rocks through scattering of the incident rays of energy (Kalinowski et al., 2004). In addition, the TIR data for most systems including ASTER and Landsat are affected by bush fires, which are common in many tropical areas, especially within Africa's Savanna vegetation due to the tendency of some people to use the system as a way of clearing vegetation for farming and hunting some wild animals. This may result in abnormal colour bands and false anomalies due to increased surface temperatures, decrease in soil/surface moisture and decrease in albedo (Pereira, n.d.; Pereira et al., 2017). Remote sensing sensors mainly detect the exposed surface features while airborne geophysical sensors have capacity to detect hidden intrusions and geological structures. Radiometric surveys' detection of buried geological bodies, such as igneous intrusions, decreases with depth (Reeves and Zeil, 1990) but this can be compensated by integrating gravity and electromagnetic data.

In addition, the use of combined techniques complements each other for areas where one technique may be limited. Airborne geophysical survey campaigns are, indeed, expensive. For example, the airborne geophysical survey of Malawi conducted in 2013 cost nearly US$10million for a land area of 94,000km^2 for the countrywide aeromagnetic and radiometric data with three selected gravity survey blocks. Operational challenges with airborne geophysical survey include navigation of the aircraft as close as possible to the target feature and the locating the tie line path to plot the path on the map (Reeves and Zeil, 1990). Remote sensing data provide a better aid for such cases since they contains less geometric distortion and have a bigger spatial coverage in one scene. For both remote sensing and airborne geophysical spectrometry studies, ground-truthing is very necessary.

4.17 Conclusion

This Chapter has reviewed the use of remote sensing and airborne geophysical radiometric data in geological mapping. It is appreciated that remote sensing and airborne radiometric data are used extensively in geological research. While the choice of sensors is dependent on the features to be studied, satellite sensors that cover the TIR wavelength region of the electromagnetic spectrum are potentially more effective for nepheline syenites and related silicate rocks. This is because nepheline syenites show key emissivity minima in the TIR region. Combined use of ASTER data, DEM/DTMs and high-resolution airborne geophysical data offers potential for delineation of nepheline syenite intrusions for alternative potash sources using these methods. Figure 4.1 shows a summary diagram of the different techniques reviewed and the expected indicators of possible nepheline syenite intrusions.

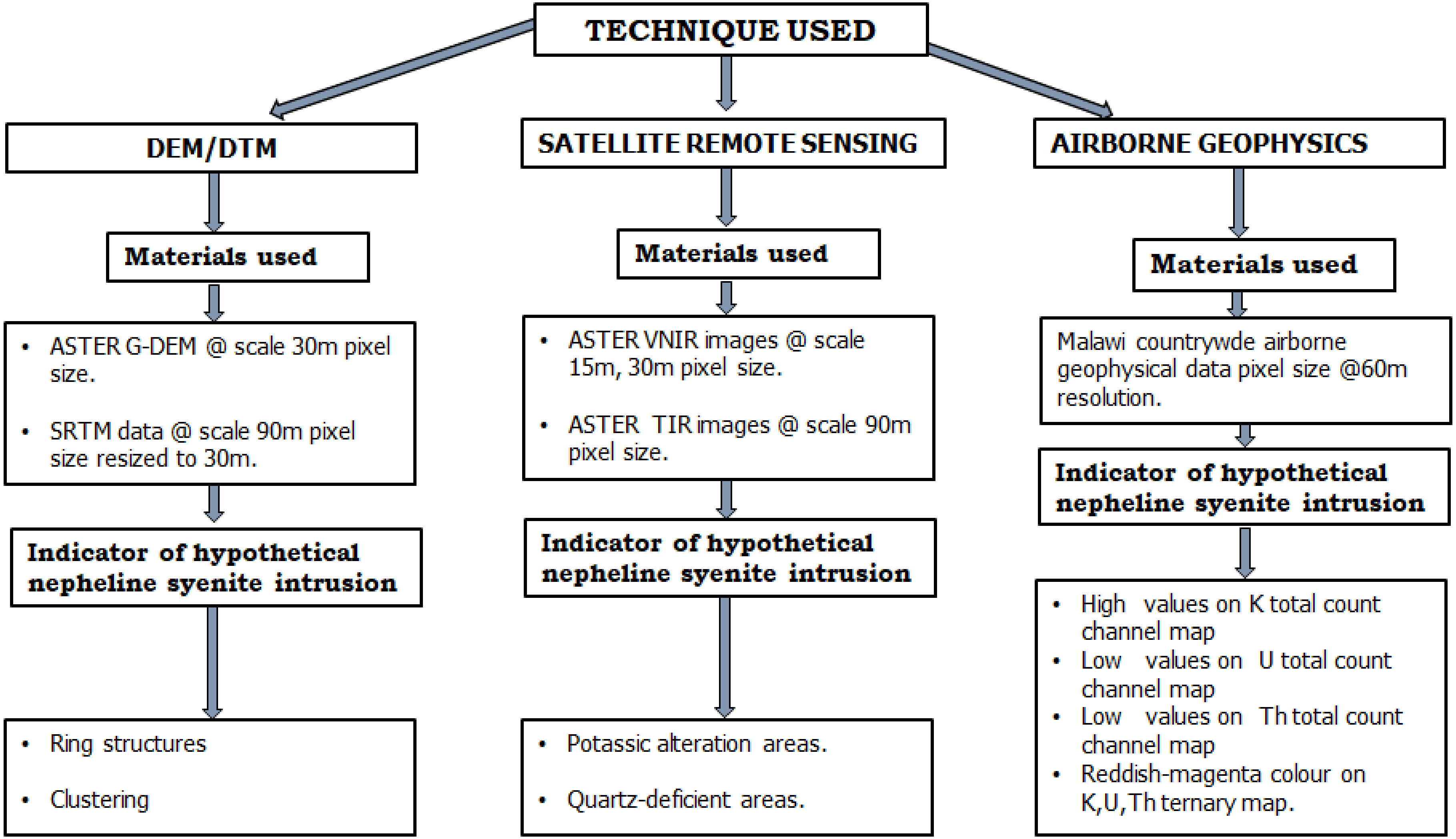

Figure 4.1: Summary diagram of different techniques and their possible indicators of a hypothetical nepheline syenite intrusion.

Chapter 5: Nepheline syenites as alternative sources of potash fertiliser: exploration

5.0 Introduction

This chapter used recent airborne gamma-ray spectrometry data from Malawi's countrywide high resolution airborne geophysical survey and combines these, partially, with remote sensing data, especially digital terrain models/digital elevation models. This chapter presents results of these DTMs/DEMs airborne gamma-ray data analyses and subsequent fieldwork in Malawi. The first part of the chapter addresses the study's Objective 3 which sought *to process gamma radiometric data to map the composition of surface rocks by specifically, interpreting K, U and Th data and combine with remote sensing results for delineation of nepheline syenite targets*. The second part of the chapter responds to Objective 4 of the project *(i.e. to conduct ground-truthing to validate remote sensing and airborne geophysical results and develop an identification scheme/model for potential nepheline syenites).* To achieve this objective, ground-truthing was conducted in Malawi between 14th August and 10th September, 2016. This was done in selected areas which were identified mainly through airborne geophysical gamma-ray spectrometry techniques and digital terrain models.

The fieldwork aimed to validate the effectiveness of remote sensing and airborne geophysical survey radiometric data in delineating nepheline syenites and related rocks. From Objective 4, minor objectives were formulated to guide the field work. These were to: (a) collect rock and soil samples from the identified key potential areas to validate use of remote sensing techniques and airborne geophysical survey spectrometry, (b) conduct field gamma-ray spectrometry for various rock units in the target areas and (c) make a basic assessment of vegetation cover and key biotic communities in the sampled areas to determine whether their growth could be associated with potassium presence in the soils.

5.1 Target areas for the fieldwork

The study covered the entire country and thirty-six areas were identified as possible nepheline syenites/syenites. Some these alkaline rocks were identified using our geophysical spectrometry analysis, but areas were selected for ground truthing based on their potential K content using the K, U, Th total count and ternary maps. Due to budget limitations and long distances, some areas of potential interest were not sampled at this time and thirteen of the identified key areas were surveyed (Figure 5.1). Some areas, for example, in clusters (C) and part of (D) and new findings and were not documented as alkaline rocks in the previous literature before this study.

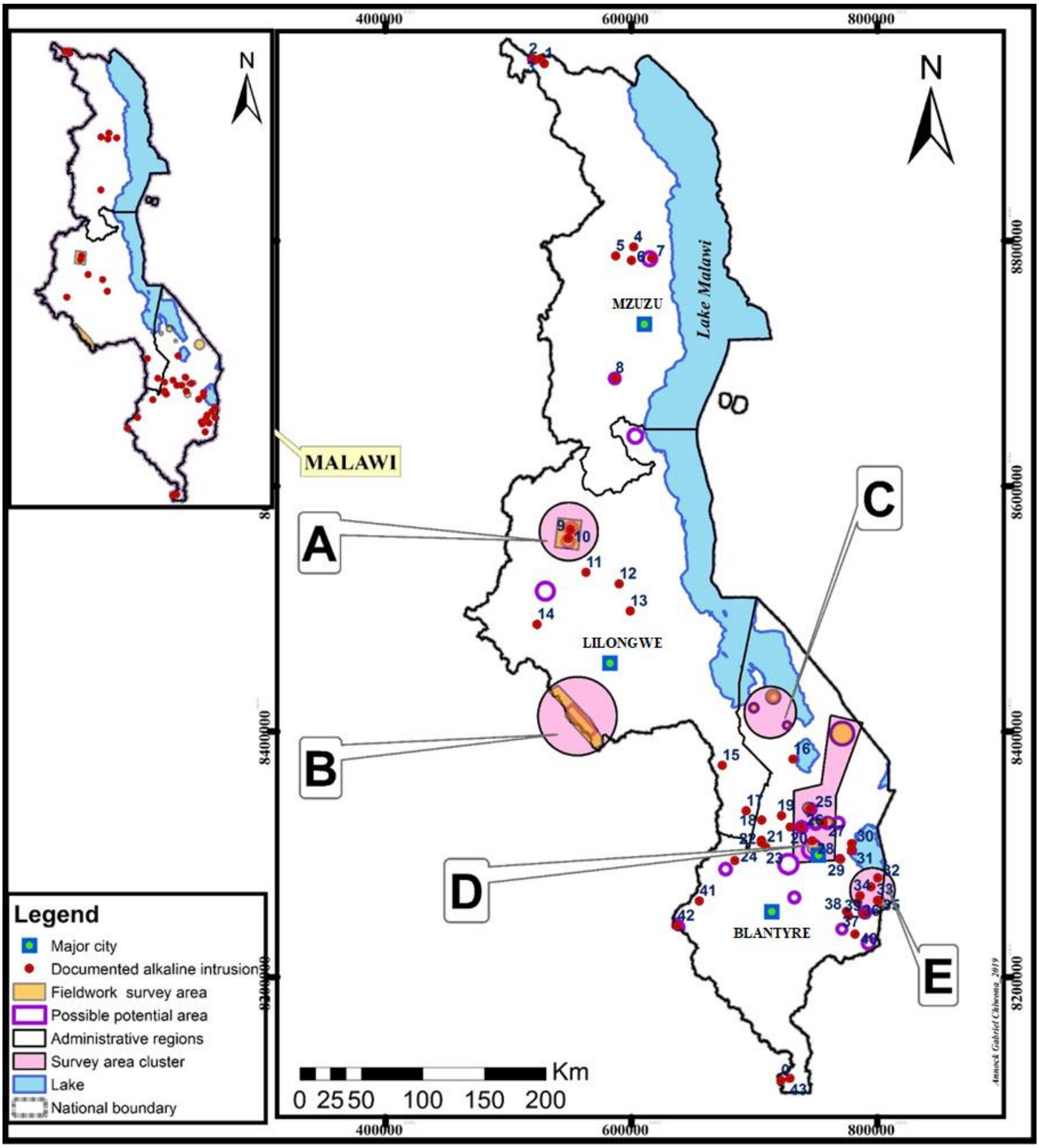

Figure 5.1: Map of Malawi showing areas surveyed and other potential areas identified in this study namely (A) central Malawi nepheline syenites; (B) central Malawi alkaline granites; (C) S.E Malawi quartz syenites; (D) S. Malawi nepheline syenites and syenites; (E) Carbonatite-associated nepheline syenites and insert map shows previously documented areas in Fig 1.4.

5.2 Methods and materials

5.2.1 Airborne geophysical gamma-ray data processing

Airborne gamma-ray spectrometry data were acquired by Sanders Geophysics Limited as part of Malawi's 2013 countrywide geophysical mapping programme, using Exploranium GR-820 gamma-ray spectrometers (Bates and Mechenneff, 2013a). Specifications and procedures for the gamma-ray acquisition and correction are discussed in the survey's official reports (Bates and Mechenneff, 2013a, 2013b). The airborne geophysical survey pixel size on the ground depends on the number of samples collected per second by the sensors. Most airborne geophysical surveys are conducted at a sampling rate of 1 count per second which is equivalent to 50-80m pixel size on the ground (Horsfall, 1997; Beamish, 2014). Malawi's airborne geophysical gamma-ray data were acquired at a line spacing of 250m. Ground clearance was 60 meters +/-20 meters and the aeroplane's average ground speed was 135 knots. The data were recorded and windowed in 256 channel spectral format at 1 sample/count per second (Bates and Mechenneff, 2013a) and were gridded at 50m grid cell size (Bates and Mechenneff, 2013b).

Several corrections were done by the survey contractor including correcting for dead-time, effective height above ground level, height adaptive filter, cosmic radiation and aircraft background radiation, radon background, stripping, altitude attenuation correction, effects of precipitation, conversion to radio element concentration and finally micro-levelling, after which the data were gridded at 50m grid cell size (Bates and Mechenneff, 2013a). This study re-processed and gridded the data using the guidelines for Geosoft's airborne geophysical survey processing (Whitehead, 2014). Due to attenuation effects and other technical factors (Bates and Mechenneff, 2013a), the data have gaps in some areas (Figure 5.2).

For airborne geophysical data grids with such small areas of missing data, interpolation was done by filling in 'dummies' using the squares method in Geosoft's Oasis Montaj software, to minimise the effect of such gaps. This interpolation technique is a method in which the gaps are filled using averages of the neighbouring pixels. The interpolation runs from all sides of the square/area, hence gives a reliable estimated value to fill the data voids. Oasis Montaj is Geosoft's core software platform specially designed for working with large volumes of airborne geophysical datasets. It is equipped with a free viewer and a licensed mapping and processing system (Whitehead, 2014) and extensions for ArcGIS software.

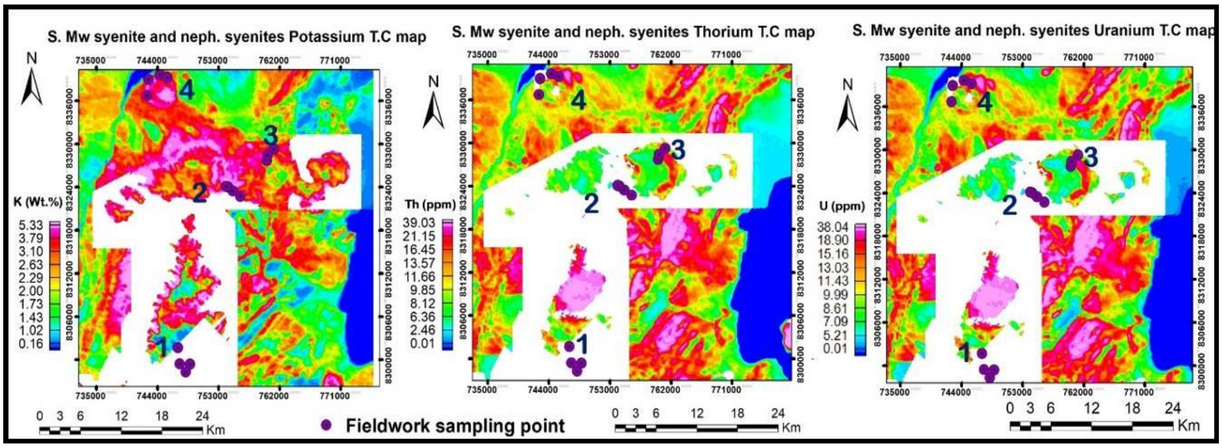

Figure 5.2: The (a) K (b) Th (c). U total count maps for the S. Malawi nepheline syenites namely: 1. Zomba Mt 2. Mongolowe, 3. Chaone and 4. Junguni areas, showing missing data.

5.2.2 Digital terrain/elevation models (DTM/DEM)

As reviewed in chapter 4, nepheline syenites, carbonatites and other alkaline rocks are usually associated with ring structures, lineaments and clusters (Jaireth et al., 2014; Woolley and Kjarsgaard, 2008). In order to delineate these rock structures, the Shuttle Radar Topography Mission (SRTM) and ASTER Global Digital Elevation Model (GDEM) datasets were used. Both the SRTM and GDEM are freely available to the public, and have global coverage. However, ASTER GDEM has higher spatial resolution than SRTM data (Aster Gdem Validation Team, 2009; Guth, 2010). SRTM DEM maps and ASTER G-DEM mosaics were therefore also used to support identification of some potential nepheline syenite areas in addition to gamma-ray data.

The processing of the DEM data using the approach of Onuma et al. (2013) was followed using the ENVI software package. The raw data were selected and loaded into ENVI software and combined into a mosaic image. The hill-shade image was then created with the output hill-shade Image Sun Elevation Angle set at 30^o and the Sun Azimuth Angle 45^o. The output mosaic was produced both as a colour and grey-scale map saved as a Geotiff file. The output Geotiff files produced in ENVI were then loaded into the ArcGIS environment and pyramids were calculated to produce a 4-bands image. The Geotiff image opens ArcGIS with four grayscale bands. Then, using the properties' symbology tool, the ASTER GDEM colour images were further enhanced by setting the four bands to RGB: 1, 2, 3 and the alpha band to 1 respectively. The standard deviation was set to 2.5 and Z value was 100 and hill-shaded. The ASTER GDEMs were then overlaid on the SRTM DEM map (in ArcGIS) to show lineaments, clustering and ring-structures that indicate nepheline syenites and related alkaline intrusions, as outlined in Section 5.3.2 of this chapter.

5.2.3 Field sampling

Field gamma-ray data were collected using an RS 125 gamma-ray field spectrometer (Terraplus, 2016), acquired from the Geological Survey of Malawi; Figure 5.3) to obtain K, U and Th concentrations in different rocks in the areas surveyed. The RS 125 gamma-ray spectrometer is a portable high sensitivity, easy to use and self-stabilizing spectrometer. The spectrometer has assay mode readout for K (wt%), U and Th in ppm (Madi et al., 2014). The Total Count readout at a 1x/sec rate was used in the Survey Mode (Terraplus, 2016) with sampling time set at 60 seconds. Field sampling was done at a sampling interval of 1-15m^2. Different rock units were sampled but the focus was on nepheline syenites to assess their potential as potassium silicate fertiliser sources.

Figure 5.3: Field gamma-ray spectrometry data acquisition using the RS 125 gamma-ray spectrometer.

5.2.4 Field sampling process

Purposive sampling was the main method used to select target areas for fieldwork such that high priority areas were identified from remote sensing and airborne geophysical gamma-ray data. Since the results from remote sensing and gamma-ray data processing covered the whole country, proportional sampling was used. The total areas identified were assigned in proportions based on the country's three administrative regions and the same percentages were used to select the number of target areas for the fieldwork. Nearly 70% of the priority areas identified fell in southern Malawi. Therefore, 70% of the field survey areas were in the southern region and the remainder in the central region. Northern Malawi was not surveyed due to time and budget limitations. Sampling was done with a sampling density of at least 1-2 sampling points per km^2 to maximize areal coverage.

Within the selected areas, samples were collected for both nepheline syenites and other rock types within a sampling area of $15m^2$ to match with the pixel size of ASTER data. Rock chips from various outcrops (especially the fresh part of the outcrops) within the sampling unit area for each point were collected randomly, by ensuring that samples were unsystematically taken from different outcrops within the unit area. This helped to get sample representativeness for each locality of the outcrops. Field gamma-ray measurements were taken at each outcrop from which a rock sample was collected. Soil sampling involved collecting materials weathered from the dominant rock in sampling areas. Focus was on soil underneath major outcrops to avoid sampling soils transported from other places.

5.2.5 Vegetation assessment

Data on vegetation cover were collected using the diagnostic species method of the EcoVeg approach for classifying natural vegetation as presented by Faber-Langendoen et al. (2014). In this task, the vegetation percent cover determination was done by estimating the total crown cover on a relative scale from 1% to 100% within an area of approximately $15m^2$ and then assessing the plant structure and growth forms and determining the dominant plant communities/species of the natural vegetation. The area used was the same in which rock sampling was also done, for easier comparison with satellite imagery. The dominant vegetation species were diagnosed and classified using the classification for the biomes of Malawi which is used by Malawi Department of Surveys (2008), as shown in Figure 5.21.

5.2.6 Data analysis

The airborne geophysical gamma-ray spectrometry data were analysed for selection of potential areas by producing total count maps of the individual radioactive elements (K, Th and U). Ternary maps were produced by making composite maps of the three radioactive elements to delineate K anomalous areas. Descriptive statistics were computed for the U, K and Th values which were extracted from the airborne geophysical spectrometry survey grids and the data acquired from the fieldwork. The Pearson's correlation was used to assess the relationship between the data from the airborne and field spectrometry.

5.3 Results of processing

5.3.1 Airborne geophysical gamma-ray spectrometry results

The potential nepheline syenite areas were selected for fieldwork based on results from the gamma-ray spectrometry processing and analysis. Figure 5.4 (A) shows many areas with high potassium content all over the country. Figure 5.4 B on the other hand, shows that most of the areas in southern Malawi which showed high K in Figure 5.4 (A) have low U content and low Th content in Figure 5.5 (A). These areas with high potassium contents in Figure 5.4 (A) and on the ternary composite map (Figure 5.5 B) but low U and Th contents suggest greater potential potassium anomalous areas and possible nepheline syenite/alkaline bodies.

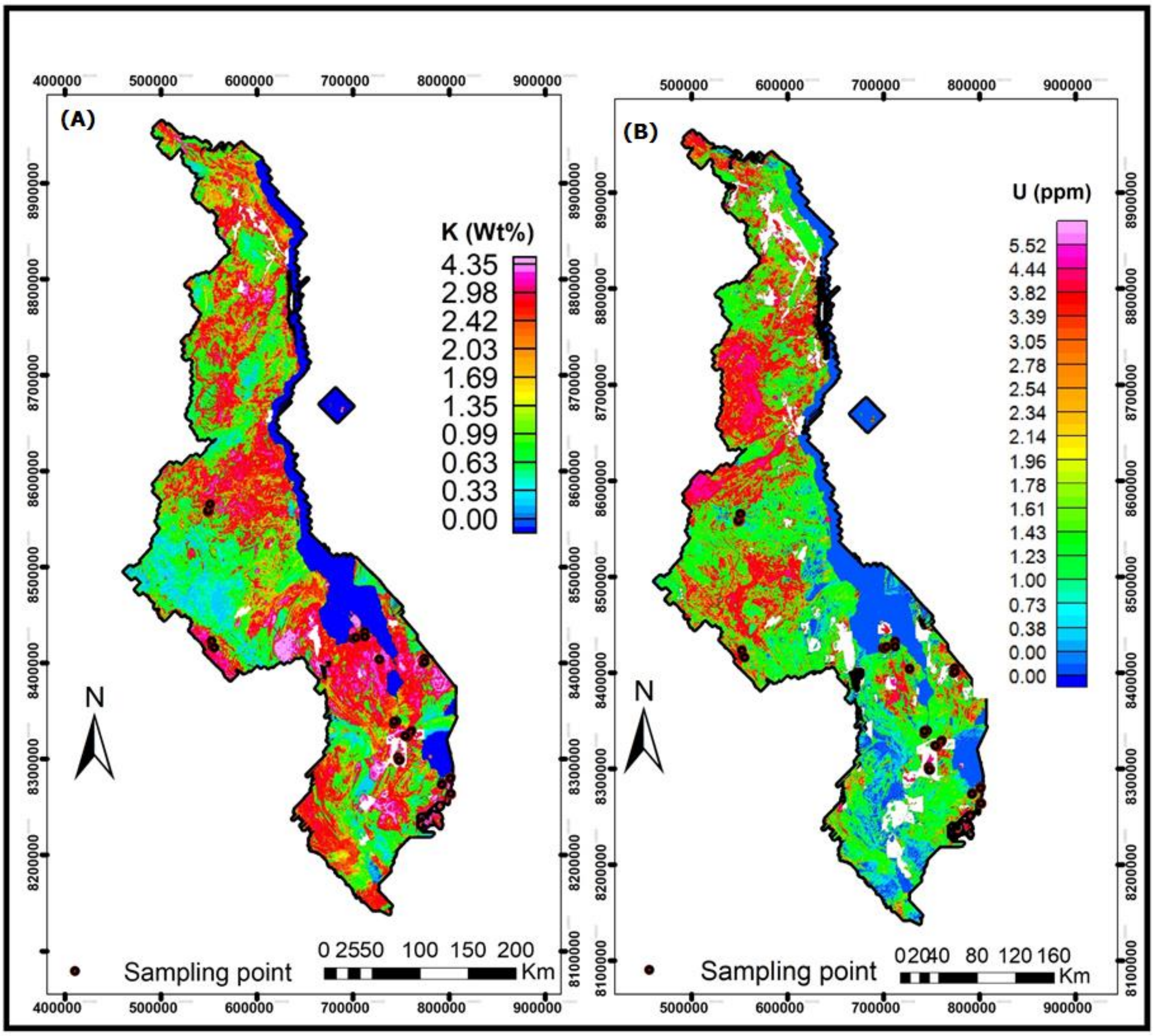

Figure 5.4: Airborne geophysical survey gamma-ray maps for Malawi (A) K total count map and (B) U total count map.

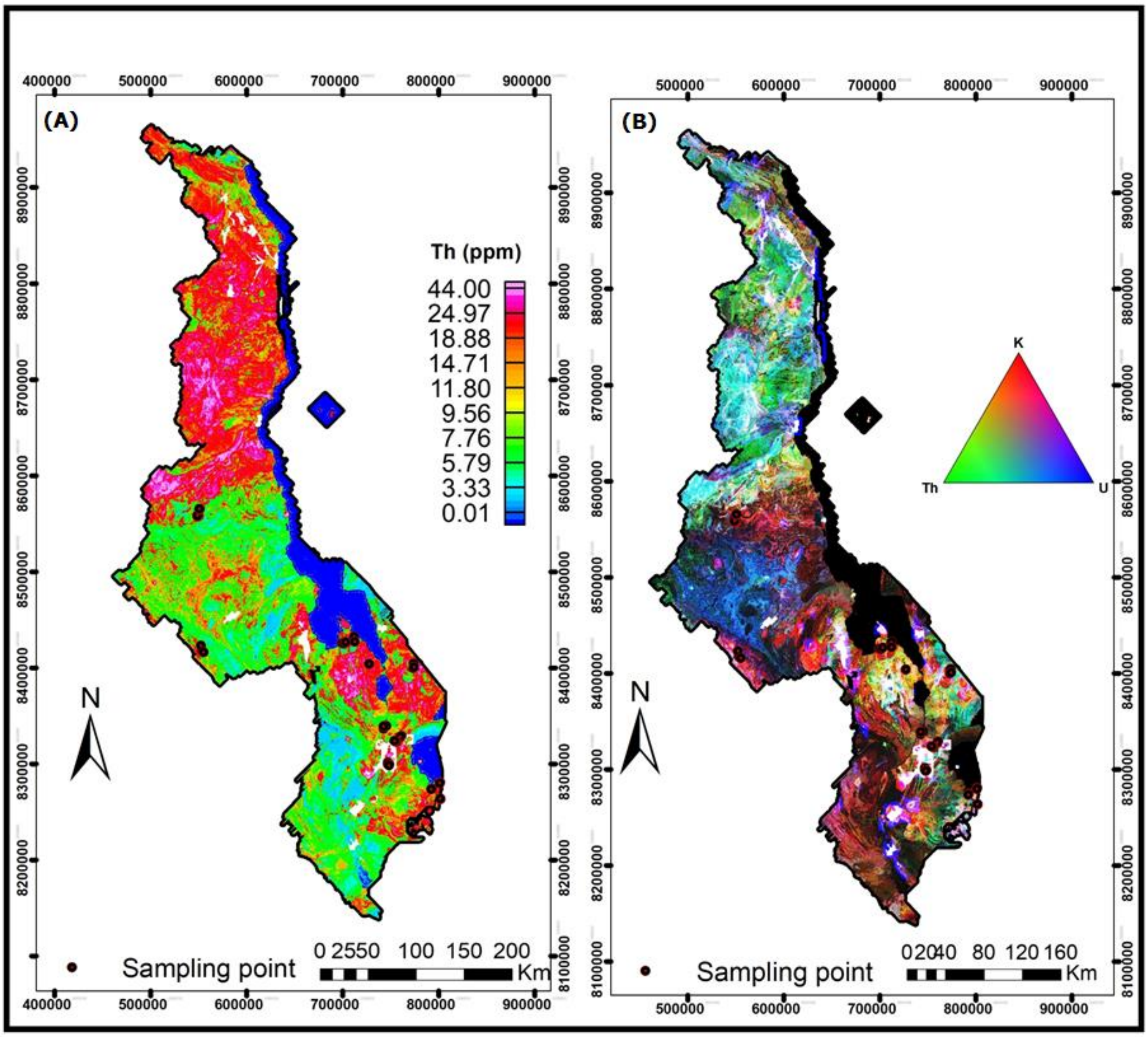

Figure 5.5: Airborne geophysical survey gamma-ray maps for Malawi (A) Th total count map and (B) K-Th-U ternary composite map.

Figures 5.6-5.10 show total count gamma-ray geophysical maps for different areas which were selected for fieldwork in Malawi. Most of these areas show have high potassium content and this qualified them for preliminary selection for sampling as possible nepheline syenites areas. In these Figures, the total count maps also show that some areas also have high Th and U values. For example, the central Malawi nepheline syenites and alkaline granite and the carbonatite-associated nepheline syenites show high K and U and Th elemental values. The total count maps were not enough to select an area as a potential sampling area for the fieldwork.

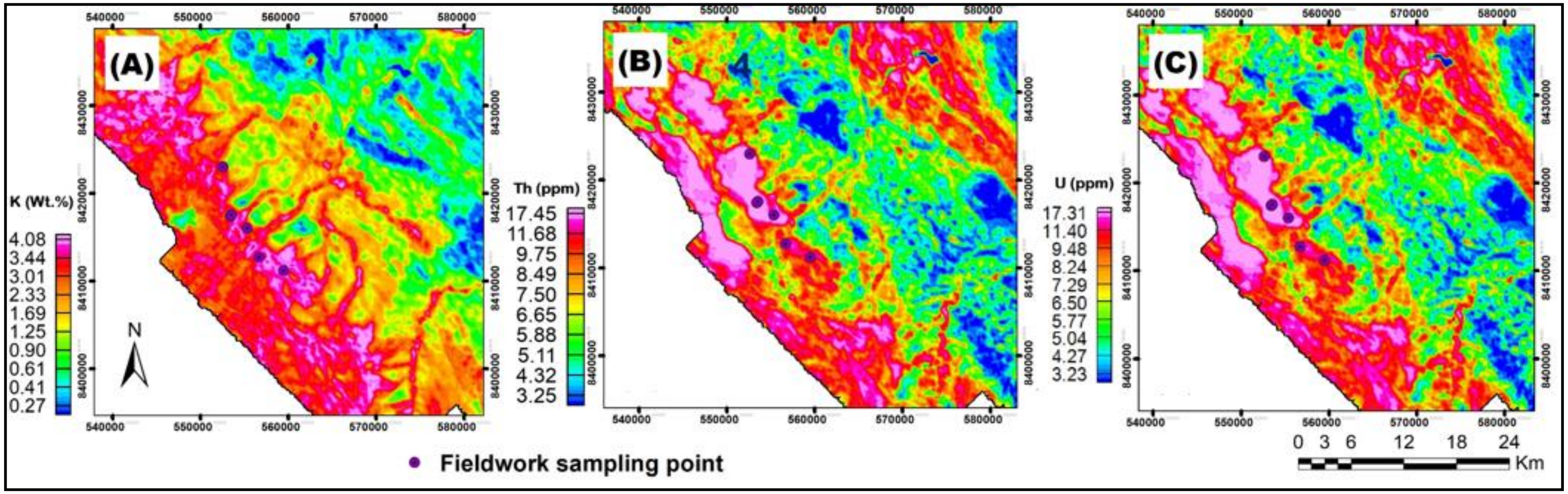

Figure 5.6: Gamma-ray maps for central Malawi's Dzalanyama alkali granites (A) K total count (B) Th total count and (C) U total count.

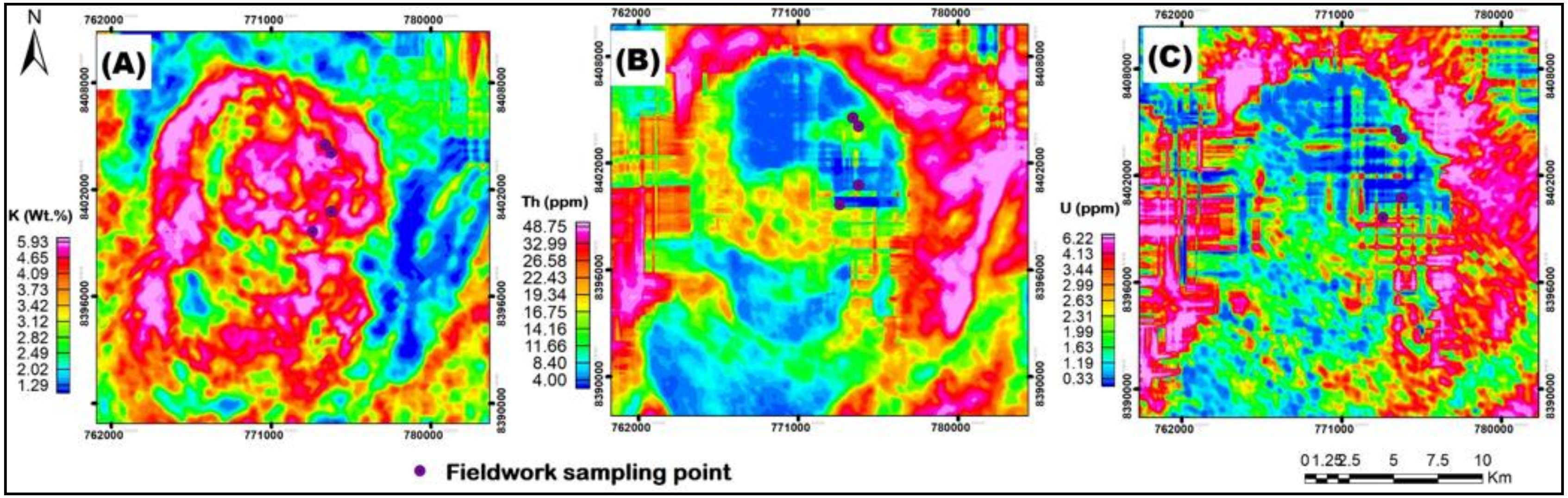

Figure 5.7: Gamma-ray maps for Mangochi Hill syenites intrusion (A) K total count (B) Th total count and (C) U total count.

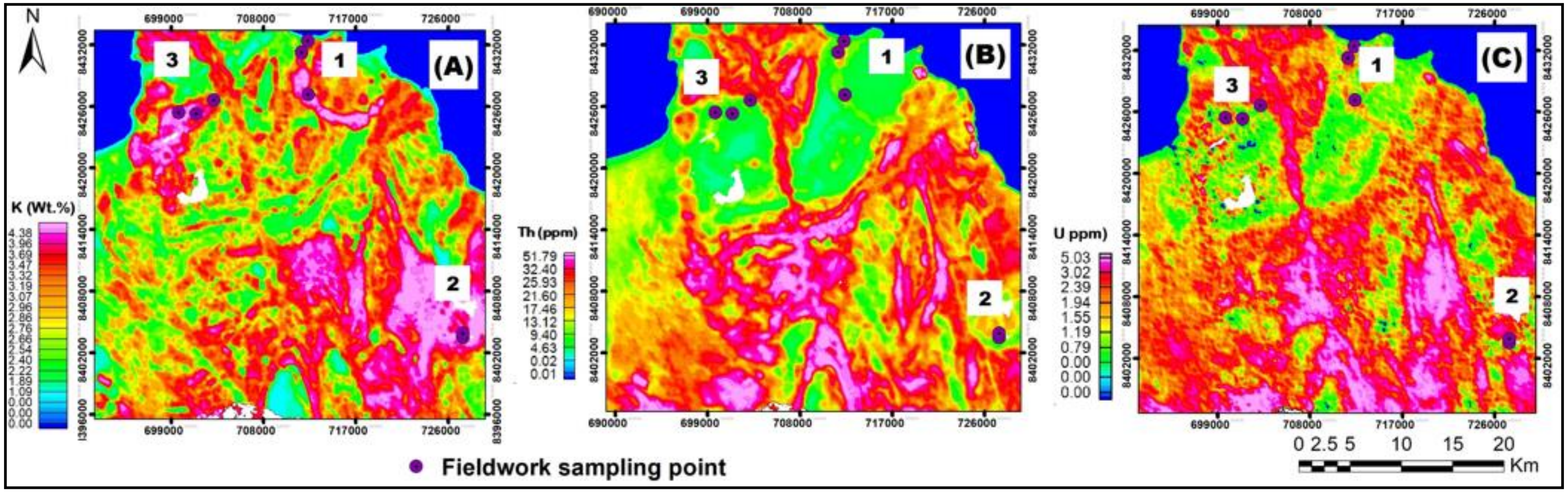

Figure 5.8: Gamma-ray maps for S. East Malawi quartz syenites namely (1) Nkhuzi Bay (2) Mauni and (3) Chantulo intrusions (A) K total count (B) Th total count and (C) U total count.

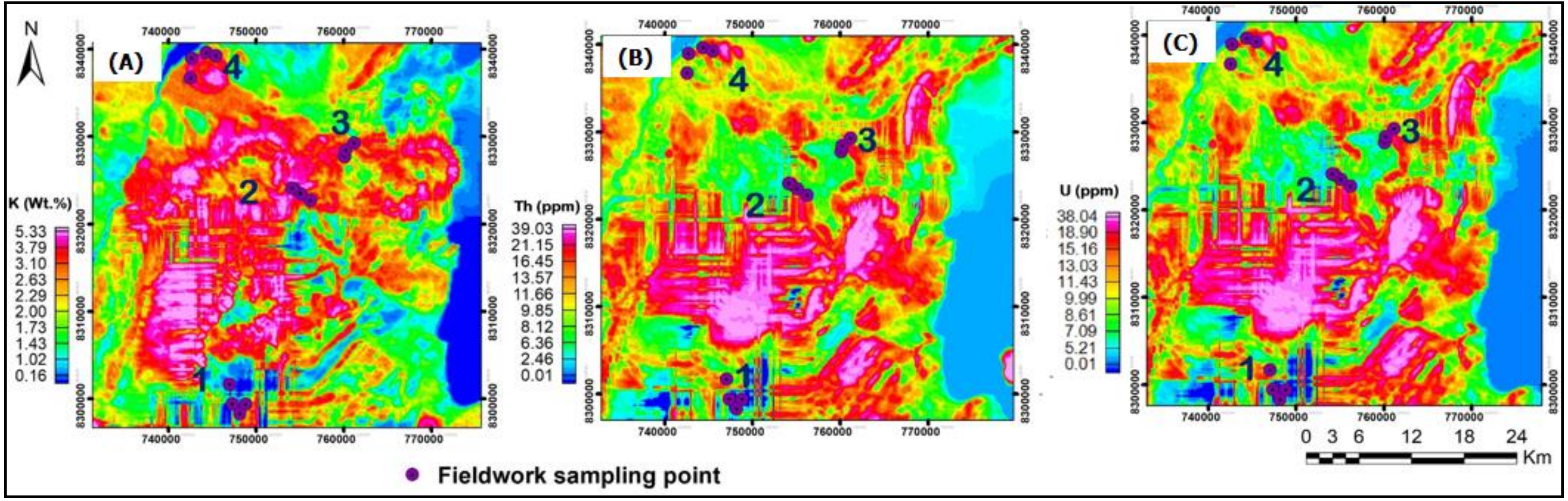

Figure 5.9: Gamma-ray maps for South Malawi syenite and nepheline syenites (1) Zomba (2) Mongolowe (3) Chaone and (4) Junguni intrusions (A) K total count (B) Th total count and (C) U total count.

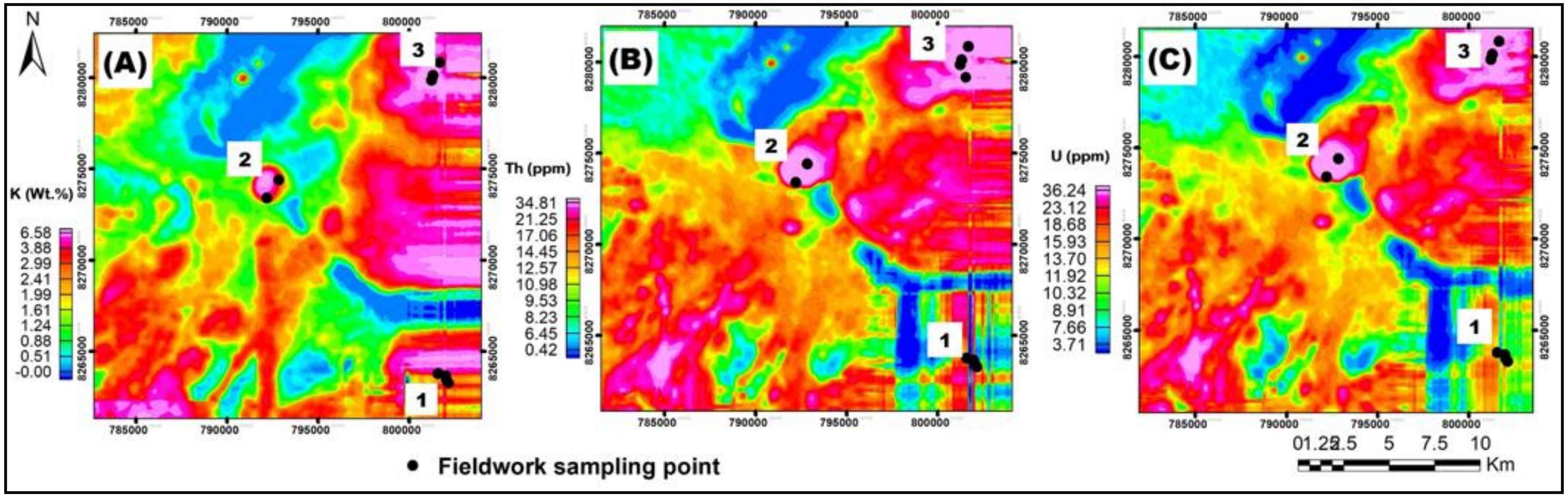

Figure 5.10: Gamma-ray maps for carbonatite-associated nepheline syenites (1) Songwe-Mauze (2) Nkalonje (3) Tundulu intrusions (A) K total count (B) Th total count and (C) U total count.

Although some areas showed high potassium content on the individual potassium total count map, they could not be selected as K anomalies and possible nepheline syenite intrusions if they also showed had high U or Th content. This is because geochemically, nepheline syenites show high K content relative to Th and U as already noted in chapter 4, Table 4.3 (Tye et al., 2017). On the ternary maps, the nepheline syenites, the quartz syenites and alkali granites show high potassium content. The ternary composite maps which combine the three radiometric channels were therefore used select potential areas which showed high K content (Figure 5.11). The selected areas were then considered as potential sampling areas for the fieldwork.

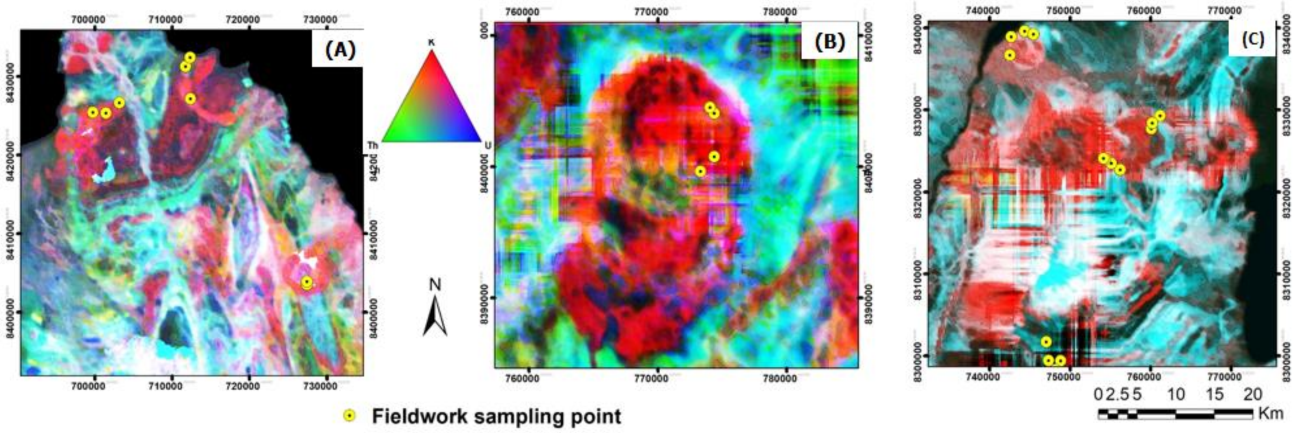

Figure 5.11: Examples of gamma-ray ternary maps for (A) S.E Malawi quartz syenites [1. Nkhuzi bay 2. Chantulo, 3. Mauni] (B) Mangochi hill syenite and (C). S. Malawi intrusions [1. Zomba 2. Mongolowe 3. Chaone and 4. Junguni].

5.3.2 Remote sensing digital elevation models (DEMs)

Digital elevation models (DEMs) show that the alkaline rocks are more elevated than the other lithologies. They also appear as ring structures and, in some cases, especially the carbonatite, associated complexes appear as clusters. Areas with anomalous (high) K values as presented in section 5.2.1 and which also showed ring structures or clustering on the DEMs were considered as best targets for fieldwork. The colour-coded DEMs show that the alkaline intrusions are more elevated than the other rock types while the grayscale images portray better the ring structures, lineaments and clustering of the intrusions. Figures 5.12- 5.17 show structural detection using DEMs for areas surveyed in this study.

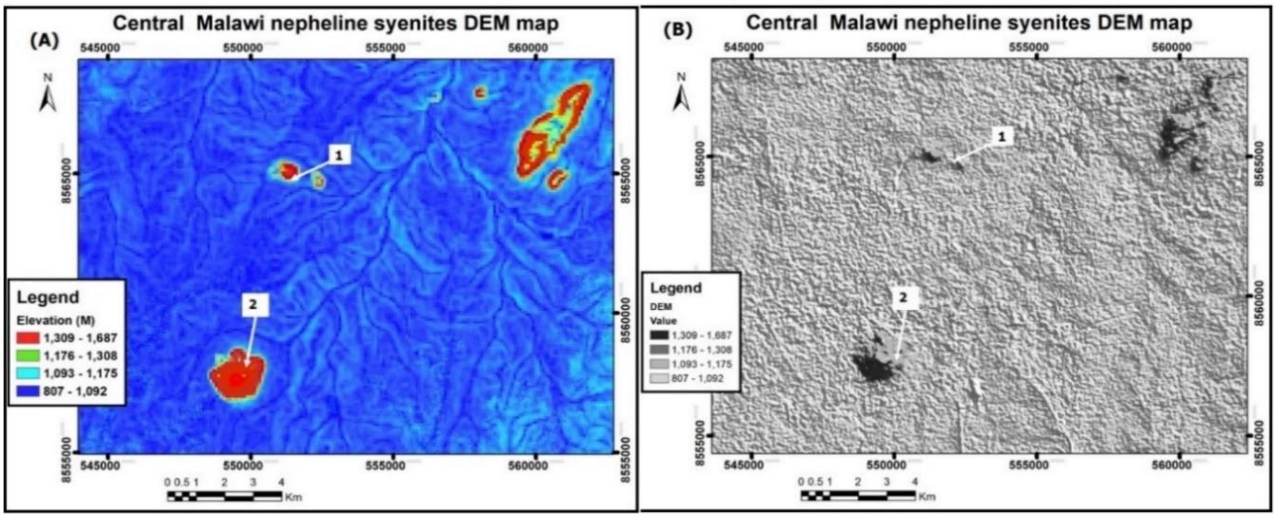

Figure 5.12: ASTER colour DEM and (B) grayscale DEM maps for namely (1) Kasungu (b) Kasungu-Chipala.

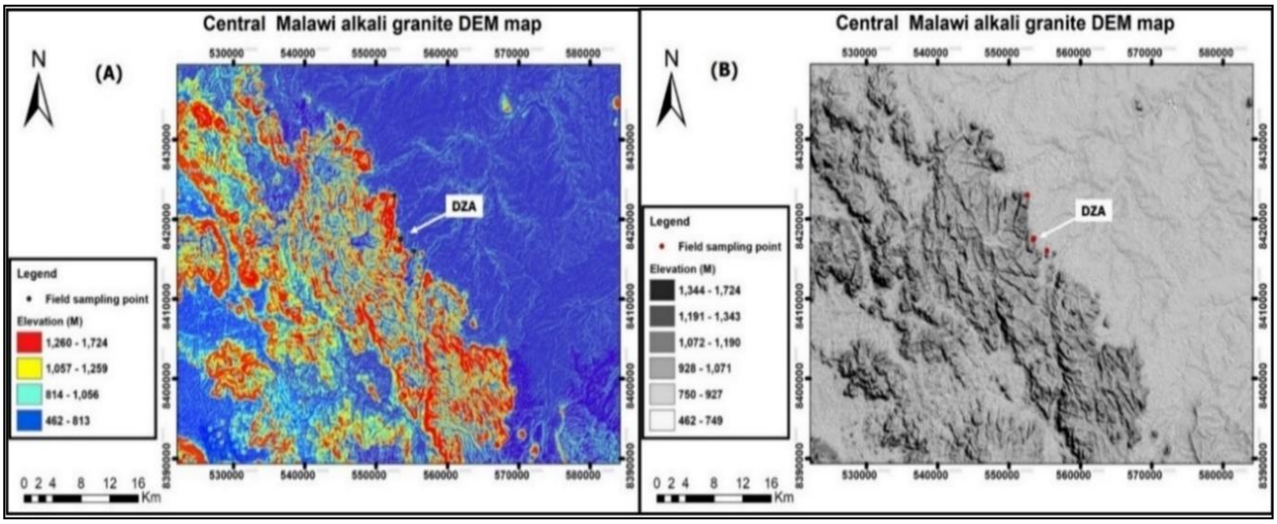

Figure 5.13: ASTER colour DEM and (B) grayscale DEM maps for central Malawi’s alkali granites.

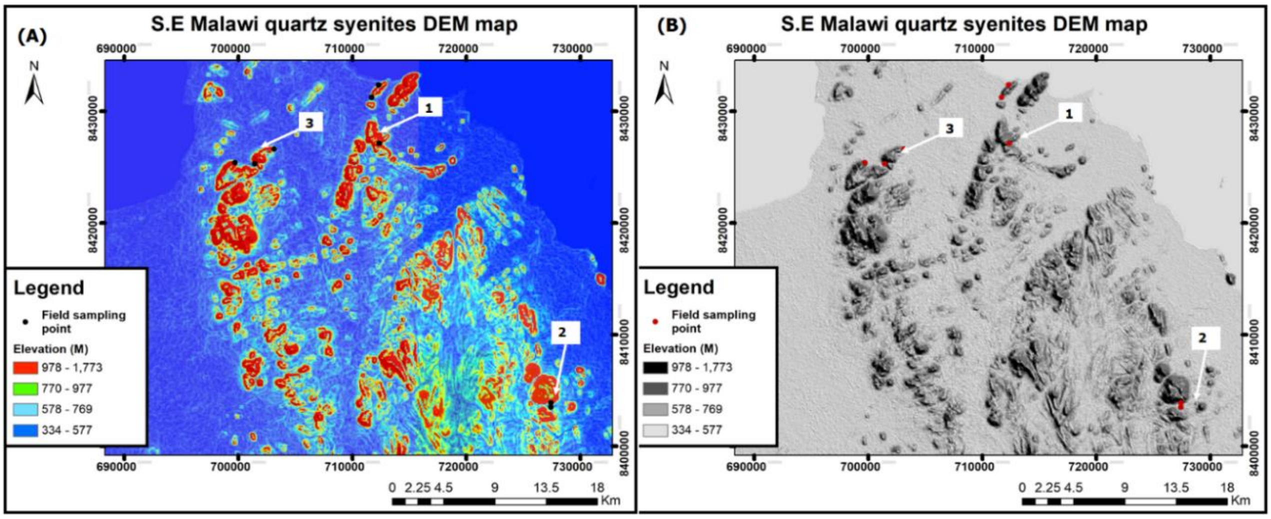

Figure 5.14: (A) ASTER colour DEM and (B) grayscale DEM for S. East Malawi quartz syenites namely (1) Nkhuzi Bay (2) Mauni and (3) Chantulo intrusions.

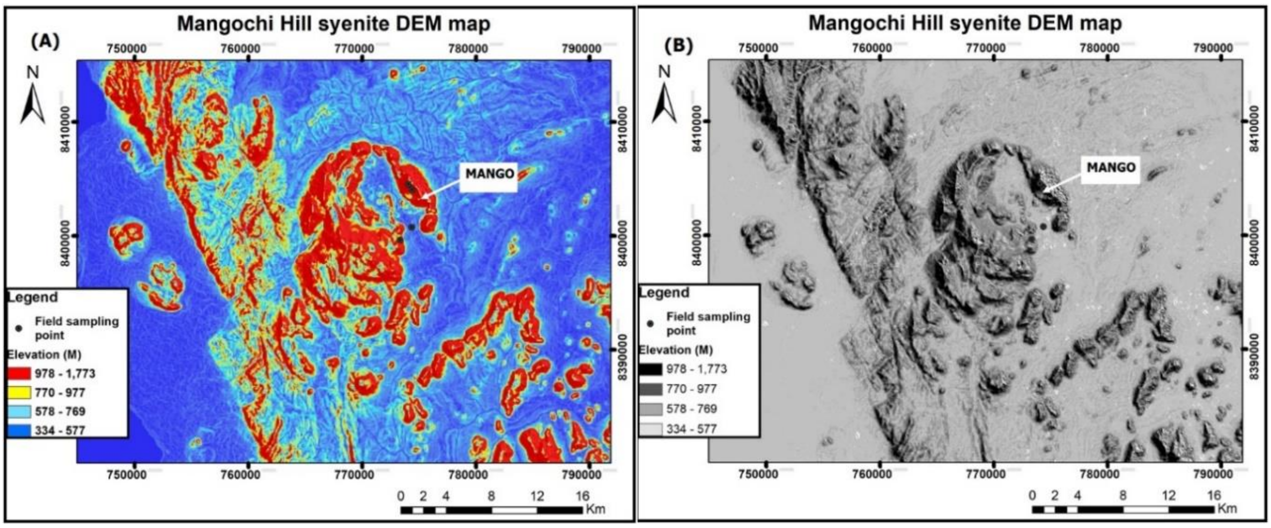

Figure 5.15: ASTER colour DEM and (B) grayscale DEM maps for Mangochi Hill syenite showing semi ring structure on target area.

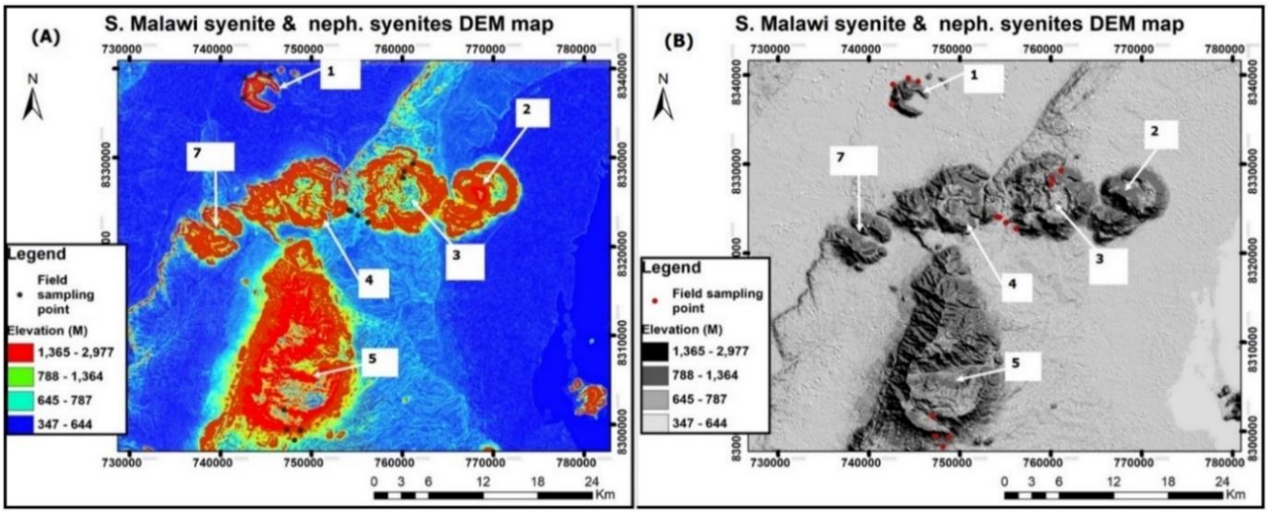

Figure 5.16: ASTER colour DEM and (B) grayscale DEM maps for South Malawi syenite and nepheline syenites namely, (1) Zomba (2) Mongolowe (3) Chaone and (4) Junguni areas showing ring structures.

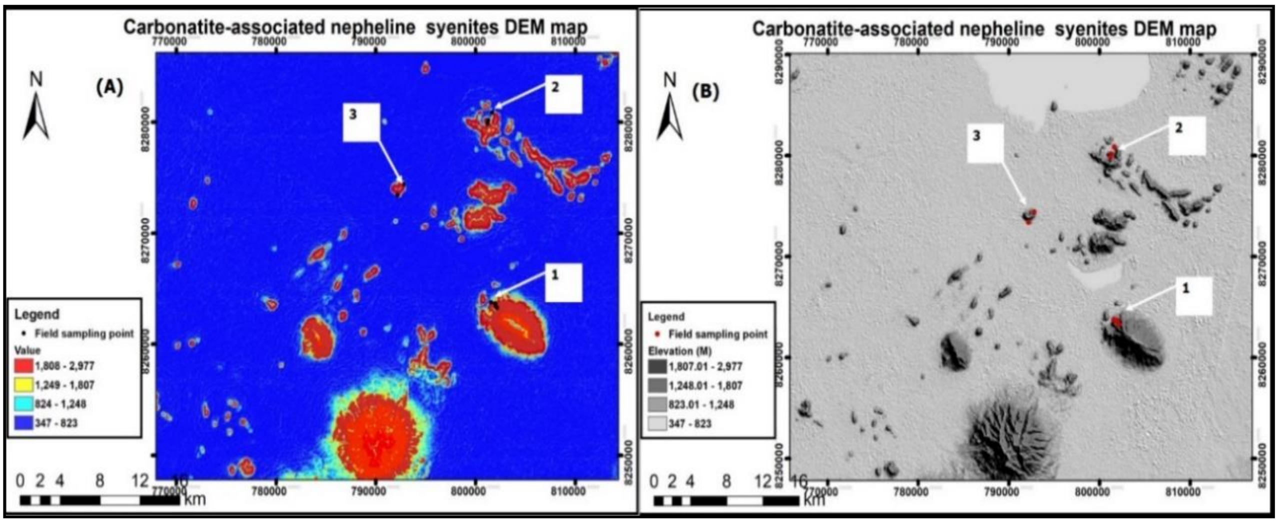

Figure 5.17: ASTER colour DEM and (B) grayscale DEM maps for the carbonatite-associated nepheline syenites (1) Songwe-Mauze (2) Nkalonje (3) Tundulu.

5.4 Geology and field observations of the surveyed areas

The samples of nepheline syenites, syenites and other rock types were collected from the different areas that were surveyed. As shown in Figure 5.1 the areas were grouped in clusters based on the locations where they occur. Figure 5.18(A-D) shows the general geology of four out of the five clusters which were surveyed, namely clusters A, C, D, E in Figure 5.1 which are shown as A, B, C and D respectively in Figure 5.18. The maps in Figure 5.18 are for clusters which included at least a nepheline syenite or syenite intrusion, therefore, Cluster B of Figure 5.1 was not included in Figure 5.18.

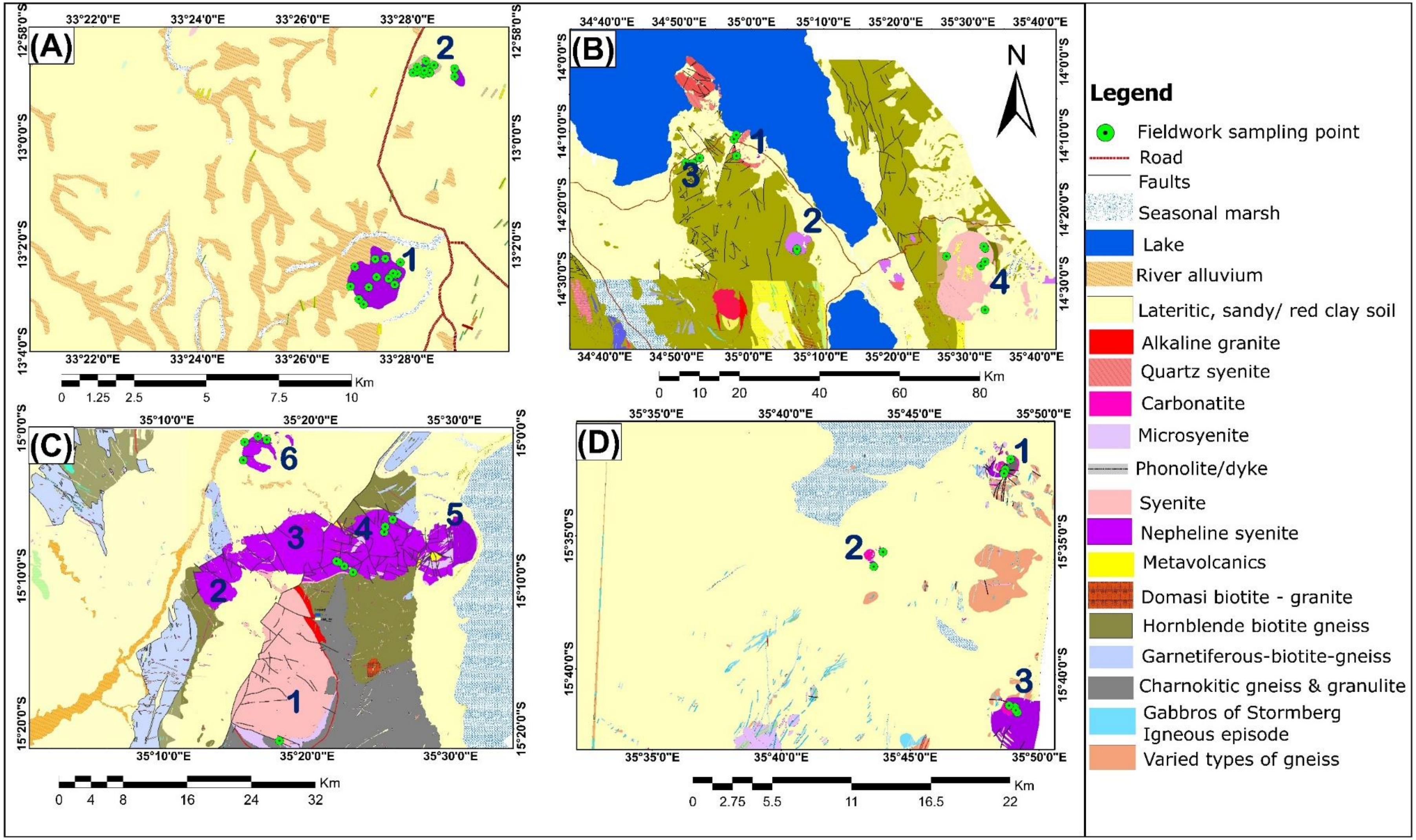

Figure 5.18: General geology of clusters A, C, D, E. of Figure 5.1 namely (A) central Malawi nepheline syenite namely, 1. Kasungu hill, 2. Kasungu-Chipala hill areas (after Peters, 1969); (B) South-east Malawi quartz syenites namely, 1. Nkhuzi bay 2. Mauni, 3. Chantulo, 4. Mangochi Hill syenite. (after King and Dawson 1976); (C) South east nepheline syenites and syenite namely: (1) Zomba syenite, (2) Chinduzi, (3) Mongolowe, (4) Chaone, (5) Chikala and (6) Junguni nepheline syenites (modified after Eby et al., 1998); (D) the carbonatite-associated nepheline syenite area, namely: 1. Tundulu, 2. Nkalonje, 3. the Songwe-Mauze, intrusions.

5.4.1 *Central Malawi nepheline syenites (Figure 5.18 (A))*

The central Malawi unit comprises the Kasungu and Kasungu-Chipala nepheline syenites (areas 1 and 2 respectively in Figure 5.18 (A)), which were intruded in a suite of medium to high-grade metamorphic rocks of the Mozambique Orogenic Belt, dated ~500 Ma (Eby et al., 1998). In hand specimens, nepheline syenites from both intrusions are medium to coarse-grained and contain xenolithic inclusions of gneisses and diorites. Mesocratic, very coarse-grained nepheline syenites, which grade into syeno-granites, occur sparsely. The rocks are variably weathered; lichens and small herbaceous plants are abundant.

The Kasungu-Chipala nepheline syenites (2 in Figure 5.18 (A)), are in some localities bounded by diorites, although the contact zone between these rock types is not clear (Peters, 1969). Localized faulting with some heavily folded biotite schist and fenites along the nepheline syenite-diorite contact zone occur in few locations. This may suggest a contact metasomatism event, which might have preceded micro-faulting and later quarzitic vein development (Peters 1969).

5.4.2 South East Malawi quartz syenites and Mangochi hill syenite (Figure 5.18 (B))

The south-eastern quartz syenites and syenite include the Nkhuzi Bay and Mauni intrusions (Figure 5.18 B (1 and 2 respectively). These are part of a chain of some NNE trending oval-shaped undulating hills located on the western side of Mangochi town. The Nkhuzi Bay area is characterized by coarse grained mesocratic weathered quartz syenite rocks. The weathered rocks are more altered and show a pale colour while the fresher specimens are more pinkish. King and Dawson (1976) reported that the quartz syenites in this area occur together with syenites but during this fieldwork only quartz syenites were observed. In hand specimens, the quartz syenites show more K feldspars (≥ 40%), plagioclase (≤ 25%), quartz (≥ 15%), muscovite, biotite (10%), minor occurrences of hornblende plus other unidentified minerals.

The Mangochi Hill syenite (Figure 5.18 B (4), which is located further north-east of the Junguni intrusion, shows similar mineralogy to the Zomba syenite although the Mangochi Hill syenite has more K-feldspar. The Mangochi Hill syenites are coarse to medium-grained and mesocratic. Hand specimens generally have K-feldspars (orthoclase ≥ 50%), plagioclase and micas.

5.4.3 South Malawi nepheline syenites and syenites (Figure 5.18 (C))

These nepheline syenites comprise the Junguni hill and a 36 km-long east-west-trending Chikala-(Ch), Chaone (Ca)–Mongolowe (Mo)–Chinduzi (Ci) structural chain located north-east of the Chilwa Alkaline Province (Figure 5.18 (C)). These intrusions are dated between 98 Ma-137 Ma (Eby et al., 1998; Swinden & Hall, 2012) and they mainly comprise a series of small syenite intrusions, quartz syenites and nepheline syenites. Nepheline abundance appears to increase to the west in this alkaline structural chain (Woolley, 2015). Samples were collected from the Junguni, Chaone and Mongolowe intrusions.

The Chinduzi and Chikala intrusions (area 2 and 5 respectively, in Figure 5.18 (C)) were not surveyed during the present fieldwork. The Chaone ring structure (4 in Figure 5.18 (C)), comprises coarse grained, leucocratic-mesocratic, nepheline syenite bounded by orthogneisses. The nepheline syenites are largely weathered, with lichen and moss growth evident on some of the outcrops. In some localities, the nepheline syenites have inclusions of diorite xenocrysts, which shows that the nepheline syenites are younger. The alkali granites/syenogranites probably occur within contact zones of the gneisses and nepheline syenites. This shows the possible interaction between the gneisses and nepheline syenites. The Mongolowe intrusion sits in the middle-western part of the Chinduzi-Mongolowe-Chaone-Chikala structural chain of igneous intrusions. The intrusion mainly comprises medium-coarse-grained, mesocratic weathered nepheline syenite rocks. Some outcrops are heavily weathered and show coarse-grained biotite and muscovite mica.

The Junguni nepheline syenite (6 in Figure 5.18 (C)) is a horseshoe-shaped 2.5 km diameter intrusion, situated about five km north of the Chikala-Mongolowe hills (Woolley, 2015). It comprises coarse-medium grained mesocratic nepheline syenites with K-feldspar, nepheline, biotite and pyroxene. The grain size increases uphill and field gamma-ray measurements for K_2O values also tend to be higher in the southward direction and toward the summit of the intrusion. The Zomba Mountain (area 1 in Figure 5.18 (C)) is predominantly a syenite intrusion, which also has other rocks including quartz syenites and charnockitic gneisses.

5.4.4 Carbonatite-associated nepheline syenites (Figure 5.18 (D))

Carbonatite-associated nepheline syenites from the Tundulu, Nkalonje and Songwe-Mauze complexes were also studied and sampled (Figure 5.18(D)). The nepheline syenites at Tundulu (1 in Figure 5.18(D)), are coarse to very coarse grained, mesocratic to slightly melanocratic, less altered and occur adjacent to carbonatites. In hand specimen these rocks are coarse-grained, mesocratic to melanocratic, and little weathered. The key porphyritic minerals in hand specimens include coarse-grained K-feldspars, mostly orthoclase (≥35%), nepheline (≥15%), plagioclase (≥20%), biotite (10%) and pyroxenes (5%). The nepheline syenites at Nkalonje Complex (2 in Figure 5.18 (D)).occur south west of this complex and are also coarse-grained, and less weathered but are slightly melanocratic compared to the ones at Tundulu complex.

The Songwe-Mauze complex (3 in Figure 5.18 (D)), contains fine-grained, mesocratic to light-reddish, highly weathered carbonatite rocks, which are localized on the Songwe-Mauze area. The nepheline syenites occur east of the Songwe-Mauze Hill and on Mauze Hill. The complex is also characterised by fenites, which occur mostly along the carbonatite and nepheline syenite contact zones. The fenites are fine-medium grained, mesocratic to light reddish weathered rocks consisting of calcite and quartz, with some mafic minerals banded with orthoclase and plagioclase. The fenites which occur close to the Mauze nepheline syenite intrusion are dark-coloured suggesting nepheline syenite metasomatism while those closer to or on the edges of Songwe-Mauze hill carbonatite are light-reddish coloured suggesting carbonatite metasomatism with the country rocks or carbonatite-nepheline syenite interaction (Swinden and Hall, 2012). These authors have also argued that mineralisation in this complex is associated with potassic fenitisation alteration and low temperature hydrothermal/carbohydrothermal secondary alteration. The occurrence of these carbonatites and nepheline syenites may suggest carbonatite-nepheline syenite magma liquid immiscibility (Robb, 2005). Field spectrometry found that in these three complexes fenites in the carbonatite complexes are more potassic than the nepheline syenites.

5.5 General description of the rock in hand-specimens

The nepheline syenite samples collected from the field show differences in colour, grain size, texture and mineral compositions. In hand specimen, nepheline crystals are not easily identifiable in most of the nepheline syenites. Weathering varied in intensity and samples were taken from outcrops for which visible weathering was limited to a thin (<1cm). Figure 5.19(A-D) shows typical photographs of the collected rock samples.

Figure 5.19: Examples of rock samples collected from the field: (A) nepheline syenite from Kasungu (KU-009), (B) nepheline syenite from Kasungu-Chipala (KUCP-008), (C) carbonatite from Tundulu (TUND-01A) and (D) foid syenite from Nkhuzi bay (NKHU-002).

Table 5.1 provides a summary of the rocks based on the observations in the field. In Table 5.1, for the purpose of grain size classification, the hand specimens were classified as fine-grained (<1mm), medium-grained (<3mm) and coarse-grained (>3mm) according to Gill (2010). The mineral proportions are classified and given in their order of abundance.

Table 5.1: Description of samples based on field observations

Location	**Sample Code**	**Minerals (in order of decreasing abundance)**	**Grain Size**	**Colour**	**Lithology Description**	**Rock Name**
South Malawi Nsy	CHA 002	Kfs, Pl, Bt, Ne (?)	Medium to coarse grained	Mesocratic/pinkish-pale light grey	Highly weathered rocks associated with coarse-grained syeno-granite and/diorite xenocrysts.	Nepheline syenite
South Malawi Nsy	JUN 001	Kfs, Bt, Ne (?), Px	Coarse-medium grained	Mesocratic-leucocratic	Slightly weathered to weathered rocks.	Nepheline syenite
South Malawi Nsy	JUN 002	Kfs, Bt, Ne, Px	Medium-coarse grained	Mesocratic	Less weathered to weathered rock	Nepheline syenite
South Malawi Nsy	JUN 004	Kfs, Bt, Ne, Px	Coarse grained	Mesocratic-pinkish toward hill summit	Slightly weathered rocks with increasing Kfspar uphill.	Nepheline syenite
Central Malawi Nsy	KU 002	Kfs, Pl, Ne, Ms	Medium-coarse grained	Melano-mesocratic	Weathered rocks with lichens growth.	Nepheline syenite
Central Malawi Nsy	KU 003	Qtz, Pl, Bt, hbl	Medium grained	Mesocratic	Weathered with inclusions of dolerite	Quartz syenite
Central Malawi Nsy	KU 006	Kfs, Pl, Ne, Bt, Ms	Coarse-v. coarse grained	Mesocratic	Weathered rock with pegmatitic veins	Nepheline syenite
Central Malawi Nsy	KU 011	Kfs, Pl, Ne, biot.	V. coarse-coarse grained	Mesocratic	Mixed with gneisses in some parts	Nepheline syenite
Central Malawi Nsy	KUCP 001	Qtz, Pl, Bt, Ms hbl, grnt	Medium to coarse grained	Mesocratic	Weathered with pegmatitic inclusions and quartz veins.	Diorite
Central Malawi Nsy	KUCP 005	Qtz, Pl, Bt, Ms hbl, grnt	Medium grained	Meso-melanocratic	Weathered with pegmatitic inclusions and quartz veins.	Quartz syenite
Central Malawi Nsy	KUCP 006	Kfs, Pl, Ne, px/ol (?)	Medium grained	Meso-melanocratic	Weathered rocks with developed soils	Nepheline syenite
Central Malawi Nsy	KUCP 007	Kfs, Pl, Ne, px/ol (?)	Medium grained	Meso-melanocratic	Weathered rocks with much developed soils.	Nepheline syenite
Central Malawi Nsy	KUCP 008	Kfs, Pl, Ne green minerals, ol (?)	Medium to coarse grained	Meso-melanocratic	Nsy bodies bounded by quartz-feldspathic gneisses with sharp contact between Nsy and gneisses.	Nepheline syenite
S.E Malawi Syenite	MANGO 002	Kfs, Pl, Ms Bt, hbl	Coarse grained	Mesocratic-pinkish	Weathered to highly weathered rocks, much K-Feldspar (pinkish colour)	Syenite
S.E Malawi quart-syenite	MAU 001	Kfs, Qtz, Bt, Px	Coarse-v. coarse grained	Mesocratic	Highly weathered to weathered rocks. Sporadic fine-medium grained granites in some places	Syenogranite/ Quartz syenite
South Malawi Nsy	MOG 001	Kfs, Pl, Bt, hbl, Ne	Coarse grained	Mesocratic-leucocratic	Weathered rocks with relatively well-developed soils	Nepheline syenite
S.E Malawi quart-syenite	NKHU 002	Kfs, Pl, Qtz, Ms Bt, hbl	Coarse grained	Mesocratic	Weathered rocks with altered showing pale colour and fresher specimens show pinkish colour	Quartz syenite
S.E Malawi quart-syenite	NKHU 003	Kfs, Pl, Qtz, Ms Bt, hbl	Coarse grained	Mesocratic	Weathered rocks with abundant K-Feldspar	Quartz syenite
Carbonatite-associated Nsy	SONG 002	Kfs, Pl, Bt, Ms Ne	Coarse-v. coarse grained	Mesocratic-lightly-red coloured	Fine grained, slightly red coloured fenites along contact of Mauze and Songwe-Mauze	Nepheline syenite
Carbonatite-associated Nsy	TUND 001A	Kfs, Pl, Bt, Ms Ne	medium-coarse grained	Mesocratic-slightly melanocratic	Relatively fresh rocks, occur mostly on S to SW edge of Tundulu	Nepheline syenite
South Malawi Nsy	ZA 002	Kfs, Pl, Bt, Ms Ne	Coarse-medium grained	Mesocratic	Weathered rocks	Syenite
South Malawi Nsy	ZA 003	Kfs, Pl, Bt, Ms Ne	Coarse-medium grained	Meso-melanocratic	Less weathered	Syenite

5.6 Vegetation cover in the surveyed areas

Gowela and Masamba (2000) report that Malawi's two major vegetation types are the miombo woodlands comprising *Branchystegia*, *Jubernardia* and *Isoberlinia species,* on one hand and the *Acacia-Piliostigma-Combretum* wooded savanna on the other hand. Montane grassland vegetation is also dominant in high altitude plateaus, while the Savanna bush-grassland with thickets dominate the lakeshore plains and the river valleys. Between 1990-2002, vegetation in Malawi was affected by serious deforestation rates estimated at 2.6% p.a (about 33,000/ha^{-1}), which has further increased in recent years (Makungwa et al., 2013). Figure 5.20 shows examples of the dominant vegetation in some of the surveyed during the fieldwork in Malawi.

The Kasungu nepheline syenite area is characterized by natural vegetation with a mixture of tall (20-25m) and medium height natural deciduous Savanna tropical trees, mostly of the *Brastegia spp.* (Figure 5.20A), shrubs, and tall (±1.5m) dry Savanna grassland. On the other hand, in the Kasungu-Chipala area vegetation is mainly very short scattered shrubs, where a few trees of *Sterculia qttinqueloba* type grow in rock cracks with short dry grass. Tall grasses and abundant herbaceous plants are common, especially in areas where nepheline syenites occur. This could suggest that soils weathered from nepheline syenites are more fertile than those weathered from the gneisses.

The Central Malawi alkali granite of Dzalanyama area mainly has a tall (15-30m), 50-80% cover of mature, natural deciduous green trees with thick cover of natural short dry Savanna grasses (Figure 5.20B). According to Missanjo and Kamanga-Thole (2015) the dominant biotic communities are *Brachystegia spp.* (Miombo woodlands), but other species like *Uapaca spp.* (Msuku) and some *Eugenia cordata* (Nyowe) trees also grow in the area. The Dzalanyama forest area is divided into four sections comprising 818 km^2 of *Brachystegias* spp., 32km^2 of *Pinus* species and *Eucalyptus* plantation, 38 km^2 of the *Eucalyptus globulus* trees, and 96 km^2 of wetland (Missanjo and Kamanga-Thole, 2015). Field observations confirmed earlier studies that there is considerable distinction in terms of the height and size of trees on the soils distal and those proximal to the Dzalanyama ridge (Missanjo and Kamanga-Thole, 2015) with much denser vegetation towards the ridge.

In the South east Malawi's quartz syenite areas and other lakeshore plains, the key vegetation species, are the *Acacia spp., Sterculia spp., Cordyla africana* the *Adansonia digitata* (baobab) as well as *Hyphaene ventricosa* and some Savanna bush-grassland according to Gowela and Masamba (2002). For example, vegetation in the Chantulo and Mauni areas comprises small and short to medium height scattered trees and tall and short dry grasses. The Nkhuzi Bay largely comprises scattered tall (10-20m) deciduous natural tall trees including the *Sterculia. Quinqueloba* species (Figure 5.20C), and short grasses. Furthermore, the Mangochi Hill Forest area is characterised by 40-60% cover of mixed, natural vegetation comprising tall (20-35m) large trees. The dominant vegetation types are the *Uapaca kirkiana* trees (Figure 5.20D) which are associated with thick Savanna grasses.

In the South Malawi nepheline syenites areas different types of vegetation were observed. In the Chaone area, vegetation is similar to the central Malawi alkali granites and consists of tall green *Brastegia* trees (Figure 5.20E) and *Uapaca* types and some shrubs (Kamangadazi et al., 2016). The Mongolowe hills have mixed species of mature natural deciduous trees mainly of the *Brachystegia miombo* woodlands and *Uapaca spp.* trees with short Savanna grassland. Furthermore, in the Junguni area, which also falls within a protected wildlife national park, dominant trees are the Mopane woodland type (Figure 5.20F), with mixtures of various shrubs and pockets of python vines and sporadic presence of small *Adansonia digitata* (baobab trees). Kamangadazi et al. (2016) add that the area has seventeen tree species which also include the *Annona senegalensis, Bauhinia petersiana madagascariensis*, *Brachystegia bussei, Burkea africana, Catunaregam spinosa.* Other species include the deciduous Mopane woodland vegetation, some *Candelabra Euphorbia*, short dry grasses and various shrubs.

In the Zomba Massif, (area 1 in Figure 5.20(D)), vegetation includes the *Protea* scrub and the exotic evergreen conifer *Pinus* trees, *Eucalyptus globulus*, some mixed natural trees and short healthy green grasses (Bloomfield, 1965) as shown in Figure 5.20G. The streams in the area are covered by evergreen trees such as *Khaya nyasica* and *Adina microcephala* whilst the *Brachystegia* woodland grows on the escarpments.

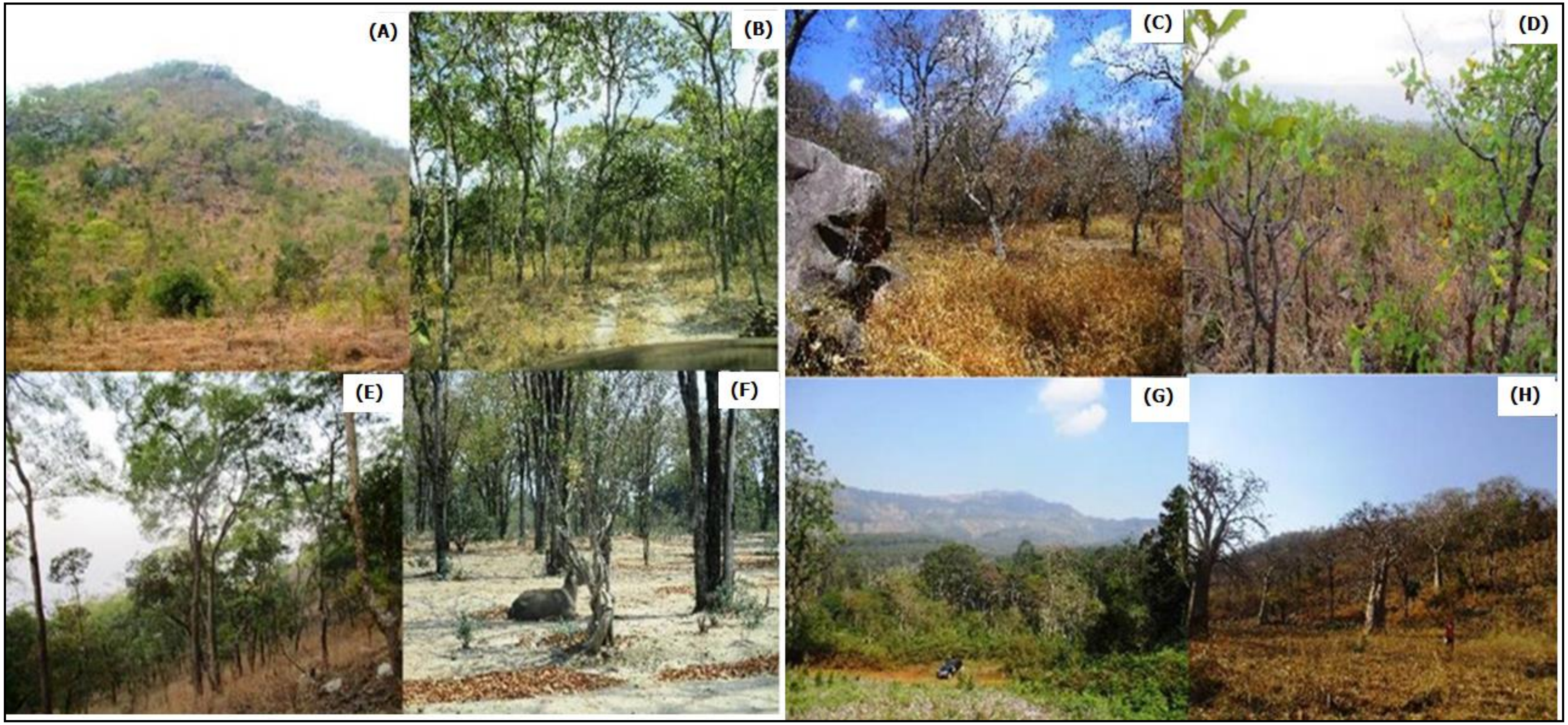

Figure 5.20: Vegetation for selected areas namely: (A) the Sterculia qttinqueloba of Kasungu; (B) the Brachystegia spp. (Miombo woodlands) of Dzalanyama, (C) the deciduous natural tall trees of Nkhuzi Bay (D) the Uapaca kirkiana trees from Mangochi hill forest (E) the Brachystegia spp. (Miombo woodlands) of Chaone (F) the Mopane woodland of Junguni; (G) mixed natural vegetation of Zomba mountain (H) mainly the Adansonia digitata of Nkalonje carbonatite complex.

As shown in Figure 5.20(H), in the carbonatite associated nepheline syenite areas of Figure 5.18(D), vegetation consists of about 50-70% vegetation cover composed of short to relatively tall mature trees, abundant shrubs which blend with some grasses. *Sterculia qttinqueloba* is notable on the three hills which form the Tundulu complex while *Adansonia digitata* (Figure 5.20H) is common on the plain of both Nkalonje and Tundulu complexes. For the Songwe-Mauze complex, areas with nepheline syenite on Mauze hill show a relatively thicker canopy of *miombo* woodland forest (40-50% cover). The dominant community comprises medium-height *Colophospermum* mopane woodland mixed shrubs and short grasses. On the carbonatite-rich Songwe-Mauze hill, small short trees, scattered shrubs and dry short grasses are the main vegetation.

As shown in the preceding section, different areas are associated with different vegetation. Figure 5.21 shows that there is no vegetation type/biotic community which appears to be preferentially associated with nepheline syenites. The K_2O (wt %) data as measured using the gamma ray field spectrometer for the surveyed areas also suggest that the abundance of potassium within the sampled rocks is not preferentially related to the major biotic communities.

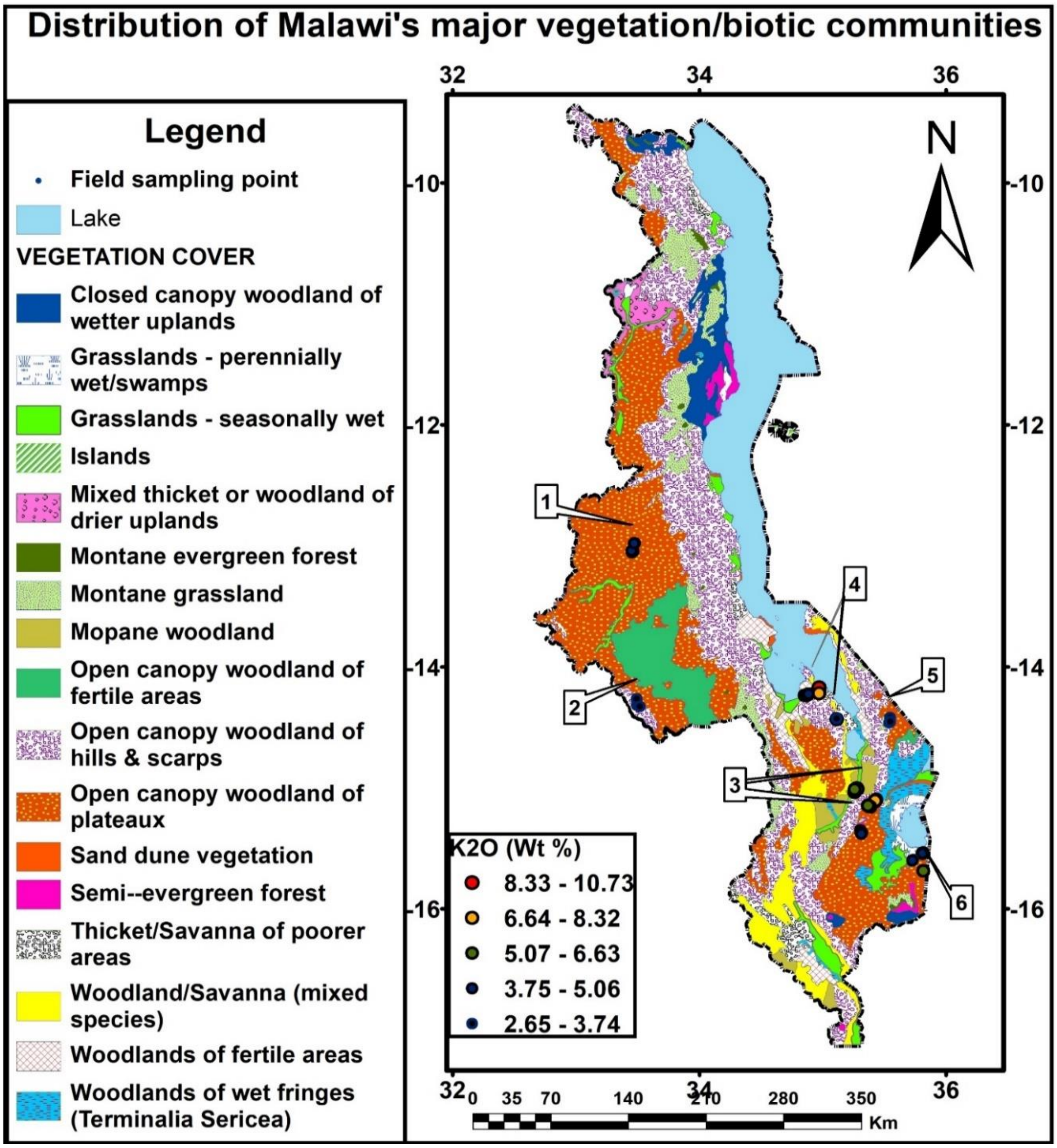

Figure 5.21: Distribution of main vegetation canopy for Malawi with gamma-ray field spectrometry K_2O values for areas sampled during this study's fieldwork namely: (1) central Malawi nepheline syenites(2) central Malawi alkali granites (3) South Malawi nepheline syenites (4) S.E Malawi quartz syenites (5) Mangochi Hill syenite (6) carbonatite-associated nepheline syenites. Shapefiles for vegetation were accessed from Malawi Department of Survey's database (2008).

5.7 Ground versus Airborne Geophysical Gamma-ray data

Gamma-ray field spectrometry was done for 166 points (Appendix 5.2). Table 5.2 shows descriptive statistics of the data while Appendix 5.1 shows the samples which were selected for further geochemical and petrological studies as described in chapter 6.

Table 5.2: Descriptive statistics for data from the field and airborne geophysical surveys.

Parameter	**U Airborne (ppm)**	**U Ground (ppm)**	**Th Airborne (ppm)**	**Th Ground (ppm)**	**Th/U Airborne (ppm)**	**Th/U Ground (ppm)**	**K_2O Airborne (Wt %)**	**K_2O Ground (Wt %)**	**Vegetation (%)**
Mean	4.42	2.83	17.72	19.31	4.58	10.37	3.66	4.69	35.81
Std. dev	2.21	2.66	7.73	9.80	1.80	11.17	1.17	1.56	21.54
Variance	4.90	7.05	59.82	96.10	3.24	124.87	1.37	2.45	464.03
Minimum	1.07	0	5.59	2.10	2.84	0	0.92	2.65	5.00
Maximum	8.27	18.50	40.54	57.30	9.16	49.60	5.90	10.73	90.00
Count	**99**	**166**	**99**	**166**	**99**	**165**	**134**	**166**	**166**

The field gamma-ray spectrometry has also shown that the nepheline syenites and alkaline rocks vary considerably in their K content. The results also show that there is a weak correlation between data from airborne and ground geophysical surveys (Table 5.3).

Table 5.3: Correlation results for pairs of different elements measured using gamma-ray field spectrometer.

Sample	K_2O (ground)	Th (Airborne)	U (ground)	U (Airborne)
K_2O (Wt % (Airborne))	0.05845	0.04741	0.82929	0.0073
K_2O (Wt % (ground))	--	0.01156	0.70567	0.00244
Th (ppm (Airborne))	0.01156	--	0.01024	1.78E-07
Th (ppm (ground))	0.01637	0.02967	0.18463	0.01677
U (ppm (ground))	0.70567	0.01024	--	0.02955
U (ppm (Airborne))	0.00244	1.78E-07	0.02955	--

Airborne and ground geophysical data acquisition methods were also compared to check which one is more ideal for detecting the concentration of the radionuclides (K, Th and U) within the rocks. Figure 5.22 shows airborne vs ground gamma-ray spectrometry as of the K, U and Th content in the areas surveyed during this study's fieldwork. The K channel shows that field spectrometry shows higher values unlike airborne geophysical spectrometry. However, there are no notable differences for Th while slightly higher values were noted using airborne spectrometry compared to field gamma-ray spectrometry. This suggests that ground geophysical surveys could be more suited than airborne geophysical surveys for mapping K-bearing rocks. This suggests the gamma ray detector works better when more proximal to the rock surfaces than at long distances, consistent with attenuation of signal with distance. However, further analyses are needed using a larger sample size than the one used in this study to confirm this assumption.

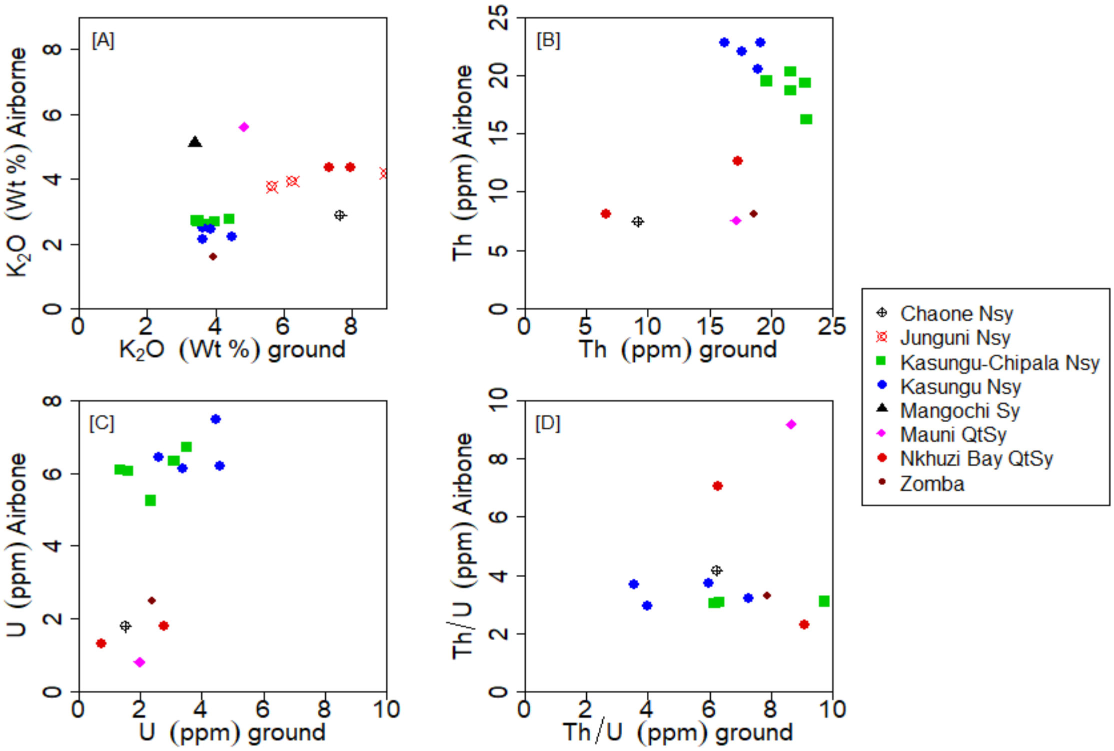

Figure 5.22: Comparisons airborne vs ground gamma-ray spectrometry as techniques for geophysical data acquisition showing airborne vs ground gamma-ray data for (a) potassium. (b) thorium. (c) uranium (d) thorium /uranium.

5.8 Soil as an indicator for potassium-rich parent material

Data from the Sorter soil database (Leenaars, 2013) shows that most of the areas surveyed fall within the luvisol and leptol soil types. The fieldwork also confirmed that soils are mostly products of the parent material from which the soils are weathered. For example, soils weathered from gneisses are different from those weathered from syenites and nepheline syenites in terms of the colour, visible mineral particles and the plant growth in these soils.

5.9 Airborne geophysical survey compared with field gamma-ray spectrometry

It has also been shown that combined use of remote sensing, particularly the DTMs/DEMs and airborne geophysics, has potential to delineate nepheline syenites and other alkaline rocks. For example, the Chinduzi-Mongolowe-Chaone and Chikala chain of intrusions, the Dzalanyama range, and Nkhuzi bay and Mauni alkali granites and the Junguni nepheline syenite intrusion, were easily delineated using both the digital terrain model and gamma-ray spectrometry. The DEM/DTMs have also helped in mapping ring structures and alkaline clusters (as shown in Figures 5.12- 5.17), which are key diagnostic features of most of high K nepheline syenites and related alkaline rocks. The areas within the rift system, whether nepheline syenites, granites or carbonatites, have higher K content compared to those within the Malawi Basement Complex (central Malawi nepheline syenites and alkali granites).

Furthermore, airborne geophysical surveys are very important in delineating potassium-rich intrusions including nepheline syenites. Airborne geophysical radiometric surveys can capture signal interactions for radionuclide elements for a depth of at least <60 cm of the soil profile (Beamish, 2013). Results in this chapter have also shown that there is no apparent association between the K content and soil type. It is also shown that soils weathered from gneisses differ substantially from those weathered from syenites and nepheline syenites. However, it is not clear whether differences are completely due to the parent material from which the rocks are weathered. The effect of soil erosion and leaching of K is not fully clear at this stage because this was not assessed in this study. There is need for a detailed soil survey to establish the nutrient status, physical and chemical variations in the soils from different rock units.

5.10 Conclusion

This chapter has shown that airborne gamma-ray geophysics and digital terrain models are useful in mapping nepheline syenites and other alkaline rocks. More importantly, field gamma-ray spectrometry has been very helpful in filling gaps from the airborne geophysical survey. Fieldwork results also suggest that some of Malawi’s nepheline syenites have high potential as alternative sources of potassium fertilizer. Vegetation cover and soil data have not yet shown much potential as indicators of nepheline syenites or alkaline intrusions. There is however, need for a detailed soil survey to establish the variations in the soils from different rock units.

Chapter 6: Petrology and geochemistry of nepheline syenites and related rocks of Malawi

6. Introduction

Chapter 5 has shown how airborne geophysical gamma-ray data and digital elevation models can be used to map nepheline syenites and other related K-rich alkaline intrusions. This chapter addresses Objective 5 of this study which sought *to conduct petrological and geochemical laboratory sample analyses for determination of K release from nepheline syenite rocks.* X-ray fluorescence (XRF) analysis and Scanning Electron Microscopy (SEM) coupled with the Energy Dispersive spectrometry and petrographic studies on thin section were done to achieve this objective. Therefore, the aim of this chapter was to conduct petrological and geochemical laboratory sample analyses and provide a discussion of the geochemistry and petrology of the rock samples acquired from the fieldwork in Malawi.

6.1 Methods and materials

The study used rock samples collected from the field work in Malawi as described in chapter 5. Twenty-two fresh rock samples were selected from different areas that were surveyed. These samples were processed for their geochemical and petrological analysis.

6.1.1 X-ray Ray Fluorescence (XRF) Analysis

The rock samples were finely ground using a tungsten carbide grinding mill and an agate mill. Major element concentrations were measured on 40mm-diameter fused glass discs; about 0.9g of sample powder was mixed with a borate flux using a 5:1 (flux: sample) dilution. Thereafter, the samples were fused and heated in Pt-5% Au crucibles at 1100°C. The trace element concentrations were measured on pressed pellets with ~8g of powder used to make 40mm diameter pellets. Major and trace elements were analysed by X-Ray fluorescence (XRF) using the Panalytical PW2404 instrument hosted at the University of Edinburgh's School of Geosciences.

6.1.2 Petrography

A detailed petrographic study of the samples was carried out on polished thin sections prepared by the Sample Preparation Facility of the School of Geosciences, University of Edinburgh. Samples were studied using conventional petrography and using Back-Scattered Electron (BSE) images generated by the Zeiss SIGMA HD VP Field Emission scanning electron microscope (SEM) hosted at the University of Edinburgh. Semi-quantitative chemical analyses were performed on the mineral phases using the Oxford AZtec Energy Dispersive Spectrometer (EDS) fitted to the system, which was calibrated on a cobalt standard.

6.1.3 *Weathering intensity of the rocks*

The Parker chemical alteration index (CIA) and the plagioclase alteration index (PIA) (Meunier et al., 2013; Mohanty et al., 2016; Nordt and Driese, 2010) were used to determine the alteration states of the rocks and whether K_2O and nepheline abundance could be related to this. The CIA degree of alteration ranges from 0-100. The optimum index value for fresh/ less altered rock is <50 whereas 100 is the maximum index value for ‘complete’ alteration (Price and Velbel, 2003). The PIA focusses more on plagioclase alteration. Using molecular proportions of elemental oxides the two indices are calculated (Price and Velbel, 2003) as follows:-

$$CIA = \left((100) * \left(\frac{Al_2O_3}{Al_2O_3O+K_2\mathrm{O}}\right)\right) \tag{6.1}$$

$$PIA = \left(100 * \left[\frac{(Al_2O_3-K_2\mathrm{O})}{Al_2O_3+\mathrm{CaO}+Na_2O-K_2\mathrm{O}}\right]\right) \tag{6.2}$$

6.1.4 *Analysis of results*

The values extracted from the airborne geophysical gamma-ray channels for K, U and Th and the field gamma-ray measurements were analysed mainly using descriptive statistics. Different geochemical classification diagrams were also used to assess the relationships among the areas surveyed and those from other parts of the world using geochemical and petrographic analytical results of samples from this study and some from existing literature.

6.2 Presentation of results

6.2.1 *Whole-rock geochemistry: Major elements*

The results show that Malawi’s nepheline syenites and syenites are heterogeneous, with some differences among the areas sampled. The whole rock geochemistry shows that the rocks are generally silica undersaturated, and their SiO_2 content ranges from 44.6 wt. % to 69.57 wt. %, with an average of 57.69 wt. %. They also have low CaO content (0.56 wt. % to 6.86 wt. %, average 2.79 wt. %), MgO (0.07 wt. % to 2.78 wt. %, average 1.23 wt. %), TiO_2 (0.25 wt. % to 2.05 wt. % average 1.18 wt. %), very low MnO (0.16 to 0.27 wt. %, average 0.17 wt. %)

and P_2O_5 (0.03wt. % to 0.80 wt. %, average 0.40). Based on the CIPW norms (Johannsen, 1939), normative nepheline appears in 16 of the 22 samples and ranges from 4.6 wt% to 40.26 wt% with an average of 16.11 wt%. Therefore, of the 22 samples, 16 of them were confirmed as nepheline syenites based on presence of normative nepheline and using geochemical classification plots such as the total silica alkali (TAS) plot (Figure 6.1). Normative leucite varies from 0 wt % to 45.90 wt% and has an average 29.92 wt%. In these rocks, normative orthoclase ranges from 0 to 45.95 wt% with an average of 23.85 wt%.

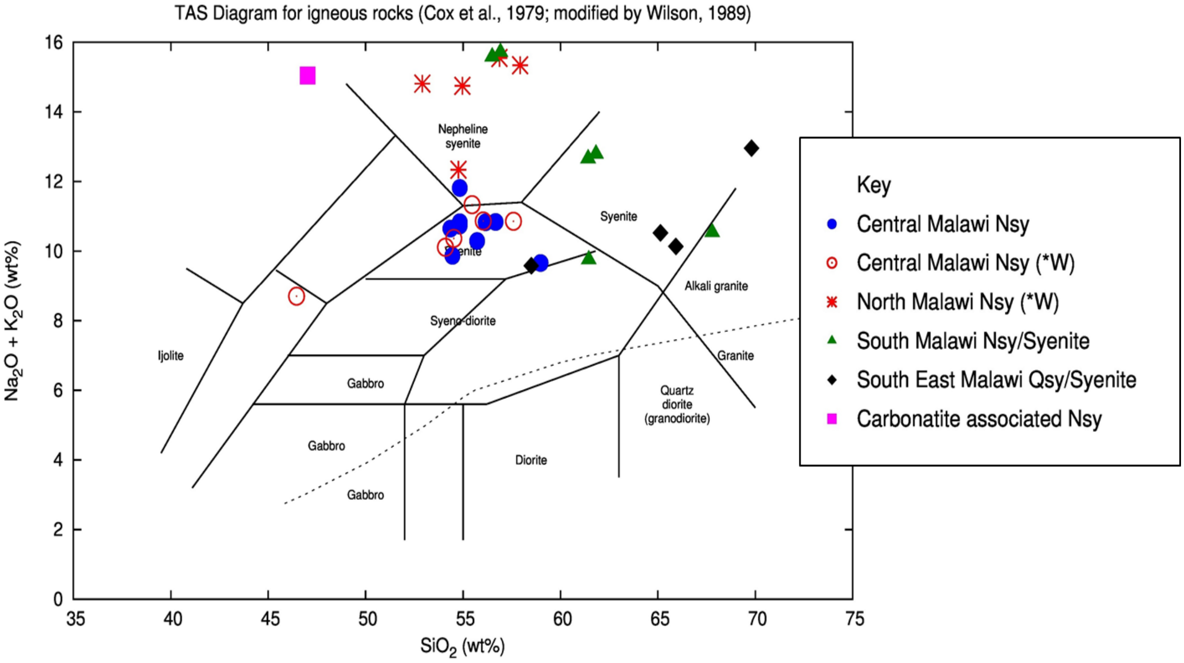

Figure 6.1: TAS diagram for the nepheline syenites and other alkaline rocks from Malawi (after Cox (1979) and modified by Wilson (1989).

Figure 6.2 shows SiO_2 vs major element variation diagrams, which demonstrate that geochemical similarities exist between/among some of the intrusive bodies. The central Malawi nepheline syenites are the least potassic of all the clusters but show high TiO_2 and FeO contents. The K_2O/Na_2O ratio for the nepheline syenites varies from 0.41 to 1.28 wt. % with an average of 0.65 wt. %, which shows that the nepheline syenites are more sodic than potassic; however, they have variable K and Na content. The K_2O content for nepheline syenites only ranges from 3.17 wt. % to 11.32 wt. % with an average of 5.22 wt. %. The K_2O content for all the other rock types varies from 3.17 wt. % to 9.14 wt. % with an average of 5.22 wt. %. The alkali ($Na_2O + K_2O$) contents for these nepheline syenites range from 9.62 wt.% to 17.77 wt% and an average of 13.26 wt.%, while the average total alkali content for all the rock units is 11.92 wt.%.

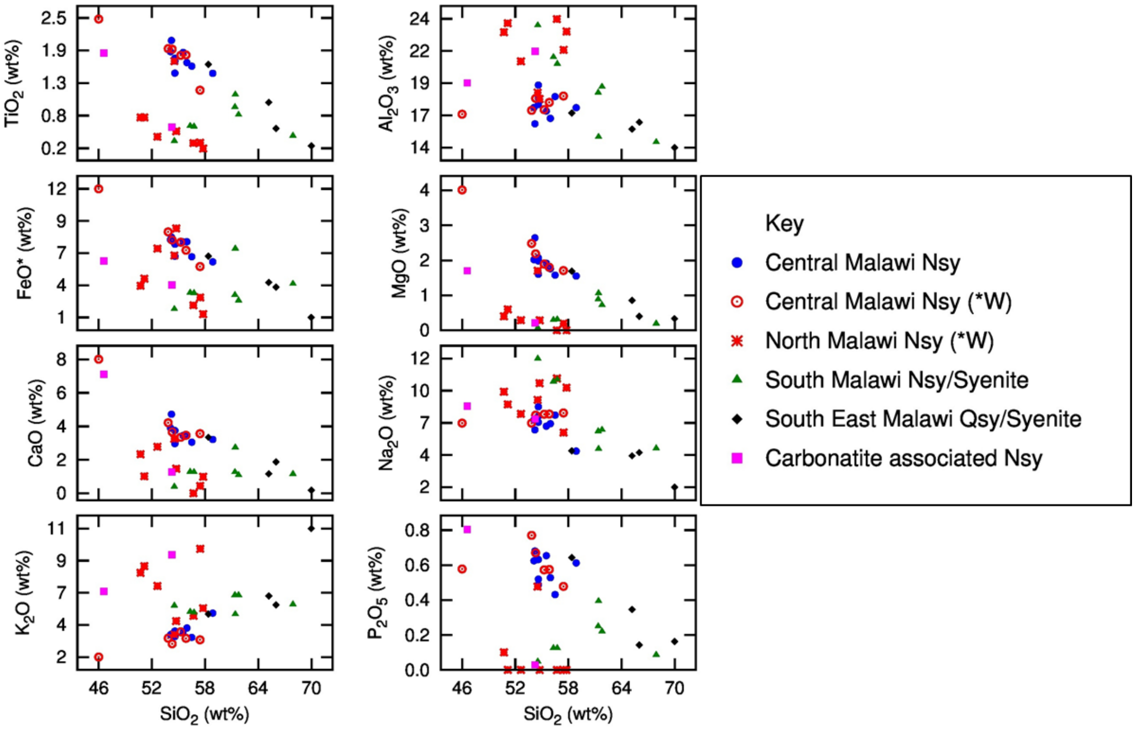

*Figure 6.2: Harker diagrams for major elements. *W denotes data from Eby et al. (1998).*

The R_1-R_2 chemical variation diagram (De la Roche et al., 1980) was also used to study the geochemical relationships among different and geographically dispersed intrusions of Malawi and other parts of the world. In comparison with other parts of the world, the geochemical data shows that Malawi's nepheline syenites portray similar characteristics to nepheline syenites used as potash sources in other parts of the world. The De la Roche et al. (1980) R_1-R_2 scheme is based on an *x*-*y* bivariate graph of Ratio 1 (R1) vs Ratio 2 (R2) for cation proportions expressed as millications of key components in the igneous rocks as follows:

$$R_1 = [4Si - 11(Na + K) - 2(Fe + Ti)] \qquad (6.3)$$

$$R_2 = (Al + 2Mg + 6Ca) \qquad (6.4)$$

The R_1- R_2 classification scheme for intrusive rocks has confirmed that most of the rocks which were sampled are nepheline syenites (Figure 6.3). Based on the geochemical data, it shows that the methods used for delineating these rocks have been effective.

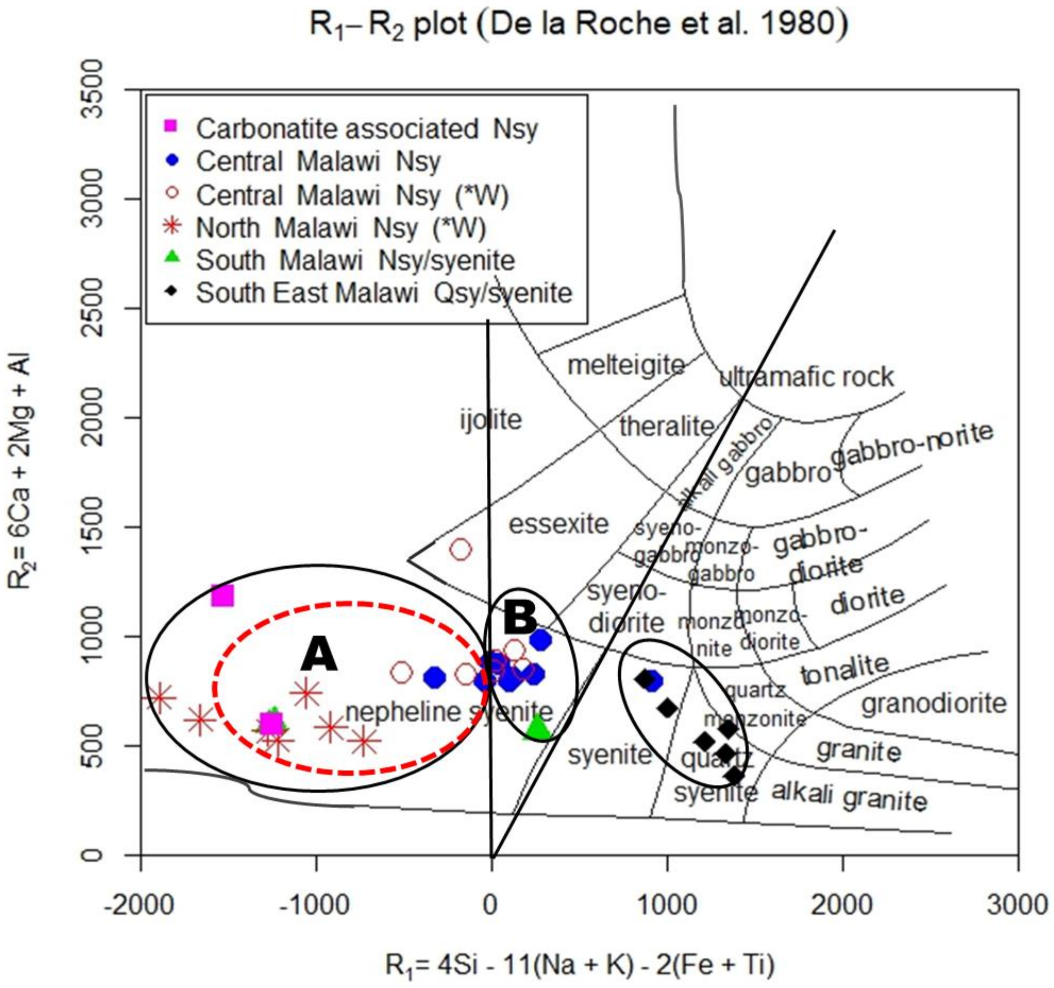

*Figure 6.3: Classification of alkaline rocks from Malawi after De la Roche et al., (1980). *W stands for data from Eby et al., (1998). Red dashed circle shows positions for alkaline rocks from other parts of the world after De la Roche et al. (1980).*

Based on the R_1-R_2 scheme, two major groups of the nepheline syenites can be identified, which this work has classified as Group A and Group B (Figure 6.3). Group A nepheline syenites are of greater potential as potash sources because of their abundance of K unlike the Group B nepheline syenites. Group A includes the Tundulu, Songwe-Mauze, Junguni and Mongolowe intrusions, which also have higher normative nepheline and K contents. These rock units are heterogeneous and may be further divided into three subgroups: (i) the central Malawi nepheline syenites in the Malawi basement complex, (ii) south Malawi and north Malawi rifting-associated nepheline syenites and (iii) carbonatite-associated nepheline syenites, which can be classified in both groups with either (i) or (ii). Group B is slightly silica saturated (Figure 6.3) and comprises mostly the Central Malawi nepheline syenites. Among the nepheline syenites, rock samples from the Songwe-Mauze Complex (eg. SONG 02 in Table 6.1) show the highest amount of K_2O with up to 9.14 wt. % (K_2O), which agrees with Croll et al. (2014) who also reported up to 14.99 wt. % (K_2O) in the area.

Table 6.1: Major and trace elements analyses by XRF method for representative alkaline rocks from Malawi.

Sample / Element	**KUCP 01**	**KUCP 05**	**KUCP 06**	**KUCP 07**	**KUCP 08**	**KU02**	**KU03**	**KU06**	**CHA-02**	**KU-11**	**MANG 02**	**MAU-01**	**MOG 03**	**NKHU 02**	**NKHU 03**	**SONG-02**	**TUND 01A**	**JUN-01**	**JUN-02**	**JUN-04**	**ZA-02**	**ZA-04**
SiO_2	55.20	53.81	54.50	55.75	58.76	54.30	53.69	54.11	61.36	56.33	58.04	65.58	56.12	64.51	69.57	53.07	44.60	54.19	56.57	60.94	67.27	60.83
Al_2O_3	17.08	17.34	19.10	16.57	17.44	17.58	17.85	16.16	18.95	18.23	16.95	16.31	21.21	15.72	14.40	21.25	18.39	23.53	20.72	18.49	14.75	15.12
Fe_2O_3	8.17	8.37	6.92	8.21	6.43	8.05	7.87	8.62	2.94	6.86	6.90	4.14	3.64	4.55	1.43	4.24	6.20	2.16	3.61	3.42	4.43	7.57
MgO	2.01	2.12	1.69	1.85	1.64	2.08	2.15	2.78	0.76	1.66	1.78	0.42	0.31	0.90	0.35	0.22	1.71	0.07	0.33	0.93	0.20	1.11
CaO	3.68	4.10	3.26	3.70	3.47	3.96	3.18	4.90	1.43	3.31	3.58	2.18	1.62	1.50	0.56	1.59	6.86	0.76	1.60	1.59	1.49	2.99
Na_2O	6.65	7.18	8.30	6.88	4.62	6.99	7.41	6.38	6.37	7.60	4.61	4.48	10.40	4.19	1.59	7.14	7.98	12.26	10.58	6.24	4.82	4.76
K_2O	3.542	3.364	3.437	3.869	5.001	3.642	3.190	3.418	6.318	3.169	4.893	5.605	5.067	6.235	11.32	9.136	6.285	5.508	5.033	6.314	5.628	4.885
TiO_2	1.845	1.854	1.494	1.673	1.486	1.688	1.720	2.053	0.783	1.611	1.636	0.549	0.585	0.987	0.252	0.562	1.750	0.330	0.577	0.907	0.424	1.117
MnO	0.208	0.228	0.184	0.226	0.131	0.209	0.198	0.240	0.110	0.173	0.138	0.068	0.243	0.089	0.016	0.160	0.268	0.079	0.243	0.127	0.138	0.187
P_2O_5	0.682	0.652	0.509	0.553	0.638	0.544	0.648	0.705	0.230	0.453	0.675	0.147	0.131	0.359	0.172	0.026	0.802	0.047	0.131	0.257	0.087	0.412
LOI	0.57	0.77	0.25	0.29	0.40	0.43	1.83	0.18	0.54	0.49	0.29	0.29	0.58	0.78	0.15	2.32	4.95	1.01	0.80	0.35	0.53	0.58
Total	**99.63**	**99.78**	**99.64**	**99.56**	**100.0**	**99.47**	**99.74**	**99.55**	**99.8**	**99.89**	**99.49**	**99.77**	**99.91**	**99.81**	**99.80**	**99.72**	**99.80**	**99.94**	**100.2**	**99.57**	**99.77**	**99.58**
Trace Elements (ppm)																						
Zn	96	105.4	86.2	103.6	143.5	102.2	112.8	85.9	46.4	96	149.9	79.5	91	111.1	18.2	64.8	125.7	17.5	164.6	56.1	142.7	112.1
Cu	5.6	3.9	4.6	6.4	5.4	7.9	3.4	10.5	2.4	6.3	4.7	3.5	2.1	4.3	4.3	3.8	6.9	2	2.6	3.2	3.9	6.2
Ni	1	2.3	0.1	1.7	2.4	1.2	2.2	1.2	-1.4	0.4	2.7	-0.7	-2.6	0.4	1.1	0.4	3.1	-3.4	-0.4	-0.4	0.7	1.4
Cr	2.4	3.4	2.5	5.2	2.9	2.6	2.9	1.1	4.6	2.2	3.2	3.7	3.1	5.1	13.9	2.4	0.8	4.6	5.8	6	8.7	4.3
V	55.7	59.9	45.6	50.5	51	59.9	68	71.4	4.1	50.6	50.4	4	0.2	6.9	16.7	62.5	129.9	6.9	13.4	5.7	1.6	30
Ba	624.1	607.5	614.8	578.8	3146	528.1	670.8	602.8	894.5	630.1	3049	2206	99.6	2802	679.8	4917	2407	68.5	602.1	901.2	343	837.9
Sc	6.4	5.2	4.1	5.2	14	4.4	5.3	6.1	4.8	4.5	14	6.1	0.5	11.6	2	-1.3	3	-0.1	0.7	4.9	2.7	10
La	55.3	70.4	76.6	85.6	143.7	76.6	98.7	95	33.6	78.1	150.5	30.4	45.7	99.6	48.1	107.1	130.5	16.7	78.3	38.3	131	91.1
Ce	112.1	130.5	157.1	174.1	275.4	148.6	150.7	185.7	58.9	154.2	290.6	70.7	88.7	243.4	74.7	120.6	240	36.9	137.5	66.2	256.8	182.3
Nd	42.7	48	60.2	66	124.9	53.8	85.6	71.3	19.8	56.1	134.4	37.1	28.9	95.1	23.6	19	86.4	11.1	39.3	25.4	116.3	81.1
U	5.9	3.4	6.3	1.4	0.4	8.5	14.8	1.5	0.5	5.3	0.5	1.7	1.3	2	2.9	0.8	1.8	1.6	10.3	0.4	3.7	1.8
Th	19.3	11.5	20.8	11	4.1	29.1	19.6	8.9	3.2	18.8	4.3	4.6	5.2	11.1	42.1	9.9	7.6	4.6	34.3	3.3	17.4	8.5
Pb	11.8	11.3	12	6.9	29.2	14.7	10.5	7.8	5.3	10.8	28.9	22.7	14.3	28.7	17.7	7.5	5.2	7.6	27.7	5.2	14.4	11.4
Nb	247.6	222.2	191.5	190.7	43.7	240	219	257.1	34.9	213.4	45.8	32.5	122	68.2	11.2	54.2	250.9	52.2	225.9	40.7	91.2	70
Zr	973.3	528.7	715.1	613.2	741.9	1068	937.3	562.5	125.6	650.7	784	480.5	218.1	739.7	256.3	166.6	532.9	164.3	982.4	127.6	771	667.1
Y	52.9	52.5	49.4	48	66.1	49.3	60.7	58.7	13.8	51.2	71	32.5	24.3	54	12.4	15.4	36.5	8.9	43	16.5	91.8	53.4
Sr	408.5	454.8	397.5	353.7	820.1	555.5	560.4	560.5	283	520.3	819.6	492.7	32.9	297.2	75.8	2501	2047	109	605.2	279.7	51.7	189.9
Rb	129	116.1	148.5	126.2	81.6	144	146.6	81	57.9	120.1	80.8	134.9	112.8	149.1	292.8	172.9	202.3	107.7	182.7	59.3	126.6	77.7

Table 6.2: CIPW normative minerals for Malawi alkaline rocks (the shaded rows show key minerals of interest for fertiliser in this study).

Mineral (Wt %)	**KUCP-01**	**KUCP-05**	**KUCP-06**	**KU5P-07**	**KUCP-08**	**KU02**	**KU03**	**KU06**	**CHA-02**	**KU-11**	**MANGO-02**	**MAU-01**	**MOG-03**	**NKHU-02**	**NKHU-03**	**SONG-02**	**TUND-01A**	**JUNG-01**	**JUNG-02**	**JUNG-04**	**ZA-02**	**ZA-04**
Quartz	0	0	0	0	0.2	0	0	0	0	0	0	10.3	0	9.03	16.2	0	0	0	0	0	12.5	4.17
Albite	42.68	37.32	37.34	40.51	39.09	36.82	40.61	37.17	45.41	45.9	38.38	37.91	27.48	35.45	10.59	0	0	16	27.25	44.25	40.78	40.28
Anorthite	6.07	4.93	4.49	2.69	10.94	5.64	5.78	5.14	4.13	6.04	10	7.04	0	4.65	0	0	0	0	0	3.47	1.86	5.16
Orthoclase	21.39	20.32	20.76	23.28	31.84	21.91	19.34	20.64	37.99	19.19	31.13	34.73	30.02	38.88	67.37	45.9	0	32.6	30.18	37.97	33.51	29.48
Nepheline	7.36	12.7	17.82	9.59	0	12.09	11.97	9.11	4.6	9.97	0.34	0	28.9	0	0	29.8	31.4	40.3	27.6	4.63	0	0
Leucite	0	0	0	0	0	0	0	0	0	0	0	0	0	0	0	9.11	30.5	0	0	0	0	0
Diopside	6.47	9.3	6.98	10.01	1.92	8.74	4.88	12.2	1.27	6.23	2.94	2.43	5.93	0.43	1.38	6.92	22.2	2.88	5.97	2.32	4.1	5.8
Hypersthene	0	0	0	0	9.61	0	0	0	0	0	9.89	4.42	0	6.62	1.8	0	0	0	0	0	3.66	8.31
Olivine	7.41	6.84	5.81	6.09	0	6.81	8.09	7.2	3.03	5.83	0	0	1.62	0	0	1.59	0	0.9	1.62	3.32	0	0
Larnite	0	0	0	0	0	0	0	0	0	0	0	0	0	0	0	0	0.5	0	0	0	0	0
Acmite	0	0	0	0	0	0	0	0	0	0	0	0	0.73	0	0.29	0.85	1.25	0.44	0.73	0	0	0
Na_2SiO_3	0	0	0	0	0	0	0	0	0	0	0	0	1.48	0	0.59	1.02	1.9	3.01	2.46	0	0	0
Ilmenite	3.51	3.52	2.84	3.18	2.82	3.21	3.27	3.9	1.49	3.06	3.11	1.04	1.11	1.88	0.48	1.07	3.33	0.63	1.1	1.72	0.81	2.12
Magnetite	0.83	0.85	0.7	0.83	0.65	0.81	0.8	0.87	0.3	0.69	0.7	0.42	0	0.46	0	0	0	0	0	0.35	0.45	0.76
Apatite	1.58	1.51	1.18	1.28	1.48	1.26	1.5	1.63	0.53	1.05	1.56	0.34	0.3	0.83	0.4	0.06	1.86	0.11	0.3	0.6	0.2	0.95
Zircon	0.14	0.08	0.11	0.09	0.11	0.16	0.14	0.08	0.02	0.1	0.12	0.07	0.03	0.11	0.04	0.02	0.08	0.02	0.15	0.02	0.11	0.1

Note: CHA=Chaone; JUN=Junguni; KU=Kasungu; KUCP=Kasungu Chipala; MANGO=Mangochi Hill; MAU=Mauni; NKHU=Nkhuzi Bay; SONG=Songwe-Mauze; TUND=Tundulu; ZA=Zomba

There is also positive association between TiO_2 and P_2O_5, which strongly suggests fractional crystallisation in formation of these rocks (Pasquarè et al., 2008). This is also supported by low Zr/ TiO_2 ratios, which also may suggest that some of the alkaline rocks have undergone much continental crust assimilation. The TiO_2 vs P_2O_5 diagram (Figure 6.4) also shows two major groups, which also correspond to those identified in Figure 6.3. The carbonatite-associated nepheline syenites plot in group A on the R_1-R_2 but some plot into B on the TiO_2 vs P_2O_5 plot (Alle, 2007).

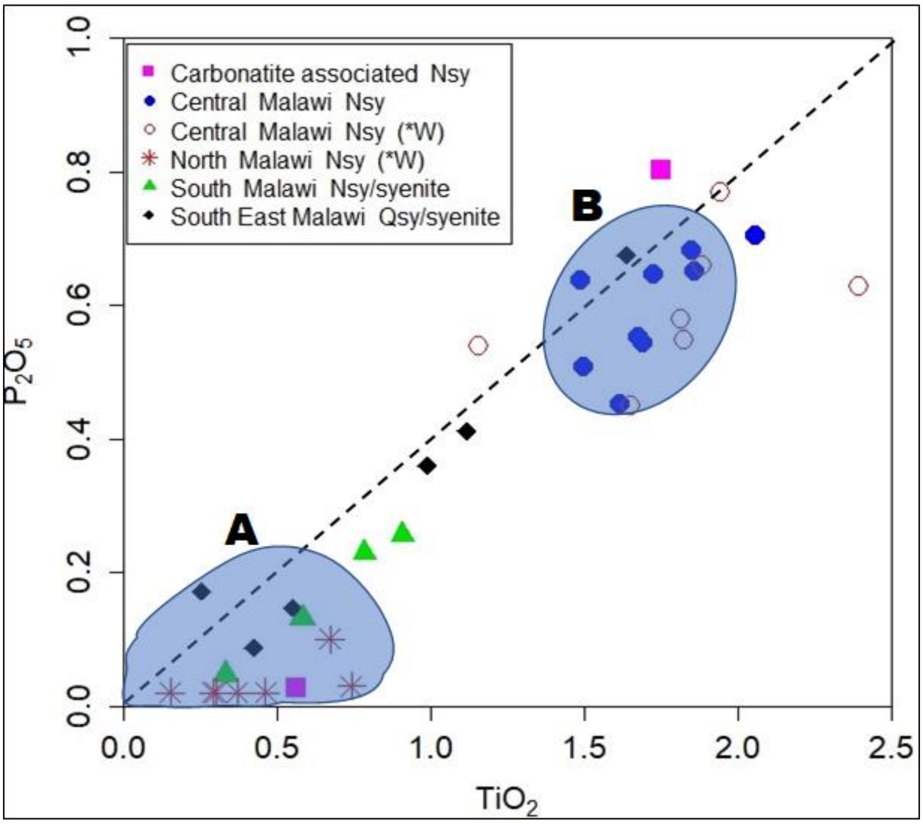

Figure 6.4: TiO_2 (wt. %) vs P_2O_5 (wt. %) plot for Malawi nepheline syenites showing similar groups to the classification in Figure 6.3.

6.2.2 Trace elements

The nepheline syenites and related rocks from Malawi contain varying amounts of trace elements. The south Malawi and carbonatite-associated intrusions tend to be more enriched in LREEs in contrast with the rocks from the north and central areas. These trace element concentrations are typical of alkaline rocks (Viana and Battilani, 2014). The Malawi rocks are characterised by abundance of large ion lithophile (LIL) elements such as Rb, Sr, Ba, Nb, Ta, Th, U, LREEs (Figure 6.5). The abundance of Ba, Rb and Ce suggests replacement of K feldspars. This is because Ba and Rb substitute for K in K-feldspar, micas or hornblende (Deer et al., 1982). Some trace elements are essential for plant growth, and all may be toxic above certain concentrations; Figure 6.6 shows variations in selected trace elements in relation to K_2O content.

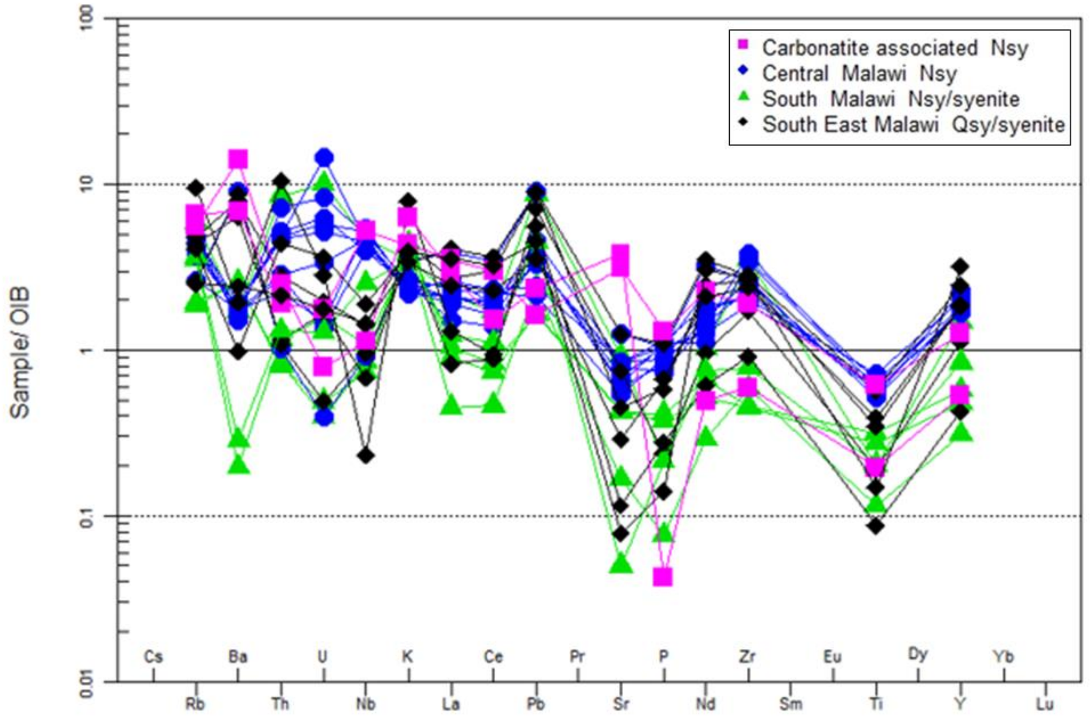

Figure 6.5: Concentration of trace elements within Malawi's alkaline rocks (after Sun and McDonough 1989 and modified by McDonough and Sun, 1995).

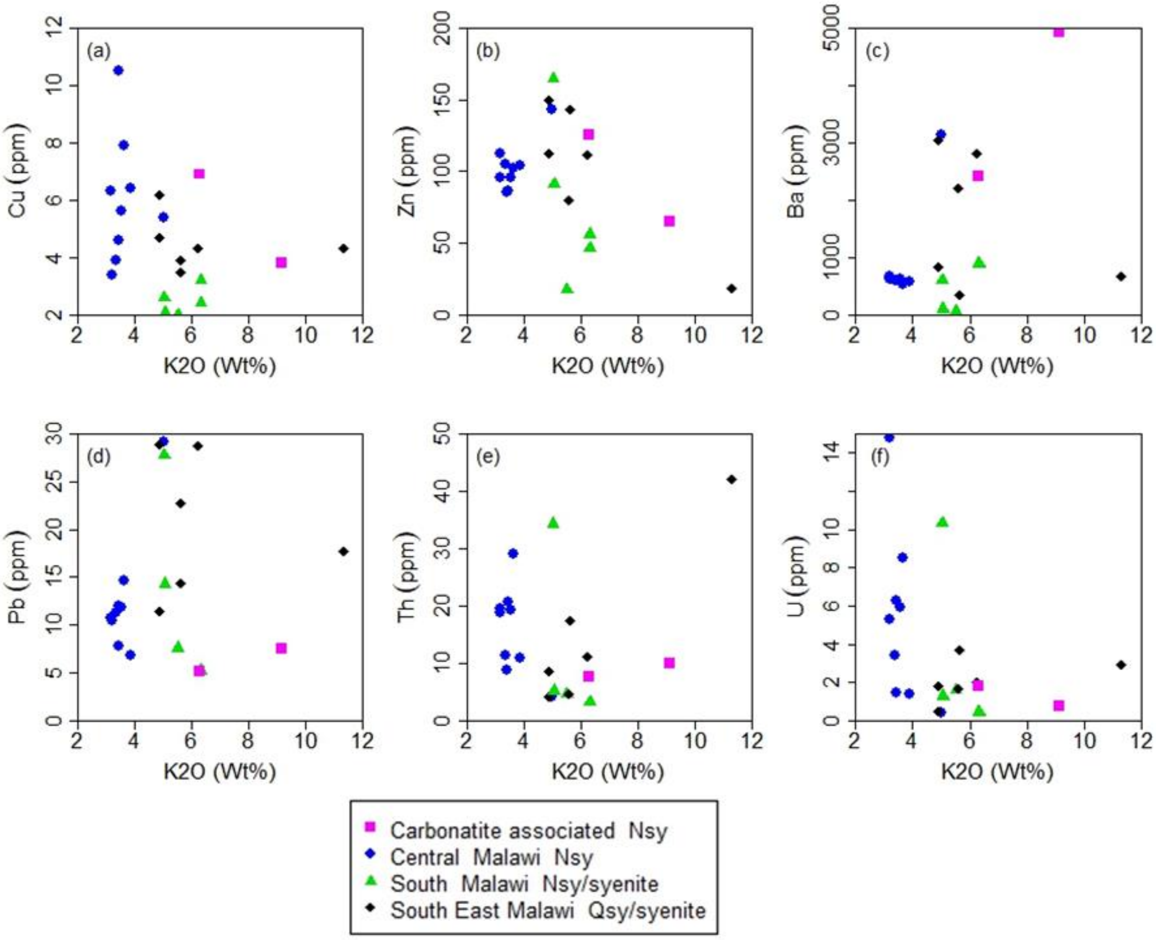

Figure 6.6: Concentration of some trace elements relative to K_2O (wt %) in Malawi's alkaline rocks.

6.3 Petrography

In most nepheline syenite thin sections, nepheline is etched around the grain boundaries and shows alteration. Orthoclase and plagioclase also show alteration to clays. Figure 6.7 shows examples of thin sections for selected rocks, and Figure 6.8 shows BSE images. Nepheline is clearly identifiable in the Tundulu nepheline syenite (Figure 6.7B; Figure 6.8A &B). Some opaque minerals also are also present in some highly altered rocks such as Junguni (Figure 6.7C). In terms of composition, the modal nepheline amounts to about 15-30% in most of the the nepheline syenite thin sections such as in Figure 6.7(B) and Table 6.3. In some foid syenites and nepheline syenites, a mineral first taken to be quartz appears yellower than the normal first-order interference colour quartz (Figure 6.7D). If this were due to the thin section thickness, adjacent feldspars would also show similar interference colours. SEM analysis showed that this high birefringence mineral was davidsmithite (see later). Composition of most rocks in thin sections (as shown in Table 6.3) confirm the field observations of the rocks' mineralogy in hand specimens (shown in Table 5.1).

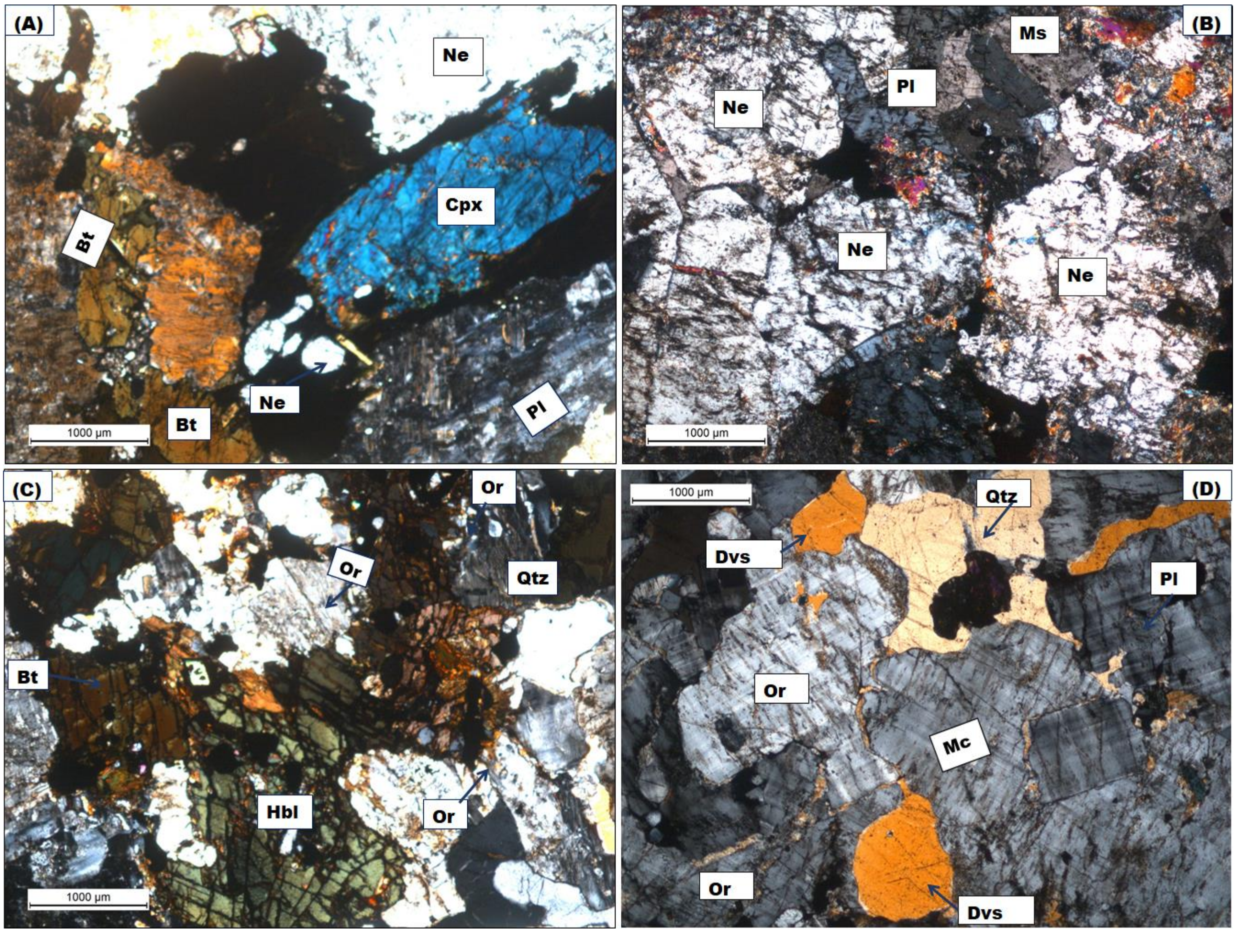

Figure 6.7: Photographs of selected rocks showing minerals in thin sections of selected rocks for (A) Junguni nepheline syenite {JUN-004}; (B) Tundulu nepheline syenite {TUND-01A}; (C) Mangochi syenite {MANGO-002} and (D) Nkhuzi bay foid syenite {NKHU-002} showing (davidsmithite (dvs ?)), Scale: x1000um.

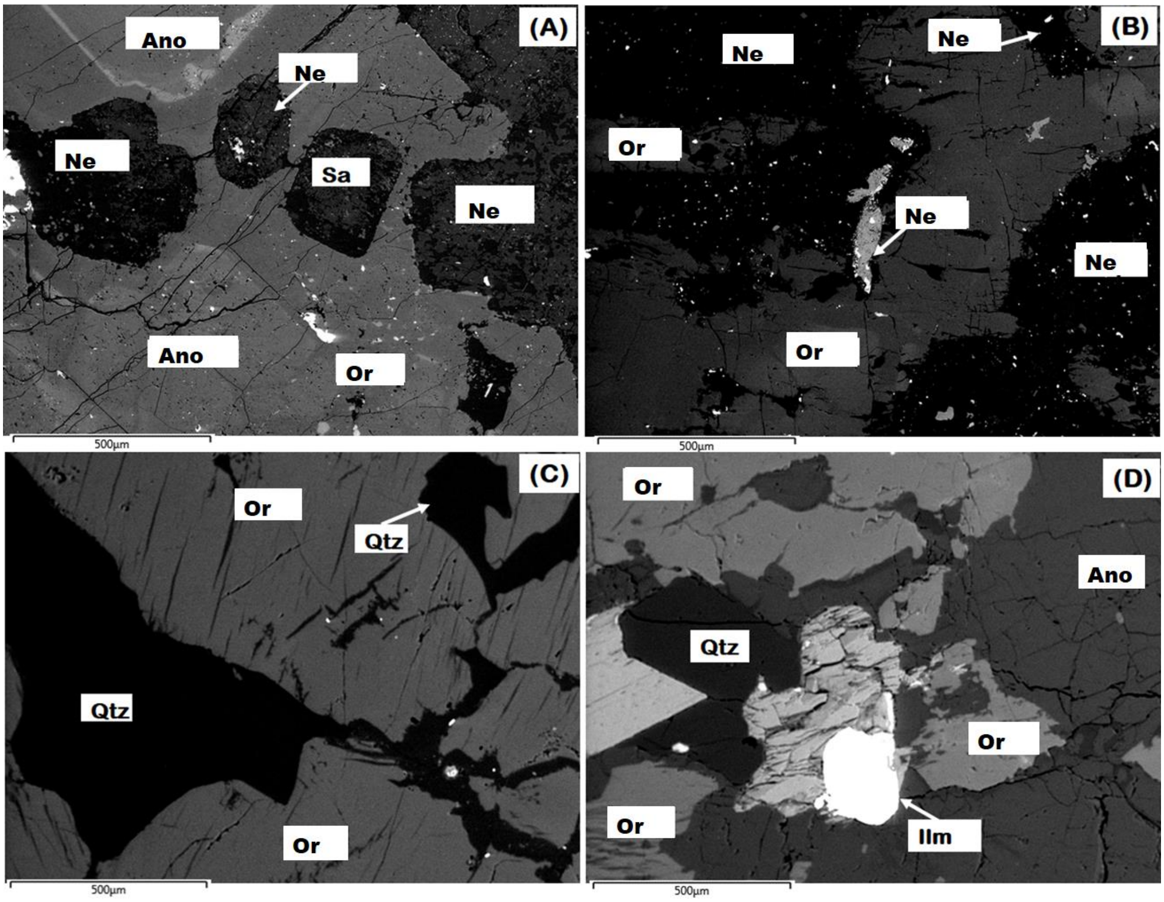

Figure 6.8: Back-Scattered electron (BSE) (BSE) images of selected rocks showing minerals for (A) Songwe-Mauze Nsy {SONG-002}; (B) Tundulu Nsy {TUND-01A}; (C) Nkhuzi bay Qtz Sy {NKHU-002} and (D) Mangochi Sy {MANGO 002002}}; Scale: x500um.

Table 6.3: Composition, mode of minerals and brief description of selected rock samples in thin section.

Location	**Sample location & Code**	**Minerals and relative mode**	**Grain Size**	**Brief description**	**Rock Name**
South Malawi Nsy	Chaone and Mongolowe	30%Pl, 25% Or, Bt,5% Ne,,,5-15% Ms.	Medium to coarse grained	Dominated by plagioclase which is etched on edges and altered to clays. Nepheline less visible and interlocking with plagioclase	Nepheline syenite
South Malawi Nsy	Junguni JUN04	25%Ne, 15% Or, 20% Bt; 10% Pyx, 10% Pl, 10% Opq	Coarse-medium grained	Much altered, feldspars and micas show replacement by secondary minerals.	Nepheline syenite
Central Malawi Nsy	Kasungu (KU03)	15% Or,10% Ne, 10% Pl; % 20% Bt, 5% Ms 20% Opq	Medium-coarse grained	Highly weathered with nepheline and feldspars replaced by secondary minerals hence abundance of opaque minerals.	Nepheline syenite
Central Malawi Nsy	Kasungu-Chipala (KUCP08)	15% Or,15% Ne, 10% Pl; % 20% Bt, 5% Ms, 20% Opq	Very coarse grained	Highly weathered with nepheline and feldspars replaced by secondary minerals hence abundance of opaque minerals	Nepheline syenite
S. East Malawi Syenite	Mangochi Hill (MANGO02)	20% Or, 15%Mc, 15%, 15% Bt; 10% Pl; % 10%Pyx, 5% Qtz	Coarse grained	Weathered to highly weathered rocks, much K-feldspar (pinkish colour).	Syenite
S. East Malawi quart-syenite	Nkhuzi Bay (NKHU03)	20% Or, 15% Mc, 15% Bt; Plag; %,5% Qtz, 4% Pyx, 3%, Dvs (?)	Coarse grained	Weathered rocks with altered showing pale colour and fresher specimens show pinkish colour.	Foid syenite
Carbonatite-associated Nsy	Mauze-Songwe (SONG02)	25%Ne, 18% Mc; 15% Or, 5% Pyx, 15% Bt; 10% Pl 3% Dvs (?),%10% Opq	Coarse-very coarse grained	Relatively less altered, dominated by nepheline K-feldspar.; minor davidsmithite (?) occurrence. Abundance of microcline suggests exsolution of albite (Na-rich) out of a K-feldspar host.	Nepheline syenite
Carbonatite-associated Nsy	Tundulu (TUND01A)	35%Ne, 18% Mc; 15% Or, 10% Pl, 5% Pyx, 15% Bt; 3% Dvs (?),	Medium-coarse grained	Less altered, dominated by nepheline K-feldspar; minor davidsmithite (?) occurrence. Abundance of microcline suggests exsolution of albite (Na-rich) out of a K-feldspar host.	Nepheline syenite

Confirming the petrographic observations using EDS, the key minerals in the nepheline syenites include anorthoclase, albite, actinolite, nepheline, orthoclase, sanidine, titanite, fluorapatite, calcite, biotite and iron oxide. The quartz syenites contain an abundance of K feldspars, quartz and plagioclase (mainly andesine). Figure 6.10 shows the K/Na bivariate x-y graph for atomic proportions of Na [cfu] vs K [cfu], calculated from the EDS output, for the K feldspars and nepheline. While alkali feldspars show a continuous compositional range, nepheline clusters around $(K_{0.25}Na_{0.75})\ AlSiO_4$.

Some of the EDS analyses also show the occurrence of a calcium-rich variety of nepheline $(Na,Ca)AlSiO_4$ or $(KNa)_8CaAl_8Si_8O_{32})$ in the nepheline syenites (Figure 6.9 & Figure 6.10). This occurrence has not been previously reported in Malawi. This mineral, *davidsmithite* (Kechid et al., 2017), is an uncommon silicate mineral of the nepheline group and is associated with the heterovalent replacement of Ca^{2+} for K^+ and as such it is K-deficient (Kechid et al., 2017; Rossi et al., 1989), whose occurrence has been reported in few areas. Its crystallographic and physical properties have been described in detail by Kechid et al. (2017).

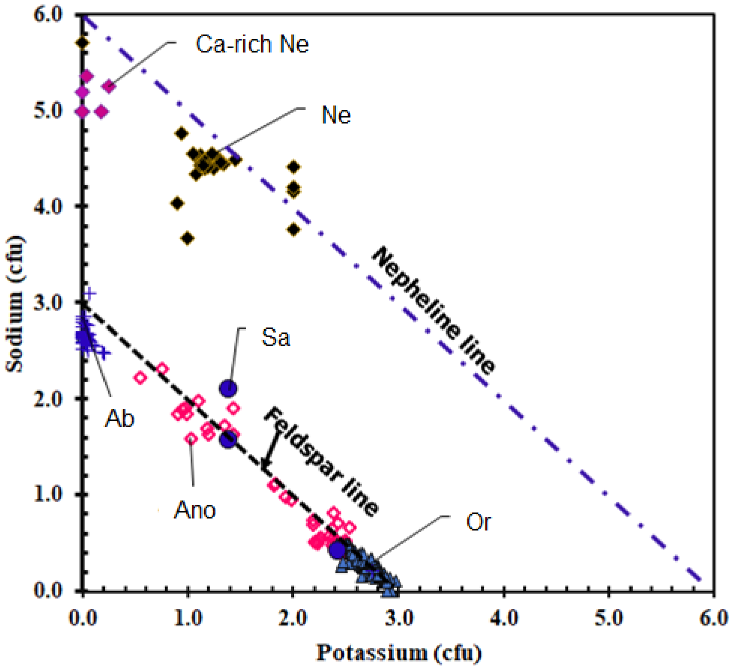

Figure 6.9: K (at prop) vs Na (at prop) plot for modal feldspars and nepheline showing fields for orthoclase (Or), anorthoclase (Ano), sanidine (Sa), Albite (Ab), nepheline (Ne) and Ca-rich nepheline (Ca-rich Ne).

Considering that SEM-EDS semi-quantitative data would not be sufficient to establish the identification of davidsmithite, microprobe analytical work has been done for some rocks to confirm the occurrence of this mineral and accurately determine its composition. Preliminary results of these microprobe analysis confirm presence of the mineral in some samples. Details from this work will be presented in a separate manuscript which is currently in preparation.

Table 6.4: Semi quantitative analyses from the SEM-EDS for selected nepheline grains and number of cations for nepheline based on 4 oxygens..

(a). Nepheline analyses (wt. %)

	Sample ID																	
Element (Wt. %)	KU 09	KU 09	KU 09	KU 09	KU 09	KU 09	KU 09	KU 09	KU 09	KU 09	KU 09	SONG 02	SONG 02	SONG 02	SONG 02	SONG 02	SONG 02	SONG 02
SiO_2	45.8	42.8	48	42.4	42.9	42.8	42.8	46.3	45.67	42.7	42.8	41.2	45.9	48.1	41.4	43.5	43.3	41.9
Al_2O_3	34.26	34.62	31.64	34.79	35.13	34.54	34.46	32.52	32.97	35.03	34.79	35.05	37.48	31.37	35.33	34.13	34.18	35.01
Fe_2O_3	-	-	-	-	-	-	-	-	-	-	-	-	0.55	0.23	0.3	-	0.31	-
CaO	1.04	0.51	0.61	0.4	0.43	0.38	0.26	0.61	0.52	0.49	0.5	-	0.44	-	-	-	-	-
Na_2O	13.4	15.8	14.8	15.9	15.6	16.1	15.7	15.1	15.2	15.8	15.9	15.9	7.71	13.7	15.8	16.1	15.8	15.9
K_2O	5.5	6.3	4.9	6.4	5.8	6.2	6.8	5.4	5.6	5.9	6.7	7.8	7.85	6.67	7.23	6.33	6.44	7.13
TOTAL	100	100	100	100	100	100	100	100	100	100	100	100	100	100	100	100	100	100

(b). Number of cations for nepheline based on 4 oxygens

Element (Wt %)	KU 09	KU 09	KU 09	KU 09	KU 09	KU 09	KU 09	KU 09	KU 09	KU 09	KU 09	SONG 02	SONG 02	SONG 02	SONG 02	SONG 02	SONG 02	SONG 02
Si	1.079	1.027	1.129	1.02	1.027	1.027	1.028	0.934	0.934	1.022	1.025	1	0.934	1	1.042	1.038	1.013	1.046
Al	0.951	0.98	0.877	0.986	0.989	0.977	0.977	0.922	0.922	0.989	0.983	1.003	0.922	1.007	0.964	0.967	0.995	0.962
Ca	0.026	0.013	0.015	0.01	0.011	0.01	0.007	0.016	0.013	0.012	0.013	0	0	0	0	0	0	0
Na	0.612	0.734	0.674	0.745	0.724	0.747	0.734	0.693	0.7	0.735	0.738	0.748	0.626	0.741	0.746	0.736	0.743	0.74
K	0.165	0.194	0.149	0.196	0.179	0.191	0.208	0.333	0.333	0.333	0.186	0.243	0.333	0.223	0.194	0.197	0.219	0.192
K/ (Na)	0.213	0.209	0.181	0.209	0.198	0.203	0.221	0.325	0.323	0.312	0.201	0.245	0.347	0.231	0.206	0.211	0.228	0.206

Note: KU=Kasungu; SONG=Songwe-Mauze.

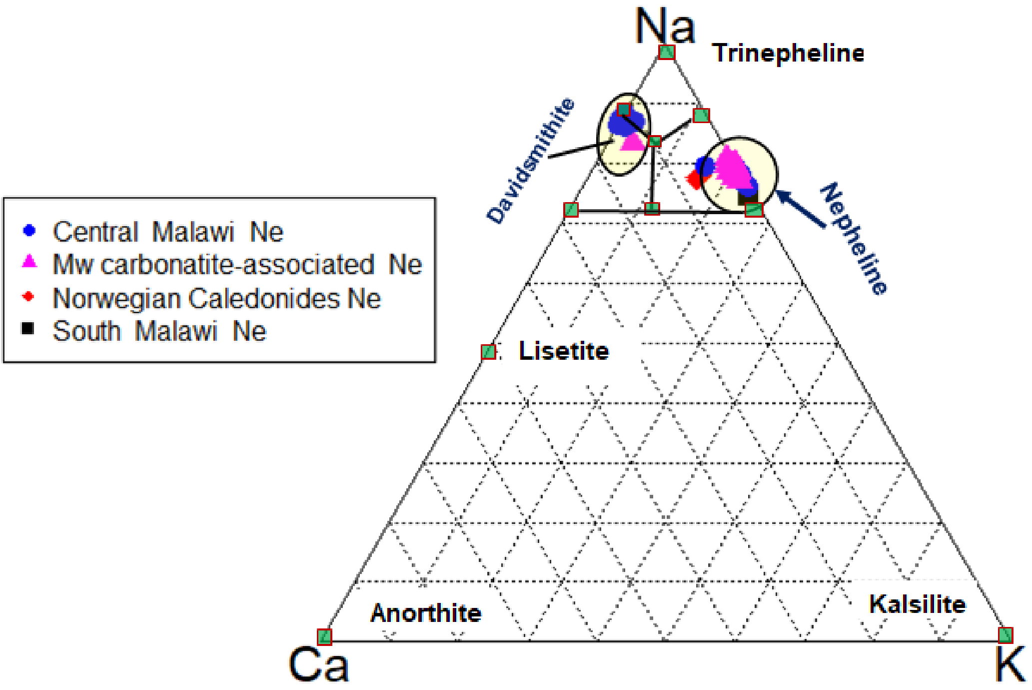

Figure 6.10:Plot of cations using 32 oxygens for Malawi and Norwegian Caledonides nephelines showing davidsmithite and positions of related minerals (after Kechid et al., 2017). The green squares denote mineral end-member compositions.

6.3.1 Weathering intensity of the rocks

Based on the CIA scale, almost all the rocks were relatively fresh with their CIA<50 (Figure 6.11 and Table 6.2). The Tundulu nepheline syenite was the least altered sample whereas the Nkhuzi Bay, Chaone and Kasungu nepheline syenites had some of the most altered rocks. The results show almost no association between the chemical index of alteration and nepheline abundance in the rocks. This suggests that nepheline concentration is less influenced by intensity of weathering but is perhaps more dependent on the petro-geochemical conditions of formation of the rocks. However, a weak positive association was noted between the chemical index of alteration and normative orthoclase.

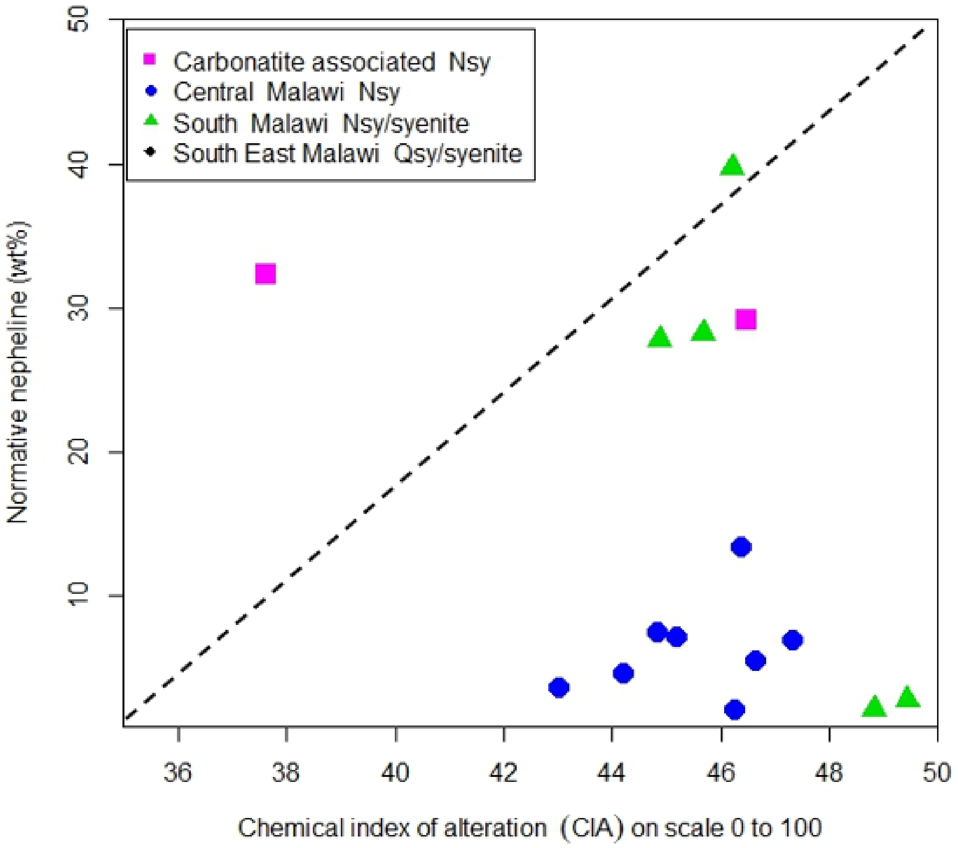

Figure 6.11: The chemical alteration index (CIA) vs normative nepheline content for the rocks.

6.3.2 Comparison of XRF results with airborne and ground gamma-ray spectrometry

Similarities and differences were observed in data acquired from the airborne and ground spectrometry compared to XRF analyses (Figure 6.12 and Tables 8.5 & 8.6). The XRF K_2O values vary from 3.17 -11.32 wt. % (average 5.22 wt %). The airborne gamma K_2O values range from 0 to 5.62 wt. % with an average of 2.78 wt. %, while the ground gamma-ray spectrometry gave K_2O values which range from 3.40-8.98 wt. % and 4.89 wt. % (average).

The XRF Th values range from 3.20-42.10 ppm and an average of 13.60 ppm. The airborne gamma Th values range from 0-22.81 ppm and an average of 10.27 ppm. The ground gamma-ray spectrometry shows Th values which range from 6.47–30.43 ppm and average of 18.42 ppm. There are low values for the data from ground spectrometry for Th and U channels, relative to measurements by airborne spectrometry and XRF analysis (Figure 6.12D-I). Ground spectrometry, however, shows highest results for the K channel. This shows the need for follow up ground geophysical surveys for detailed characterisation of nepheline syenites.

Table 6.5: Chemical index of alteration (CIA) for selected individual samples.

Sample ID	**R1**	**R2**	**Chemical index of alteration (CIA)**	**Intrusion Name**	**Location group/cluster**
CHA-02	255.39	562.43	49.44	Chaone	South Malawi Nsy/ Sy
JUNG-01	-2092.63	546.34	46.21	Junguni	South Malawi Nsy/ Sy
JUNG-02	-1269.41	594	44.88	Junguni	South Malawi Nsy/ Sy
JUNG-04	259.38	578.97	48.82	Junguni	South Malawi Nsy/ Sy
KU-02	39.59	871.77	45.17	Kasungu	Central Malawi Nsy
KU-03	-40.83	797.08	47.31	Kasungu	Central Malawi Nsy
KU-06	272.36	979.23	43.01	Kasungu	Central Malawi Nsy
KU-11	100.43	794.13	46.62	Kasungu	Central Malawi Nsy
KUCP-01	236.62	828.53	46.26	Kasungu-Chipala	Central Malawi Nsy
KUCP-05	-7.72	884.03	44.82	Kasungu-Chipala	Central Malawi Nsy
KUCP-06	-331.05	807.33	46.38	Kasungu-Chipala	Central Malawi Nsy
KUCP-07	118.53	812.72	44.21	Kasungu-Chipala	Central Malawi Nsy
KUCP-08	906.02	794.76	49.48	Kasungu-Chipala	Central Malawi Qsy
MANGO-02	871.33	803.86	48.81	Mangochi	South East Malawi Sy
MAU-01	1349.56	574.02	48.9	Mauni	South East Malawi Qtz Sy
MOG-11	-1244.37	604.76	45.68	Mongolowe	South Malawi Nsy/ Sy
NKHU-02	1212.87	513.51	50.31	Nkhuzi Bay	South East Malawi Qtz Sy
NKHU-03	1382.28	359.75	48.2	Nkhuzi Bay	South East Malawi Qtz Sy
SONG-02	-1255.08	597.87	46.48	Songwe-Mauze	Carbonatite associated Nsy
TUND-01A	-1530.15	1179.58	37.62	Tundulu	Carbonatite associated Nsy
ZA-02	1331.89	458.68	47.17	Zomba	South East Malawi Sy

Note: Nsy denote nepheline syenite; Sy denote syenite; Qtz denote quartz

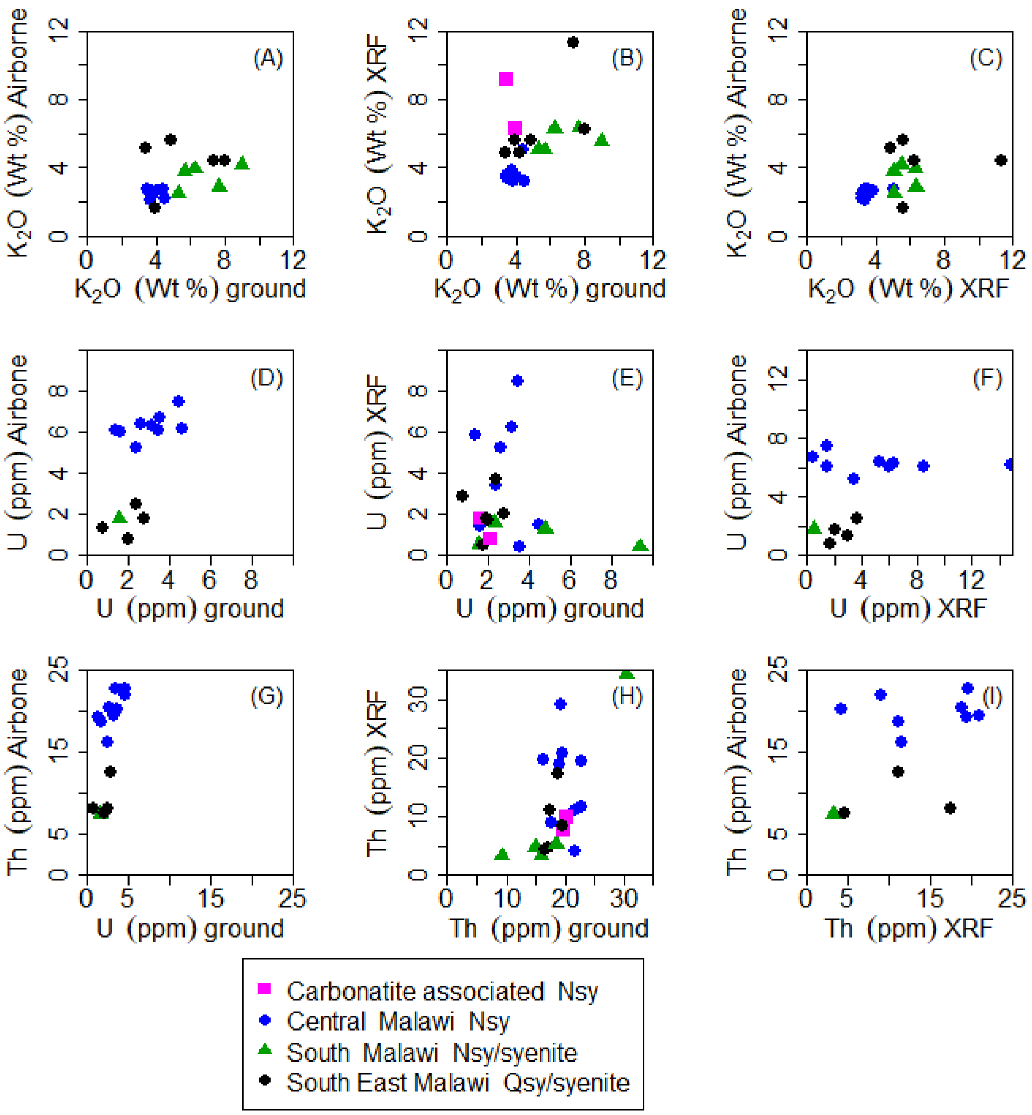

Figure 6.12: XRF analyses compared with measurements of radionuclide elements (K, U, Th) from airborne and ground spectrometry.

There is generally, moderate positive agreement between K data acquired by the airborne and ground gamma-ray surveys and XRF geochemical analysis. There is moderate positive association between K_2O analysed by XRF and field gamma-ray spectrometry (0.56), and 0.76 for K_2O analysed by XRF vs airborne gamma-ray spectrometry. There is also moderate positive association for K_2O analysed by XRF vs field gamma-ray spectrometry (0.55). There is also positive association for Th acquired by airborne and field spectrometry (0.58) as well as for U by acquired by airborne and field spectrometry (0.58). There were no correlations among the other pairs of the elements.

Table 6.6: Radionuclide elemental concentration for K, Th, and U as acquired by airborne and ground gamma-ray spectrometry and laboratory XRF analyses

Sample ID	**CHA 002**	**JUN 001**	**JUN 002**	**JUN 004**	**KU 002**	**KU 003**	**KU 006**	**KU 011**	**KUCP 001**	**KUCP 005**	**KUCP 006**	**KUCP 007**	**KUCP 008**	**MANGO 02**	**MAU 001**	**MOG 001**	**NKHU 002**	**NKHU 003**	**SONG 002**	**TUND 001A**	**ZA 002**	**ZA-04**
K_2O (Wt% (XRF))	6.32	5.51	5.03	6.31	3.64	3.19	3.42	3.17	3.54	3.36	3.44	3.87	5	4.89	5.6	5.07	6.23	11.32	9.14	6.29	5.63	4.89
K_2O (Wt% (AIRB))	2.87	4.18	3.76	3.93	2.48	2.47	2.13	2.21	2.73	2.7	2.69	2.6	2.77	5.1	5.62	2.52	4.36	4.37	0	0	1.6	0
K_2O (Wt% (Ground))	7.65	8.98	5.66	6.25	3.62	3.86	3.62	4.5	3.43	3.49	3.98	3.74	4.4	3.4	4.84	5.3	7.95	7.31	3.41	3.98	3.94	4.22
Th (ppm (XRF))	3.2	4.6	34.3	3.3	29.1	19.6	8.9	18.8	19.3	11.5	20.8	11	4.1	4.3	4.6	5.2	11.1	42.1	9.9	7.6	17.4	8.5
Th (ppm (AIRB))	7.43	0	0	0	22.81	22.78	22.02	20.51	19.33	16.2	19.5	18.71	20.29	0	7.54	0	12.61	8.12	0	0	8.15	0
Th (ppm (Ground))	9.18	15	30.43	15.92	19.15	16.25	17.65	18.9	22.8	22.9	19.63	21.6	21.6	16.63	17.18	18.45	17.33	6.67	20.17	19.63	18.63	19.5
U (ppm (XRF))	0.5	1.6	10.3	0.4	8.5	14.8	1.5	5.3	5.9	3.4	6.3	1.4	0.4	0.5	1.7	1.3	2	2.9	0.8	1.8	3.7	1.8
U (ppm (AIRB))	1.79	0	0	0	6.11	6.21	7.46	6.43	6.1	5.24	6.34	6.06	6.72	0	0.82	0	1.79	1.32	0	0	2.49	0
U (ppm (Ground))	1.53	2.3	7.17	9.36	3.4	4.6	4.45	2.6	1.35	2.35	3.1	1.6	3.5	1.73	1.98	4.75	2.77	0.73	2.07	1.63	2.37	1.9

Note: CHA=Chaone; JUN=Junguni; KU=Kasungu; KUCP=Kasungu Chipala; MANGO=Mangochi Hill; NKHU=Nkhuzi Bay; SONG=Songwe-Mauze; TUND=Tundulu; ZA=Zomba

The U values from X-ray fluorescence (XRF) analyses range from 0.40 - 14.80 ppm and an average of 3.49 ppm. Airborne gamma U values range from 0 -7.46 ppm and an average of 2.95 ppm, while the ground gamma-ray spectrometry show U values which range from 0.73 - 9.36 ppm and an average of 3.06 ppm. The Nkhuzi Bay area shows the highest K_2O content among all the rocks samples. The highest K_2O content among the nepheline syenites only is noted in the Songwe-Mauze nepheline syenites as shown in Figure 6.12 and Table 6.6 above. The nepheline syenites of Malawi also show similar geochemistry to rocks of other parts of the world. For example, Figure 6.13 (A) shows that the XRF results indicate that there are no major differences compared with the North Cape nepheline syenite, which has been used as a source of crushed rock potash. Figure 6.13 (B) shows that the Junguni nepheline syenites are closely related to the North Cape nepheline syenites. These are followed by the rocks from Chaone, and Mongolowe which also form one cluster with those from Junguni.

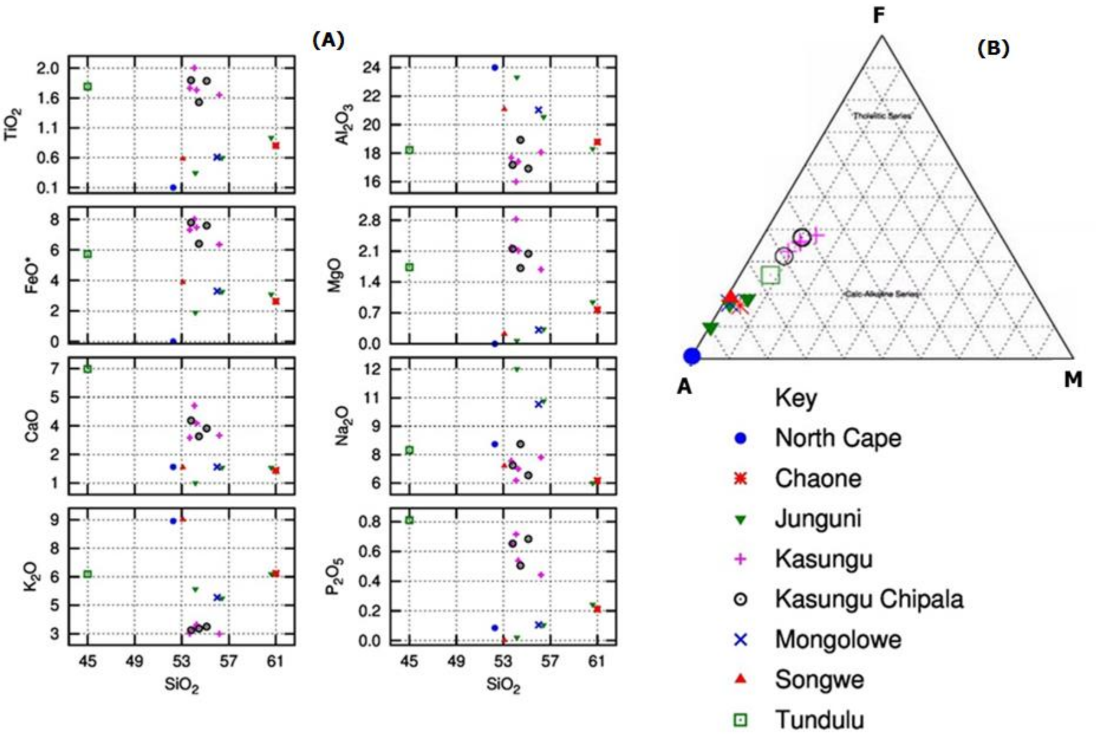

Figure 6.13: (Left) Harker diagram for nepheline syenites from different sites of Malawi and North Cape nepheline syenites and (right) is AFM ternary plot for the samples.

6.4 Discussion

The results have shown that, in general, there is some agreement between the K content (recalculated as K_2O) reported by the handheld gamma-ray spectrometer and the results obtained using XRF or airborne spectrometry. The carbonatite-associated nepheline syenites show poor agreement, and this may be due to sample heterogeneity or weathering. There is also less agreement for Th for most rocks but almost no agreement for U. This strongly suggests that, for determination of K content, hand-held field spectrometry is satisfactory and can be used where laboratory XRF analysis is not available.

In geochemical plots, some of the carbonatite-associated and the South Malawi nepheline syenites, (particularly, the Junguni, Tundulu and Songwe-Mauze nepheline syenites), fall into the same cluster (Figure 6.3 and Figure 6.4). However, the rocks from the Junguni intrusion have the highest amount of normative nepheline (40%) as shown in Table 6.4. These results agree with geochemical studies done by Woolley (2015), who found up to 60% modal nepheline in some rocks of the Junguni intrusion, with strong peralkalinity characterized by acmite values of up to 28%.

The field gamma-ray measurements for K_2O values also tend to increase in the southward direction and toward the summit of the Junguni intrusion. The Songwe-Mauze and Tundulu intrusions also show high normative nepheline coupled with presence of normative leucite. Results have also shown a positive correlation between normative nepheline and the normative K-feldspar (orthoclase). This suggests that when mapping nepheline syenites, it is likely that the other alkaline rocks which are geochemically closely related to the nepheline syenites could be mapped together with nepheline syenites. This also shows that it is not easy to distinguish clearly members of the silicate family from each other, and agrees with previous studies by Hecker et al. (2010).

The weathering indices have further shown that the rocks are relatively less altered, within three clusters. One cluster comprises the Junguni, Songwe-Mauze and Mongolowe nepheline syenites, which are relatively least altered. The second cluster has the Kasungu, Kasungu-Chipala and some of the Junguni nepheline syenites; and rocks in this group are moderately altered. The third group is for the most altered nepheline syenites and includes the Chaone and Kasungu-Chipala nepheline syenites.

It has also been noted that the carbonatite-associated nepheline syenites at Tundulu differ characteristically, from all the other intrusions. Whether this is because of differences in the level of alteration or geochemical composition of the rocks is not clear. However, both factors may have an impact because the Tundulu nepheline syenite is also the only intrusion which does not show normative orthoclase (as shown in Table 6.2). Previous geochemical data by Eby et al. (1998), for some of northern Malawi nepheline syenites (such as the Illomba, the Ullindi), and this study's data some of the Southern Malawi nepheline syenites (notably, Chaone, Songwe-Mauze, Junguni and Tundulu complexes), are similar in chemical and mineralogical composition to the nepheline syenites from other parts of the world, especially, the Northern Cape (Norway), which have been considered as viable potash sources. The results, therefore, suggest that Malawi's nepheline syenites could equally be ideal as potash sources. The results also show that the Tundulu complex is very different from the other nepheline syenites. The distinctive characteristics of the Tundulu nepheline syenite may be interpreted as possible evidence of the carbonatite–nepheline melt mixing/interaction similar to the emplacement mechanisms of the Ol Doinyo Lengai carbonatite complex of Tanzania (Mitchell, 2009; Potter et al., 2017). The nepheline syenites surround the apatite-rich carbonatite (Broom-Fendley et al., 2016).

Mineralogically, the Malawi nepheline syenites resemble those from other parts of the world. The identification of davidsmithite is a significant though unexpected finding. At Liset eclogite pod, Liset, Selje, Western Gneiss Region (WGR), Norway, (Del Giovine and Fabietti, 2005; Kechid et al., 2017), davidsmithite is associated with retrograde eclogites. However, it could also be suggested that presence of davidsmithite in Malawi's nepheline syenites may be due to carbonatite-nepheline metasomatism for the carbonatite-associated rocks and Na-K metasomatism for the other nepheline syenites. This could be similar to plagioclase-Ca-rich-nepheline intergrowths within syenites in the Marangudzi Complex where the *nephelinization* is associated with plagioclase alteration and resorption by late-stage magmatic fluids (Henderson and Gibb, 1972).

Possibly, this mineral could also have formed through Na-K metasomatism of plagioclase at high temperatures as noted by Mitchell and Platt (1979) in the Coldwell Complex (Ontario) nepheline intergrowths. The presence of the davidsmithite (if confirmed), could add to potential value of these rocks. This is because both K and calcium which form part of the davidsmithite chemistry are important elements for plant nutrition. The electron microprobe analysis will, therefore, be helpful to confirm the presence of this mineral in nepheline syenites from Malawi.

6.5 Conclusion

This chapter has presented the geochemical and petrological analyses of Malawi's nepheline syenites and related rocks collected during the fieldwork in Malawi. The results have further shown that some of Malawi's nepheline syenites have similar geochemistry to those from other parts of the world. As shown in chapter 3, some of these nepheline syenites particularly, those from North Cape have been found suitable as potash fertiliser. This suggests that Malawi's nepheline syenites could also be potentially suited as a potash source. The results have also shown that, in general, there is some agreement between the K2O analysed by the handheld gamma-ray spectrometer (in chapter 5) and the results obtained using XRF or airborne spectrometry in this chapter.

This chapter has also shown that a rare mineral called davidsmithite, which had never been reported in Malawi, could be present in some of the foid and nepheline syenites from Malawi. However, at the time of preparation of this thesis its occurrence had not been fully confirmed. Further studies are being done to certainly confirm the presence and processes which lead to formation of davidsmithite in these rocks.

Chapter 7: Field spectroscopy and remote sensing as tools for distinguishing nepheline syenites and related igneous rocks

7. Introduction

This chapter addresses Objective 6 of this study, which aimed to use field spectroscopy to guide satellite remote sensing processing and data analysis to delineate nepheline syenite targets. On one hand, the chapter aimed to assess spectral properties and separability of nepheline syenites from other silicates, especially other alkaline rocks. On the other hand, the chapter also aimed to use these datasets to map nepheline syenite intrusions in Malawi. The ultimate goal was to use these techniques for mapping nepheline syenites, which can be considered as an alternative potash fertiliser for agriculture. In this chapter, field spectroscopy data acquired using the Analytical Spectral Device (ASD) and satellite image data were used as the basis for mapping nepheline syenites using satellite image data.

Field spectroscopy is a remote sensing technique which involves acquisition of quantitative measurements of the reflectance, reflected radiance, or irradiance of materials such as rocks, minerals, vegetation and other objects under solar illumination (Danner et al., 2015; Milton, 2003). This technique has become an important tool in geoscientific research because of its capacity to generate high resolution quantitative remotely-sensed data (Ben-Dor et al., 2009) but at comparatively higher costs than using satellite data. This study used field spectroscopy data to assess the spectral properties of nepheline syenites and related rocks, which were collected from the fieldwork in Malawi.

While field spectroscopy provides high-resolution optical data for remote sensing, it is limited in terms of spatial coverage by factors such as funding for large areas and spatial coverage for regional mapping. This is where satellite data become more useful as they have large spatial coverage. Prior to this study, no research had been conducted on nepheline syenites of Malawi and the East African Rift System (EARS), using field spectroscopy. This chapter is important because it provides new information about the spectral characteristics of Malawi’s nepheline syenites and use of field spectroscopy for exploration in the EARS.

Most of the commonly used field spectrometers have a narrow wavelength region, which provides spectral data in the visible to near infrared to short wave infrared radiation (VNIR-SWIR) wavelength regions. A few spectrometers, such as the Fourier Transform

Interferometers, can collect spectral data in the thermal infrared radiation (TIR) wavelength region. Previous studies had argued that VNIR/SWIR data were not ideal for discriminating silicate minerals and rocks within the VNIR-SWIR because only features of rocks with mineral groups such as iron, hydroxyl/water, sulphates, carbonates and phosphates (Ferrier et al., 2016; Hecker, 2013) can be distinguished in this region. Other studies have further argued that there are no SWIR features for non-OH-bearing materials, including silicate minerals (Hecker, 2013). However, this conclusion appears to be much generalised because no previous study had exclusively mapped nepheline-bearing rocks using remote sensing data.

This chapter also uses ASTER satellite remote sensing to delineate nepheline syenites by applying results from the ASD field spectroscopy as the basis for satellite image analysis for geologic mapping. ASTER images have been widely used in geological mapping and have global coverage. As shown in chapter 4, ASTER data have been used in various areas of the world for mapping surface alteration zones of minerals such as carbonates, sulphates, hydrothermal deposits, and surficial deposits, because the ASTER sensor has mineralogically sensitive wavelengths in the VNIR/SWIR bands (Guha et al., 2015; Guha and Vinod, 2016).

7.1 Field spectroscopy in geologic remote sensing

In geology, field spectroscopy involves analysis of the spectral reflectance of minerals and rocks within the visible (400nm-700nm), near-infrared (700nm-1000nm) and short-wave infrared (1000-2500nm) wavelength regions of the electromagnetic spectrum (Hauff, 1983). Field spectroscopy is helpful in discrimination of materials because it is a swift and non-destructive analytical method (Izzuddin et al., 2017a) which allows contiguous statistical analysis of spectral data of minerals, rocks, soils and other materials. This has also proved to be an important tool for determining key diagnostic features of rocks and minerals because different rocks and minerals have distinctive spectral signatures (Kruse, 2012; Sabins, 1999a; Ferrier et al., 2016). Field spectra have been used in some studies, including in the identification of multi-style hydrothermal alteration, using integrated compositional and topographic remote sensing datasets by Ferrier et al. (2016), the use of thermal infrared spectroscopy on feldspars by Hecker et al. (2010) and exploration for precious metals by Hauff (1983). In addition, Carrino et al. (2015) have also successfully used field spectroscopy for hydrothermal alteration and geology mapping while other studies have been conducted using the technique to assess soil properties (Ibraheem, 2015; Prado et al., 2007; van der Meer, 1999). Despite successes reported by the previous research, no study has been conducted to map nepheline syenites using either field spectroscopy or satellite imagery.

Successful application of remote sensing to map nepheline-bearing rocks provides new information to the geologic remote sensing community.

The reason for using satellite data was to delineate nepheline syenites using low-cost remote sensing data, which has regional coverage, in addition to airborne gamma-ray geophysical and DTM/DEM data. Data from two of the most widely used sensors in geological mapping, namely Landsat and ASTER, have global coverage and are available at no cost (Ninomiya and Fu, 2016), In this chapter, ASTER data were used because ASTER bands have higher spectral and spatial resolution than Landsat's (Abrams and Hook, 2002). In addition, the Geological Surveys of the Southern African Development Community (SADC), including Malawi, enjoy regional technical cooperation and support from Japan through the Japan Oil, Gas and Metals National Corporation (JOGMEC, 2017). Under this cooperation, these countries have basic technical skills and intra-regional networks for using mostly ASTER data in mineral and geological exploration. Therefore, skills transfer would be easier for mapping nepheline syenites suited for K fertiliser, in these countries, using ASTER data.

7.2 Materials and methods

The rocks studied in this chapter contain, largely, minerals of the tectosilicate and phyllosilicate mineral groups. The rock and soil samples used were collected from the fieldwork in Malawi whose sampling procedure has already been outlined in chapter 5. Six types of silicate rocks were studied, namely: nepheline syenite, syenite, alkaline granite, quartz syenite, granite, basalt and a few carbonatites. The soil samples that were studied were also largely products of weathering of these rock units. Five pure mineral samples, namely orthoclase, albite, biotite, muscovite and calcite, were also examined as accessed from Newcastle University's School Natural and Environmental Sciences while two samples of nepheline (unpolished and polished, respectively), were accessed from Prof. David Manning's personal archive. They were studied to examine their properties and diagnostic features, which would then help in satellite imagery classification of these rocks and minerals.

7.2.1 ASD Spectra data collection and pre-processing

The ASD spectral data were collected in the laboratory. Therefore, the impact of such factors as changes in sun angle, cloud cover, topography, and atmospheric attenuation (Izzuddin et al., 2017b) was minimal. The spectral data were collected at Newcastle University using the Analytical Spectral Device (ASD) FieldspecPro spectrometer of Newcastle University's School of Engineering. The spectra were collected following the Natural Environment

Research Council (NERC) ASD Field Spectroscopy Facility guidelines (MacArthur, 2007). Appendix 7.1 shows technical specifications of the ASD FieldspecPro instrument that was used. Data were collected with the integration times of 25 cycles of 10ms per measurement with sampling intervals of 1.4 nm at 350 to 1000nm and 2nm at 1000 to 2500 nm. The ASD spectrometer has a spectral range of 350-2500 nm. Data from between 350–400 nm were deleted because they too noisy to be used.

Twenty (20) rock-chips, twenty-nine (29) soil samples and seven (7) mineral specimens were studied. Approximately 427 rock and soil reflectance spectra were measured of which 171 spectra were from polished rock surfaces and 100 spectra from unpolished surface of rock samples collected in selected areas in Malawi. Thirty-seven (37) spectra were collected from mineral samples while 121 spectra were from soil samples. Twenty rock samples were cut into about ~50×50mm flat surfaces and then polished using 60nmgrit and later the 160nm grit abrasive papers to minimize rock unevenness and scratches. This was done to enhance better optical coupling when using an ASD contact probe and for better quality spectra collection (Ferrier et al., 2016).

For the soil spectra, the ASD field spectrometer was used with a high-intensity 100W quartz-halogen lamp and a pistol grip (Castaldi et al., 2012) and a 1-degree field of view (FOV) fore-optic attached to the grip; the spectrum file was measured as reflectance data. The soil samples were first air-dried, then sieved and placed in petri dishes, having a thickness of about 2 cm. The fore-optic attached to the grip was placed about 5 cm above the petri dish so that the soils were not in physical contact with the fore-optic and the soil spectral measurements were done in a darkroom to avoid interference from sunlight.

For the ASD FieldspecPro instrument, the minimum wavelength was 350nm, the step value of 1 while the maximum wavelength was 2500nm. The ASD FieldspecPro instrument digitizes spectral values to 16 bits. The join between the VNIR and SWIR1 sensors was 1000nm while the join between SWIR1 and SWIR2 sensors was 1830nm. Twenty-five (25) measurements were taken per data value and the data were compared to a white reference. Three to four spectra were collected from each rock or soil sample from different faces, by rotating the rock-chips or petri dish containing soil sample. This was done to increase the representativeness of the spectra and to cater for the sample heterogeneity. Absolute reflectance values were calculated by calibrating each batch of 4 to 5 repeat measurements of each sample against a Spectralon white reference panel. The white reference panel was also measured at the end of each sample batch to check for instrumental drift.

To cater for the rock samples' compositional heterogeneity, for each batch of repeat measurements, the spectra were averaged following the approach of Ferrier et al. (2016). Correction to relative reflectance spectra was done using the Newcastle University ASD Panel calibration file of 2013 as a standard, as proposed by Walker (2009). Absolute reflectance was calculated from the raw ASD spectra. Box and whisker plots were used for analysis of the peaks, and troughs of the spectra were also calculated in JMP13 Pro software package in order to assess the relationship (Hole, 2009) and separability of the different rocks and minerals at different wavelengths. The Field Spectroscopy Facility (FSF) Toolbox (Robinson & MacArthur 2011) for Matlab software was used for most data processing tasks in this chapter.

7.2.2 Removal of water absorption bands

Water absorption bands occurred between 1350-1460 and 1790-1960nm in all spectral measurements made using the field spectrometer. Presence of high-water absorption affects the data quality in that it shows up as highly noisy areas because the water greatly reduces irradiance on the Earth surface thereby amplifying errors in the absolute reflectance. If they are not removed, water bands may be mistaken for diagnostic features for rocks or minerals. The water bands were eliminated from the spectra using a Matlab function *'removewater'* which is available in the FSF Post Processing Toolbox (Robinson & MacArthur 2011).

7.2.3 Processing and spectral data analysis

This chapter used spectral derivative analysis to understand the different reflectance and absorption patterns of the rocks and ultimately to determine separability of nepheline syenites from other rocks, especially other silicate rocks, within the VNIR-SWIR wavelength region. The Savitzky-Golay filter for calculation of spectral derivatives (Robinson and MacArthur, 2011) was used. Data were smoothed using the Savitzky-Golay filter in Matlab using a polynomial order of 3 and frame size of 31. While other derivative algorithms including the Fourier Transforms may also be useful, the Savitzky and Golay filter was chosen based on successes and recommendations by some previous studies as the most efficient, hence the most commercially preferred technique (Owen, 1995; Zhang and Li, 2014). Owen, (1995), further noted that noise in spectral data is amplified with increasing order of the derivatives. Therefore, the 1st and 2nd order spectral derivatives were used. The first derivatives help to highlight changes in the absorbance rates of a material with respect to wavelength (Owen, 1995) and are useful for depicting the spectra's local maxima and local minima. The second derivatives on the other hand depict the changes in the first derivatives in which a positive slope suggests that the first derivative is increasing and vice versa (Bos, 1974).

7.2.4 Resampling to satellite imagery bands

Spectral data were resampled to ASTER sensor bands in order to match the response of ASTER bands and to determine specific wavelengths where nepheline syenites show diagnostic absorption and reflectance features to help distinguish them from other rocks. The ASD spectra data were resampled to ASTER following the method proposed by the Aleks and Oliver (2004) and Yajima (2014). A spectral library was first built using the field spectra as input data and then the spectral library files were convolved to ASTER VNIR-SWIR bands. Continuum removal was further applied to the resampled data in order to normalize the reflectance spectra and enhance comparison of the spectral absorption features from a common standard. Continuum removal transforms and normalises spectral data and then joins the spectra's minima using a convex hull fitting above the spectrum line of the data (Sowmya & Giridhar, 2017). The resampled spectral data were also overlaid on the ASTER bands to determine key spectral patterns.

7.2.5 Satellite data pre-processing and processing

One hundred and forty scenes of ASTER (AST_L1B), which were processed, were accessed from the Geological Survey of Malawi at no cost. To reduce the impact of cloud cover, an additional eighty-three scenes of ASTER (AST_L1T) data were downloaded from the United States Geological Survey (USGS) website: https://earthexplorer.usgs.gov/ to replace those which had more than 15% cloud cover. Most of the images were collected between May and October for the years 2005 and 2006, the time which coincides with the period for Malawi's dry season. This helped to minimise the effect of green vegetation, seasonal grasses and crops on the satellite data. A few images were collected between February and April because no scenes for the months of May to October were available for some areas. The scene cloud cover for most of the images was less than 10% but a few areas from higher altitudes had up to 20% scene cloud coverage. Table 7.1 shows characteristics of ASTER satellite sensor data. Each ASTER image was processed separately using the Environment for Visualizing Images (ENVI) 4.5 software, which is also effective for processing large multiband multispectral data of Hierarchical Data Format (HDF) files. No geometric corrections were performed because we used ASTER images which were geometrically corrected, rotated to a north-up UTM projection, and calibrated at-sensor radiance data (Ninomiya and Fu, 2016). However, various pre-processing and processing tasks were performed. For effective classification, vegetation, clouds, and water bodies were masked (Takeda, 2010; Onuma et al., 2013).

Table 7.1: Wavelength and description of ASTER satellite sensor bands (after Abrams et al., 2000;Ninomiya and Fu, 2016).

Visible and Near Infrared Subsystem: 8 bits, 60km swath width			
Wavelength description	Band number	Range of band wavelength (µm)	*Spatial resolution*
Green	1 (nadir)	0.520 - 0.600	15m
Red	2 (nadir)	0.630- 0.690	
Visible and near Infrared	3 (nadir)	0.780- 0.860	
Visible and near Infrared	3N (backward)	0.780- 0.860	
Short Wave Infrared Subsystem: 8 bits, 60km swath width			
Short Wave Infrared	4	1.600 - 1.700	30m
	5	2.145 - 2.185	
	6	2.185 - 2.225	
	7	2.235 - 2.285	
	8	2.295 - 2.365	
Thermal Infrared Subsystem: 12 bits, 60km swath width			
Thermal Infrared	10	8.125 - 8.475	90m
	11	8.475 - 8.825	
	12	8.925 - 9.275	
	13	10.250- 10.950	
	14	10.950-11.650	

7.2.6 Data cleaning

The crosstalk effect occurs mainly due to the incident photons bouncing back in band 4 because band 4 has relatively higher solar output unlike the other bands in the SWIR region. Some of the incident photons in ASTER band 4 spill over to the detectors of other SWIR bands thereby causing the crosstalk effect, especially in ASTER band 5, due its detectors' proximity to band 4 detectors. Therefore, data cleaning was done to remove bad pixels by building a mask band using the density slicing algorithm. In density slicing, the DN values of one band which is a subset of all the bands of a particular image scene are classified into several ranges (slices) based on similar properties of the pixels in each slice (Lillesand, Kiefer and Chipman, 2008). A threshold of 'maximum data value of 0.5'for ASTER band 1 was used as the input to build a mask for areas which cover the bad pixels (Onuma et al., 2013). The mask was then applied to all the VNIR-SWIR bands to get images with meaningful data for further processing.

7.2.7 Atmospheric correction for VNIR/SWIR and TIR data

In order to convert at-sensor radiance into surface reflectance values, atmospheric correction of satellite image data was necessary. For VNIR and SWIR data, atmospheric correction was done using the Fast Line-of-Sight Atmospheric Analysis of Spectral Hypercubes (FLAASH) model based on MODTRAN4 radiative transfer code (Palluconi et al., 1999; Research Systems, 2000). Model parameters for the atmospheric correction were set to 50km initial scene visibility value. This scene visibility value was selected because the images were acquired in clear weather conditions and aerosol retrieval for ASTER is not required for such data (Breunig et al., 2009). The mean sensor altitude of Malawi for ASTER was 705km, and the Tropical Atmosphere and Rural aerosol model was used (Breunig et al., 2009).

However, atmospheric correction for the thermal infrared radiance data (bands 10-14) was done using the Thermal Atmospheric Correction model in ENVI 4.5 software (HARRIS Geospatial Solutions, 2016). This algorithm identifies wavelengths which usually show the maximum brightness temperature. These are then used as reference data to normalise and calculate the atmospheric compensation for the entire image scene. For the the thermal infrared (TIR) data, atmospheric correction is done on the assumption of a uniform atmospheric conditions over a scene which is also assumed to be covered by a blackbody surface whose location is however not important the correction process (HARRIS Geospatial Solutions, 2016). Based on this the thermal atmospheric correction calculates wavelengths of the maximum temperature whose result is then applied in the determination of the atmospheric compensation of the rest of the scene. The reference radiance values of the blackbody values are paired against the absolute measured radiance values of the scene to estimate the compensate for the atmospheric correction (Johnson and Young, 1998) (HARRIS Geospatial Solutions, 2016).

7.2.8 Masking of unwanted features on images

In order to improve data quality and enhance geological and structural interpretation, features such as water bodies, cloud cover and cloud shadow were masked by using the density slicing approach of Onuma et al. (2013). A mask band was then produced using a grayscale image of respective bands which most clearly exhibits the features to be masked and then using density slicing thresholds for masking the feature were decided for each of the features to be masked (e.g. clouds cover). The mask band was applied on all image bands in order to mask the whole image. Using this method, masking was done for areas covered by clouds, shadow of clouds, vegetation and water bodies. The threshold of a data minimum value of 100 was used to mask cloud covered areas while the cloud shadow and water features were masked using the threshold of a data maximum value 17 and 30 on ASTER band 3. Vegetation was masked using the threshold of a value between 0.15 and 0.25 as the maximum value data on Band 1. The threshold values for the mask were determined by trying different values on a band which best highlights the feature being masked (e.g. vegetation and water features) until the optimum value is found, because this varies depending on the intensity of the feature.

7.2.9 False colour composite images

Different combinations have been used to identify different minerals and rocks within the SWIR and VNIR wavelength regions as noted in chapter 4. For example, most minerals show absorption features in ASTER bands 4,6,8 which is why ASTER band combinations of 4, 6 and 8, assigned as red, green, blue (RGB) respectively, are commonly used for mapping geological units and potassic alteration (Aleks and Oliver, 2004; Yajima, 2014). Therefore, composite images were also assessed using the radiance and atmospherically corrected ASTER TIR image data.

7.2.10 Band maths and spectral indices for geological mapping

Some spectral indices which were devised by Ninomiya and Fu (2016), Guha and Vinod (2016) and Aleks and Oliver (2004) were assessed to determine a basis for developing some nepheline syenite indices. The spectral indices were developed using products of radiance at-sensor-corrected ASTER data (Ninomiya and Fu, 2016). Therefore, a Nepheline Syenite Index (NSI) for the optical bands in the SWIR wavelength region, herein after referred to as NSI (O), was calculated using the main absoption band and its shoulders as follows:

$$NSI(O) = \left(\frac{b5*b7}{b6*b6}\right) \tag{8.1}$$

where in each case ‘b’ denotes ASTER band; Integer = input ASTER band number

In addition, other spectral indices by Guha and Vinod (2016) are also helpful for general mapping of igneous rocks using ASTER TIR data. These indices include the mafic rocks index (MRI), the felsic rocks index (FRI) and the quartz rocks index (QRI). These indices were computed using band maths calculations in ENVI. The three indices were necessary because igneous rocks mainly fall into these three groups. The Felsic Rocks Index (FRI) was calculated using the equation:

$$FRI = \left(\frac{b10}{b11}\right) * \left(\frac{b12}{b11}\right) \tag{8.2}$$

The Mafic Rocks Index (MRI) was calculated using the following equation:

$$MRI = \left(\frac{b12}{b13}\right) * \left(\frac{b14}{b13}\right) \tag{8.3}$$

The Quartz-rich Rocks Index (QRI) was calculated using the following equation:

$$QRI = \left(\frac{b10}{b12}\right) * \left(\frac{b13}{b12}\right) \qquad (8.4)$$

where in each case 'b' denotes ASTER band; Integer = Input ASTER band number.

For each of the indices, the brighter areas suggest higher index values and potential presence or abundance of the target igneous rock group while the dark areas suggest the absence of the targets. The indices can be used to map geology by making composite band combinations using the three indices as inputs (e.g. RGB=368 in Appendix 7.9).

However, the indices by Guha and Vinod (2016) are more effective in mapping the major groups of the igneous rocks but not the specific rock units. There was, therefore, need for an index which can exclusively discriminate nepheline syenites from the other felsic rocks. Geochemically, nepheline syenites are silica-undersaturated and do not have modal or normative quartz (Mitchell and Platt, 1979; Tanner, 2016). Therefore, the felsic rocks index (FRI) by Guha and Vinod, (2016) and the Quartz Index (QI) formed the basis for developing a Nepheline Syenite Index using ASTER TIR data. The Quartz Index (QI) was calculated using the equation by Ninomiya and Fu, (2016) as:

$$QI = \left(\frac{b11 * b11}{b10 * b12}\right) \qquad (8.5)$$

where 'b' denotes ASTER band; Integer = Input ASTER band number.

As highlighted in chapter 2.3, one of the key geochemical charsteristics of nepheline syenites is the absence of quartz in their composition. Therefore, one assumption of this chapter was that a spectral index which removes quartz from the alkaline rocks could help to delineate the nepheline syneites. Based on this, for the thermal infrared bands, a NSI, here-in after referred to as NSI (T), was devised from the QI and FRI, to delineate the nepheline syenite rocks. Before processing the results, it was difficult to calculate theoretical range of values for nepheline syenites using the NSI (T). However, the highest NSI (T) values were expected to be associated with nepheline syenites. NSI (T) absolute values of nepheline syenites were later deduced from the results. The expectation was that the NSI (T) could map out potassium-rich but quartz-deficient felsic rocks and was calculated using the following equation:

$$NSI(T) = \left(\left(\left(\frac{b10}{b11}\right) * \left(\frac{b12}{b11}\right)\right) - \left(\frac{b11 * b11}{b10 * b12}\right)\right) \qquad (8.6)$$

where ‘b’ denotes ASTER band; Integer = input ASTER band number. Using this index, the brighter areas indicate strong potential for nepheline syenite’s anomalous areas while dark areas suggest areas without nepheline syenite or nepheline mineral.

7.2.11 Spectral pixel matching with satellite image classification

The field spectra for nepheline syenites were used in classification and identification of the rocks using ASTER optical bands. The spectral angle mapper (SAM) Target Finder with BandMax algorithms (Kar et al., 2016; Process et al., 2013), were used to classify nepheline syenite and syenite areas on the ASTER images. The SAM Target Finder with BandMax method is an improvement over the normal SAM (Kar et al., 2016).

The SAM Target Finder with BandMax follows six (6) key steps. Firstly, the input image scene was selected for classification and the required image bands which best show diagnostic features of the nepheline syenite rocks were subset. Secondly, a subset of the ASD field spectra for nepheline syenites were inputted as target spectra for the classification of the ASTER images in the SAM Target Finder with BandMax algorithms. Thirdly, the background spectra or bands were selected to minimise errors. The fourth step was the identification of significant bands for the SAM analysis process and inputting background spectra or bands. The background spectra/bands *subset-out* features or bands which were not necessary for the classification. This was done by inputting mask bands of features which should not be classified by the algorithm, e.g. mask bands for cloud cover, water features, cloud shadow and vegetation. Bands not related to the target spectra could also be subset by manually sub-setting out those bands from the input file in step 1. Vegetation masking removes information associated with both vegetation and nepheline syenites. Therefore, in this method, vegetation was not masked for the TIR data.

Although nepheline syenites showed notable absorption features in ASTER band 4, this band was also omitted to reduce the impact of mapping potassium feldspar rather than nepheline because both nepheline and K feldspar (orthoclase) show key absortion features in band 4. Appendix 7.2 shows the steps for this method, while Appendix 7.3 shows the distinctive features of a subset of nepheline syenite target spectra which were used following steps 1-4 of this method. In the next step, several thresholds were tried for the SAM maximum angle threshold and for this study most nepheline syenites and syenites were classified better using the SAM Target Finder with BandMax’s maximum angle threshold value of 0.085. The final step involved assessment of the results to examine the classification products to evaluate the areas classified correctly using this algorithm.

7.2.12 Data interpretation and validation of results

Assessment methods such as a confusion matrix would have been ideal for accuracy assessment. However, there were no data that could be used as reference targets for accuracy assessment because sufficient reference samples could not be collected from the fieldwork due to limited time of the study. Therefore, to assess the relationships among the different rock types, the NSI (T) values for various areas were randomly selected and extracted from the NSI (T) image results and analysed using box plots.

The results of the NSI (T) and other ASTER image processing were then compared with geological maps produced after the fieldwork in Malawi, the DTM/DEM results and gamma-ray geophysical maps (produced in chapter 5) or other existing published geological information. Shape files were produced using the classification results from the SAM Target Finder with BandMax classification and then overlaid on the geological maps, geophysical maps and digital elevation models produced in chapter 5. Appendix 7.4 provides a summary of the data processing tasks for the ASTER satellite image data. Some regions of interest were randomly selected for different rock types and NSI values were extracted from the NSI (T) images. These areas were then compared to determine if the different rock types could be distinguished from each other and they are shown on Figures in the results section as *selected areas* in Figures 7.23-7.29.

7.3 Presentation of results

7.3.1 Peaks and absorption features of the spectra using absolute reflectance data and first derivatives and for rocks and minerals

The results of smoothed and water-removed field spectra showed that nepheline shows some important absorption features in wavelengths between 950-960nm and about 2240-2260nm while biotite and muscovite show absorption features between 2300-2360nm (Figure 7.2). The nepheline syenites tend to be closely associated with syenites and quartz syenites (Figure 7.2 and Appendix 7.3). This shows that delineation of these silicate rocks, which are also closely similar, geochemically, could be difficult. This agrees with Ferrier et al. (2016) who also noted the difficulty of delineating silicate rocks within the VNIR/SWIR regions. Nepheline syenites show reflectance peaks within wavelength ranges of 500-700nm and 1980-2050nm and distinctive absorption features between 2150-2190nm (Figure 7.1- 7.2 and Appendix 7.5). However, as shown in Figures 7.1 and 7.2, nepheline syenite, alkali granite and syenite rocks have similar reflectance curves which makes distinguishing them from each other based on raw field spectra difficult. Therefore, derivative analysis helped to determine separability of these spectra by analysing the shapes and rates of change in slopes of the spectra and identifying the inflection points of the spectra (Figures 7.3-7.4). The 1st derivatives show the inflection points of the spectra through which the locations of the peaks of the spectra are identified.

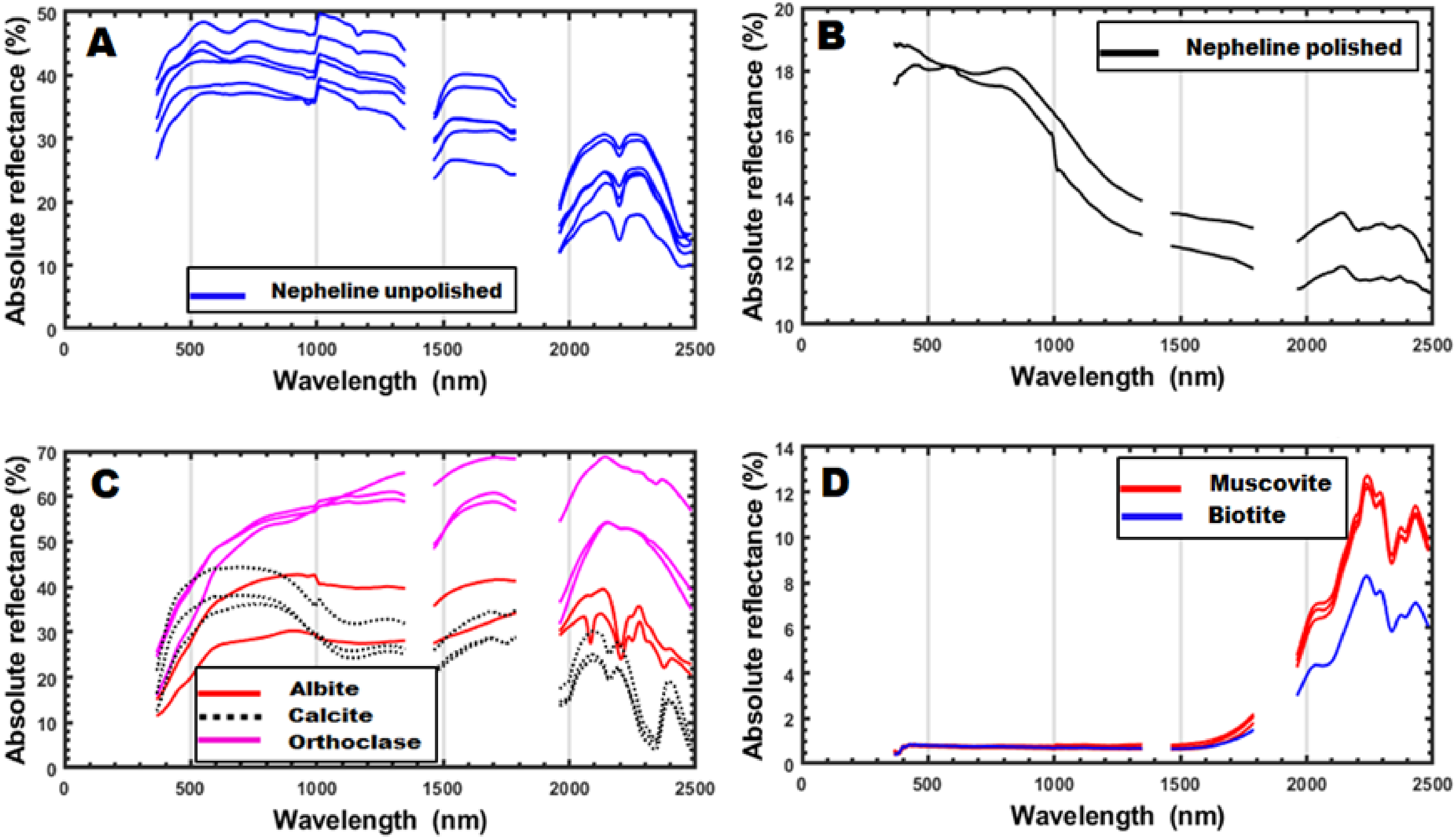

Figure 7.1: Absolute reflectance for smoothed spectra of mineral samples.

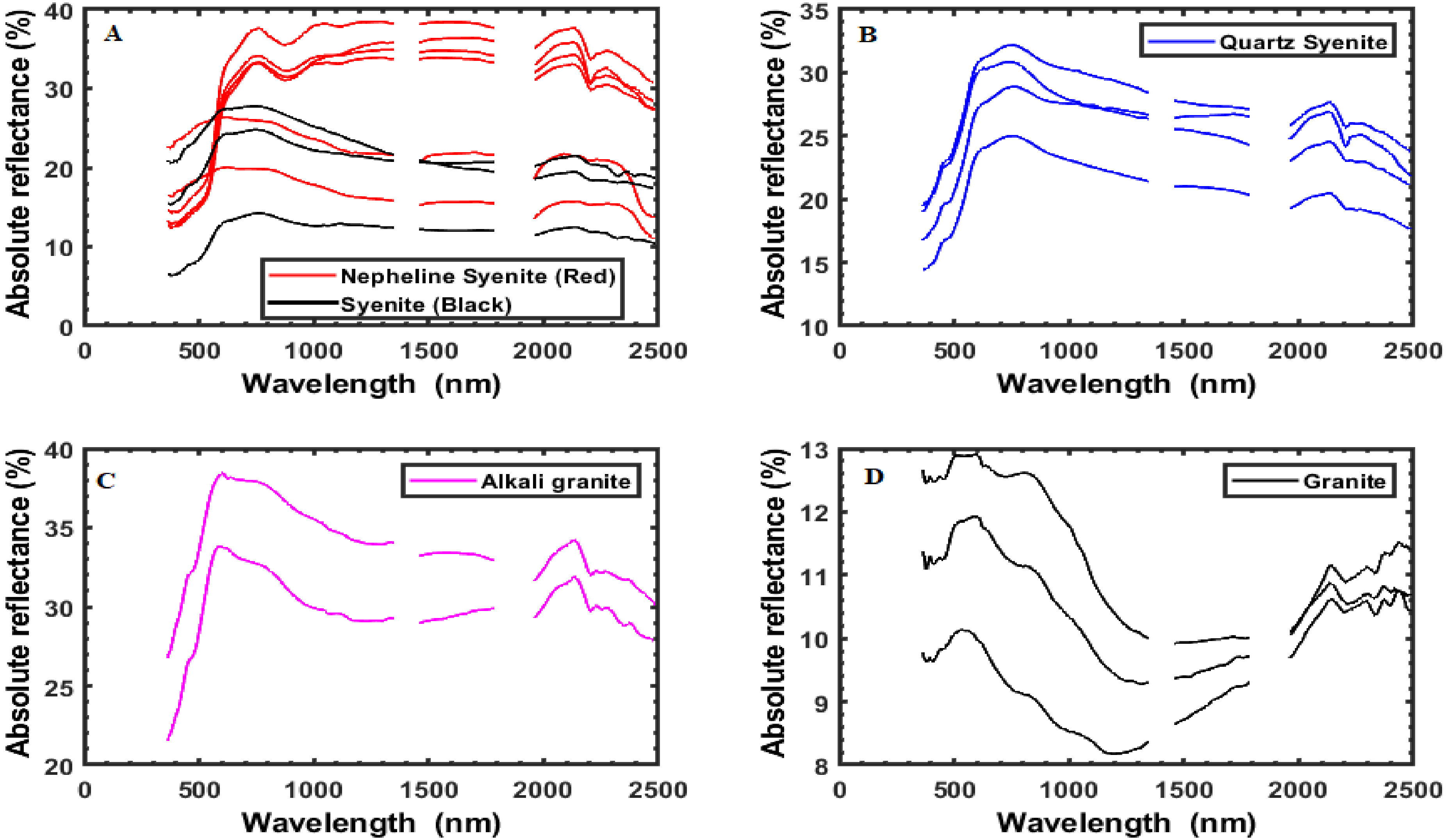

Figure 7.2: Absolute reflectance for selected smoothed spectra of unpolished rock samples collected from the fieldwork in Malawi.

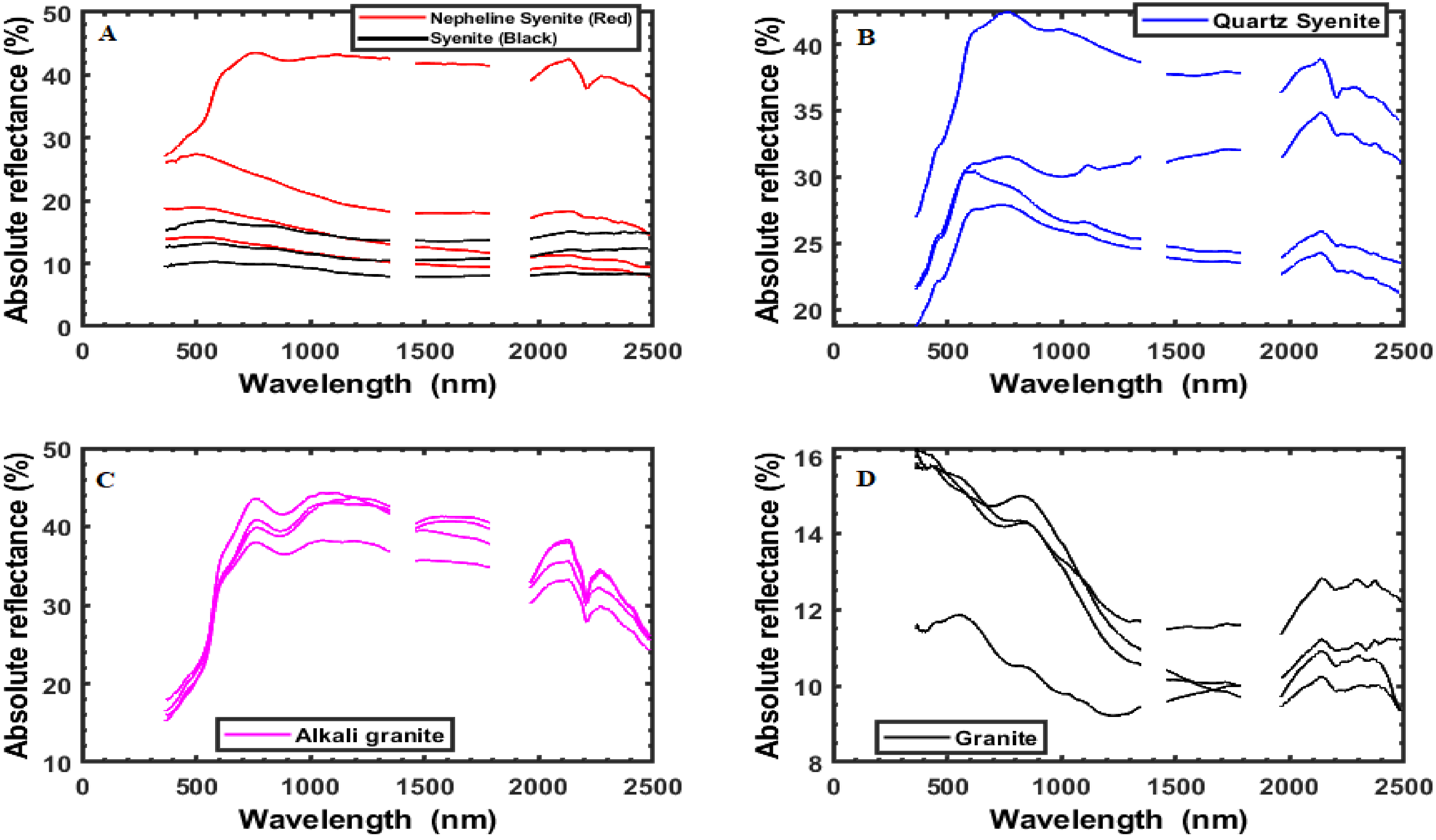

Figure 7.3: Absolute reflectance for selected smoothed spectra of polished rock samples collected from the fieldwork in Malawi.

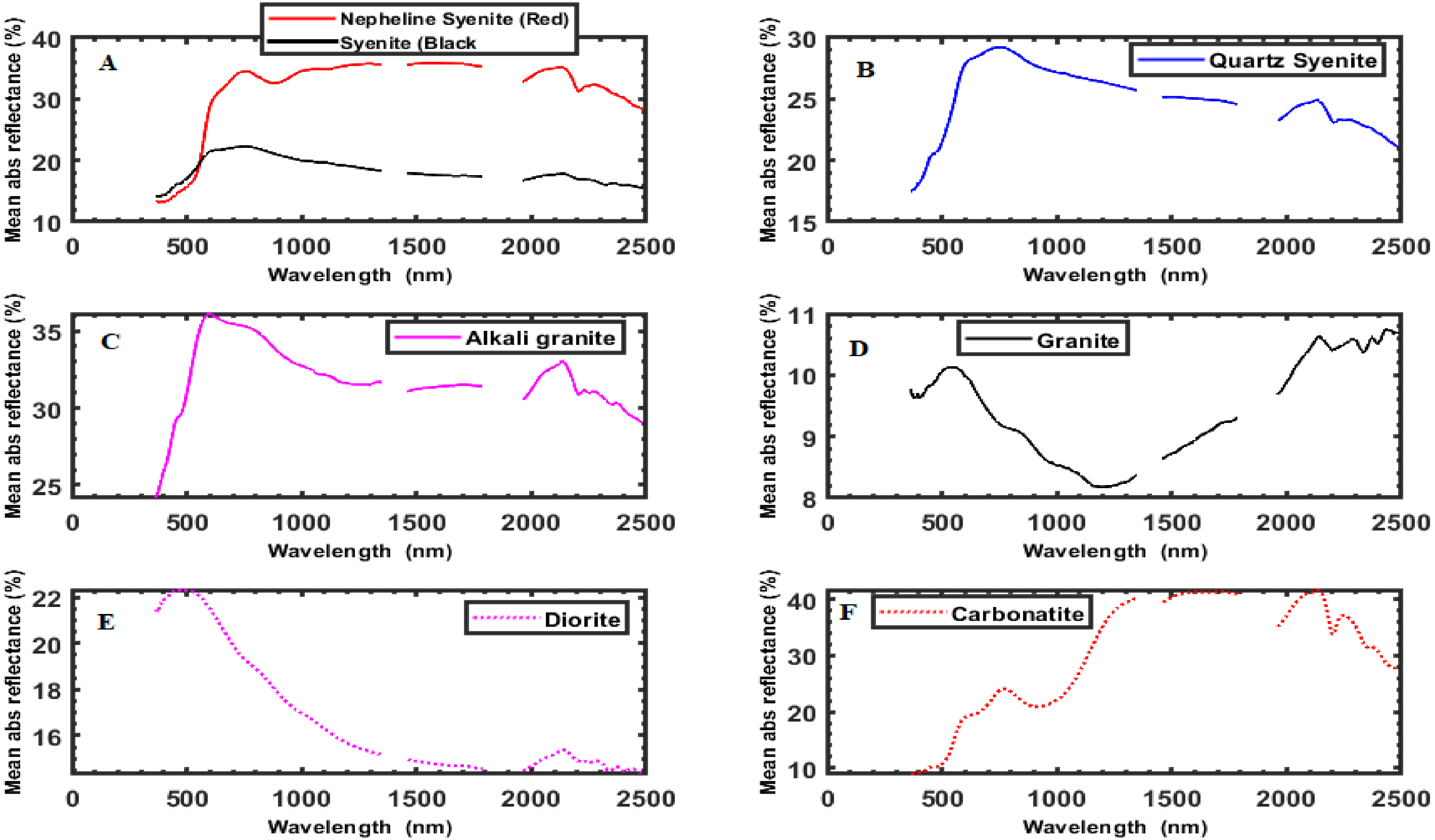

Figure 7.4: Mean absolute reflectance for selected smoothed spectra of polished rock samples collected from the fieldwork in Malawi.

Figures 7.5 and 7.6 show that the rocks and minerals can also be distinguished by assessing the key absorption features and reflectance peaks (Kletetschka et al., 2004) at different wavelengths. The minerals show diagnostic spectral features at several wavelengths in the first derivatives which makes them easier to distinguish. In Figures 7.4A-7.5A and Appendix 7.6, nepheline syenite, syenite and alkali granites show reflectance and diagnostic absorption features between at about 2190nm and show reflectance peaks at wavelengths such as 518nm, 900nm. Figures 7.5B and 7.5C also show that quartz syenites have diagnostic absorption features at 2200nm and 2170nm while alkali granites reflectance peaks occur at reflectance peaks at about 750nm and absorption features at 2250nm in the spectra.

The spectra were tested at each individual wavelength. The wavelengths which were identified as showing separability were those with no overlaps for different minerals or rocks. For example, orthoclase is separable at some wavelengths including 627nm (Figure 7.6A). Polished nepheline, unpolished nepheline and orthoclase spectra show diagnostic separability between 1961-1970nm. Both the polished and unpolished nephelines also overlap with orthoclase and (slightly) albite, but are distinct from other silicate minerals, for example, at 1964nm (Figure 7.6B). Calcite is the most easily distinguishable mineral and it is separable from the other minerals at several wavelengths. This is because calcite is a carbonate unlike the others which belong to the silicate group of minerals.

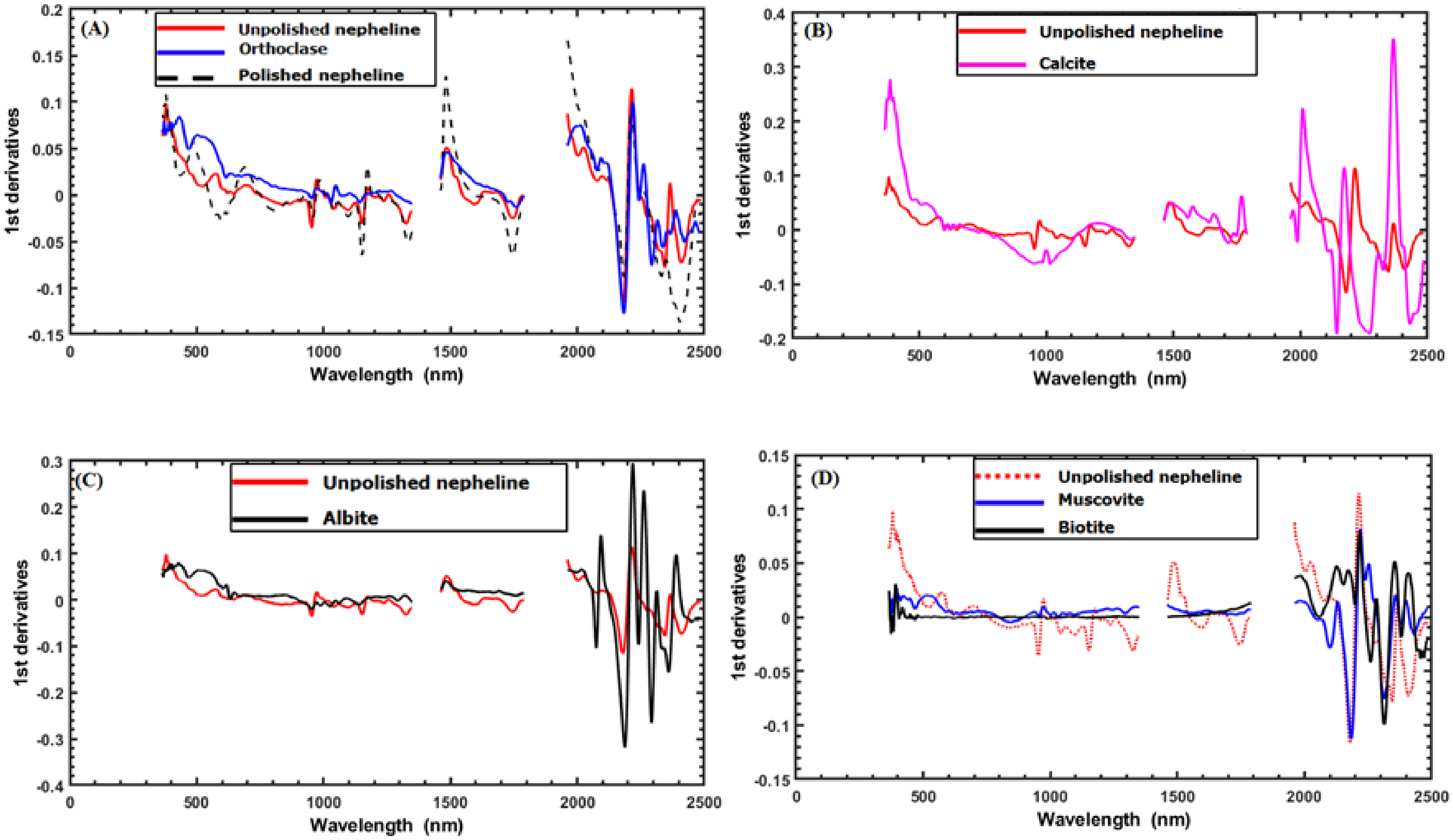

Figure 7.5: 1st order derivatives for smoothed spectra of unpolished nepheline mineral compared with smoothed representative spectra of (a) polished nepheline and orthoclase (b) calcite (c) Albite (d) muscovite and biotite.

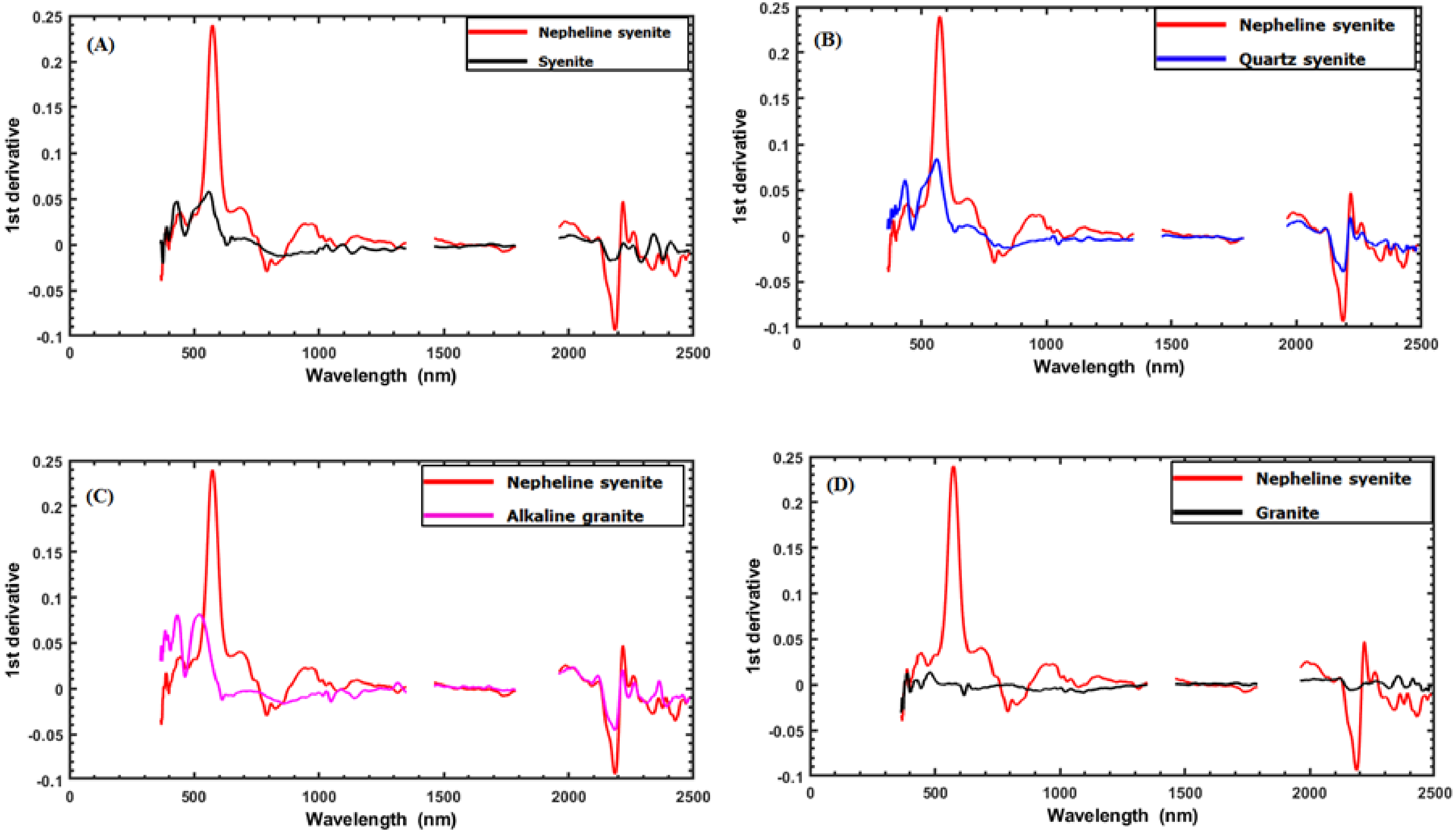

Figure 7.6: 1st order derivatives of smoothed spectra for a subset of selected polished samples of (a) nepheline syenite and syenite (b) Quartz syenite (c) alkali granite (d) granite.

The 1st order derivatives show that carbonatites are easiest to separate from other rocks at various wavelengths. However, several wavelengths showed some overlaps for different rock types especially, nepheline syenite and syenites (Figure 7.8).

The first derivatives also show that rocks can be distinguished from each other using derivative spectroscopy. Carbonates are much easier to distinguish from silicate rocks at several wavelengths as shown for example in Figure 7.7 C & D). The rock spectra show some potential separability at several wavelengths because they have distinctive absorptions features. Appendix 7.7 shows selected wavelengths at which different minerals and rocks were fully or partially separable from the other samples using first derivative data. However, soil spectra were too noisy and showed no clear separability of the different lithologies using soil spectra. This suggests that soil spectra may not suited for discriminating different geological units or there is need for another approach to use with soil spectra.

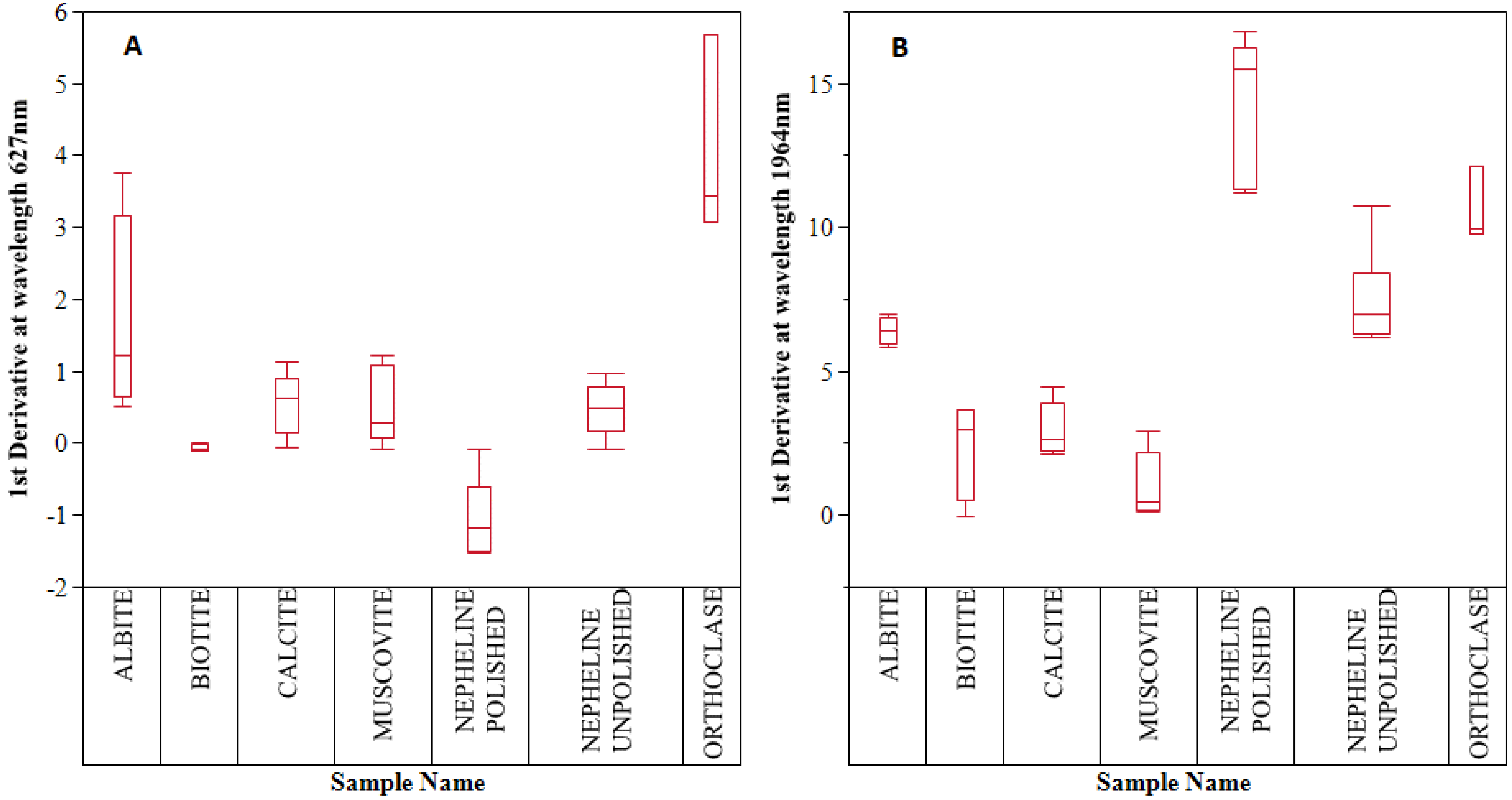

Figure 7.7: Spectral differences in 1st order derivatives (A) orthoclase at wavelength 627nm and (B) both polished and unpolished nepheline and orthoclase at 1964nm, respectively.

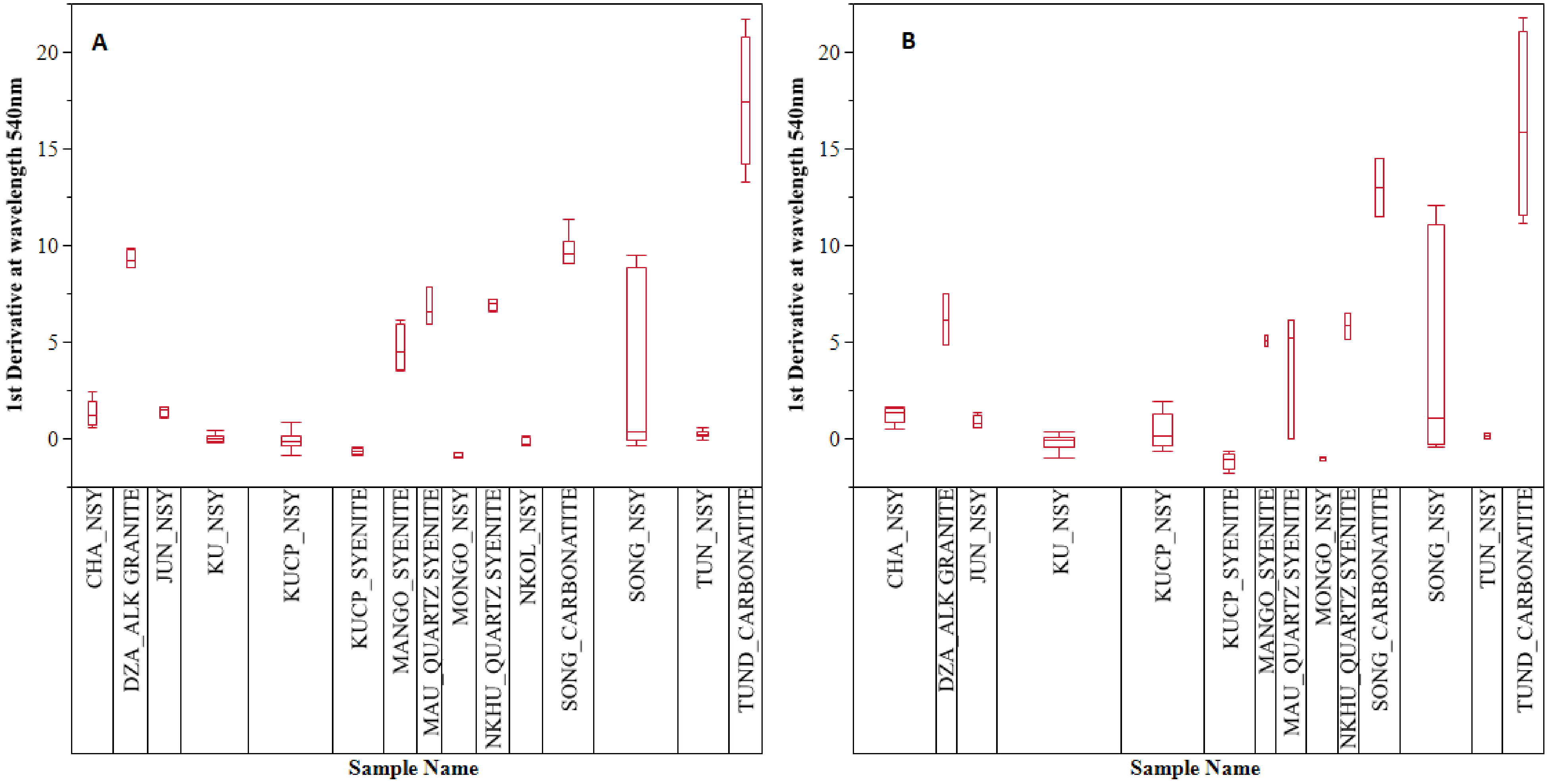

Figure 7.8: Spectral differences of rocks using first order derivatives at 540nm wavelength for (A) polished rocks and (B) unpolished rock samples.

NB: The following sample codes as used in some figure 7.7, denote: DZA= Dzalanyama, MONGO=Mongolowe, CHA=Chaone, JUN=Junguni, KU=Kasungu, KUCP=Kasungu Chipala; NKOL=Nkolonje; MANGO= Mangochi; SONG=Songwe-Mauze; TUNDU= Tundulu, MAU=Mauni, NKHU=Nkhuzi bay; NSY = nepheline syenite, while ALK GRANITE = Alkaline granite.

7.3.2 Diagnostic features for minerals and rocks using second derivative data

In the 2nd order derivatives some diagnostic features for nepheline mineral and nepheline syenite rock spectra are noticeable. For example, the 2nd derivatives show some diagnostic features for both polished and unpolished rocks at wavelength regions at 418nm and 2234nm among others as shown in Figures 7.9-7.10. In Figure 7.9 (A), the spectral features between 1000-1600nm show that orthoclase and nepheline could be difficult to separate unlike at wavelengths between 2300-2450nm.

Similarly, Figure 7.10 shows that nepheline could be distinguished from other minerals mainly between 2300-2460nm (Figure 7.10 (B-D). Nepheline syenite appears to be more separable from syenite around 518nm, 590nm and 2300-2350 (Figure 7.10 (A)). Both polished and unpolished nepheline show clear separability at 1035nm (Figure 7.11A). Albite is separable from other minerals at 2254nm (Figure 7.11B). However, both nephelines overlap with the micas at some wavelengths such as 1035nm (Figure 7.9A). These overlaps show possible challenges that could be faced in classifying nepheline syenites from other rocks. In addition, Figure 7.12 (A) shows that carbonatites are separable from other rocks at wavelength 518nm and alkaline granites 2210nm. However, nepheline syenites overlap with one or more of the other felsic rocks and this makes it difficult to delineate nepheline syenites from other rocks. This suggests that the mineral composition of these rock samples could be very similar because the rock spectra are, mostly, controlled by the petro-geochemistry of the rocks. Appendix 7.8 shows selected wavelengths at which different rock samples collected from the fieldwork were fully or partially separable from the other samples using first derivative data. Carbonates, alkali granites and quartz syenites were more separable than nepheline syenites and syenites.

However, at most wavelengths there were some overlaps for different rock types which showed that clear full separability of these rock types especially nepheline syenite and syenites is not easy. The soil spectra were also not effective for discriminating the different lithologies. This could be because the spectra were too noisy to be used for the classification or alternatively there is need to try other methods using soil data.

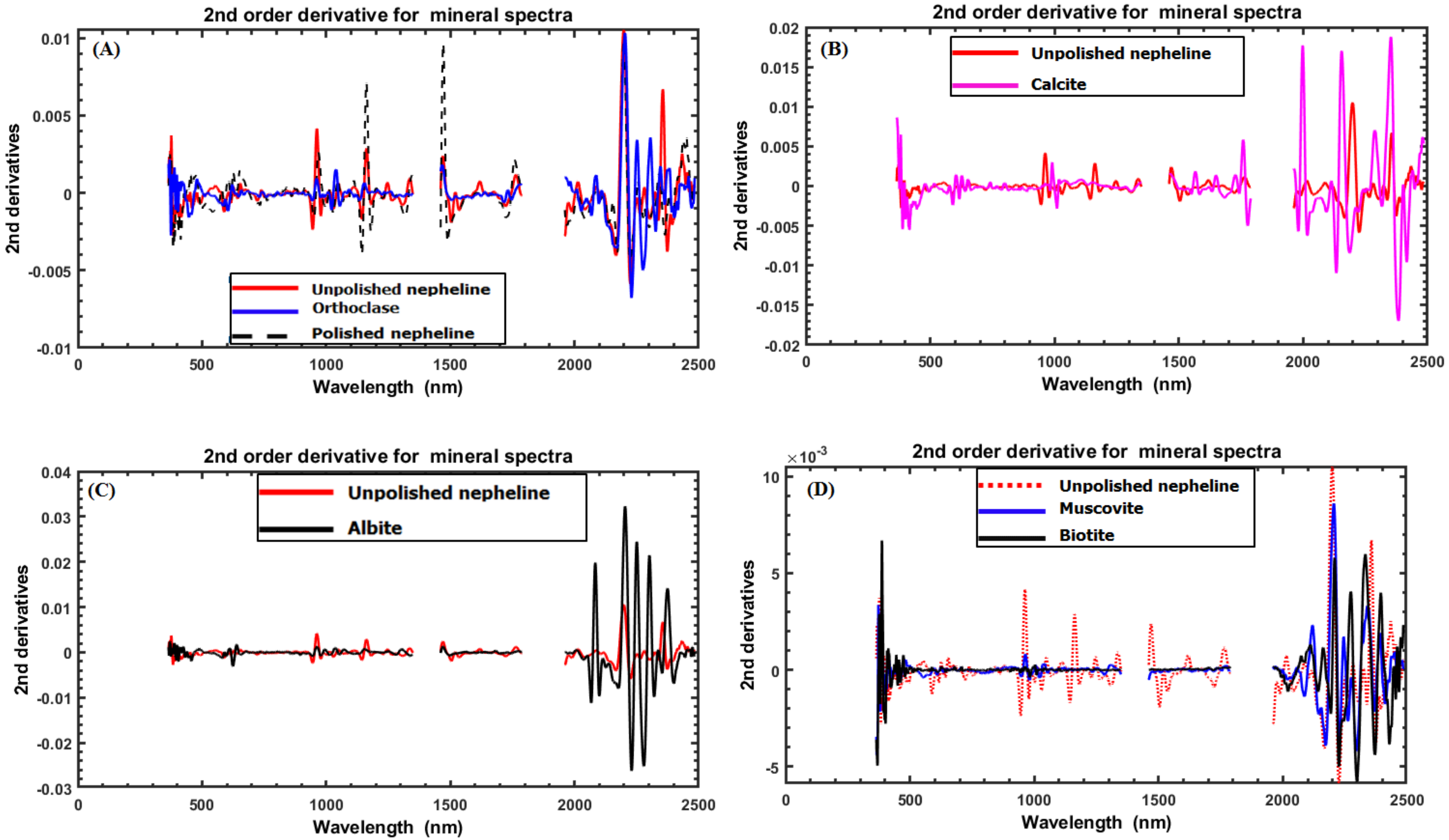

Figure 7.9: 2nd order derivatives for smoothed spectra of unpolished nepheline mineral compared with smoothed representative spectra of (a) polished nepheline and orthoclase (b) calcite (c) Albite (d) muscovite and biotite.

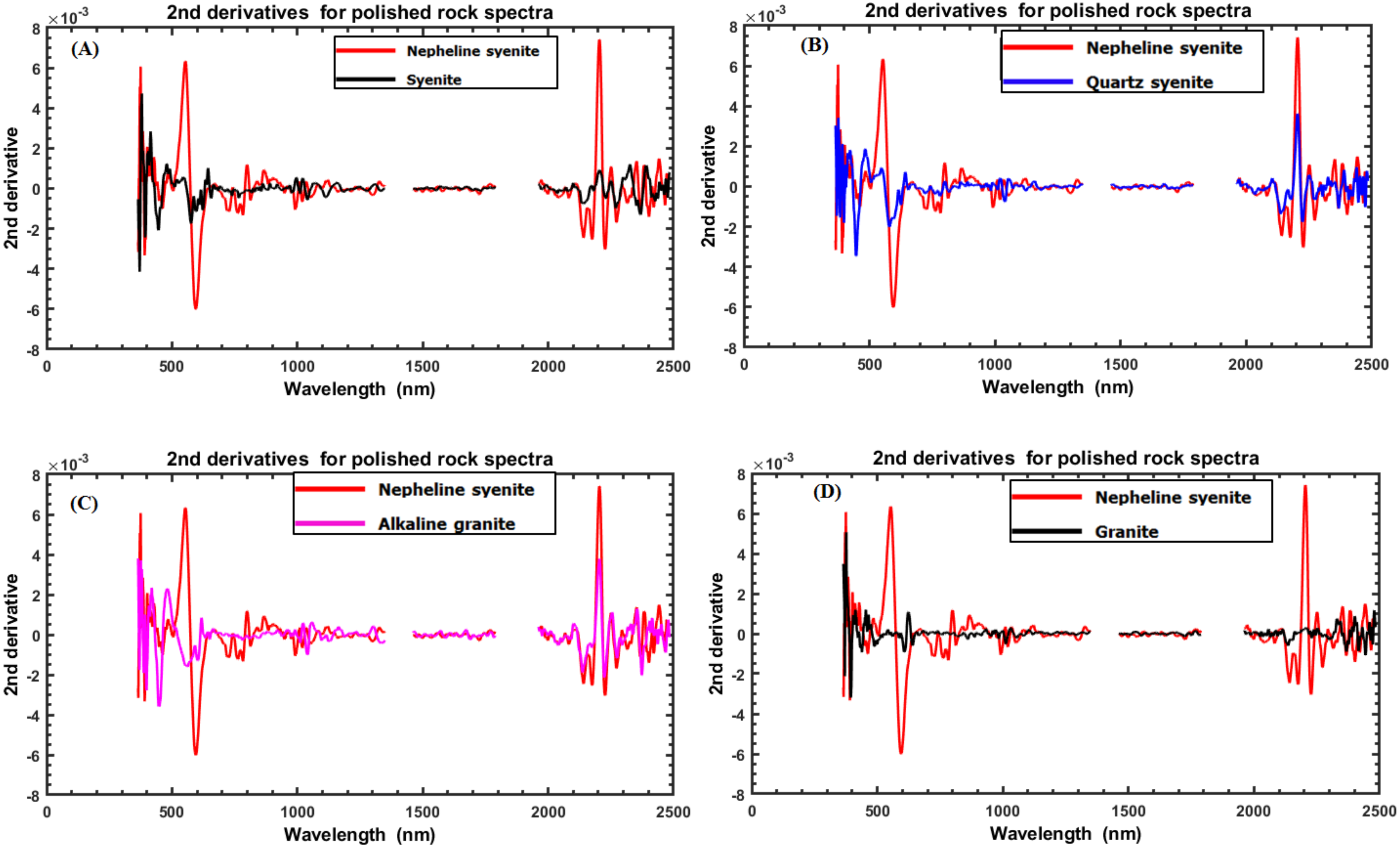

Figure 7.10: 2nd order derivatives for smoothed spectra unpolished for representative smoothed unpolished spectra of (a) nepheline syenite (b) Quartz syenite (c) alkali granite (d) granite.

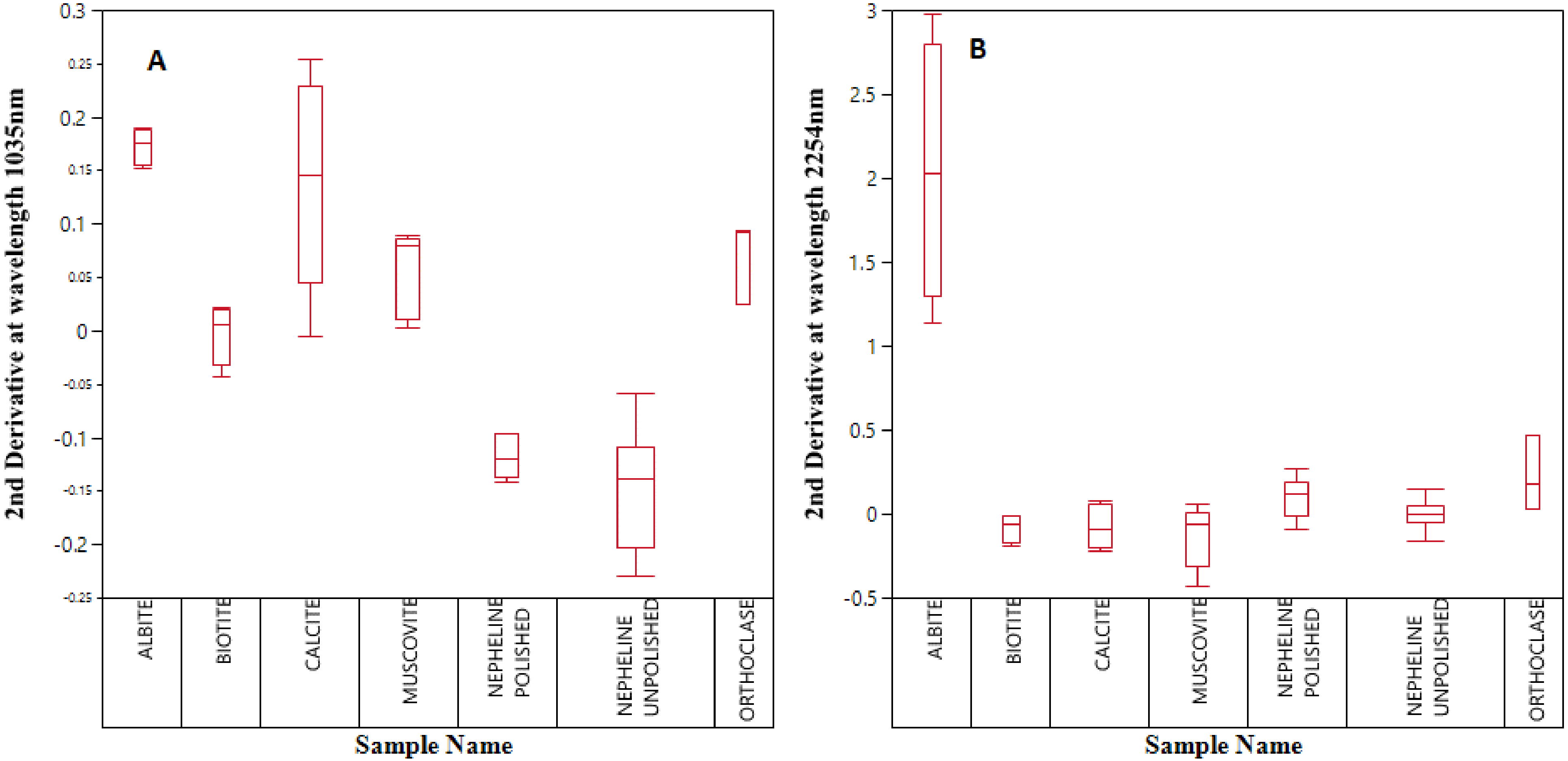

Figure 7.11: Second derivative separability by absorption pattern for (A) polished and unpolished nepheline at wavelength 1035nm, and (B) albite at wavelength 2254nm, respectively.

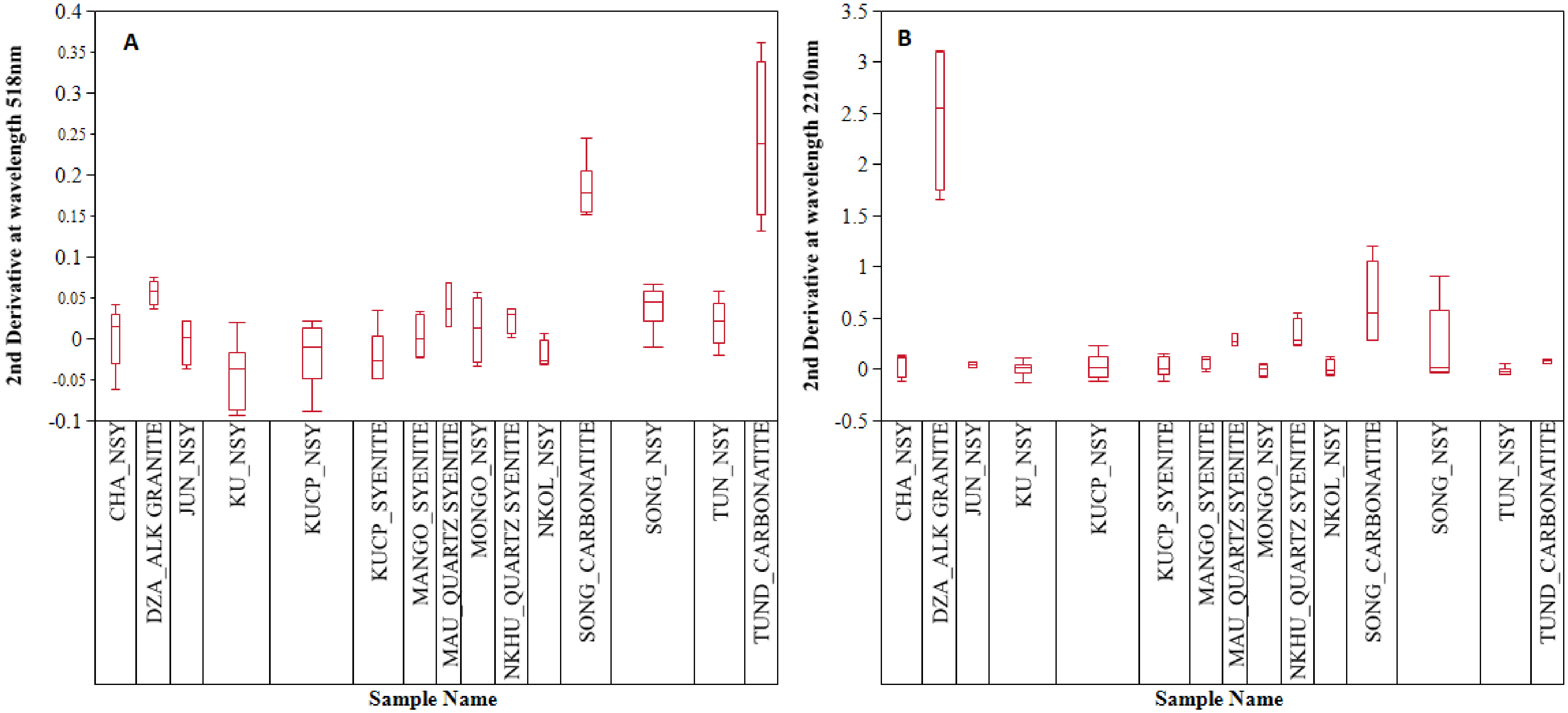

Figure 7.12: Second derivatives for polished rocks at wavelength 518nm and 2210nm. (A) shows that carbonatites are separable from silicates rocks at wavelength 2210nm while (B) shows that alkaline granites are from the other rocks at wavelength 2210nm. Nepheline syenites (Nsy) overlap with other rocks, and they mostly fall below the above the not separable. Unpolished rock samples show similar results at wavelength 518 but no separability at 2210nm.

NB: The following sample codes as used in some figure 7.7, denote: DZA= Dzalanyama, MONGO=Mongolowe, CHA=Chaone, JUN=Junguni, KU=Kasungu, KUCP=Kasungu Chipala; NKOL=Nkolonje; MANGO= Mangochi; SONG=Songwe-Mauze; TUNDU= Tundulu, MAU=Mauni, NKHU=Nkhuzi bay; NSY = nepheline syenite, while ALK GRANITE = Alkaline granite.

7.3.3 Field spectra resampled to ASTER satellite bands

The field spectra resampled to ASTER bands showed that nepheline mineral and nepheline syenites rocks portray diagnostic absorption features at wavelengths of 900nm, between 2254-2290nm and 2354nm. The wavelengths correspond to ASTER bands 3, band 6 and band 8 respectively, which suggests that these bands could be useful for classifying nepheline syenites and other alkaline rocks. Carbonatite and granite rocks do not show distinctive diagnostic spectral features in bands 3 and 4 which make it much easier to separate them from the alkaline rocks. Figure 7.13 shows field spectra resampled to ASTER for different rocks including nepheline syenites. Figure 7.13 show that diagnostic absorption features for nepheline syenite occur at 1650nm (B4) and 2207nm (B6) and some reflectance peaks in bands 5 and 7. In addition, some alkaline rocks also show absorption features in Bands 4, and 6 which explains the potential difficulty in discrimination of the rocks from each other. This is because alkaline rocks and nepheline syenites contain potassium feldspars as key minerals.

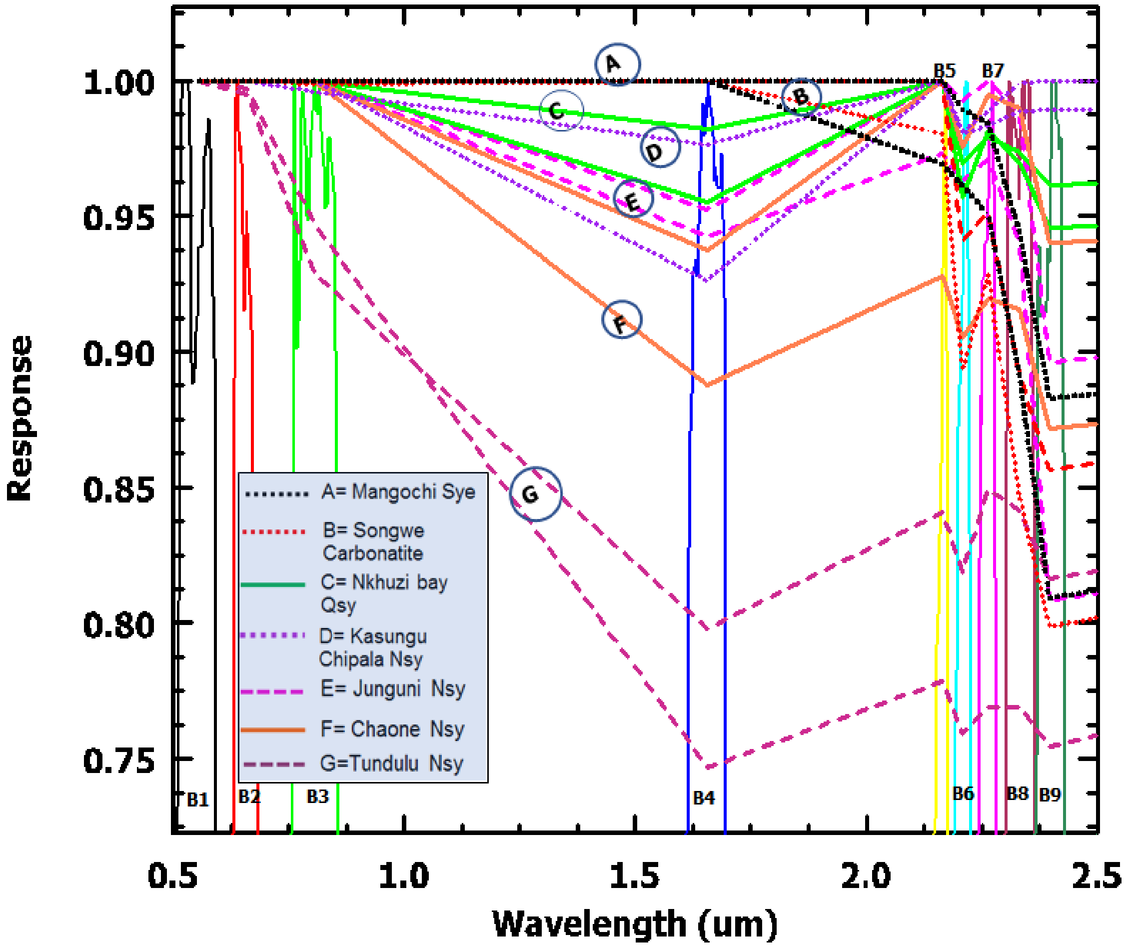

Figure 7.13: A subset of field spectra resampled to ASTER, continuum-removed and overlayed on ASTER bands (B1-B9). The spectra are from (A): Mangochi syenite, (B): Songwe carbonatite, (C): Nkhuzi bay quartz syenite, (D): Kasungu-Chipala nepheline syenite, (E): Junguni nepheline syenite, (F): Chaone nepheline syenite (G): Tundulu nepheline syenites.

Geochemically, nepheline ($KNa_3Al_4Si_4O_{16}$) is closely associated with the K-feldspars, especially, orthoclase ($KAlSi_3O_8$), because they both have K atoms in their mineral chemistry. Orthoclase also shows relatively similar absorption features to nepheline in band 6. Unlike nepheline, orthoclase does not show notable features in band 3 which suggests that combining bands 6 and 3 could separate nepheline syenites from other rocks (Appendix 7.8). Nepheline and orthoclase are very similar and are therefore difficult to separate in bands 4 and 6 (Figures 7.14 and 7.15).

Based on the resampled data, bands 3, 4, 5, 6 and 8 were identified as being potentially useful for mapping nepheline syenites. However, band 4 is usually associated with mapping phyllic minerals, such as smectite and sericite, and potassic alteration in composite band combinations of RGB:4, 6 and 8 (Di Tommaso & Rubinstein, 2007; Feizi & Mansouri, 2014). Therefore, considering that the rocks were generally altered, nepheline syenites could be mapped using ASTER band combinations RGB: 3, 6 and 8 (Appendix 7.9). This was done to minimise the possibility of mapping other alteration, especially phyllic minerals, instead of nepheline bearing rocks.

In spectra from the USGS spectral library (Clark, 2004) for the thermal region, nepheline syenite and nepheline mineral show diagnostic emissivity minima in Band 12, at 9.297μm for nepheline syenite and at 9.225μm for nepheline, respectively (Figure 7.14). The other felsic rocks, especially granite and alkali granite, show diagnostic emissivity minima in Band 11 at 8.512μm and they show high emissivity in Band 12 at wavelengths where the nepheline syenite and nepheline mineral show emissivity minima.

Figure 7.14 shows that nepheline syenite and orthoclase mineral have emissivity maxima in Band 11 while nepheline mineral has emissivity maxima in Band 12. These two ASTER bands are, therefore, vital for mapping nepheline syenites using TIR data. In Band 11, both nepheline syenite and orthoclase show high emissivity but for nepheline the response begins to increase sharply. Band 12 shows emissivity minima for nepheline syenite at 9.297 μm and for nepheline at 9.2245μm. Orthoclase is also a key mineral in alkaline rocks which makes their separation uneasy.

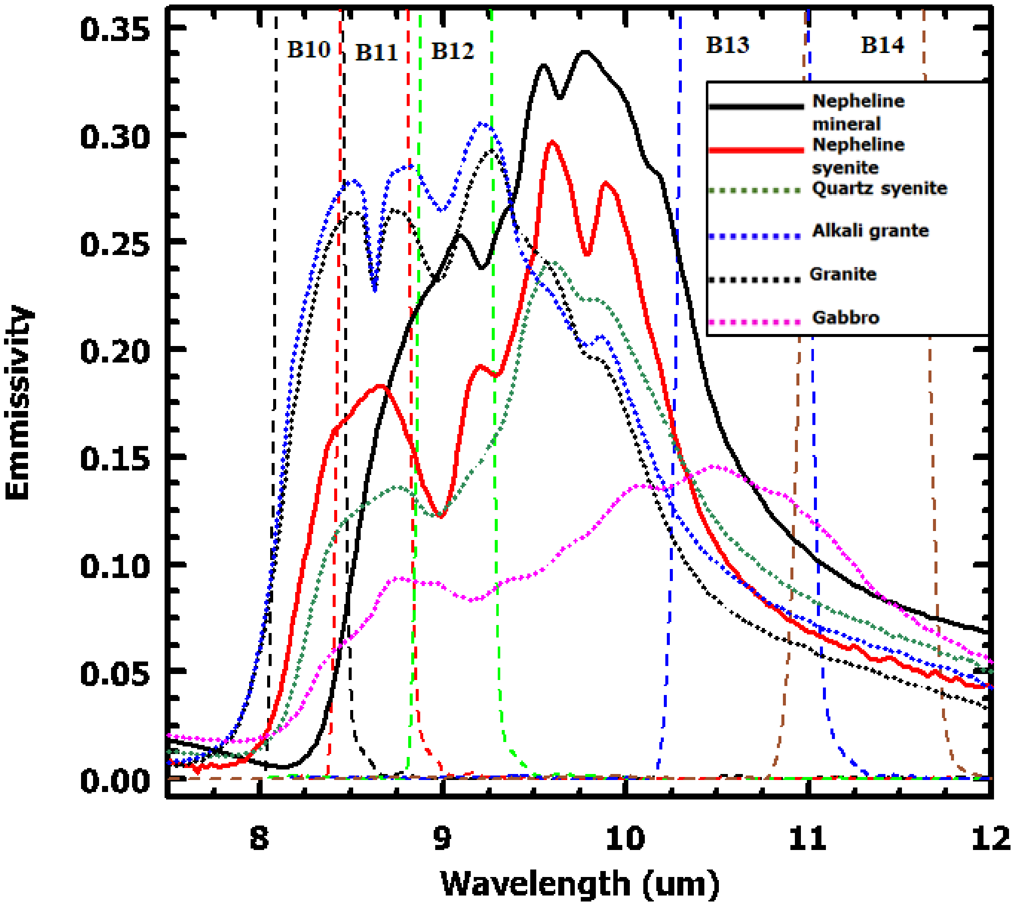

Figure 7.14: Emissivity response of some selected rocks' spectra and nepheline mineral (as accessed from Clark, 2004) and superimposed on ASTER TIR bands (B10-B14).

All the three samples in Figure 7.14 (above), show low response in ASTER band 10. This suggests the ASTER 11 and 12 are important for discrimination of nepheline syenites. The emissivity maxima for both orthoclase and nepheline syenite in Band 11 also suggests that nepheline syenites spectral response is affected more by the K (orthoclase) composition rather than nepheline mineral which shows emissivity maxima in Band 12. This possibly explains why other rocks of the syenite family, notably syenites and quartz syenites (Figure 7.14), are difficult to distinguish from nepheline syenites using ASTER data. The resampled spectral data in Figure 7.15, shows that nepheline syenite and orthoclase mineral have emissivity maxima in Band 11. Nepheline has emissivity maxima in Band 12. This is important because it suggests that these two TIR bands (Band 11 and Band 12), could help to discriminate nepheline from orthoclase.

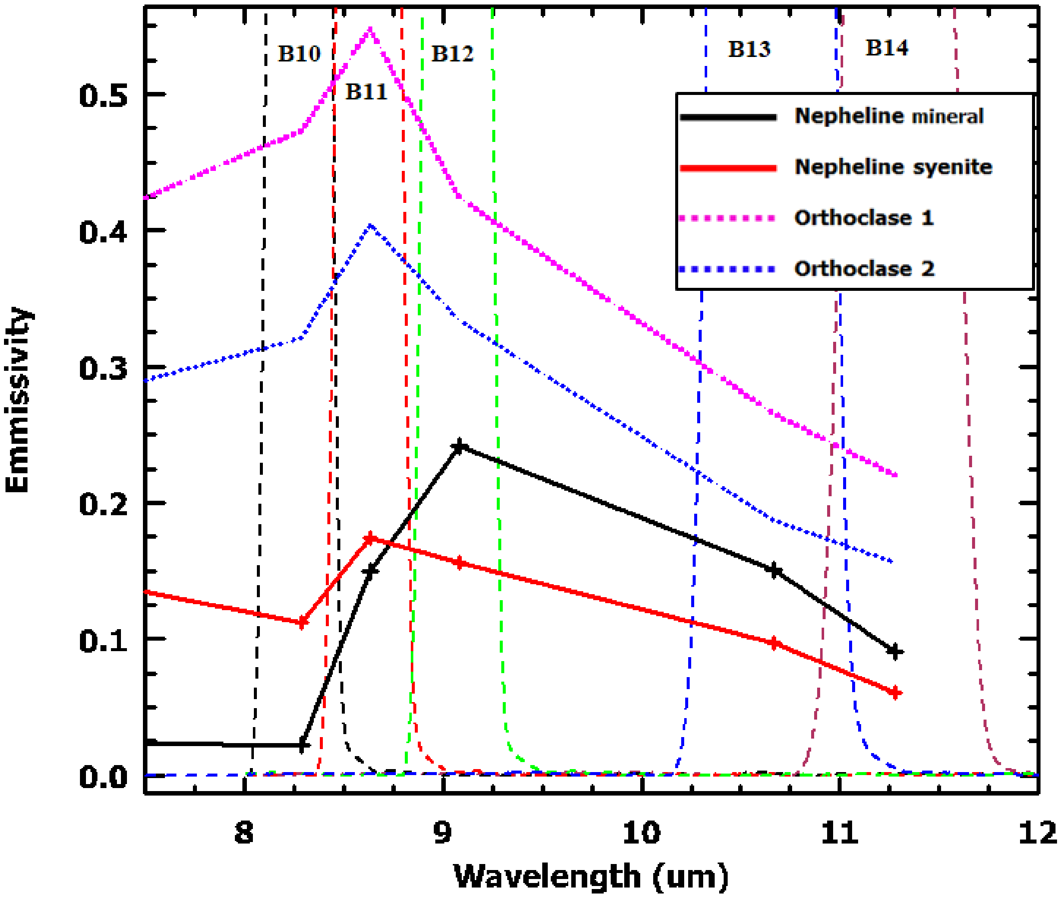

Figure 7.15: Spectra for nepheline syenite, nepheline and orthoclase minerals (accessed from Clark, 2004) resampled to and overlayed on ASTER TIR Band 10 to Band 14.

7.3.4 Spectral indices for geological mapping

The ASTER band composite combinations and nepheline syenite spectral index using optical bands could not separate the nepheline syenites reliably. This was because of the masking of vegetation which also removed subtle geological infromation. For example, based on the resampled ASD data bands, ASTER composite band combinations RGB:3, 6, 8 may be used for identifying some nepheline syenite/syenite areas. Figures 7.16-7.19 show some of the areas delineated using the NSI (T). These include some areas which were sampled during the field work. The names of the rock types' naming system used in this section is based on the geochemical classification, which in turn is based on geochemical and petrological analyses and classification systems as outlined in chapter 6 (for example, Figure 6.3) and in some cases the published geological maps of the Malawi Geological Survey. The term 'possible/potential nepheline syenites', as used in this thesis, describes rocks which show features of nepheline syenites from the remote sensing and gamma ray data, but they have not been confirmed by geochemical data. However, in Figure 7.17 (below), some areas in the lake, for example, north of area 3, exhibit characteristics of potential nepheline syenite/syenite targets. These may be false positives or may also suggest incomplete masking of the water body feature using the threshold value that was applied for masking the water bodies. A higher threshold value was not used because this could remove other areas which were not water body features.

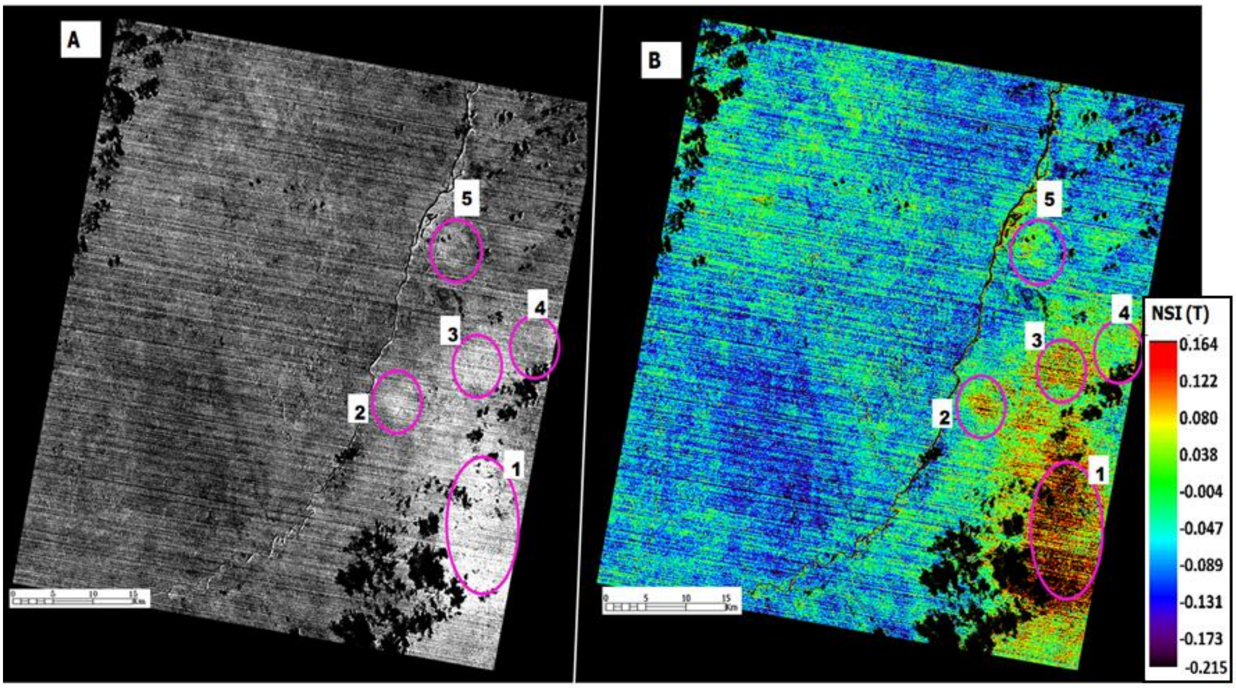

Figure 7.16: (A) Grayscale and (B) color-coded image of areas delineated using NSI (T) for the south Malawi intrusions namely (1) Zomba Mt syenite (2) Chinduzi (3) Mongolowe-(4) Chaone (5) Junguni nepheline syenites. NSI (T) values for the known and potential nepheline syenite areas range between 0.038-0.164.

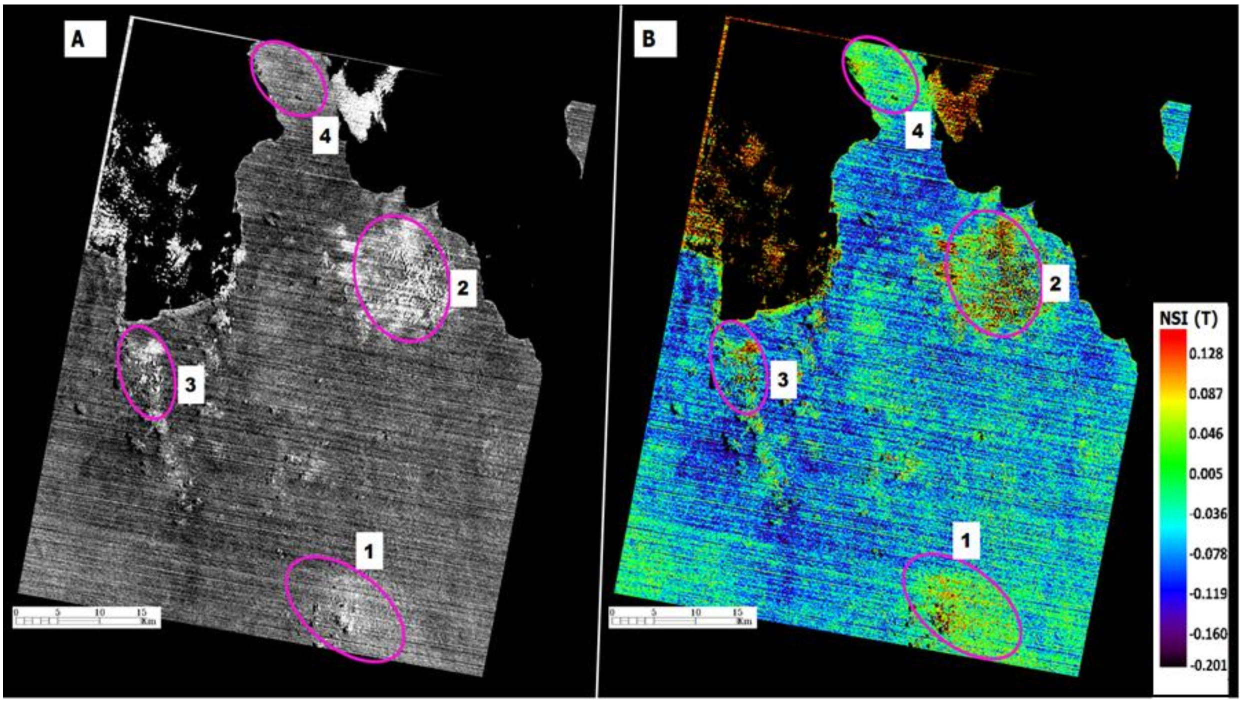

Figure 7.17: (A) Grayscale and (B) color-coded image of areas delineated using NSI (T) for the south east Malawi quartz syenites namely (1) Mauni Southwest area (2) Nkhuzi bay, (3) Chantulo west and (4) Monkey bay area intrusions. Syenite and quartz syenite shows that NSI (T) values range between 0.005-0.128.

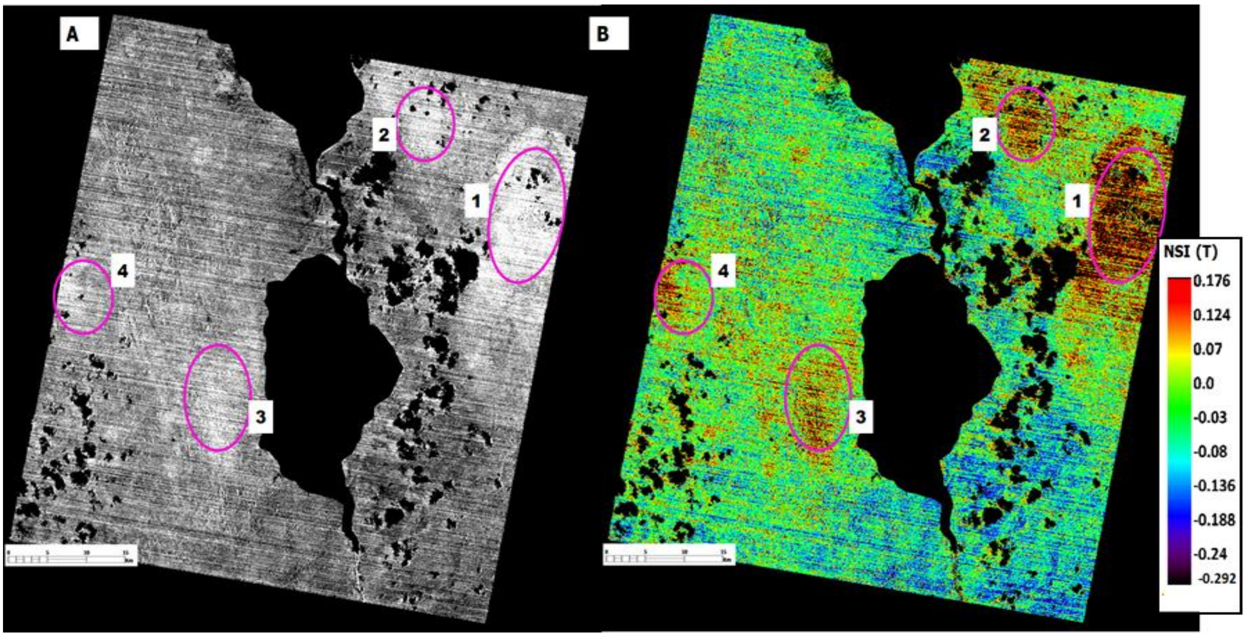

Figure 7.18: *(A) Grayscale and (B) color-coded image of areas delineated using NSI (T) for south Malawi's Mangochi Hill syenite areas namely (1) Mangochi Hill syenite (2) Mangochi east intrusions (3) Lake Malombe West (4) Lake Malombe north west intrusions. Potential nepheline syenite/ syenite areas show NSI (T) values between 0.70-0.80 while quartz syenite syenite/nepheline syenite show lower values between 0.45-0.70.*

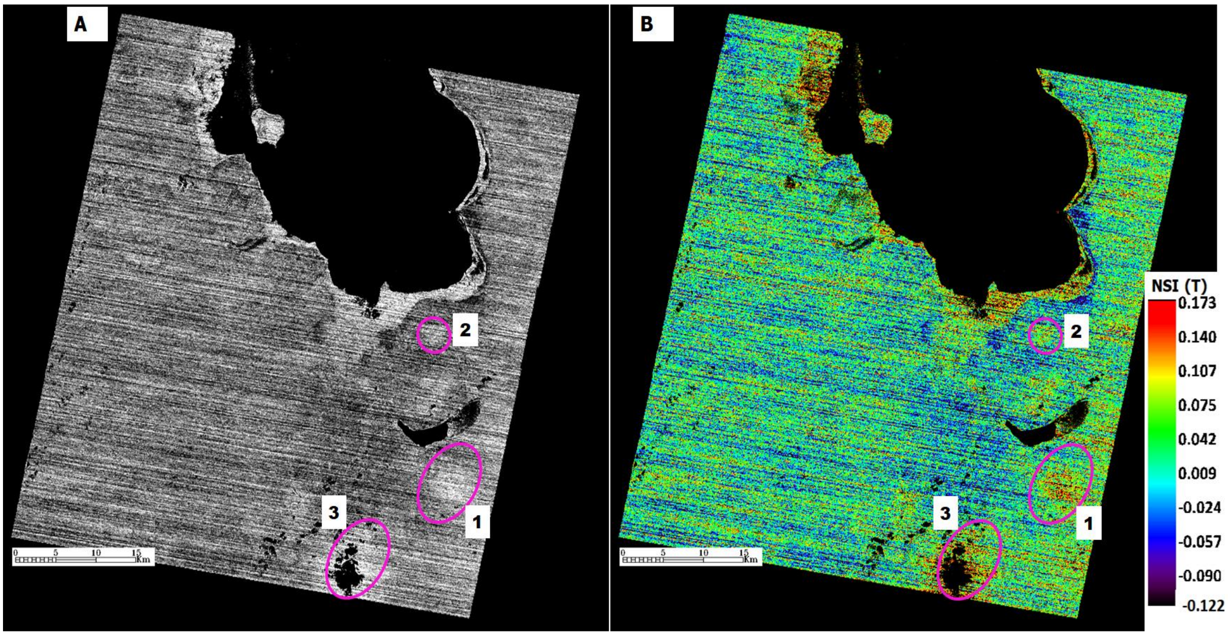

Figure 7.19: NSI (T) (A) Grayscale and (B) colour-coded images for carbonatite-associated nepheline syenite (1) Songwe-Mauze (2) Tundulu and (3) Songwe-Mauze South west complexes. Known and potential nepheline syenite areas show NSI (T) values ranges between 0.038-0.164.

Figures 7.20 and 7.21 show NSI (T) differences for some rock units which were randomly extracted from the NSI (T) images as shown by the *selected areas* as described in Table 7.2 Comparisons of the rock units showed that silica undersaturated rocks notably have higher

NSI (T) values. The names of the rock units are based on the associated geology map of the areas. The nepheline syenites have NSI (T) means above threshold value of -0.035. The mean values for nepheline syenites range from -0.033 to -0.004. The absolute NSI (T) values for nepheline syenites range from -0.065 to -027.

The results in Figures 7.16-7.19, show that absolute NSI (T) values for the nepheline syenites differ from one area to another. The absolute NSI (T) values can be normalised on a scale of 0 to 1. The results show that the nepheline syenites, generally, range from 0.75 to ≥0.95, while the quartz syenites and syenites range between 0.4 to ≥0.70. These NSI (T) values would be expected to decrease more for non-alkaline nepheline deficient rocks. Therefore, the theoretical assumption for finding other nepheline syenite intrusions would be to consider rocks with (NSI (T) normalised values ≥0.80 on after normalising the absolute values on a scale of 0-1could possibly be nepheline syenites.

Table 7.2: Description of some selected areas for comparison of NSI (T) values

Area of study	**Selected area number on Figure. and name**	**Figure referred**	**Rock nomenclature basis**
S. Malawi nepheline syenites	Zomba syenite (1)	Figs 7.26 & 7.27	This study's whole rock geochemistry (chapter 6)
S. Malawi nepheline syenites	Chinduzi Nsy (2)	Figs 7.26 & 7.27	Existing geological map
S. Malawi nepheline syenites	Mongolowe Nsy (3)	Figs 7.26 & 7.27	This study's whole rock geochemistry (chapter 6)
S. Malawi nepheline syenites	Chaone Nsy (4)	Figs 7.26 & 7.27	This study's whole rock geochemistry (chapter 6)
S. Malawi nepheline syenites	Junguni Nsy (6)	Figs 7.26 & 7.27	This study's whole rock geochemistry (chapter 6)
S. Malawi nepheline syenites	Chinduzi N. West (7)	Figs 7.26 & 7.27	Existing geological map
S. Malawi nepheline syenites	Zomba gneisss (8)	Figs 7.26 & 7.27	Existing geological map
South east quartz syenites	Nkhuzi Bay Qsy (1)	Figs 7.28 & 7.29	This study's whole rock geochemistry (chapter 6)
South east quartz syenites	Monkey bay area (4)	Figs 7.28 & 7.29	Existing geological map
South east quartz syenites	Nkhuzi Bay Sw area (5)	Figs 7.28 & 7.29	Existing geological map
South east quartz syenites	Chantulo gneiss (7)	Figs 7.28 & 7.29	Existing geological map
Mangochi syenite area	Mangochi Hill syenite (1)	Figs 7.32 & 7.33	This study's whole rock geochemistry (chapter 6)
Mangochi syenite area	Mangochi Granite /syenite (2)	Figs 7.32 & 7.33	Existing geological map
Mangochi syenite area	L Malombe North (3b)	Figs 7.32 & 7.33	Existing geological map
Mangochi syenite area	L Malombe East (4b)	Figs 7.32 & 7.33	Existing geological map
Mangochi syenite area	L Malombe W area (5)	Figs 7.32 & 7.33	Existing geological map
Carbonatite-associated nepheline syenites	Tundulu Nsy (1)	Figs 7.34 & 7.35	This study's whole rock geochemistry (chapter 6)
Carbonatite-associated nepheline syenites	Songwe-Mauze Nsy (3)	Figs 7.34 & 7.35	This study's whole rock geochemistry (chapter 6)
Carbonatite-associated nepheline syenites	Songwe-Mauze Sw Nsy (4)	Figs 7.34 & 7.35	Existing geological map
Carbonatite-associated nepheline syenites	Nkalonje Nw (5)	Figs 7.34 & 7.35	Existing geological map

The mean threshold for nepheline syenites was about -035 NSI (T) value. The Zomba syenite (1) and Chinduzi area (2) rocks (Figure 7.16 and 7.23), are mapped as syenites. In Figure 7.20

the Zomba syenite (1) and Chinduzi area (2) rocks show characteristics of nepheline syenite. On the existing geological map, the Chinduzi is indeed mapped as a nepheline syenite while Zomba Mountain is mapped as syenite. This suggests some parts of Zomba Mountain could be nepheline syenites or else this suggests some syenites are easily mapped as nepheline syenites.

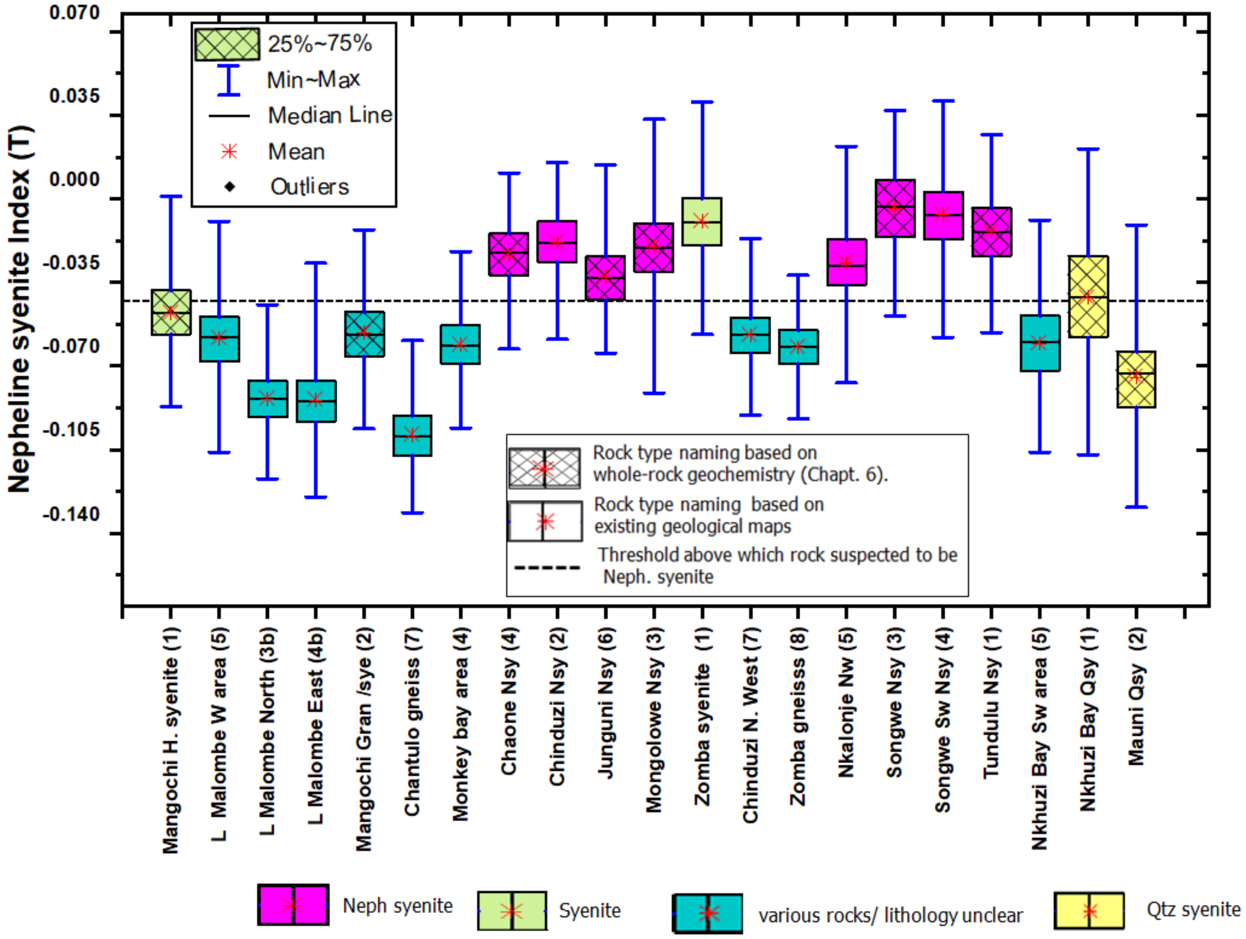

Figure 7.20: Boxplots for the NSI (T) for the different randomly sampled rocks in this chapter. Nepheline syenites show higher mean NSI (T) values followed by syenites then granites and gneisses.

Figure 7. 21 shows the box and whisker plots for nepheline syenites only. Two main groups were identified in chapter 6 based on the R1-R2 (De la Roche et al., 1980) classification of igneous rocks. Figure 6.3 showed that Junguni, Tundulu, Mongolowe and Chaone nepheline syenites can be classed into group (A) which is characterised by high normative nepheline and orthoclase content. However, in Figure 7.21 the NSI (T) results slightly agree with Figure 6.3.   The NSI (T) results generally show that there are some overlaps with other nepheline syenites which fall into Group B of R1-R2 (De la Roche et al., 1980) classification of igneous rocks. The NSI (T) results show that there is no clear disnticntion between the two groups which futher suggests that these nepheline syenites may have similar geochemistry.

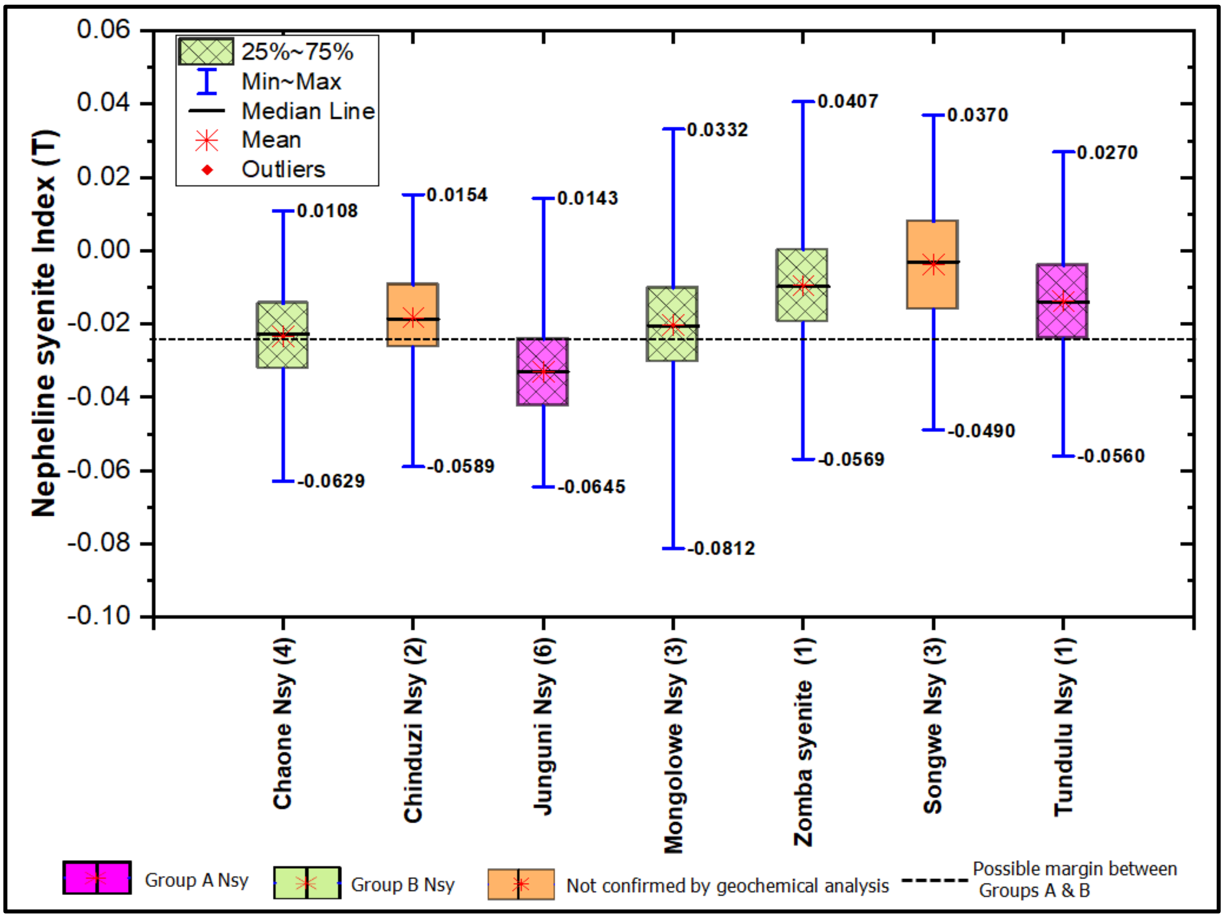

Figure 7.21: Boxplots for the NSI (T) for nepheline syenites only sampled rocks in this chapter (see Figures 7.23-7.29).

7.3.5 Spectral pixel matching with satellite image classification

Thirty-three endmembers of nepheline syenite ASD field spectra from various areas of this study's fieldwork were used as target spectra (reference spectra) for ASTER satellite image classification. Classification of optical bands of ASTER images using composite band combinations and the Nepheline Syenite Index for optical bands (the NSI (O)) did not yield reliable results because locally known and potential nepheline syenite areas were not effectively delineated by these methods. This was probably because most areas of the known nepheline syenite occurrences were also covered by vegetation which was masked. Therefore, masking the vegetation resulted in some information for nepheline syenites being removed.

The SAM Target Finder with BandMax algorithm, attempted to classify most of the key areas using the ASTER VNIR-SWIR data. The results of the SAM Target Finder with BandMax show good agreement with the results of the NSI (T) processing and results from ASTER GDEM/DTMs and airborne gamma ray spectrometry. For example, Figure 7.25 shows that most of the areas identified using the NSI (T) are also delineated by the SAM Target Finder with BandMax classification. In these figures, the areas in the circles were also delineated using the NSI (T) image processing as shown earlier in Figures 7.16-7.29. The identified areas not circled are new findings for this study using the SAM Target Finder with BandMax algorithms. Figure 7.22 shows some of the previously undetected areas (in this study), which have been delineated using this method.

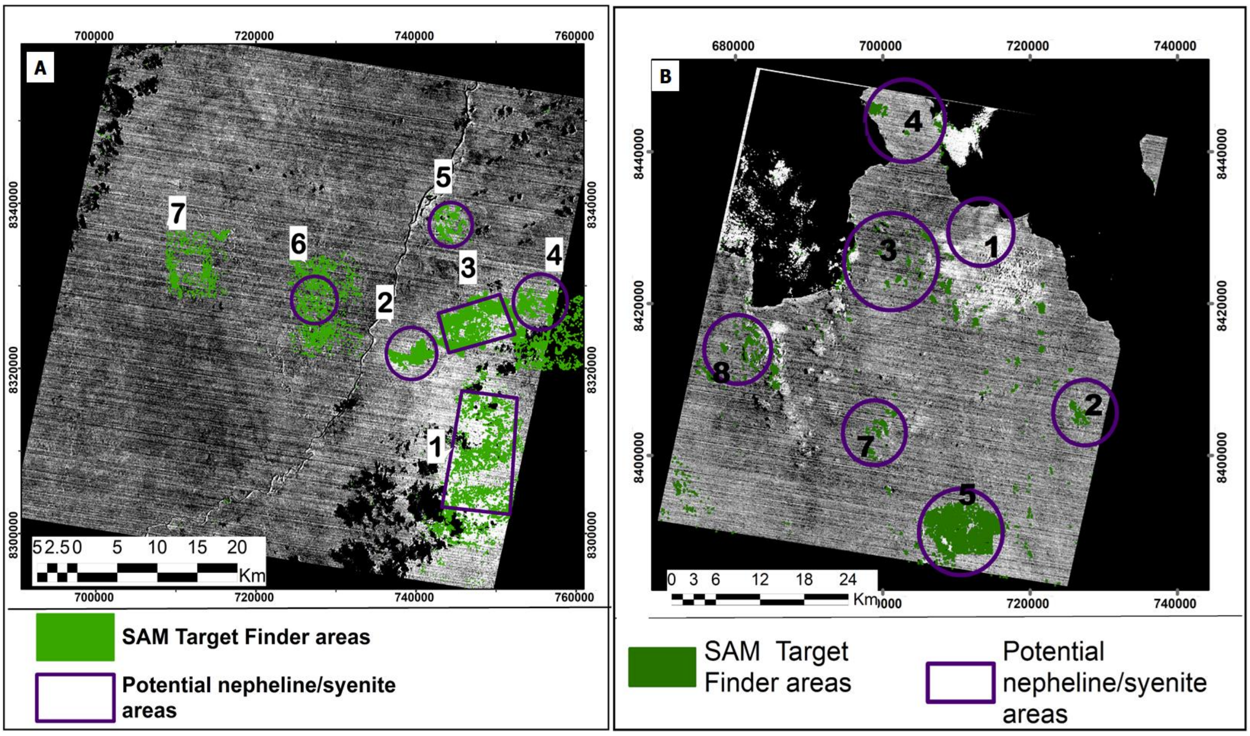

Figure 7.22: (A) shows results of SAM Target Finder with BandMax algorithm overlaid on an NSI (T) grayscale image for the south Malawi alkaline intrusions namely (1) Zomba Mt syenite (2) Chinduzi (3) Mongolowe-(4) Chaone (5) Junguni nepheline syenites and 2 other new areas (6 &7). (B) shows results of SAM Target Finder with BandMax algorithm overlaid on an NSI (T) grayscale image for the south Malawi quartz syenite intrusions namely (1) Nkhuzi bay (2) Mauni and (3) Chantulo quartz syenites.

7.3.6 Validation of the results

Most of the results of the image processing, especially those from the SAM Target Finder with BandMax algorithms, showed good agreement with the geological maps, while a few of them also showed false positives. Figures 7.23-7.24 shows the SAM Target Finder results compared with the geology, the ASTER GDEM and airborne geophysical gamma–ray maps for the South Malawi nepheline syenite and syenites including the Zomba mountain syenite, the Chinduzi, Mongolowe, Chaone, Chikala and Junguni nepheline syenites. Results show good agreement with the geological map because 6 out of 7 which were classified as possible/potential nepheline syenites (Nsy) were also identified by DTM and geophysical techniques, for example Figure 7.23 A and 7.24B.

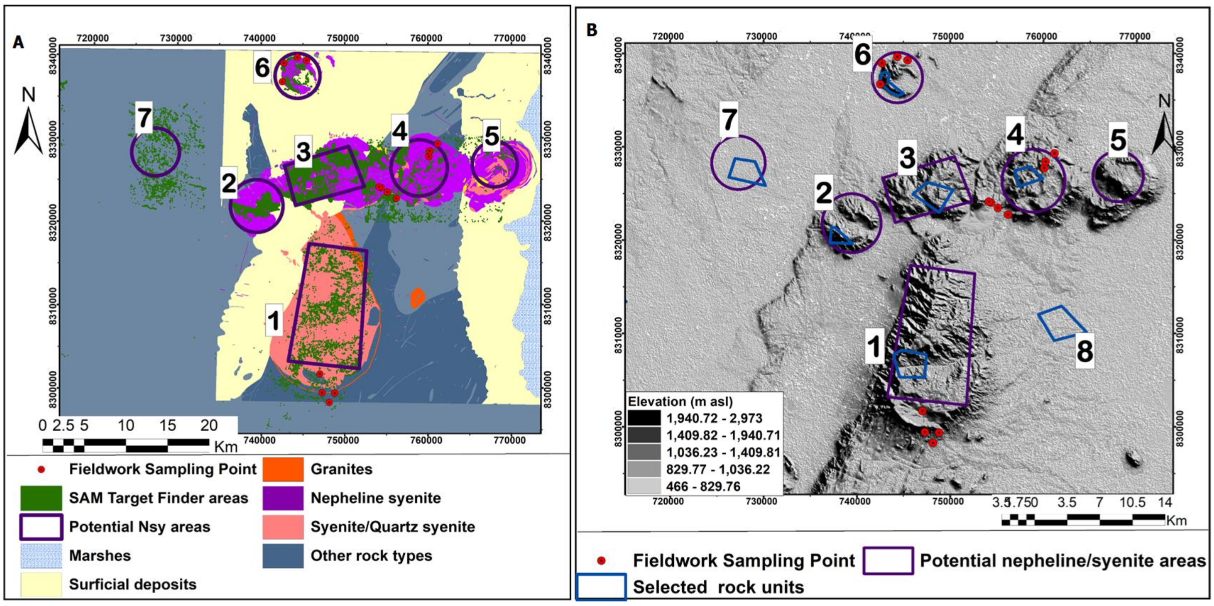

Figure 7.23: Results of SAM Target Finder with BandMax classification overlayed on (A) Geology and (B) ASTER GDEM for the S. Malawi nepheline syenite/syenites namely (1) Zomba Mt syenite (2) Chinduzi (3) Mongolowe-(4) Chaone (5) Chikala (6) Junguni nepheline syenites and (7) Chinduzi North West area.

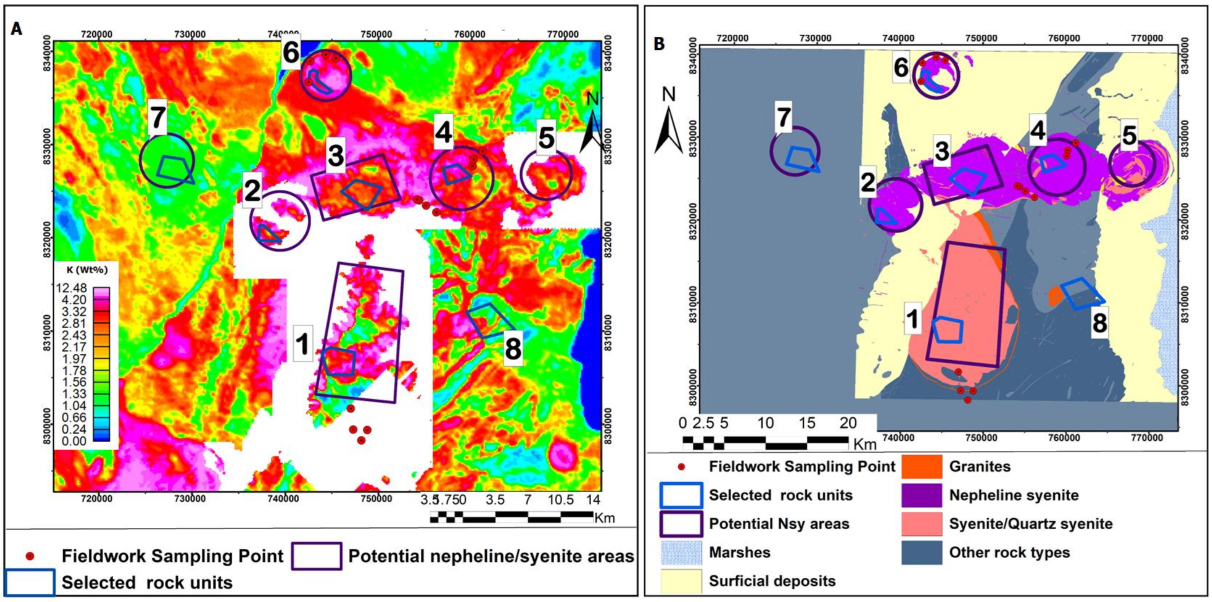

Figure 7.24: (A) Airborne geophysical gamma ray map and (B) Geology map for the S. Malawi nepheline syenite/syenites namely (1) Zomba Mt syenite (2) Chinduzi (3) Mongolowe-(4) Chaone (5) Chikala (6) Junguni nepheline syenites and (7) Chinduzi North West area.

Figure 7.25 and Figure 7.26 show that ASTER image classified results for the Southeast quartz syenites area agree with results from other techniques, for example, some areas notably 1-3, which were earlier delineated by DTM and geophysical methods (in chapter 5, sections 5.31 and 5.3.2). Areas 4-8 are additional possible nepheline syenite areas as identified using the SAM Target Finder with BandMax classification in this chapter. The published geological map shows that Area 4 (in Fig. 7.26) was mapped as pink granites while areas 5 and 6 were mapped as micro-syenites.

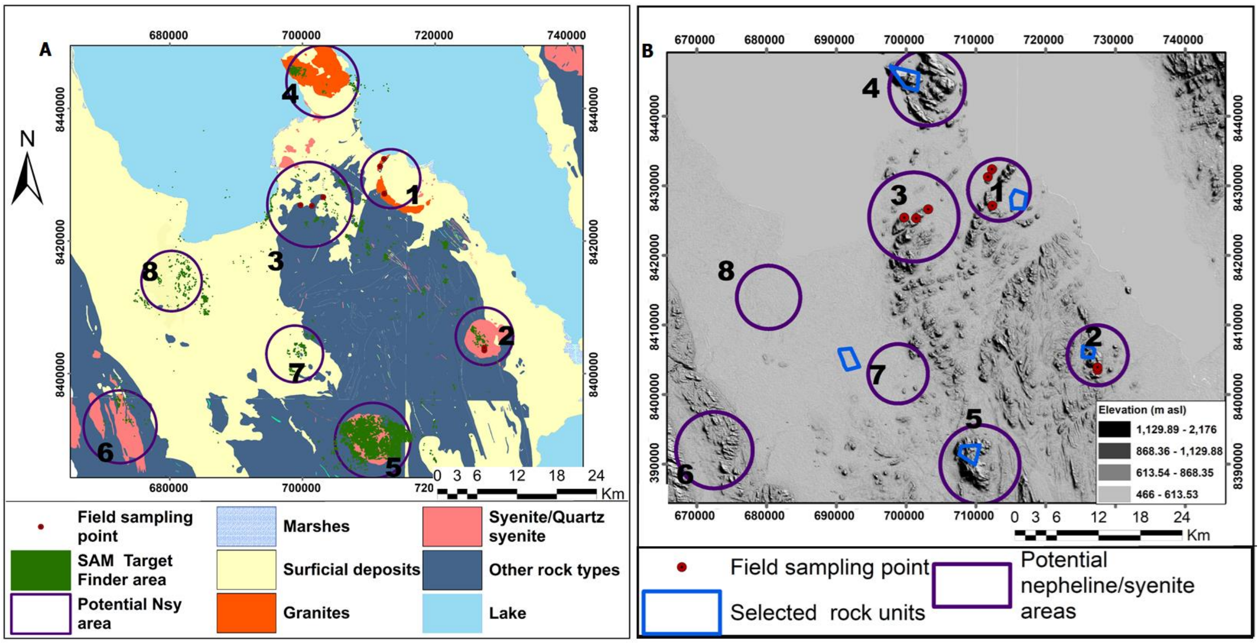

Figure 7.25(A): Result of SAM Target Finder with BandMax classification overlayed on geology map and (B) ASTER GDEM for the S. East Malawi quartz syenites. Areas 1-3 were surveyed during this study's fieldwork but areas 4-8 are new findings from this chapter.

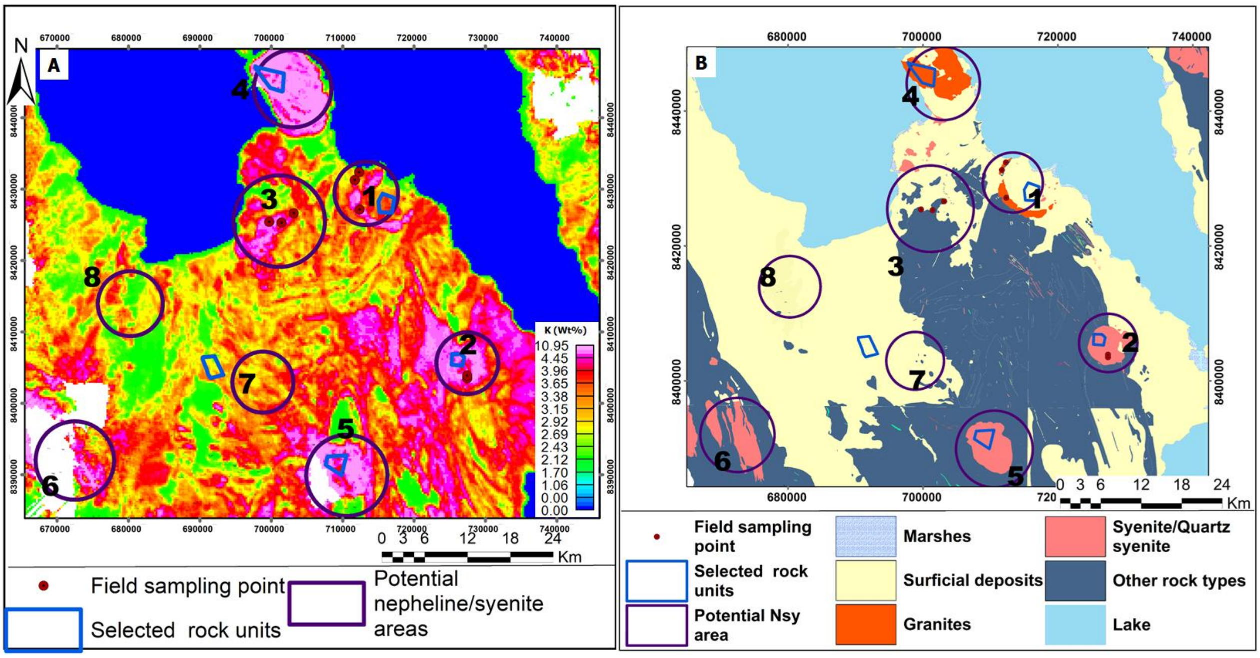

Figure 7.26A: Results of SAM Target Finder with BandMax classification compared with the geology for the S. East Malawi quartz syenites and (B) the geology map for the S. East Malawi quartz syenites including the (1) Nkhuzi Bay (2) Mauni (Chantulo (4) Monkey bay areas.

In Figures 7.27 and 7.28, for the Mangochi Hill syenite area, area 1 and 3 are known syenite and quartz syenite areas, respectively, as earlier delineated using gamma ray geophysical map and DTMs in chapter 5, sections 5.31 and 5.3.2. and verified by this study's fieldwork. Areas 2, 4 and 5 are new findings using the SAM Target Finder with BandMax algorithms. These areas could be nepheline syenites or syenites but ground truthing would be needed to confirm the geology of these areas. Some false positives in some areas, for example to the south and surrounding Area 4 in Figure 7.27, may be associated with weathering and deposition of nepheline and potassium minerals from upland areas.

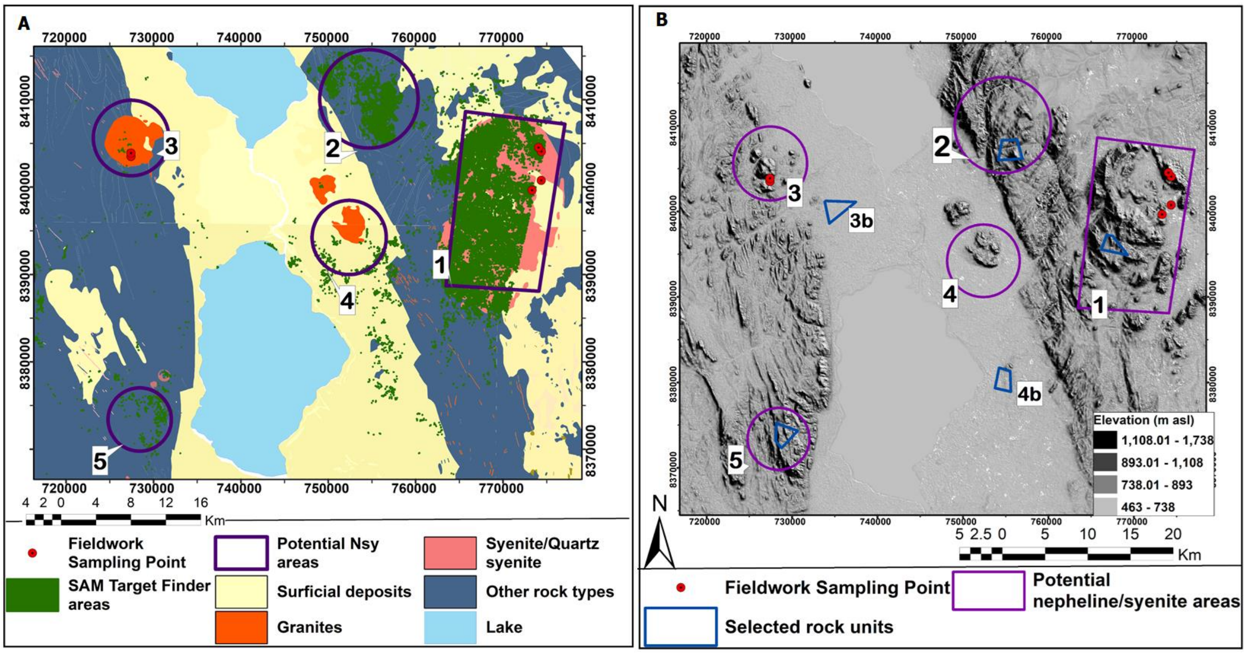

Figure 7.27: Result of SAM Target Finder with BandMax classification overlayed on the geology map and (B) shows the ASTER GDEM for the Mangochi Hill syenites.

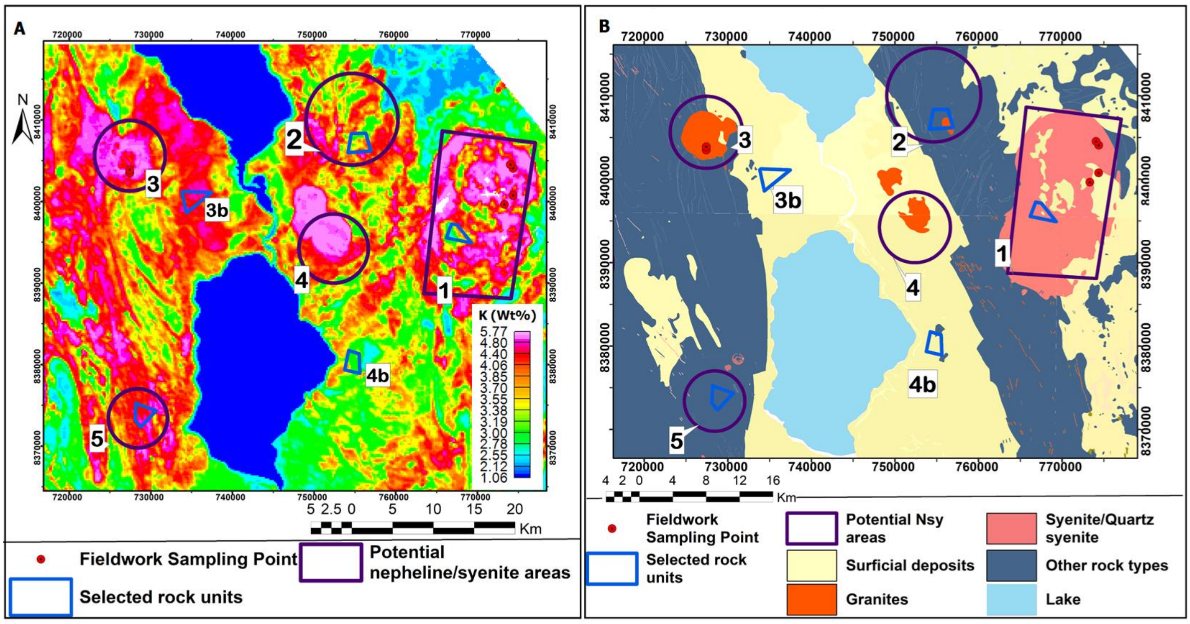

Figure 7.28: Airborne gamma ray geophysical map and (B) geology map for Mangochi Hill syenites. Areas 1, 2, 3b, 4b and 5 were randomly selected for detailed analysis of the NSI (T) values in Figures 7.24 and 7.25.

The previous literature and fieldwork have shown many of the regional geological maps of southern Malawi are inconsistent or the rock units were misclassified. Therefore, although the areas show good agreement with the existing literature, some of the areas show mismatch. This could be because most of the old regional geological maps were mapped by different people at different times. During that time, the use of the Geographical Information Systems

(GIS) and modern geospatial data archival systems was limited. Some structures are named differently in two adjoining geological maps. This is evident for the Mangochi Hill syenite (B) which is classified as syenite by King and Dawson (1976) and classified as perthitic gneiss/quartz syenite by Dawson (1970). Part of the area was mapped as lakeshore and river deposits (RD) by King and Dawson (1976) but other workers mapped as clay and sandy clay soils (Qb) (as shown in Appendices 7.10-7.11).

Some areas of known alkaline intrusions near the Malawi border with Mozambique were not fully covered during the airborne survey because of international border restrictions. Malawi was not permitted to fly over some parts of Mozambique by the Mozambican government due to internal political conflicts in Mozambique (Bates and Mechenneff, 2013a). These areas were mapped using the SAM Target Finder with BandMax algorithm and results were cross-checked with the methods used earlier in chapter 5, sections 5.31 and 5.3.2. Figures 7.29-7.30 show the carbonatite-associated complexes, which include the Nkalonje, Tundulu and Songwe-Mauze complexes (numbers 32,33, 35 in chapter 1, Figure 1.3). Figure 7.31 shows the south-west Malawi alkaline complexes including the Salambidwe and Thambani intrusions (numbers 42 and 41 respectively, in chapter 1, Figure 1.3). Figures 7.29 A and B, Figure 7.31 B and Appendix 7.11 (A) and (B) show that satellite remote sensing image and DEM data are more suited for such areas because of its unrestricted coverage over national borders. Such areas, which could not be mapped using geological/geophysical mapping, have been mapped using ASTER satellite imagery and ASTER GDEM data.

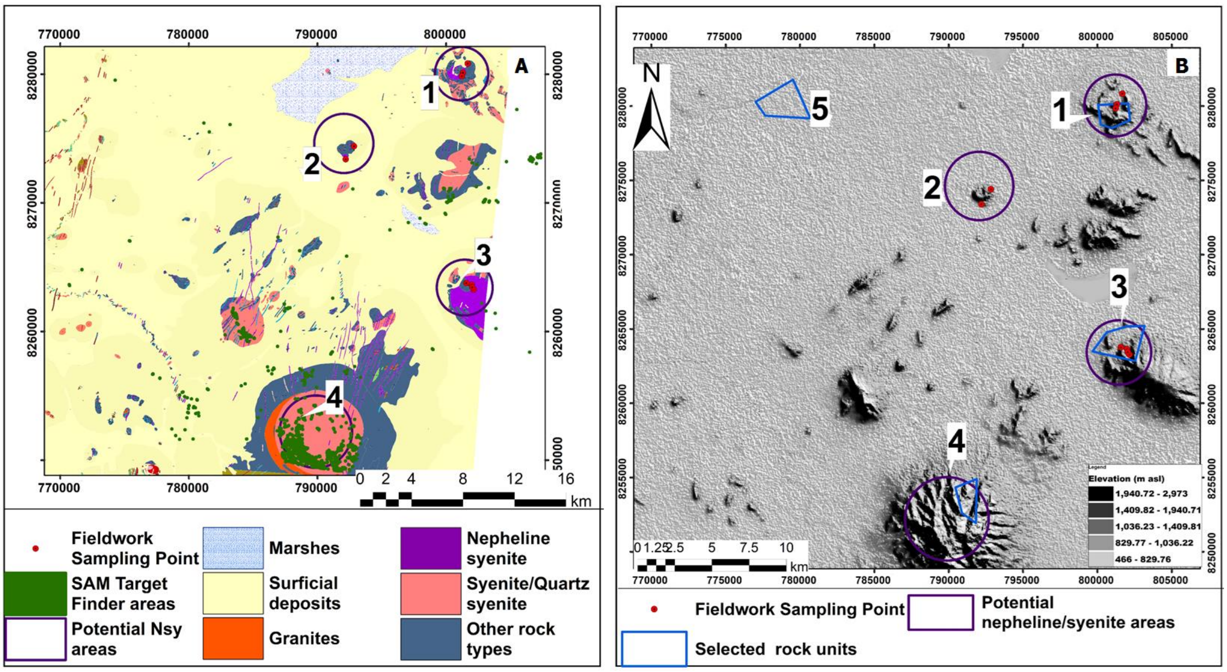

Figure 7.29: (A) Results of SAM Target Finder with BandMax classification overlayed on the geology map and (B) ASTER GDEM for the carbonatite-associated nepheline syenites namely (1) Tundulu (2) Nkalonje (3) Songwe-Mauze and (4) South west Songwe-Mauze while (5) is a newly mapped area.

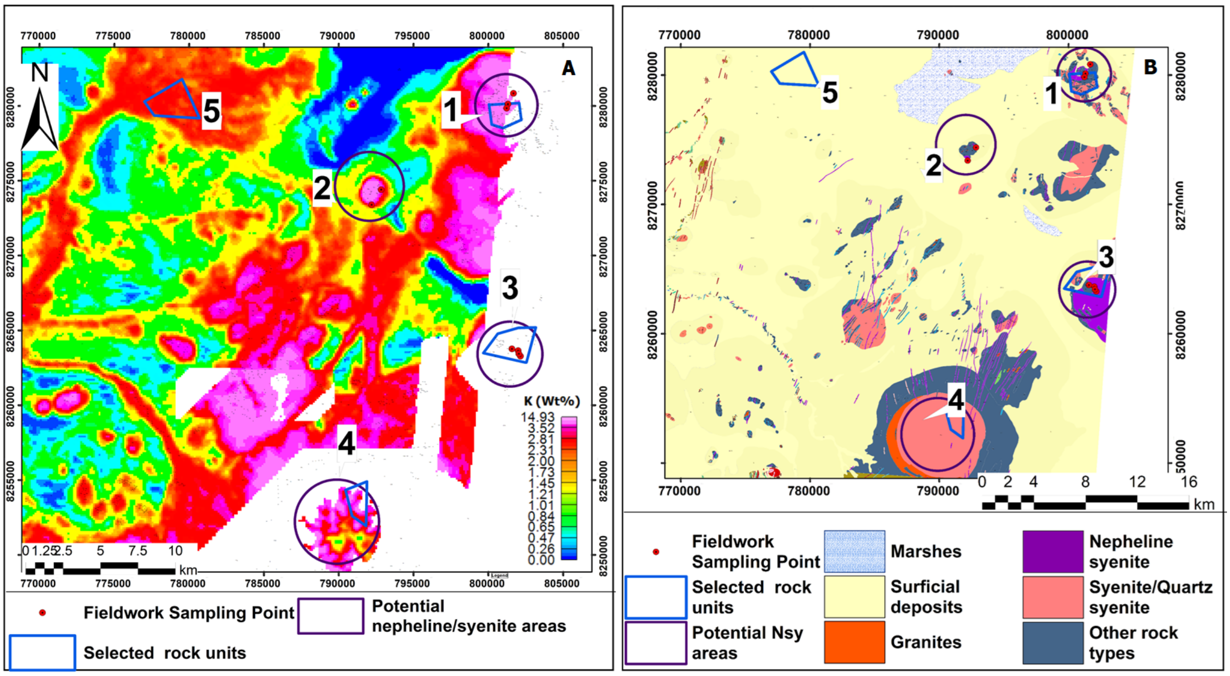

Figure 7.30: (A) Airborne gamma ray map (B) Geological map and rock units randomly selected for analysis in Figures 7.20-7.21 for the carbonatite-associated nepheline syenite areas namely (1) Tundulu (2) Nkalonje (3) Songwe-Mauze and (4) Southwest Songwe-Mauze areas in Figures 7.20 and 7.21.

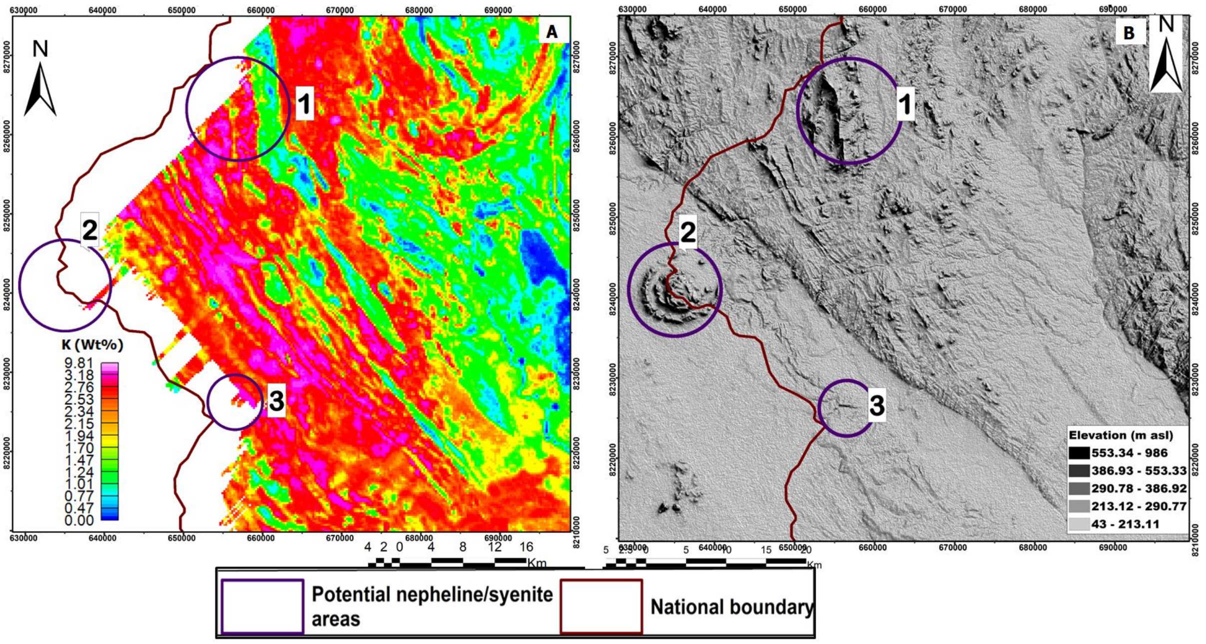

Figure 7.31: (A) Airborne geophysical gamma ray map and (B) ASTER GDEM for the South west Malawi's (1) Thambani syenite (2) Salambidwe nepheline syenite and (3) Chikwawa North West area. In A the the circles show areas identified as possible nepheline syenite/syenite intrusion.

Figure 7.31A shows that some of the important areas notably area 2 (Salambidwe and Thambani intrusions were not captured on the airborne geophysical survey and partly by the geological map. However, these have now been mapped using ASTER satellite imagery (Figure 7.29B) and the ASTER GDEM (Figure 7.31B). The results also show that there is almost no relationship between K_2O data acquired using both field gamma ray spectrometry and NSI (T) data. In Figure 7.32, a scatter plot for K_2O content in rocks vs nepheline syenite index (T) showing negative and almost no association. In Figure 7.32 (A) the data from field/ground spectrometry survey show that some nepheline syenites with low K content are associated with low NSI (T) values while other nepheline syenites having low K content are associated with high NSI (T) values. However, both the field survey and airborne spectrometry data show that the other alkaline rocks, namely alkaline granite, syenites and quartz syenites, have high NSI (T) values. Two possible explanations are derived from these results. Firstly, this may suggest that the high NSI (T) results are mostly associated with potassic alteration rather than the abundance of nepheline minerals within the samples. If the high NSI (T) values reflected the abundance of nepheline, then all nepheline syenites would probably show high NSI (T) values. Secondly, it may suggest that the nepheline syenites proper could be the samples which show low K_2O content. This is because the geochemistry of different felsic rocks shows that nepheline has lower K_2O content compared to felsic minerals such as K-feldspar as shown in chapter 3, (Table 3.1).

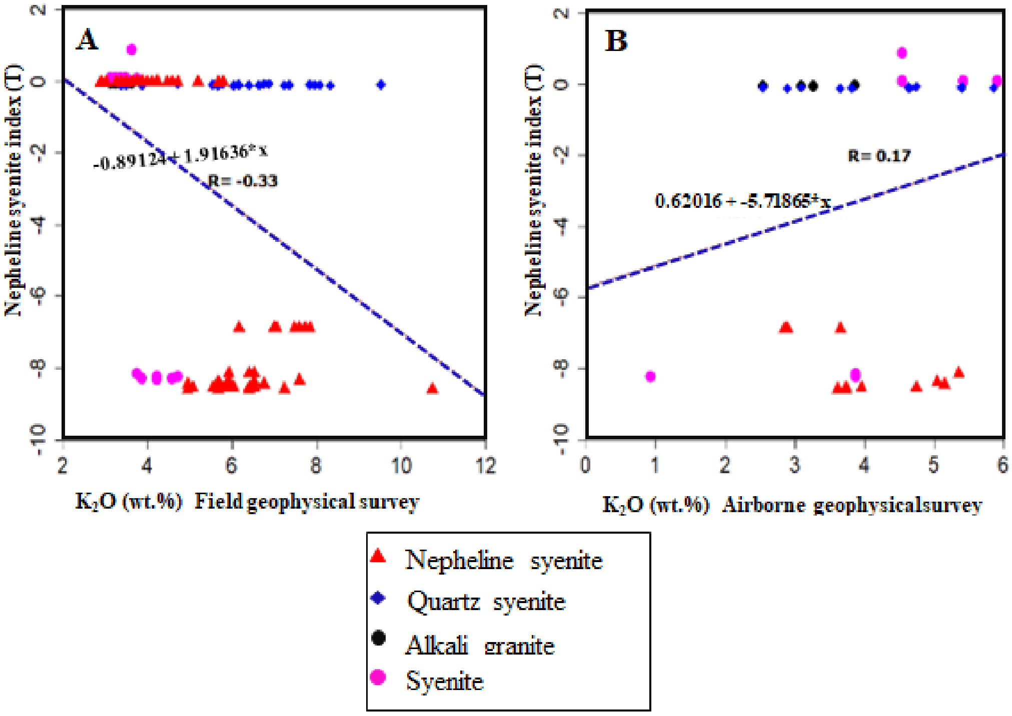

Figure 7.32: Scatter plot for K_2O content in rocks vs Nepheline syenite index (T) showing negative and almost no association, respectively, for (A) using data from ground/field geophysical survey and (B) using data from airborne geophysical survey.

7.4 Discussion

The results from the field spectroscopy have shown that carbonates are much easier to discriminate within VNIR-SWIR region than silicates. The identification of many absorption and reflectance peaks confirms the argument that spectroscopy has very high sensitivity to subtle absorption and reflectance features of materials (Clark, 2004; Kletetschka et al., 2004) which makes it a potentially useful diagnostic tool for rocks and minerals. The carbonates show distinctive absorption features within the infrared and near-infrared region due to the overtone and mineral crystal vibrations which are strongest between wavelengths 2.30μm to 2.35μm of the electromagnetic spectrum (Clark, 2004). The use of the field spectra resampled to ASTER bands was more helpful than the raw spectra. It was easier to distinguish nepheline syenites from the other rocks using the resampled field spectra. ASTER bands 3, 4 and 6 are were quite useful for nepheline syenites.

The resampled spectral data show that nepheline syenites are separable around 900nm (Band3) at 1655nm (B4) and 2207nm (Band 6) as shown in Figure 7.15. In addition, nepheline ($KNa_3Al_4Si_4O_{16}$) is closely associated with the K-feldspars, especially orthoclase ($KAlSi_3O_8$), because they both have K atoms as part of their mineral chemistry. Therefore, the two minerals' spectra are similar as observed in Figures 7.7-7.8 and 7.13. The same situation is also observed among geochemically related rocks, for example Figures 7.1 and 7.2, which have also shown similar reflectance curves for nepheline syenite, alkali granite and syenite rocks. This suggests that when mapping nepheline syenites, it is likely that the other alkaline rocks or those closely related with the nepheline syenite would likely be mapped together with nepheline syenites due to a complex relationship between the silicates' mineralogy and their reflectance (Neave et al., 2016). Such characteristics are because silicate minerals have complicated crystal structures. The same rock type (e.g. nepheline syenite), may show heterogeneous compositions from place to place due to different petrogenetic conditions (Neave et al., 2016).

Another key absorption feature for nepheline minerals occurs between band 3 and 4. However, this feature is not covered by any ASTER band. Quartz syenite also shows deep absorption features in band 6 which suggests that the spectral pattern of nepheline syenites in band 6 could be attributed to presence of both nepheline and orthoclase minerals. This suggests that although band 6 is vital for mapping nepheline syenites, other closely related potassic rocks such as syenites and quartz syenites may also be classified at some wavelengths within the same band. Silicate minerals and rocks also show strong absorption features within the TIR wavelength region of the electromagnetic spectrum due to the stretching vibrations of the Si–O bonds in silicate minerals, unlike in the VNIR-SWIR region (0.4–2.5μm), where no major spectral features are produced by these Si–O bonds (Ninomiya and Fu, 2016). This study, therefore, agrees that it is difficult to clearly separate silicate rocks and minerals of the same family/unit. However, this study does not entirely support conclusions from studies by some researchers such as Hecker (2013) and van der Meer et al. (2012) who had argued that silicate rocks cannot be mapped using VNIR-SWIR spectral bands. This is because analyses of ASD field spectra and using the SAM target finder with Band Max algorithms in ASTER image processing have identified and mapped some nepheline syenites and related rocks. However, there is need for further quantitative validation of the image classification with ample reference data to confirm this. This was not done in this study because of inadequate reference data. Ninomiya and Fu (2016) add that the Si–O stretching vibrations cause the emissivity minima of rocks to shift further to longer wavelengths as the rocks' compositions change from felsic to mafic compositions. Therefore, nepheline syenites and other different alkaline rocks have been discriminated using ASTER TIR data.

Both field spectroscopy and satellite image classification have shown that there is close similarity between nepheline syenites and syenites or alkali granites. Therefore, it was difficult to entirely separate the two rock units. The NSI (T) as proposed in this study, has shown its potential to map nepheline syenite intrusions in many areas. The results of this work show that unlike spectral indices, the use of the SAM Target Finder with BandMax classification was more effective for mapping geochemically related rocks especially rocks of the same family such as nepheline syenites and syenites as observed in Figures 7.16-7.19. As shown in Appendix 7.10, masking vegetation removes some areas of known nepheline syenite occurrences. Therefore, it is possible that some of the areas identified by ASTER data as being potential or possible nepheline syenite areas, may also be associated with the vegetation. However, using both the NSI (T) and SAM Target Finder algorithms, many possible nepheline syenites were identified and mapped. The geochemistry of some of these areas which were sampled during fieldwork and those whose previous geological literature were reviewed, have confirmed that the intrusions are mostly either nepheline syenites or syenites. In addition, if the results were more based on the vegetation features, it would be expected that most vegetated areas and protected forest in Malawi would be classified. However, the classification could delineate these intrusions, leaving out areas composed of other rock types. This shows that methods using in this chapter have potential to separate nepheline syenites/syenites from other silicate rocks.

While, this chapter has successfully managed to map some nepheline syenites and related rocks, some challenges are worth noting. Firstly, in areas with high vegetation cover, masking vegetation led to subsequent masking of some spectral features that may be associated with geological features (Grebby et al., 2012). This resulted in loss of subtle spectral data which would have been necessary for classifying the geology. For this reason, composite images using ASTER bands 3, 4 ,6 and 8 were not effective for classification in vegetated areas. The NSI (O) could still be useful in arid areas and may need further assessments. Secondly, in some cases, ASTER data could not completely discriminate geochemically related rocks such as nepheline syenites from quartz syenites and syenites. This is because of the presence in all these rocks, of orthoclase, which is also geochemically closely related to nepheline. Therefore, the spectra of these rocks show similar spectral curves as observed in Figures 7.12(b), 7.13 (b); 7.14. A possible solution to the challenge is combining use of airborne geophysical data, DEM/DTMs and existing geological information and ground truthing, in addition to remote sensing, as has been shown in 7.29 and 7.31 (B) and chapter 5. Probably, optical hyperspectral imaging could be more effective to clearly separate geochemically related rocks due to their higher spectral resolution and narrower bands, unlike ASTER data. Furthermore, as shown in Figures 7.29 and 7.31(B), airborne geophysical survey may be affected by international relations and political decisions. For example, the Salambidwe complex (Area 2) in Figure 7.31 is one important example which crosses the border and which has been easily identified using remote sensing and ASTER GDEM data despite failure do so using field techniques.

7.5 Conclusion

The results have shown that ASD field spectroscopy data can be used to process satellite imagery and delineate potential nepheline syenites to separate silicate rocks especially, nepheline syenite and syenites within the VNIR-SWIR wavelength region of the electromagnetic spectrum. Field spectroscopy has shown that nepheline syenites have diagnostic features. The results from VNIR data agree with results obtained using the NSI (T) method which uses ASTER TIR data. This shows that both optical and broadband ASTER data can be used to identify potential nepheline syenites/syenite rocks. This makes ASTER optical bands more useful especially for reconnaissance geological mapping than previously thought by earlier studies, to clearly distinguish nepheline syenites from syenites because of these rocks' similar petro-geochemistry. Therefore, hyperspectral data might be more helpful to clearly separate the closely related silicate rocks from nepheline syenites.

As shown in this chapter and chapter 4, some previous studies had suggested that silicate rocks could not be mapped using data in the VNIR-SWIR wavelength of the electromagnetic spectrum adding that diagnostic features for silicates mainly occur in the TIR. However, this chapter has shown that nepheline syenites show spectral diagnostic features in ASTER bands 6 and 3, 4 and 8 which make them separable from the other silicate rocks. Using field spectral data resampled to ASTER bands, this chapter has also shown that key diagnostic absorption features for nepheline syenites occur at 1.6548μm (ASTER band 4) and 2.2073μm (ASTER band 6). This information helped to delineate nepheline syenites and syenites/quartz syenites using the SAM Target Finder with BandMax algorithms using the field spectral data directly acquired from the fieldwork in Malawi to identify and map the target possible nepheline syenites using ASTER imagery. The advantage of this is that applying the field spectral data on ASTER imagery could map more possible nepheline syenites and related rocks even in areas which were not covered during the fieldwork such as the south west Malawi intrusions in Figure7.31.

Chapter 8: Soil quality and suitability of Malawi nepheline syenites as potash fertiliser

8 Introduction

Chapter 6 presented results on the geochemistry and petrology of the alkaline rocks and related rocks from Malawi while chapter 4 has reviewed the remote sensing and airborne geophysical gamma ray data's application in geosciences. Based on these chapters, gamma ray and (partially) remote sensing data were processed to delineate nepheline syenites and related alkaline rocks in Malawi for rock sampling. Soil samples were collected from the same areas, for a pilot study of soil quality in the context of the overall project. This chapter responds partly to Objective 5 which sought *to conduct petrological and geochemical laboratory sample analyses for determination of K release*. It also responds to Objective 6 which aimed *to assess suitability of Malawi nepheline syenites as fertiliser through plant growth experiments.* This was achieved through a plant growth experiment carried out independently in summer 2018 by Philip Baah, an MSc student in the School of Natural and Environmental Sciences and supervised by Prof. Manning. The hypothesis was that Malawi's nepheline syenites are potentially useful as an alternative potassium source.

8.1 Testing for soil quality and available nutrients

The soil analyses included determination of soil acidity (pH), total organic carbon, the cation exchange capacity (CEC) and the exchangeable cations (K, Na, Ca and Mg). The soil pH measures the active acidity, and is a vital determinant of fixation and availability of some nutrients in the soil (McKenzie, 2003; Spargo et al., 2013). A soil's cation exchange capacity (CEC) measures the negative charge of the solid phase of a soil balanced by exchangeable cations (Jaremko and Kalembasa, 2014; Reganold and Harsh, 1985). Soil cation exchange capacity is very important in agricultural studies because it helps to determine the soil physicochemical status and also determines the soil's capacity to retain and supply nutrients, in particular, the positively charged ions of nutrients such as calcium, magnesium and potassium (Spargo et al., 2013). Determination of exchangeable cations involves extracting a portion of the K, Na, Mg or Ca which are held by electrical charges on edges and surfaces of some minerals in the soil (Murrell, 2013). The exchangeable cations are extracted from these sites by an extracting solution that initiates exchange reactions.

8.2 Methods and materials

The soil samples used were those collected from the fieldwork in Malawi and they were mostly fine-silty grained, loamy soils (Appendix 8.1). Field sampling was done by collecting soil weathered from the dominant rock within a sampling unit area and they were collected together with rock samples following a sampling procedure outlined in chapter 5 (section 5.2.4). The soil analyses were conducted on samples weathered from nepheline syenites, syenite, quartz syenites, alkaline granites and a sample of quarry dust derived from a basalt (as shown in Appendix 8.1).

The soils' laboratory analyses were done using the Standard Operating Procedures (SOP) of the

School of Civil Engineering and Geosciences, Newcastle University, in accordance with the British Standard for soil quality analysis, Part 3: Chemical methods (BS7755, 1996). Specifically, the analyses conducted in this chapter focussed on the (a) determination of dry matter and water content on a mass basis by a gravimetric method (Part 3.1 Soil quality: Chemical methods); (b) determination of pH (Part 3.2 Soil quality: Chemical method); (c) the determination of the specific electrical conductivity (Part 3.4 Soil quality: Chemical methods); (d) the determination of organic and total carbon after dry combustion (Part 3.8 Soil quality. Chemical methods and (e) the determination of the potential cation exchange capacity and exchangeable cations using barium chloride solution buffered at pH = 8.1 (Part 3.12: Soil quality: Chemical methods). Both the sample preparation and the results calculation were done using the procedure set by the BS7755 (1996) guidelines.

8.2.1 Procedure for measuring soil acidity (pH)

Soil acidity was determined according to BS7755 (1996). Firstly, a 5mL scoop of air-dried soil sample was poured into a 60 mL amber glass bottle. Then 25 mL of de-ionised water was added to the 60 mL bottle using the dispenser and closed with a bottle stopper. The bottles were placed on the orbital shaker, set at 275 ± 10 revs per minute and left to shake for 1hour ± 10 minutes. After removing the bottle from the shaker, the solution was left to stand for at least 1 hour, but not longer than 3 hours, before measuring the soil pH with the Hanna HI 83141 pH meter. The pH value was recorded while ensuring that the temperature of the buffer solutions and sample suspensions did not differ by more than 1°C. The pH electrode pH and temperature probe were rinsed with de-ionised water prior to taking measurements.

8.2.2 Decarbonisation of soil for determination of organic carbon

The organic carbon content of the soils was analysed with help from Mr Phil Green of the School of Civil Engineering and Geosciences, Newcastle University. Approximately 20g of air-dried, previously crushed soil was passed through a 2mm sieve, and ground using a ball mill until the whole sub-sample could pass through a 250µm sieve. About 0.1g of soil sample, in a porous crucible, was treated with 4mol/L hydrochloric acid, to remove any carbonates. After the acid had been drained from the crucible, the crucible and sample were dried overnight at 65°C before loading into the Leco Total Carbon analyser. The organic carbon content then was calculated using the equation 1 below:

$$\text{Organic Carbon, \%} = Cs - Cbl \qquad (8.1)$$

where

Cs is the measured carbon percentage of the sample

Cbl is the measured carbon percentage of the blank.

8.2.3 Determination of specific electrical conductivity

The samples were prepared and results calculated following the BS7755 (1996) methods. 5g of soil was shaken with 25mL water at 20ºC. The samples covered with a bottle stopper and left to stand for 30 minutes, and then filtered. The specific electrical conductivity of the filtrate was measured at 25ºC, using the Hanna HI9835, with Hanna HI 76309 electrical conductivity meter with a temperature probe. The bottles were later placed to the orbital shaker, with the shaker speed set at 280 ± 10 revs per minute and left to shake for 30 minutes. Then the samples were removed from the shaker and the suspension was filtered through a Whatman No 42-filter paper into a universal tube to collect approximately 10 mL of filtrate; which was then placed on the tube rack. The bottles were left to stand for a minimum of 1 hour to allow the solution to reach 25°C. After this, electrical conductivity was measured using the conductivity meter and electrode and reported as mS/cm. The conductivity of a blank solution was also measured halfway through a sample run. The specific electrical conductivity is calculated as follows:

$$\textit{Specific Electrical Conductivity}, \text{mS/cm} = \text{Es} - \text{Ebl} \qquad (8.2)$$

Where

E_s is the measured conductivity of the sample, mS/cm

E_{bl} is the measured conductivity of the blank, mS/cm

8.2.4 Determination of potential cation exchange capacity and exchangeable cations

This was done with help from Mr Phillip Green and Dr Alex Charlton of the School of Civil Engineering and Geosciences. About <2mm of air-dried soil was shaken with buffered barium chloride solution three times to saturate the exchange sites with the barium ion. The excess barium chloride solution was removed by washing the soil with water. Thereafter, an excess of 0.020 mol/L magnesium sulphate solution was added, to precipitate all the barium present as highly insoluble barium sulphate, and to enable the exchange sites to be occupied by magnesium ions. The CEC was determined by measuring the excess magnesium concentration using the Inductively Coupled Plasma optical emission spectrometry (ICP-OES) equipment of the School of Engineering, Newcastle University. The exchangeable calcium, magnesium, potassium and sodium were also determined by analysis of the barium chloride extract using Atomic Absorption Spectrometry (AAS). Appendix 8.2 shows details of the standard operating procedures for the analyses. For ICP analysis, these samples were diluted by 10 times for more efficient elemental detection using the ICP (Environmental Protection Agency (EPA), 2006). The ICP instrument was calibrated by preparing solutions in barium chloride solution from the individual element 1000 mg/l stock solutions at the following concentrations for sodium, potassium, calcium: 0 µg/l, 20 µg/l, 40 µg/l, 60 µg/l, 80 µg/l, 100 µg/l. The stock solutions for magnesium were at the concentrations of 0 µg/l, 2 µg/l, 4 µg/l, 6 µg/l, 8 µg/l, 10 µg/l. After running the standards, the samples were also run. The 6µg/l standard for Mg and 60 µg/l standard for the other elements were run after every 8 samples to check that the instrument conditions remained stable. The extractable cations for Ca, Na, K and Mg were analysed using the AAS while the CEC for the soils was analysed using the ICP-OES.

8.2.5 X-ray Powder Diffraction for characterisation of crystalline materials

The X-ray diffraction (XRD) characterisation was used to determine the presence of nepheline and other crystalline phases within the soils. X-ray Powder Diffraction (XRD) analysis was conducted using the PANalytical X'Pert Pro Multipurpose Diffractometer (MPD) instrument owned by Newcastle University's School of Engineering. This instrument is powered by a Philips PW3040/60 X-ray generator and fitted with an X'Celerator detector. Diffraction data are acquired by exposing powder samples to Cu-Kα X-ray radiation, which has a characteristic wavelength (λ) of 1.5418 Å. X-rays were generated from a Cu anode supplied with 40 kV and a current of 40 mA.

Three of the samples were for the high CEC soil samples derived from nepheline syenite and the fourth was from nepheline syenite which had showed the lowest CEC. The fifth sample was from alkali granite-derived soil which also had high CEC values. The X'Celerator is an ultra-fast X-ray detector that uses RTMS (Real Time Multiple Strip) technology. It operates as an array of a hundred channels which can simultaneously count X-rays diffracted from a sample over the range of 2θ angles specified during a scan. The X'Celerator therefore has capability to produce high quality diffraction data in a significantly shorter time than an older style diffractometer would require. The data were collected over a range of 2-45° 2θ with a step size of 0.016° 2θ and nominal time per step of 100 s, using the scanning X'Celerator detector (hence the counting time per step). Fixed divergence and anti-scatter slits of 1/16° were used together with a beam mask of 10mm and all scans were carried out in 'continuous' mode.

Phase identification was done using the X'Pert accompanying software program called PANalytical High Score Plus and the Crystalmaker suite of software (Stare et al., 2018) in conjunction with the ICDD Powder Diffraction File 2 Database (2004), ICDD Powder Diffraction File 4 - Minerals (2015), the American Mineralogist Crystal Structure Database (March 2010) and the Crystallography Open Database (May 2013; www.crystallography.net). To identify the crystalline materials, the peak profiles of the crystalline phases were determined by fitting the profiles (Stare et al., 2018) of minerals from the ICDD Powder Diffraction File 2 Database on the XRD profiles of each soil sample that was analysed. The observed samples were compared with the references from the Crystalmaker software library by overlaying the profiles of the references on the observed samples and then comparing the profiles' peaks and their wavelengths in Crystaldiffract software.

8.2.6 Plant growth trials

Plant growth experiments were conducted by Phil Baah to assess the potential of nepheline syenites from Malawi in comparison with other materials. The experiments were done using a tomato variety called Glacier (*Solanum Lycopersicum L.*) which was purchased from Thompson and Morgan Ltd., England. The crop trials used treatments of hydro-syenite, an innovative fertiliser developed and supplied by the Massachusetts Institute of Technology (MIT, USA), nepheline syenite (acquired from this study's fieldwork in Malawi), syenite from Brazil as supplied by Terrativa SA (Manning et al., 2017), a commercial KCl fertiliser and a K-free control treatment. The experiments consisted of 21 treatments with 5 doses of

100, 330, 660, 830 and 1250 mg K kg^{-1} soil, for the four materials used namely, nepheline syenite, syenite, hydro-syenite, KCl plus the K-free control treatment.

Each of the 21 treatments had 3 replications which were grown in 1kg of high purity silica sand-based artificial soil in 13 cm pots making a total of 63 experimental pots. The experiment was conducted in uncontrolled temperature in the green house. Watering was done through capillary irrigation using ceramic hydro-spikes positioned into the soil and attached by a watering tube to a water reservoir (Thorup-Kristensen, 1994). The plants were treated weekly with a K-free Hoagland's nutrient solution, containing all required plant nutrients except K (Manning et al., 2017). At the end of the experiment, the soil, plant tissues and fruits were analysed for K, Na, Ca and Mg content, pH and the cation exchange capacity.

8.2.7 Analysis of results

Descriptive and correlation statistics were calculated to determine relationships of the different results from the geochemical analysis using MS Excel and Origin Lab software packages. Linear regression was used to assess the relationship of different parameters analysed and the extraction of cations using the ICP MS/ICP-OES versus the AAS method.

8.3 Results of analyses

8.3.1 Malawi soils geochemical analyses

The results show that the sampled soils in this chapter are slightly acidic with pH value ranges of 4.72- 9.12 with a mean of 6.1 pH. Figure 8.1 shows the sampling locations, content of mapped soil types with the results of field gamma-ray spectrometry data of K content of the parent rock.

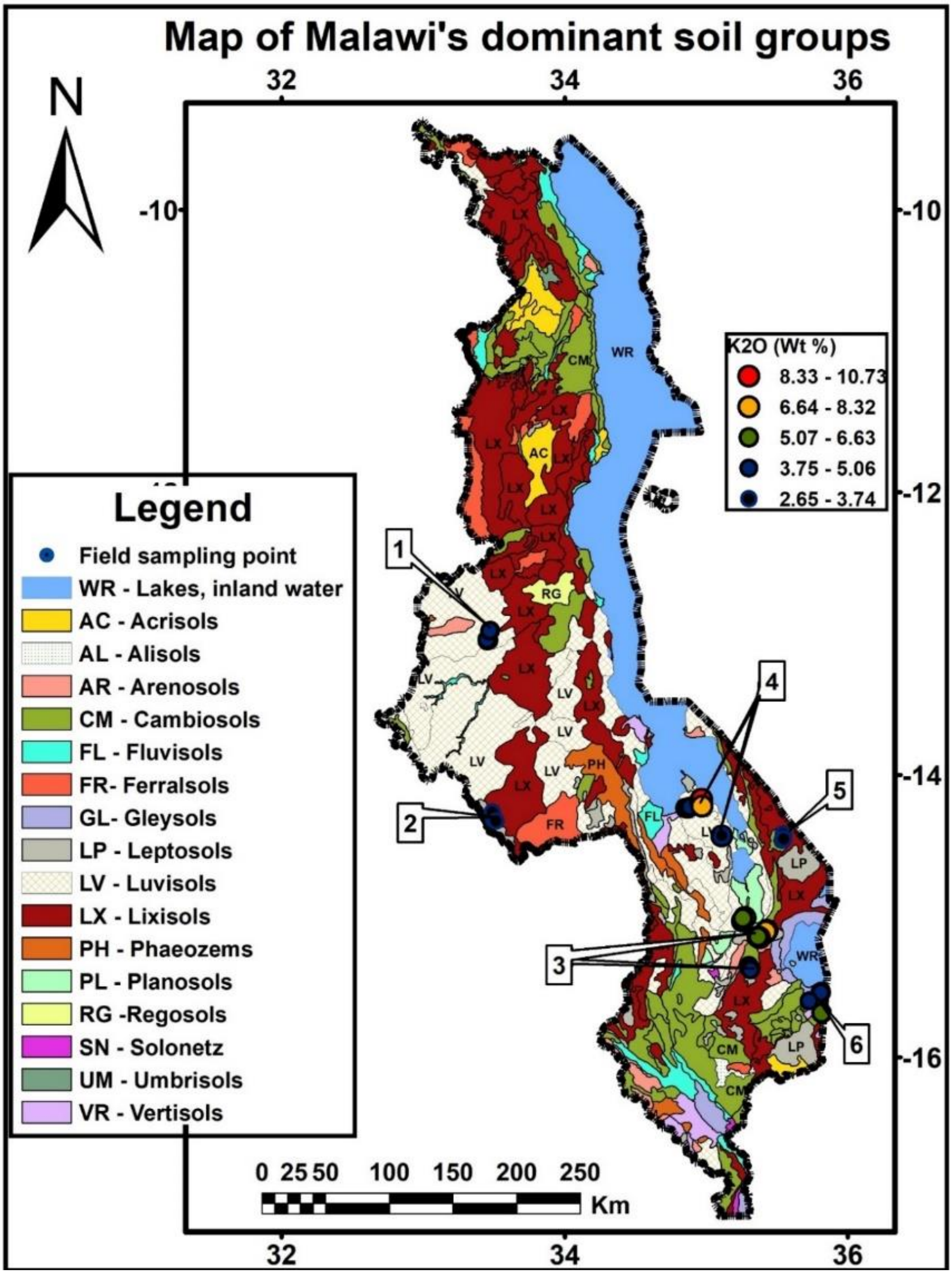

Figure 8.1: Dominant soil groups of Malawi based on World Reference Bureau (WRB) classification. Shapefiles for soil classification were accessed from Leenaars et al., (2014) and K_2O values are from gamma ray field spectrometry for areas sampled during this study's fieldwork namely: (1) Kasungu area; (2) Dzalanyama alkali granite; (3) South Malawi nepheline syenites; (4) S.E Malawi quartz syenites (5) Mangochi hill syenite (6) carbonatite-associated nepheline syenites.

The soils also show variable amounts of total organic carbon (TOC) as shown in Figure 8.2 and Table 8.1. The results show that the soils have variable exchangeable cations.

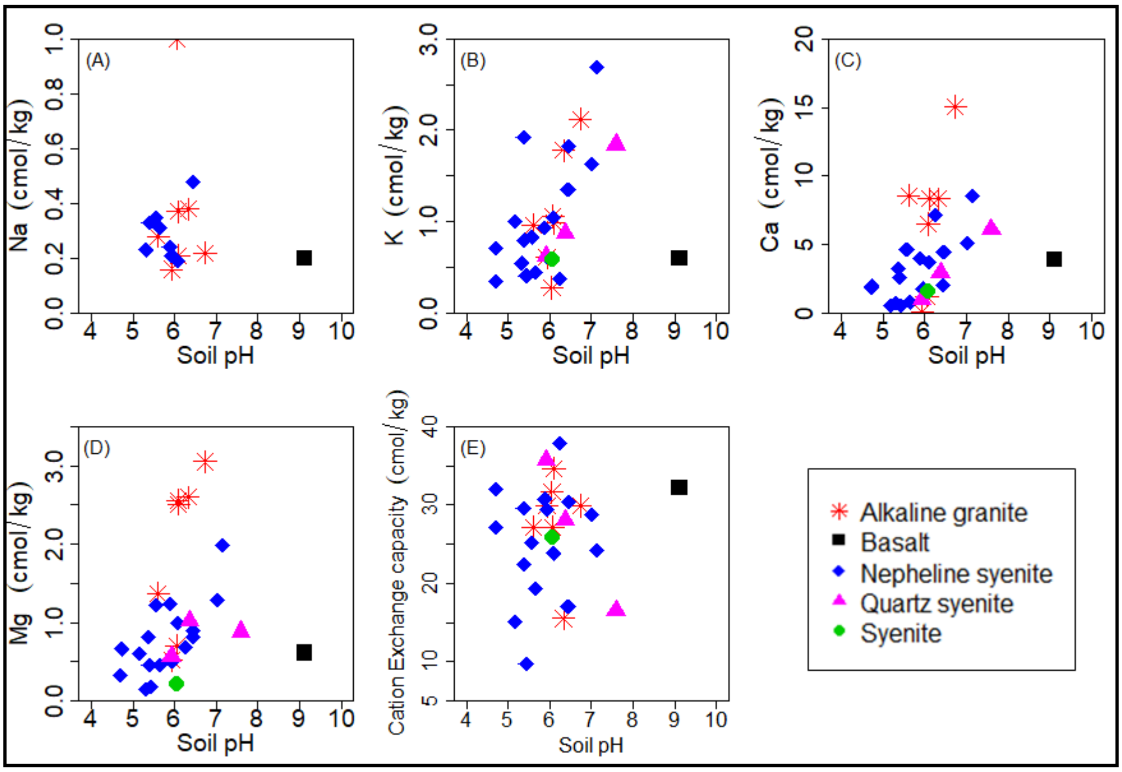

Figure 8.2: (A-D) Soil pH vs exchangeable cations for Na, K, Ca and Mg respectively and (E) shows soil pH vs Cation exchange capacity in soils from different rock units collected from Malawi during this study's fieldwork..

The highest exchangeable K was found in soils derived from nepheline syenites (Figure 8.3). This agrees with whole rock geochemistry (in chapter 7) which also showed highest amounts of K_2O and normative nepheline in these samples. In Figure 8.3 (A) the soils derived from nepheline syenites show low to moderate exchangeable cation values for K under moderate acidic conditions (between pH 5-6.5) and relatively higher K extractable cations under neutral acidic conditions. The soils' cation exhange capacity (CEC) values are also high under soil conditions of pH 5-7. The results also show that the values for extractable cations of Ca and Mg are high under alkaline conditions of the soils. pH levels are within the desirable ranges for crops growth and nutrient supply nutrient breakdown (Horneck et al., 2011).

Extractable K cations also show high values with pH between 5.5-7 soil pH. Electrical conductivity is high in soils under pH conditions of about 6.5-7.3 (Figure 8.3A). There is a slight negative relationship between soil pH and organic content and high TOC values between soil pH of 5.5-7 (Figure 8.2B). The soils also have high organic (Figure 8.3(b) and CEC which suggest good soil health (Horneck et al., 2011) especially soils from nepheline syenites. The high CEC values also shows that the soils are well textured and have sufficient clay particles which helps to promote the nutrient holding capacity.

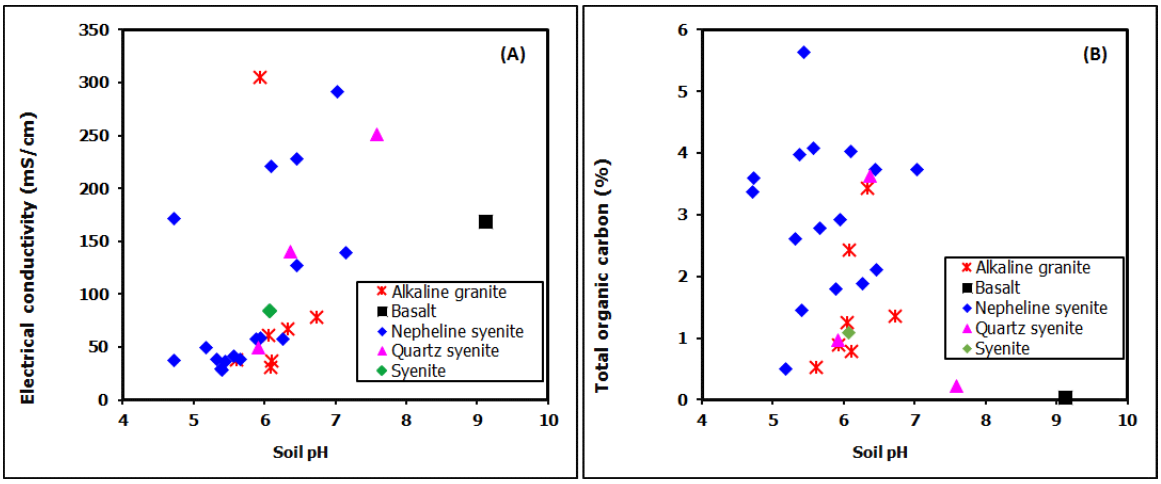

Figure 8.3: (A) Shows soil pH vs electrical conductivity and (B) shows soil pH vs total organic carbon content for soils from different rock units collected from Malawi during this study's fieldwork.

As shown in Figures 8.4 and 8.5 there are varied relationships between different pairs of the results for the different parameters. For example, there is low positive association between the exchangeable cations of Mg vs K. The positive association between K and Mg suggests that these soils have a good buffering capacity for K and Mg.

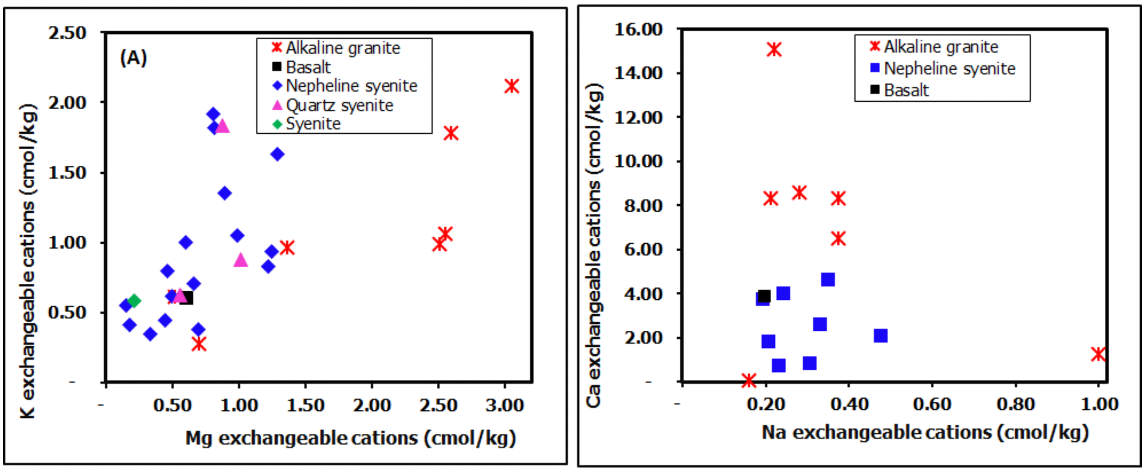

Figure 8.4: (A) Shows exchangeable cations for Mg vs exchangeable cations for K and (B) shows exchangeable Na cations vs exchangeable Ca cations in soils from different rocks.

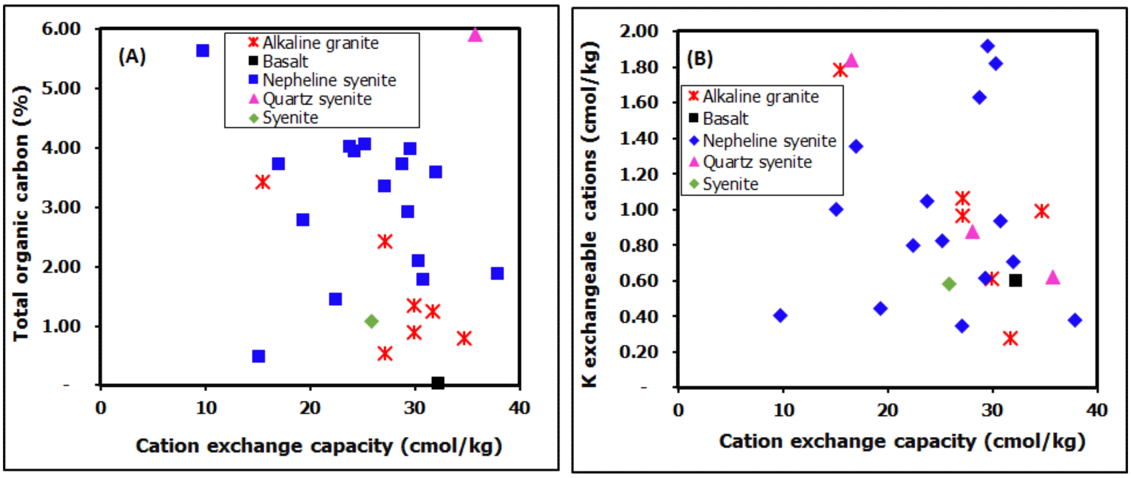

Figure 8.5: (A) Cation exchange capacity vs TOC for soils from different rock units and (B) Cation exchangeable capacity vs extractable exchangeable K cations for soils from different rock units.

Table 8.1: Soil classification after Leenaars et al (2014), soil pH, and total organic carbon, exchangeable cations and CEC for Malawi's fieldwork sampled areas.

Sampling area	Parent rock type	Soil classification	E. Condoct (mS/cm)	pH	TOC (%)	Na (cmol/kg)	K (cmol/kg)	Ca (cmol/kg)	Mg (cmol/kg)	CEC (cmol/kg)
Njuli quarry	Basalt	Fine-silty quarry dust	168	9.12	0.04	1.01	0.28	1.24	0.7	31.65
Kasungu	Nepheline syenite	Fine-silty luvisols	220.7	6.1	4.03	0.38	1.78	8.33	2.6	15.51
Kasungu	Nepheline syenite	Fine-silty luvisols	58.9	5.95	2.92	0.37	1.06	6.5	2.56	27.13
Kasungu	Nepheline syenite	Fine-silty luvisols	127.1	6.45	3.73	0.22	2.12	15.06	3.05	29.9
Kasungu	Nepheline syenite	Fine-silty luvisols	41.8	5.57	4.07	0.28	0.96	8.58	1.37	27.11
Kasungu	Nepheline syenite	Fine-silty luvisols	28	5.38	3.98	0.16	0.61	0.07	0.52	29.9
Kasungu	Nepheline syenite	Fine-silty luvisols	38	5.66	2.78	0.21	0.99	8.34	2.51	34.66
Kasungu Chipala	Nepheline syenite	Fine-silty luvisols	58	5.89	1.79	0.19	1.05	3.71	0.99	23.8
Kasungu Chipala	Nepheline syenite	Fine-silty luvisols	38	5.32	2.61	0.21	0.61	1.81	0.5	29.35
Kasungu Chipala	Nepheline syenite	Fine-silty luvisols	29.3	5.4	1.45	0.48	1.35	2.05	0.89	17.01
Kasungu Chipala	Nepheline syenite	Fine-silty luvisols	171.8	4.73	3.6	0.35	0.83	4.63	1.22	25.14
Kasungu Chipala	Alkaline granite	Fine-silty leptosols	61.5	6.05	1.25	0.33	0.8	2.58	0.46	22.37
Dzalanyama	Alkaline granite	Fine-silty leptosols	66.7	6.33	3.43	0.31	0.45	0.79	0.45	19.34
Dzalanyama	Alkaline granite	Fine-silty leptosols	31	6.08	2.42	0.24	0.93	3.98	1.24	30.77
Dzalanyama	Alkaline granite	Fine-silty leptosols	77.9	6.73	1.35	0.23	0.55	0.72	0.15	-2.64
Dzalanyama	Alkaline granite	Fine-silty leptosols	38	5.61	0.53	n.d.	1.92	3.27	0.81	29.58
Dzalanyama	Alkaline granite	Fine-silty leptosols	305	5.93	0.89	n.d.	0.71	1.84	0.66	32.01
Dzalanyama	Alkaline granite	Fine-silty leptosols	36.9	6.1	0.79	n.d.	0.41	0.57	0.18	9.79
Chaone	Nepheline syenite	Fine-silty leptosols	35.9	5.44	5.64	n.d.	1	0.59	0.6	15.05
Chaone	Nepheline syenite	Fine-silty leptosols	49.5	5.18	0.5	n.d.	0.35	1.99	0.33	27.07
Junguni	Nepheline syenite	Fine-silty leptosols and planosols	37.7	4.72	3.37	n.d.	1.63	5.08	1.29	28.69
Junguni	Nepheline syenite	Fine-silty leptosols and planosols	291.1	7.03	3.74	n.d.	0.38	7.17	0.69	37.85
Mauni	Quartz syenite	Fine-silty silty leptosols	140	6.37	3.63	n.d.	1.82	4.44	0.81	30.33
Mongolowe	Nepheline syenite	Fine-silty leptosols	57.7	6.26	1.88	n.d.	2.69	8.57	1.99	24.19
Mongolowe	Nepheline syenite	Fine-silty leptosols	227.5	6.46	2.1	n.d.	0.87	2.93	1.02	28.1
Nkhuzi Bay	Quartz syenite	Fine-silty Luvisols	49	5.92	0.96	n.d.	0.62	1.02	0.56	35.7
Nkhuzi Bay	Quartz syenite	Fine-silty Luvisols	251	7.59	0.22	n.d.	1.84	6.06	0.88	16.47
Mangochi Hill	Syenite	Fine silty cambiosols and lixisols	84.7	6.07	1.09	n.d.	0.58	1.62	0.22	25.9
Tundulu complex	Nepheline syenite	Fine-silty Vertisols	139.3	7.15	3.94	0.2	0.6	3.89	0.61	32.16

NB: n.d. refers to not detected due to machine failure

Table 8.2: Summary statistics for exchangeable cations (EC) and cation exchange capacity for the soils.

Parameter	E. Conduct. (mS/cm)	pH	TOC (%)	Na (cmol/kg)	K (cmol/kg)	Ca (cmol/kg)	Mg (cmol/kg)	CEC (cmol/kg)
Mean	102.07	6.09	2.37	0.32	1.03	4.05	1.03	25.31
Median	58.9	6.05	2.42	0.26	0.87	3.27	0.81	27.13
SD	84.78	0.88	1.46	0.2	0.61	3.42	0.78	8.59
RSD	83.06	14.43	61.71	61.94	59.79	84.41	76.08	33.93
Sample Var	69.39	0.75	2.07	0.04	0.36	11.28	0.59	71.17
Range	277	4.4	5.6	0.84	2.41	14.99	2.9	40.49
Minimum	28	4.72	0.04	0.16	0.28	0.07	0.15	-2.64
Maximum	305	9.12	5.64	1	2.69	15.06	3.05	37.85
Count	29	29	29	16	29	29	29	29

8.3.2 Characterisation of the soils using X-ray diffraction techniques

The XRD diffraction identified various mineral phases in the soils. The results are consistent with the parent rocks being nepheline syenites. The fitted profiles confirmed the presence of nepheline in the soil, but it is not abundant. The results show that four of the five soil samples that were analysed were derived from nepheline syenites; they showed nepheline phases, with peaks mainly at low angles such as 10.3^o 2θ and 27.6^o (Figure 8.5). The fifth sample did not show nepheline but showed quartz peaks at 23^o and 26.5^o suggesting the parent rock could be an alkaline granite or quartz syenite. Biotite is prominent at 9^o 2θ (in Figure 8.3 and in Appendix 8.3 suggesting possible biotite alteration to vermiculite.

However, nepheline peaks are not very prominent in the analysed soil samples which shows that the mineral is less abundant. This could suggest that nepheline undergoes fast dissolution and subsequent uptake by the plants. This probably supports findings that nepheline has highest dissolution rates as reported by Palandri and Kharaka (2004). Figures 8.6- 8.7 and Appendices 8.3 and 8.4 show peaks of nepheline, quartz, feldspars and other mineral phases and kaolinite clay as determined using the XRD diffraction.

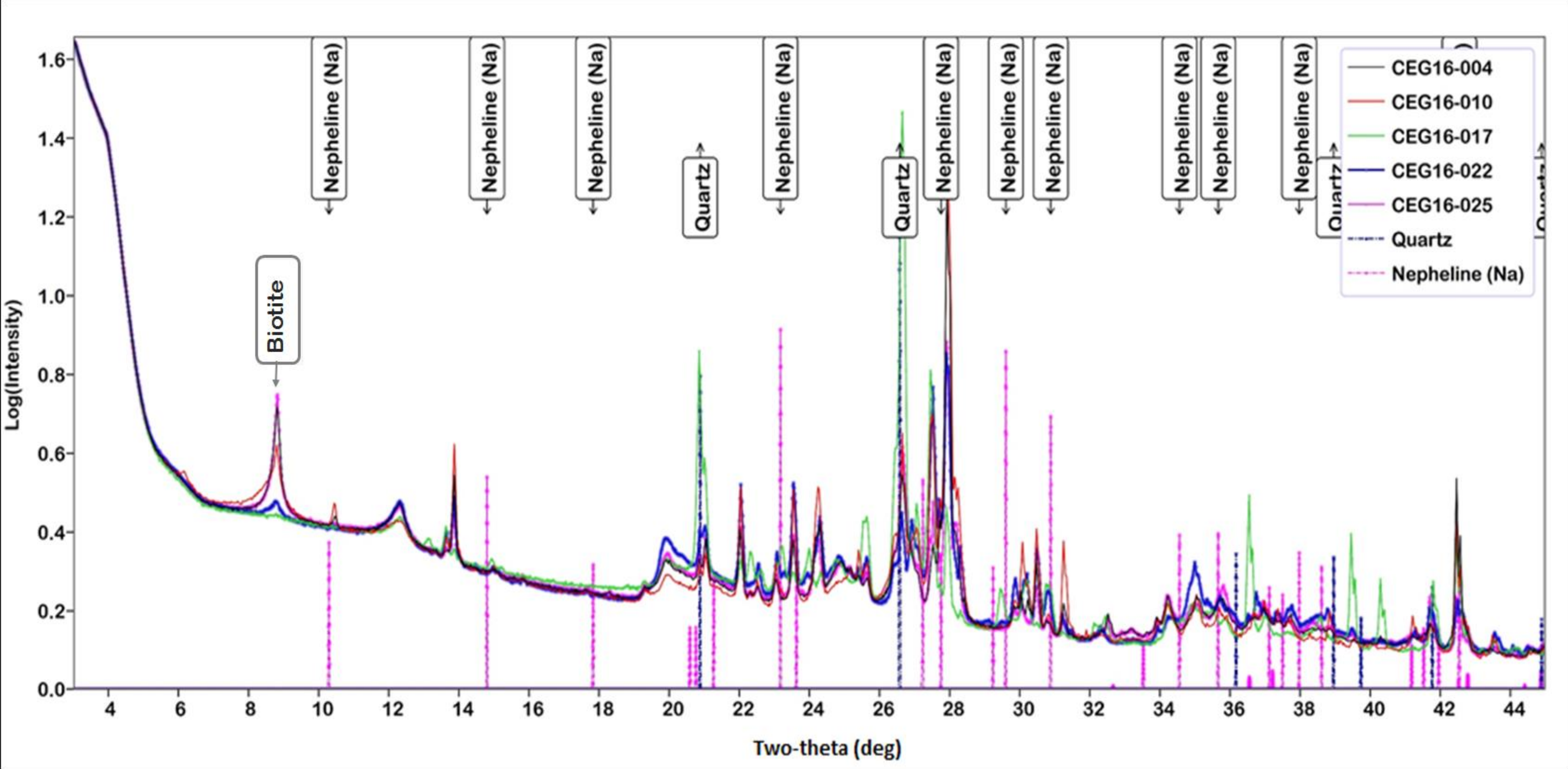

Figure 8.6: XRD profile for nepheline and quartz in the soils at lower 2θ (degrees) with position of peaks for nepheline and quartz from crystal diffract *software's library.*

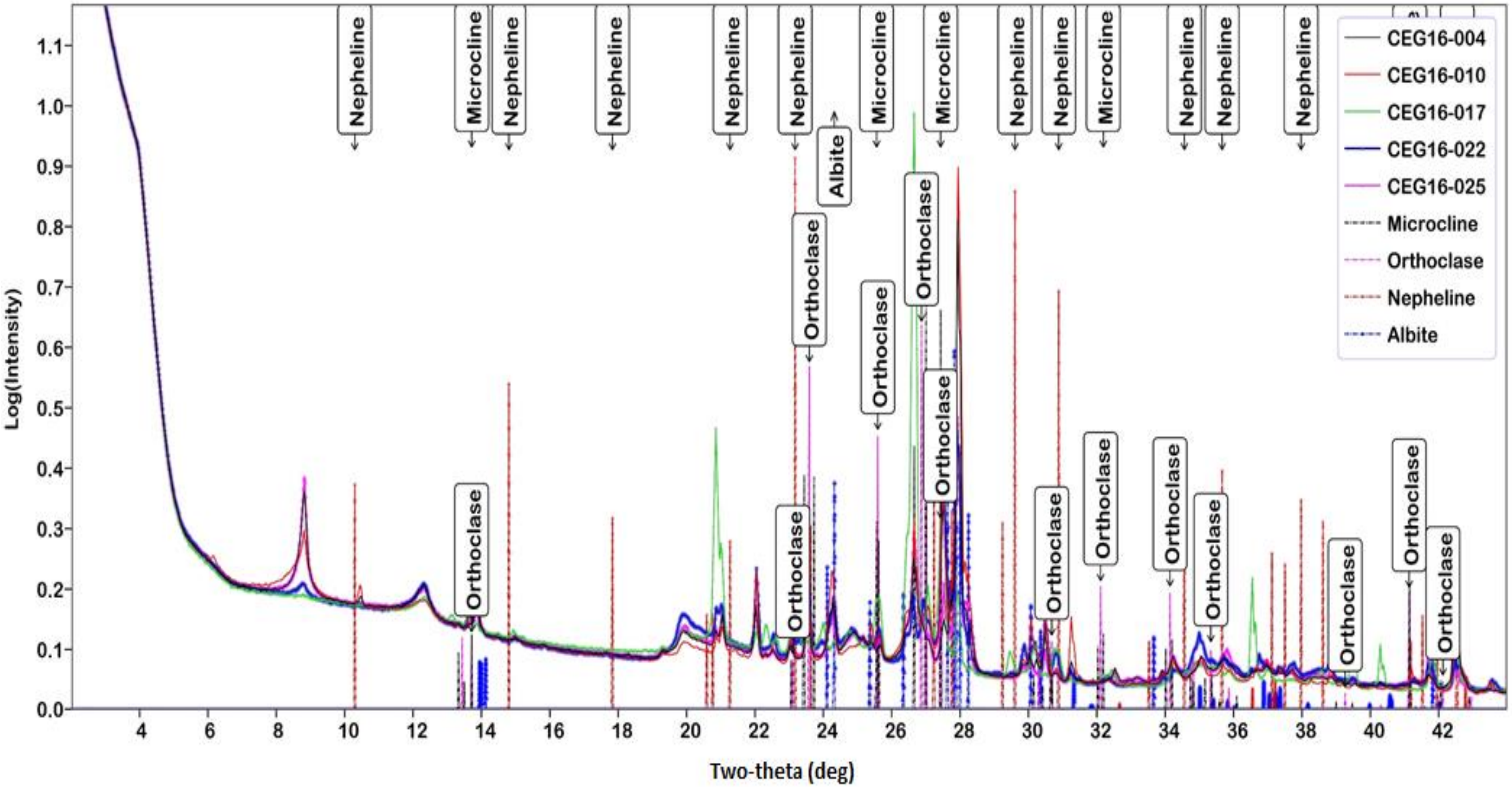

Figure 8.7: XRD profile for nepheline and feldspars in the soils namely, microcline, orthoclase and albite at lower 2θ (degrees) with position of peaks of mineral phases fitted from crystal diffract software's library.

8.3.3 Plant growth experiments

Periodic observations of the growth experiments showed that there were considerable differences in the growth, plant tissues and fruiting time for the tomatoes with different fertiliser type and application rates (Figure 8.8). All the fertiliser treatments and different application rates showed that the plant height, flowering time, fruiting time as well as the extracted nutrients differed compared to the control.

Considering soil properties, Figure 8.8 shows the effect of the treatments on soil nutrient contents at different soil pH conditions. The plant growth experiments show that the soil K was highest for plants with the treatments of KCl followed by nepheline syenite and then syenite. There was low effect from hydro-syenite and for plants with the control treatment pH between 5-8. Figure 8.8 further shows that the effect of the other soil nutrients from nepheline syenite was largely the same as or second from the KCl treatment except for calcium which show highest response from the hydro-syenite treatment. The high Na soil values shown in Figure 8.8 D are consistent with nepheline weathering, given that nepheline contains twice as much Na as K, and Na is not taken up by the plant to the same extent.

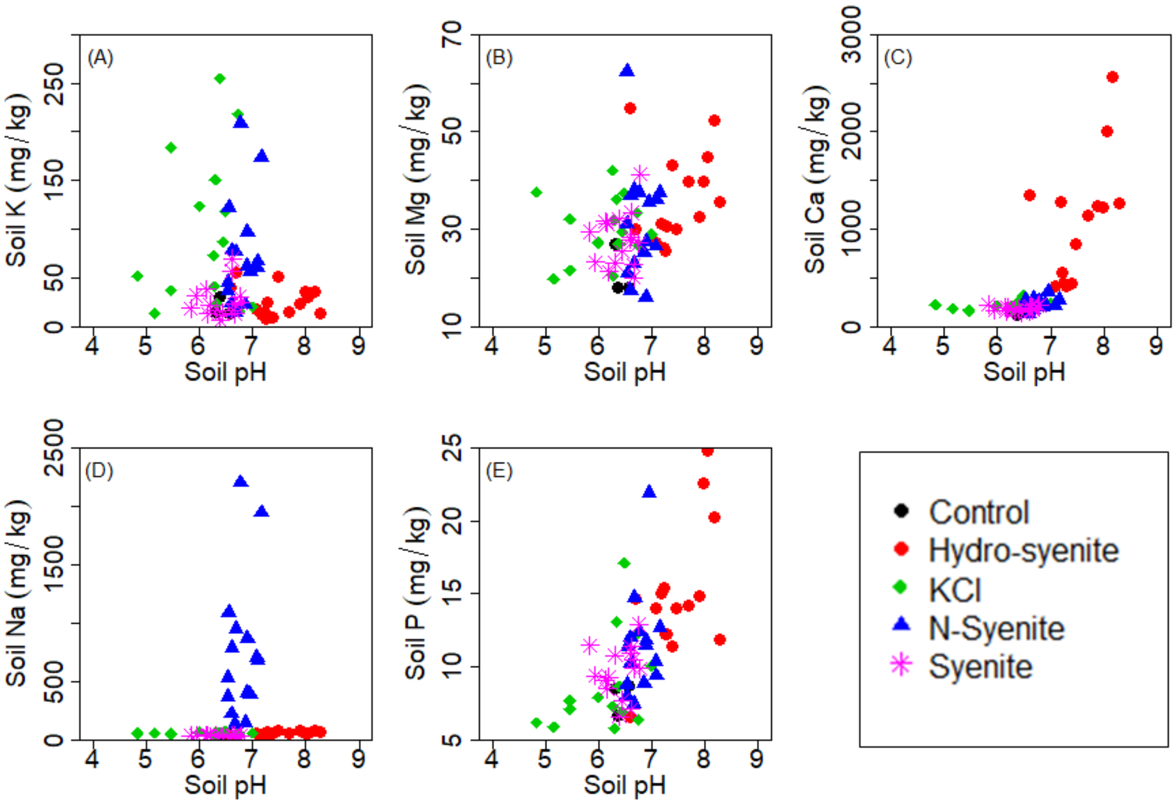

Figure 8.8: Nutrients concentration in soil in response to soil pH for (A) K (B) Mg (C) Ca (D) Na and (E) P using application rates of 0 (mg K/kg soil), 100 (mg K/kg soil), 330 (mg K/kg soil), 660 (mg K/kg soil), 860 (mg K/kg soil) and 1250 (mg K/kg soil) using data from Baah (2018).

Figure 8.9 also shows the nutrient concentration in the soil in response to K treatments from the different fertiliser sources. Figure 8.9 (A) shows that in most of the treatments, the effect on soil K was highest from KCl seconded by nepheline syenite fertilisers. The highest effect on soil Na was from nepheline syenites (Figure 8.9D). While soil Na is important for plant growth, there is need to check the Na levels in the soils. This is because with high levels of sodium, the soils may result in being rendered sterile which could also lead to death and/or damage of plants in addition to affecting the microbial activity in the soils (Cantisano, n.d.).

The nepheline syenite treatments also showed an effect on soil Mg and P, and although low for Ca it was effectively higher than hydro-syenite and syenite (Figure 8.9E).

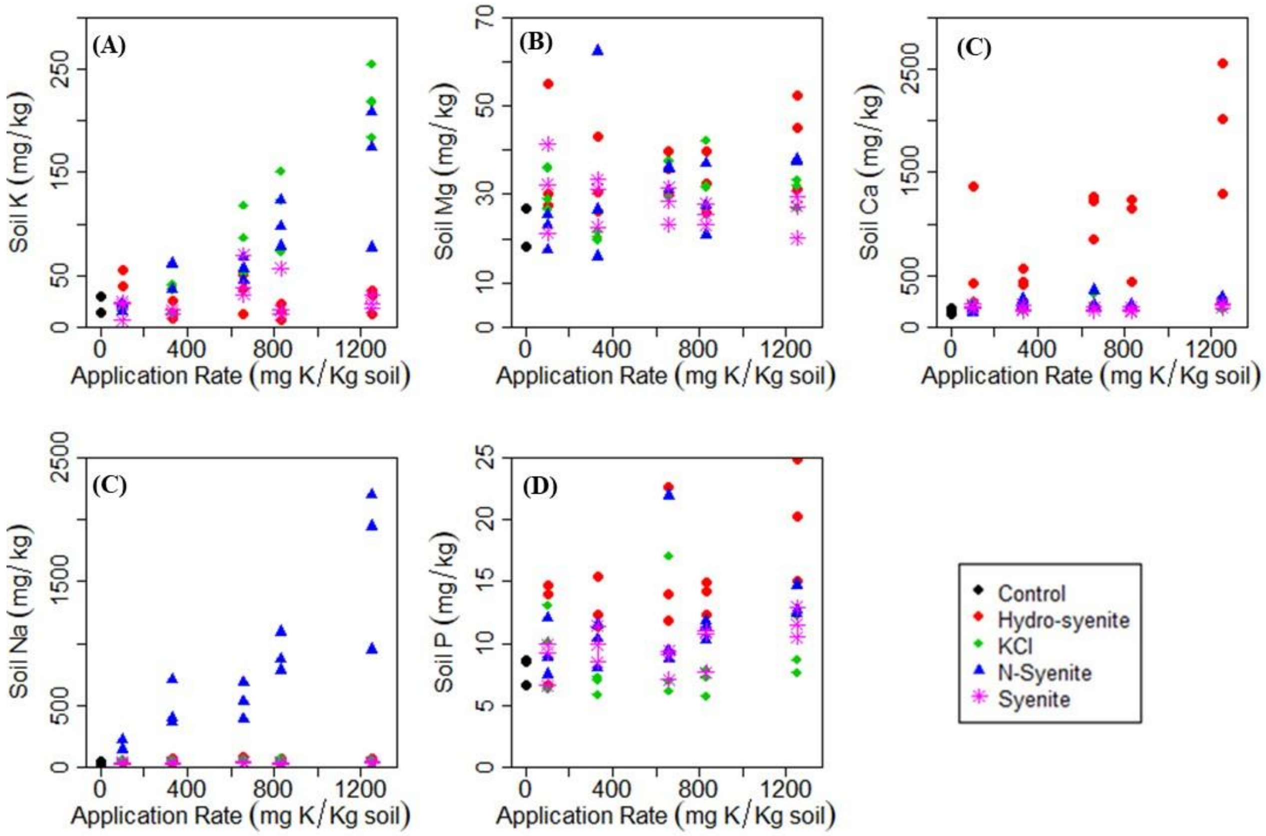

Figure 8.9: Nutrients' concentration in soil in response to K treatments from the different fertilisers for (A) K (B) Mg (C) Ca (D) Na and (E) P using application rates of 100 (mg K/kg soil), 330 (mg K/kg soil), 660 (mg K/kg soil), 860 (mg K/kg soil) and 1250 (mg K/kg soil) and a control, using data from Baah (2018).

The response of plant growth to the treatments is based on measurements of biomass (such as height) and timing of flowering and fruiting. The flowering and fruiting times for the plants in response to fertilisers from KCl and hydro-syenite treatments were similar and much earlier followed by nepheline syenite, syenite and lastly, the control. Figure 8.10 shows the averages of the plant heights at different time intervals in days at (A) 7 days (B) 14 days (C) 28 days (D) 42 days (E) 63 days and (F) at 70 days after transplanting with the standard error of the means (SEM). While the results are variable, the responses of the plants from all the fertilisers and using different application rates were higher than the control. The response from nepheline was in most cases higher than syenite and either similar to or slightly below KCl or hydro-syenite treatments. In Figure 8.10, the SEM show that there are no clear significant differences among the various fertiliser sources especially between KCl, nepheline syenite and hydro-syenite.

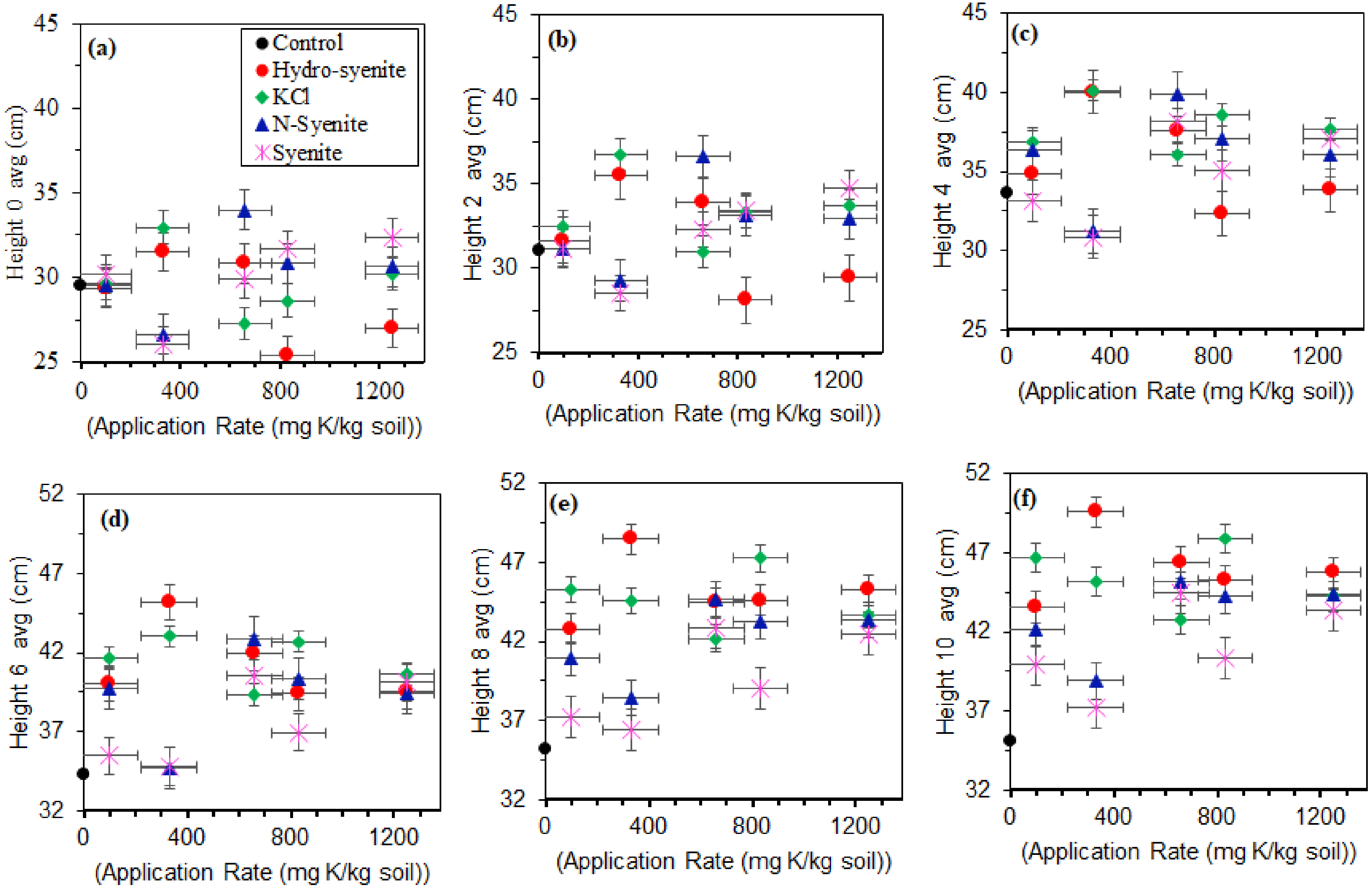

Figure 8.10: Average plant heights in response to K treatments from the different fertilisers at (a) 7 days (b) 14 days (c) 28 days (d) 42 days (e) 63 days and (e) 70 days after transplanting using application rates of 100, 330, 660, 860 and 1250 (mg K/kg soil) and a control, using data from Baah (2018).

The uptake of nutrients in plant tissue is summarised in Figure 8.11. This shows the average content of (A) K, (B) Mg (C) Ca and (D) Na in the plant dry matter (DM) as an effect of K treatment of the different fertilisers after 70 days after transplanting using application rates of 100 (mg K/kg soil), 330 (mg K/kg soil), 660 (mg K/kg soil), 860 (mg K/kg soil) and 1250 (mg K/kg soil) and a control. In Figure 8.11 the observations show greatest uptake of K, which appears to account for the observed positive effect on the plant growth and height.

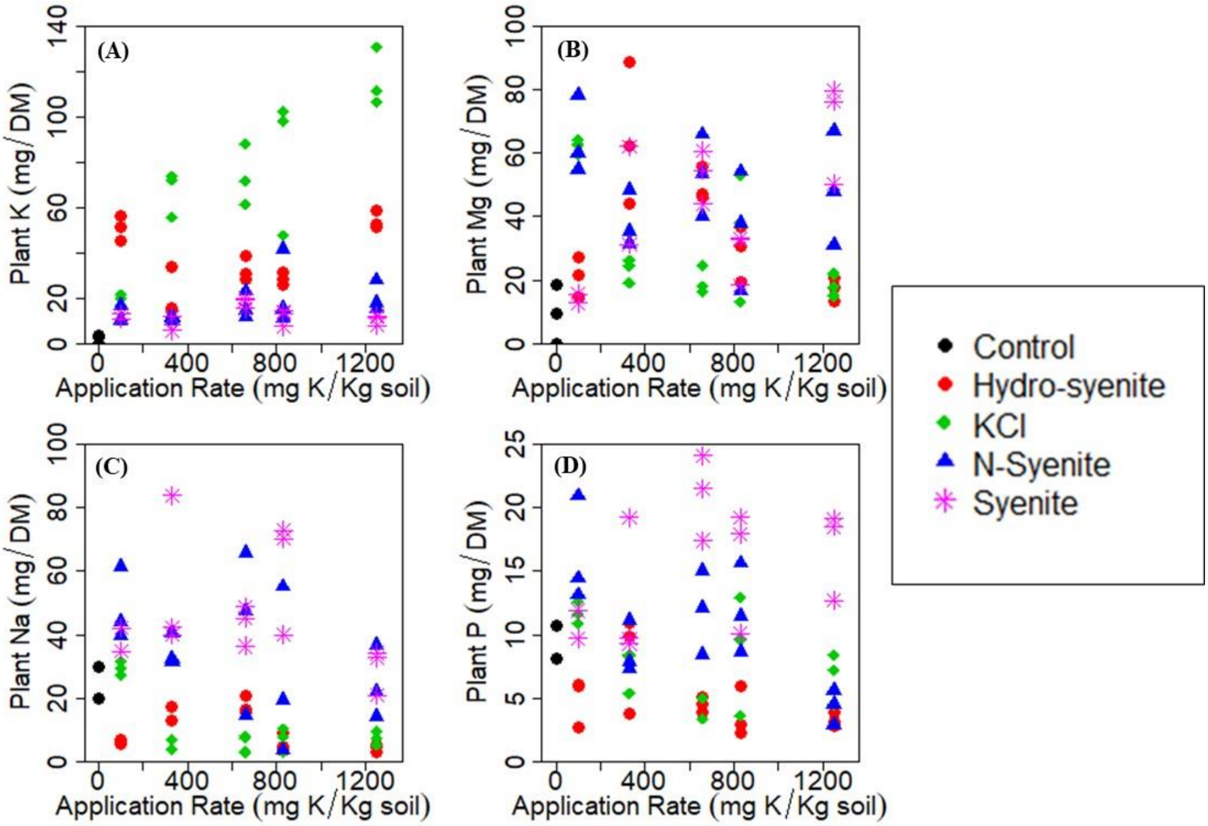

Figure 8.11: Averages of plants' dry matter content of (A) K, (B) Mg (C) Ca and (D) Na in response to K treatments from different fertilisers at 70 days after transplanting using application rates of 100, 330, 660, 860 and 1250 (mg K/kg soil) and a control, using data from Baah (2018).

Figure 8.12 shows the measurements of the content of (A) K, (B) Mg (C) Ca and (D) Na in the fruits' dry matter (DM) as an effect of K treatment from the different fertiliser sources after 70 days after transplanting using application rates of 100 (mg K/kg soil), 330 (mg K/kg soil), 660 (mg K/kg soil), 860 (mg K/kg soil) and 1250 (mg K/kg soil) and a control. The K content of fruit for the nepheline syenite fertiliser treatment was much above the control in all the application rates but lower than KCl. The results from nepheline syenite treatments were higher when using application rates of 860 (mg K/kg soil) and 860 (mg K/kg soil). Nepheline syenite also gave a high content of Ca and Na values in the fruit, but was moderately lower for Mg (Figure 8.12 C). The Na content in the dried fruits was also highest for almost all the application rates from nepheline syenite material. This could be accounted for by the relatively rapid dissolution rate for nepheline, and suggests that for plants with moderate to high Na tolerance, nepheline syenite could be an ideal fertiliser.

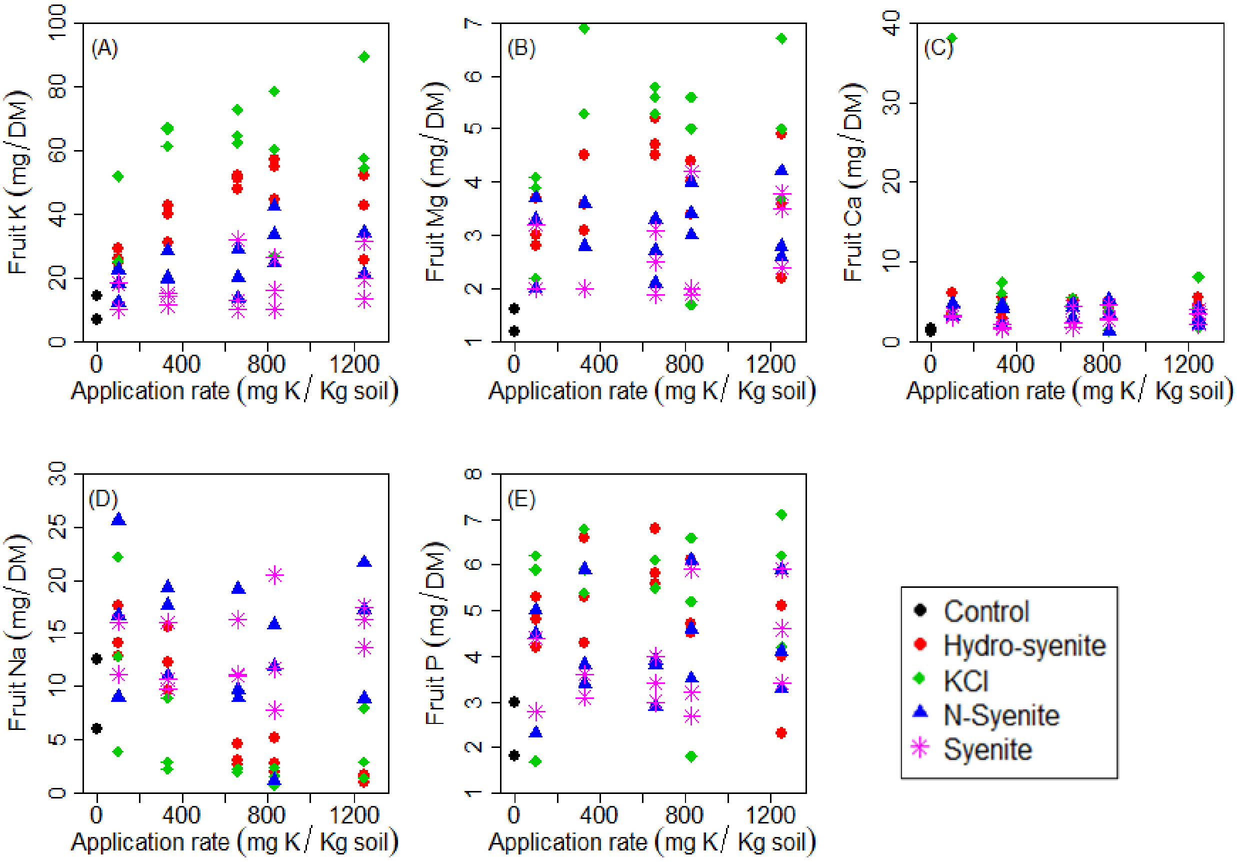

Figure 8.12: Measurements of dried fruits' content of (A) K, (B) Mg (C) Ca and (D) Na in response to K treatments from the different fertilisers at 70 days after transplanting using application rates of 100 (mg K/kg soil), 330 (mg K/kg soil), 660 (mg K/kg soil), 860 (mg K/kg soil) and 1250 (mg K/kg soil) and a control, using data from Baah (2018).

Figure 8.13 shows examples of plant growth status for the tomatoes at 5 weeks and 7 weeks after transplanting respectively, using the different treatments including nepheline syenite.

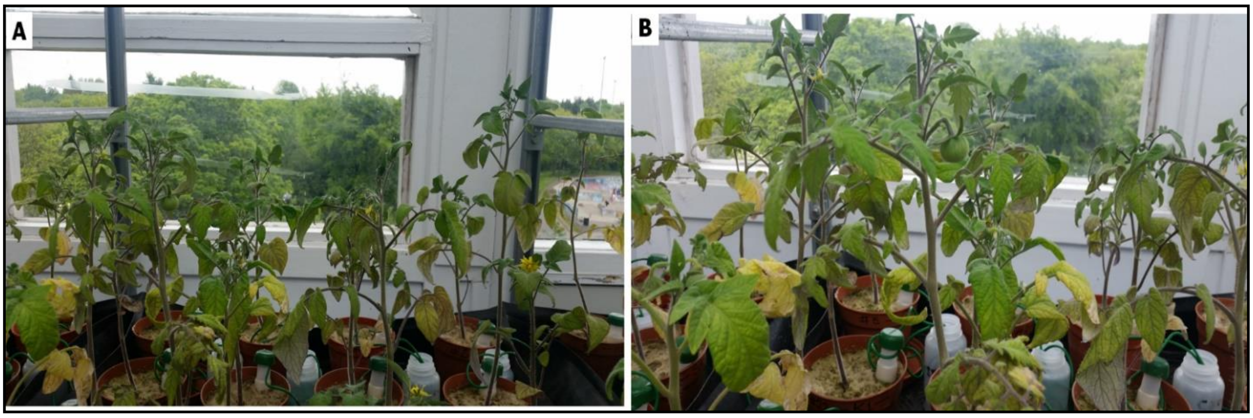

Figure 8.13: Status of the tomatoes (A) 5 weeks and (B) 7 weeks respectively, after transplanting at Newcastle University's Ridley 2 building greenhouse.

8.4 Discussion

The results have shown that the soils are slightly acidic to neutral and the soils also have high TOC (Figures 8.2 and 8.3). The pH values are consistent with other studies on Malawi's soils such as Chilimba et al. (1999), Kamanga (2011) and Lakudzala (2013) who found mean pH values of 6.3, 5.4 and 6.1 pH, respectively (Table 9.4). The soils are within the range of favourable acidity for most crops and also ideal conditions for K fixation and exchange for plant uptake (McKenzie, 2003). The organic carbon also shows high values under the same range of pH which demonstrates that the soils are well buffered with minimal changes in pH. McKenzie (2003) argues that soils with high organic matter and high cation exchange capacity (CEC) have potential for large amounts of exchangeable acidity.

The high soil organic matter within the pH range of 5.5-7 in Figure 8.1, therefore, shows that the soils are ideal for microbial activity, enhanced aeration and increased nutrient mineralisation (McKenzie, 2003; Spargo et al., 2013). The lack of correlation between soil pH and exchangeable K cations shows that the soils are either K-deficient or the available soil K is swiftly absorbed by the plants, because nepheline has a high dissolution rate (Palandri and Kharaka, 2004) thus making K readily available. The high TOC values in the same areas which have high extractable K cations further suggest that the soil release of K for plants is high, as high TOC indicates high levels of input of plant-derived material. This is supported by other studies which have shown that addition of potassium to the soils increased yield significantly in Malawi's soils (Chilimba et al., 1999; Lakudzala, 2013).

The soil analyses have further shown that the Ca:Mg ratio is high, >2:1, as observed in Figure 8.4. This is often observed for soils with a good structure (Laboratories A & L Canada, 2013), which can support plant growth and retain nutrients applied to the soils for plant growth. Studies have further recommended that there is need to ensure K:Mg balance in the soil in order to support growth of high K demanding crops (Laboratories A & L Canada, 2013) because an imbalance of either of the two leads to yield loss. Figure 8.4 has shown that there is a positive correlation in the soils derived from the nepheline syenites and alkali granites. This suggests that the fertilisers from these rocks are potentially ideal for the supply of all the major alkali metals namely K, Mg, Ca and Na needed by plants.

The results from the tomato growth experiments conducted by Baah (2018) have shown that Malawi's nepheline syenites worked well as an alternative potash fertiliser. In Figures 8.8 (A) and 8.9 (A) it has been shown that the concentration of K in soil from nepheline syenite application was generally higher than the other rock sources used in the experiment namely hydro-syenite and syenite. With extractable K concentration of 76.51 mg kg^{-1} soil, Malawi's nepheline syenite was only second to KCl at 94.38 mg kg^{-1} soil, whereas K content was 26.59 mg kg^{-1} soil from syenite and 26.09 mg kg^{-1} soil from hydro-syenite. Appendices 8.5-8.8 show standard deviations of some of the plant growth analyses.

However, while these preliminary plant growth experiments have been successful, it is important to also consider that the greenhouse conditions were not controlled or simulated to environmental or climatic conditions. Therefore, it could have been more helpful if they conducted in environmental conditions like those of the Southern Hemisphere's tropical regions, for which these alternative potash sources are largely intended. In addition, it would be necessary to use a different crop, especially the major food crops grown in Malawi in order to ascertain the importance of alternative potash sources from nepheline syenite.

8.4.1 Comparison with data from existing literature

Literature about the soil quality and nutrient status in Malawi's soils is very scant because not many studies have been conducted. The results from this study are within the expected range of soil pH and organic carbon that has been found in other studies on Malawi's soils (e.g. Benjala et al., 2015; Chilimba et al., 1999; Lakudzala, 2013; Maida, 2013; Phiri et al., 2010; Snapp, 2008), as shown Table in 8.4.

Table 8.4 also shows that most previous studies focussed on soil pH and soil organic matter determination for agricultural studies and not determination of the exchangeable cations. The data used in the previous studies also appear to have been too generalised. Perhaps the studies themselves had intentionally focused on cultivated farming areas which were easily accessible for the researchers unlike the remote bushland covered by this study's fieldwork. The results from this study also suggest that K values are higher than most of the average K data from the existing literature. This suggests that soils from nepheline syenites have higher K content. They could be confirmation of earlier studies that soil mining is high in Malawi soils where application of K fertiliser was also low (Lakudzala, 2013; Snapp, 1998).

Table 8.3: Summary of means of soil analyses from this study's fieldwork and existing literature.

Location sampled	**pH**	**TOC (%)**	**Na (cmol/kg)**	**K (cmol/kg)**	**Ca (cmol/kg)**	**Mg (cmol/kg)**	**CEC (cmol/kg)**	**Reference**
Kasungu Mt	5.86	3.16	0.27	1.26	7.81	2.10	27.37	This study
Kasungu Chipala	5.47	2.65	0.31	0.96	3.05	0.90	23.83	This study
Dzalanyama	6.13	1.57	0.28	0.82	1.96	0.57	20.17	This study
Chaone	5.31	3.07	-	0.68	1.29	0.47	21.06	This study
Junguni	5.88	3.55	-	1.00	6.13	0.99	33.27	This study
Mongolowe	6.36	2.54	-	1.78	5.75	1.51	26.15	This study
Nkhuzi Bay	6.76	0.59	1.00	0.28	1.24	0.70	31.65	This study
Mangochi Hill	6.07	1.09	1.00	0.22	0.31	0.23	23.38	This study
Tundulu complex	7.15	3.94	-	0.58	1.62	0.22	25.90	This study
Kasungu	5.49	0.94	-	-	-	-	-	(Phiri et al., 2010)
Lilongwe	4.85	5.75	-	0.27	6.98	1.12	-	(Maida, 2013)
Namwera	5.45	2.70	-	0.31	3.28	0.46	-	(Maida, 2013)
Mchinji	4.80	3.50	-	0.17	1.99	0.36	-	(Maida, 2013)
Thyolo	5.70	2.40	-	0.19	2.50	0.50	-	(Maida, 2013)
Mangochi	5.25	6.85	-	0.63	4.26	2.85	-	(Maida, 2013)
Nsuwadzi	4.49		-	0.03	2.78	0.37	3.29	(Lakudzala, 2013)
Mphonde	7.76	-	-	0.00	5.10	1.80	18.30	(Lakudzala, 2013)
Kasungu	5.03	-	-	0.05	6.40	2.35	7.10	(Lakudzala, 2013)
Bvumbwe	4.74	-	-	0.06	2.48	0.42	4.17	(Lakudzala, 2013)
Chitedze	5.37	-	-	0.02	3.16	1.14	7.53	(Lakudzala, 2013)
Mzuzu ADD	5.70	1.20	-	0.50	2.30	-	-	(Snapp, 1998)
Karonga ADD	6.20	1.30	-	0.70	3.10	-	-	(Snapp, 1998)
Lilongwe ADD	6.20	1.30	-	0.40	3.10	-	-	(Snapp, 1998)
Kasungu ADD	5.90	1.70	-	0.50	1.90	-	-	(Snapp, 1998)
Blantyre ADD	5.90	1.20	-	1.10	3.00	-	-	(Snapp, 1998)
Mpherero Estate	4.28	1.32	-	0.62	-	-	3.69	(Benjala et al., 2015)
Chitedze	5.00	1.25	-	-	-	-	-	(Chilimba et al., 1999)
Bembeke	5.53	0.83	-	-	-	-	-	(Chilimba et al., 1999)
Bolero	5.29	0.70	-	-	-	-	-	(Chilimba et al., 1999)
Mbawa	5.90	0.82	-	-	-	-	-	(Chilimba et al., 1999)
Domasi	6.17	0.36	-	-	-	-	-	(Chilimba et al., 1999)
Lunyangwa	4.42	0.86	-	-	-	-	-	(Chilimba et al., 1999)
Meru	5.90	0.97	-	-	-	-	-	(Chilimba et al., 1999)
Mkondezi	4.26	0.85	-	-	-	-	-	(Chilimba et al., 1999)
Mulanje	4.55	0.60	-	-	-	-	-	(Chilimba et al., 1999)
Mwanza	5.67	0.29	-	-	-	-	-	(Chilimba et al., 1999)
Namadzi	4.68	0.90	-	-	-	-	-	(Chilimba et al., 1999)
Nanyumbu	5.80	0.15	-	-	-	-	-	(Chilimba et al., 1999)
Nyambi	6.27	0.36	-	-	-	-	-	(Chilimba et al., 1999)
Phalombe	4.60	0.16	-	-	-	-	-	(Chilimba et al., 1999)
Rumphi	5.47	0.19	-	-	-	-	-	(Chilimba et al., 1999)
Thumbwe	5.35	0.19	-	-	-	-	-	(Chilimba et al., 1999)
Zombwe	5.49	0.71	-	-	-	-	-	(Chilimba et al., 1999)

In addition, as shown in Figure 8.14 (A and B), the data from previous studies and this study show that soils with soil pH conditions between5-7 mostly also have low organic carbon and low CEC values suggesting lower soil quality. The data further show no association between soil organic carbon, and between extractable K and extractable Mg (Figure 8.14 (C and D), respectively).

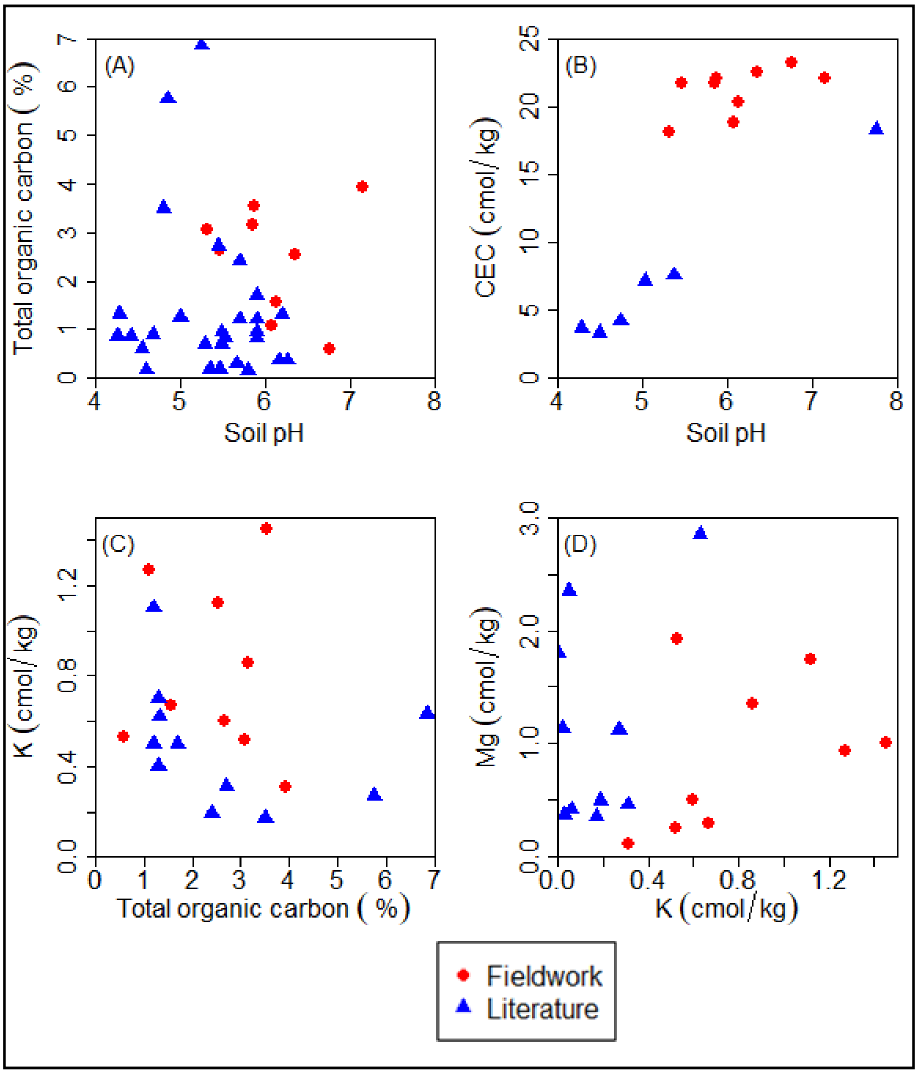

Figure 8.14: Comparison of results from this study's fieldwork and data from the literature.

This pilot study has used the soil samples collected during the fieldwork from remote areas in Malawi, which were less considered by the other previous studies. The soil samples were from areas which are not cultivated for farming or being used for forestry management. This is because either the local communities considered these lands as unfertile for farming or the areas are too far away from local communities. The work of other researchers such as Chilimba et al. (1999); Lakudzala (2013); Maida (2013) and Snapp (2008) focussed on soil nutrient audits. They focussed mainly on established farms and none of their studies tried to assess the nutrient release from the soils derived directly from the rocks. Therefore, this study provides preliminary information about the soil quality and novel information on the K release from nepheline syenites, as well as the potential of Malawi's soils to retain and supply important plant nutrients such as K, Mg, and Ca.

8.5 Conclusion

This chapter has shown that the soils from Malawi have variable extractable cations of K, Ca, Mg and Na. The soil pH and TOC results suggest the soils are of good quality for both plant growth and fixation of useful nutrients notably K. The soil pH and organic carbon determined in this study are within the same ranges as those determined by other previous studies on Malawi's soil quality. However, data on extractable cations is very limited in previous studies, but they do demonstrate greater release of Na and K from nepheline than from feldspars. It may be concluded at this point that this chapter supports the study's hypothesis that Malawi's nepheline syenites can be used as alternative potash sources. The chapter has further addressed this project's Objective 6, the Malawi nepheline syenite does provide plant-available K and is beneficial to growth. Therefore, through plant growth trials it has been demonstrated that Malawi nepheline syenites are suitable as a fertiliser.

Chapter 9: Conclusion and Recommendations

9. Introduction

This chapter mainly addresses the overarching goal of this Thesis by considering the potential of the use of nepheline syenites of Malawi, as alternative potash fertiliser sources. It also considers the location and distance of the identified nepheline syenites to agricultural communities, and the contribution of this study to the world of knowledge. This study adopted a multidisciplinary approach by combining geology, geochemistry, remote sensing and soil science.

In response to Hypothesis 1 in chapter 1, Table 1.1, chapter 1 has provided a situational overview of the potassium fertiliser challenges globally, and particularly in Africa. Most (49) of the 54 African countries are K-deficient and fertiliser is too expensive to be purchased by local subsistence farmers who make the bulk of Africa's farming communities. In addressing Objective 1, chapter 2 has shown that most alkaline rocks including nepheline syenites within the EARS could have formed by extensional tectonism. Extensional tectonism is characterised by crustal thinning in the process further initiating faulting which in many cases is associated with alkaline magmatism. For example, most of the nepheline syenites and alkaline rocks, especially in southern and northern Malawi (Figure 1.1), are concentrated within the rift system. However, nepheline syenites and carbonatites in many cases occur adjacent to each other as noted from the carbonatite associated nepheline syenites. This suggests that the two units formed contemporaneously by precipitation from melts of different chemical composition.

In response to Hypothesis 3 and Objective 5, of the Project (chapter 1, Table 1.1), the results of the petrological and geochemical analyses of the rocks from Malawi have shown relationships between geographically dispersed rocks based on the R1-R2 (De la Roche et al., 1980) classification of igneous rocks. This agrees with chapter 2 which also showed that nepheline syenites from Malawi also show similar geochemical composition to the nepheline syenites from other countries such as the North Cape in Norway. This means that the nepheline syenites from Malawi are of have potential for use just like those from other areas in other parts of the world. Such information opens doors for further exploration and exploitation of these agro-minerals by potential investors.

9.1 Relationship between remote sensing and gamma-ray airborne geophysics approaches in identification of nepheline syenites as alternative potash sources

Hypothesis 2 assumed that ASTER satellite remote sensing and gamma-ray radiometry can depict nepheline syenites, syenites and phonolites. Objectives 2-5 sought to confirm this especially through chapter 4 and chapter 5, which have shown that remote sensing and airborne geophysical gamma-ray data and structure-focussed digital terrain models can be applied in geological mapping in line with this Project's Objective 2.

Previously, some studies by workers such as Hecker (2013) and van der Meer et al. (2012) had suggested that silicate rocks could not be mapped using data in the VNIR-SWIR wavelength of the electromagnetic spectrum adding that diagnostic features for silicates mainly occur in the TIR bands (Ferrier et al., 2016; Hecker, 2013). This study has confirmed that it is not easy to distinguish the geochemically-related silicate rocks such as nepheline syenite, syenite and quartz syenite especially within the VNIR wavelength region. However, this Project has also demonstrated in chapter 7 that the assertions of the previous workers are not entirely true. Nepheline syenites have been delineated using TIR data for ASTER band 12 which has proven effective in mapping the nepheline syenites and the SAM SAM Target Finder with BandMax using ASTER VNIR data has been fairly effective.

The study has also shown that there is a good complementary relationship between remote sensing and gamma ray geophysical data. Most of the areas which were identified as possible nepheline syenite or syenites using both ASTER satellite data and SRTM or ASTER GDEM data were also delineated as potential targets using airborne gamma ray data. These techniques have been used with some considerable success as the data were processed to delineate nepheline syenites and related alkaline rocks in Malawi. These techniques have been a success because the targets which were identified and designated as possible nepheline syenites or syenites in chapter 5 and chapter 7 showed good agreement with the results from fieldwork. This has further been confirmed by the geochemical and petrological analyses in chapter 6. These techniques, therefore, compliment each other in mapping nepheline syenite and other alkaline bodies.

In addition, it should be highlighted that other methods and data which were not used in this study may be also useful with similar or even better results, if tried. For example, due to their higher spectral resolution, which makes them more sensitive and with higher detection capacity of materials, hyperspectral remote sensing data would possibly offer better results.

However, such data were not available for Malawi at the time of conducting this study. Therefore, given the time expertise of the researcher and resources available for this study, the approaches and data that have been used were possibly some of the best that could be used in similar situations.

9.2 Implications of the study to Malawi and Africa on use of nepheline syenites as potash fertiliser sources

While different governments in Africa are reporting economic development, it is regrettable that the status of agricultural industry of Africa has not been as robust as expected for many years. Between 1960-1980s there was only 2% p.a. growth in the agricultural sector (1.85% in crop yields against a corresponding 3% p.a. human population growth during the same period (Larson and Frisvold, 1996). There was also decline in per capita growth about 18% (1969–1987) and further decline by 10% decline in 1996. However, nutrient loss due to intensive farming in the Sub-Saharan Africa was about 22kg N, 2.5 kg P and 15 kg of K per hectare each year in last 30 years (Stoorvogel et al., 1993). This situation, coupled with projections that global population is likely to increase to 9 billion (of which 2 billion in Africa alone) by 2040, (Manning, 2015; Sheldrick et al., 2002), food insecurity will most likely be more serious if production is not increased.

In addition, although about 65% of Africa’s population were engaged in the agricultural sector by 2013, the sector offered low productivity because their contribution accounted for only 32% of the continent’s gross domestic product (Marquis et al., 2013). This was largely due to inadequate fertiliser utilisation, especially, in smallholder farming. The various legislative frameworks operation in different countries also contribute lot to the fertiliser markets in Africa. For example, in some African countries there are barriers to the fertiliser market which include the restrictions on who is allowed to import and sell fertiliser in certain parts of the countries. Some countries also have restrictive business policies such as tax and non-tariff regimes which put-off potential investors from investing and trading in fertiliser supply on national or regional scales (USAID and IFDC, 2015). Ott, (2012) adds that the farmgate fertiliser price is controlled by various factors including the synergies between demand and supply. These are, however, further subject to world economic factors, such as transport costs, raw materials and commodity prices, as well as population growth.

Intensification of crop production by increasing soil fertility through fertiliser use is probably the most viable option to achieve food security. It has been noted in chapter 3 that the situation is even more critical for Malawi where 96% of the arable land is occupied by small-holder farmers, with an average cereal production of 1.9 tonnes/ha, compared to large estate farmers whose cereal yield is about 3.2 tonnes/ha (Fuentes, 2013). Between 2006-2015, the price (per tonne) of subsided fertilizer with about 72%N, 18%P, 10%K, has been 95% below the commercial prices (Fuentes, 2013), from around MK 950 (US $2.88) to MK 500 (US $1.52) and then MK 1050 (US $2.36) in 2015-2016 farming year. This shows that small-holder farmers are much more affected by soil nutrient deficiency (Chirwa and Dorward, 2014). In addition, Malawi currently uses a blanket fertilizer recommendation of 92 kg N ha^{-1} and 40 kg P_2O_5 ha^{-1}. This has shown to be ineffective because it assumes a specific crop instead of considering the variable needs of different soils (Chilimba and Liwimbi, 2008; Lakudzala, 2013). Therefore, there is need for easily accessible cheap fertilizer sources and this study has shown that crushed rock fertilizer to be the solution for Malawi.

Most farming communities, particularly in Malawi and Africa, live in rural areas where it is often difficult to access conventional fertilisers. However, most of the nepheline syenite intrusions also occur in the rural remote areas. Therefore, the use of crushed rock is potentially more productive because the farmers can use locally available resources with minimal production costs. Governments could make huge savings on the import costs if they could fund and promote use of crushed-rock fertilisers which are also environmentally friendly on local soils.

9.3 Contribution of new information to the world of knowledge

The contribution of this study to the geoscientific community is worth noting. Firstly, this research has achieved its overarching goal of extending the reach of crushed-rock K fertiliser to Africa. The research's hypothesis was that Malawi's and indeed nepheline syenites from rift tectonic settings in general have potential for use a potash fertiliser. Literature review, fieldwork in Malawi and more importantly, geochemical and petrological analyses have all shown have all shown that nepheline syenites of Malawi are like other nepheline syenites in other countries which have been successfully tested as potash sources. The plant growth experiments conducted by Baah (2018) have vindicated this study's hypothesis that Malawi's nepheline syenites are potentially suited as potassium fertiliser.

Secondly, the nepheline syenites of Malawi and other similar intrusions have been delineated using the gamma-ray, remote sensing and structure-focused digital terrain models as proposed by this study. Using these techniques, some previously undocumented alkaline intrusions have been mapped. For example, the South East quartz syenites and the Mangochi Hill syenites were not previously documented as alkaline rocks (see Figure 1.1 and 5.1). Some of these previously undocumented alkaline rocks, notably the Nkhuzi Bay quartz syenite, have shown high K_2O content. Possibly, some areas such as the Nkhuzi Bay quartz syenites may have been misnamed in earlier geological mapping projects prior to this study. It would, therefore, be a good area for further investigation for alternative potash sources.

Thirdly, this study has also introduced novel techniques for mapping nepheline syenites using remote sensing. It has been shown that field spectroscopy can be used together with gamma-ray field spectrometry in reconnaissance mapping and where laboratory geochemical analysis is not available for nepheline syenites. The NSI (T) ASTER-based index is also worth implementing in future geological mapping studies focussing on nepheline syenites. Through these approaches, this study has further unveiled some hidden geological information of Malawi. The preliminary results from EPMA analyses, whose manuscript is being prepared for a separate journal publication, appear to confirm the presence of the rare calcium nepheline mineral davidsmithite. Before, this study, davidsmithite had never been documented in Malawi. Once fully confirmed, this would be an important discovery in Malawi’s rocks because it would add to the list of known minerals in Malawi.

Lastly, this study has also managed to bridge different disciplines together. As far as it is known presently, this research is the first of its kind in Malawi and possibly, the rest of Africa, which combines various diverse skills together namely: geology, geochemistry, airborne and field gamma-ray spectrometry, field spectroscopy and satellite remote sensing, soil science, as well as geographical information systems (GIS) to solve problems in agriculture. Agro-geology (as this study is also known), is an important discipline for solving soil mining and food insecurity problems globally. While it is challenging to bring together all these skills into one project, the benefits of the results far outweigh the challenges.

9.4 Recommendations from this Project

Several lessons have been drawn from this project. These require further considerations by different stakeholders including Governments, researchers, potential investors and the local communities in areas where farming and these potential K silicate sources from nepheline syenite occur for further work. Therefore, the following recommendations would need attention:

a) There is need to conduct more plant growth trials using nepheline syenites from Malawi as a fertiliser source. It would be more important if the plant growth field trials were done in Malawi or similar tropical conditions for easier technology transfer to the African farmers.

b) The plant growth trials reported in chapter 8 used samples from only one nepheline syenite intrusion (Junguni nepheline syenite) from Malawi. However, as shown in chapters 5 and 6 there are more potential silicate K sources from other nepheline syenites. Therefore, there is a need to assess the potential of the other nepheline syenite intrusions that have been identified in this project through more plant growth trials.

c) The emphasis of this project was on nepheline syenite in view of the dissolution rates of nepheline. The identification of some potential potash sources from these sources is, therefore, very important for quick solutions in remineralising the K-deficient soils. However, in terms of K concentration, it has been shown that other alkaline bodies are also high in K content. For example, the Nkhuzi Bay area quartz syenites show the highest potassium content (Figure 6.2 in chapter 6). In Malawi there are also fewer nepheline syenite intrusions compared to other potassic alkaline bodies. Therefore, it could be beneficial to consider these ultra-potassic alkaline rocks which are, essentially, not nepheline syenites could be considered for long-term slow release alternative potassium fertiliser sources.

d) In addition, it is noted that some of the studied areas had previously been wrongly mapped. For example, the Nkhuzi Bay and Mauni quartz syenites are mapped as granites on the Geological Survey’s geological maps. This shows that there is need to re-map and update the country’s geology information. Considering that most of the geology maps of Malawi were produced over three decades ago, there is need for re-mapping of such areas too to confirm the actual geology. The identification of a new mineral davidsmithite and some undocumented alkaline rocks like the Nkhuzi Bay and Mauni quartz syenites needs further detailed research into the geology of Malawi.

e) Related to the above, it has been noted that there is close association between spectra for nepheline syenites and with the alkali granite spectra. The XRD analysis for soil samples from the central Malawi’s Dzalanyama alkaline granite rock showed presence of nepheline which could suggest that the rocks could be either nepheline syenite or the nepheline observed in the XRD analyses (Figure 8.6) could be from these. Further petrological and geochemical studies on the central Malawi's Dzalanyama alkaline rocks would be helpful to confirm the geology of the area.

f) The NSI (T) ASTER index used in this study also need to be tested in other areas. It has been used on some areas which were not initially identified by the other techniques such as the South West Malawi areas of Thambani and Salambidwe complexes with positive results (Figure 7.31). However, other areas out of Malawi would need to be tested in future works. Therefore, there is need for further research to fully appraise the method.

g) In addition, ground truthing for the results of chapter 5 was not conducted in some parts of Malawi which were identified as potentially nepheline syenite/syenite areas. For example, some areas identified as possible nepheline syenites areas in the northern and south Malawi were not surveyed due to limited time and budget. Therefore, there is need for further ground-truthing in Malawi because such areas need further field geological and geophysical assessments.

h) Furthermore, while the plant growth trials have shown positive results using nepheline syenites and hydro-syenite, additional studies are needed to examine further the dissolution rates, and plant uptake of nutrients from the candidate fertilisers. Numerical modelling approaches are proposed to model the K release and extraction rates of K from the different sources of materials used. This would help to quantify effectively the actual potential of the different rocks in relation to the initial content of K at the start of experiment and the relative content released.

i) In chapter 6 (Table 6.2), it has also been shown that some nepheline syenites also contain apatite. In some areas, such as the Tundulu and Chingale Complexes, apatite is associated with phosphate fertilisers (Straaten, 2002). A local company, Optichem (2000) Malawi Limited, is already utilising the Tundulu phosphate resources for production of phosphate fertiliser (Phiri et al., 2010). Therefore, the presence of apatite in these rocks and other associated rocks, for example, in the carbonatite-associated nepheline syenite areas, and could therefore, increase the usefulness of these rocks as sources of both K and P.

j) The possible discovery of the mineral davidsmithite in Malawi is an opportunity for further research in Malawi's geology. Further geochemical and petrological studies are, therefore, needed to establish the occurrence mechanism of this mineral in Malawi's rocks. At present, this study assumes that occurrence of davidsmithite in Malawi's nepheline syenite could be related to carbonatite-nepheline metasomatism for the carbonatite-associated rocks and Na-K metasomatism for the other nepheline syenites.

k) Thus far, two important questions also need to be considered: *"(i) Can K be easily extracted at low cost? (ii) How can this alternative fertiliser be accessed more easily by* *farmers in remote areas?"* It needs to be appreciated that local Malawians are already involved in small scale mining including quarry stone and gemstone exploitation. The same expertise could also be used for making crushed rock fertiliser in the rural areas. There is need for governments to develop agricultural policies which encourage use of indigenous geological resources for agriculture. For example, this could be promoted by establishing cooperative societies. Through these cooperative societies, the rural farmers and potential small-scale local investors in crushed rock fertilisers could get support from the Government. The support could be in form of equipment for crushing the rocks for fertiliser as well as soft loans to enable investment by the vulnerable groups such as women, the youth and persons with disabilities. The same cooperatives could also help the local communities to get expert advice, for example, on mapping the nepheline syenites, rock identification and processing techniques for crushed rock fertilisers, and the agricultural extension advisers on use of crushed rock fertilisers in the farms.

9.5 Conclusion

This chapter has addressed the three important considerations which could sum up the entire study. The combination of remote sensing and geophysical gamma-ray data with the structure-focussed digital terrain models appears to be more effective in identifying nepheline syenite bodies than using only one of the two datasets. The study shows that combined use of these methods can be applied to identify similar rock units in any part of the world. While image satellite data was affected by masking and gamma-ray data were affected by attenuation factors for the aircraft used in data capture, the digital DEMs used in this study have been able to identify the alkaline rock complexes in those areas.

However, the study has shown that ASTER data may not be the best data for delineating nepheline syenites from petro-geochemically related rocks like syenites and quartz syenites. Hyperspectral datasets are therefore proposed for further work. The geochemical analyses have confirmed that nepheline syenites of Malawi are geochemically similar to some from other parts of the world that have successfully been tested as potash fertiliser. Finally, the plant growth trials performed by an independent study (as shown in chapter 8), augment the geochemical analyses of this study and demonstrate the availability of K from these rocks to plants. It is concluded that this study has indeed provided an important framework for extending the reach of crushed-rock fertiliser to Africa in general, and specifically, Malawi.

References

Aboelkhair H, Ninomiya Y, Watanabe Y, et al. (2010) Processing and interpretation of ASTER TIR data for mapping of rare-metal-enriched albite granitoids in the Central Eastern Desert of Egypt. *Journal of African Earth Sciences* 58(1): 141–151.

Abrams M and Hook S (2002) *ASTER User Handbook Version 2. Jet Propulsion*. California: Jet Propulsion Laboratory/California Institute of Technology.

Al-doski J, Mansor SB, Zulhaidi H, et al. (2013) Image Classification in Remote Sensing. *Journal of Environment and Earth Science* 3(10): 141–148.

Aleks K and Oliver S (2004) ASTER Mineral Index Processing Manual. *Remote Sensing Applications Geoscience Australia* (October 2004).

Ali EA, El_Khidir SO, Babikir IAA, et al. (2012) Landsat ETM+7 Digital Image Processing Techniques for Lithological and Structural Lineament Enhancement: Case Study Around Abidiya Area, Sudan. *The Open Remote Sensing Journal* 5(1): 83–89.

Alle (2007) Plates, plumes, and planetary processes (contents and preface). *Plates, plumes and planetary processes*.

Amer R, Kusky T and El Mezayen A (2012) Remote sensing detection of gold related alteration zones in Um Rus area, central eastern desert of Egypt. *Advances in Space Research* 49(1). COSPAR: 121–134.

An P, Chung CF and Rencz AN (1995) Digital lithology mapping from airborne geophysical and remote sensing data in the Melville Peninsula, Northern Canada, using a neural network approach. *Remote Sensing of Environment* 53(2): 76–84.

Andersen KJ and Krysell M (2005) Dry matter (DM), loss on ignition (LOI) and total organic carbon (TOC): Report on an evaluation study. Horiziontal Report 17. (December): 42.

Andersen T and Sorensen H (1993) Crystallization and metasomatism of nepheline syenite xenoliths in quartz-bearing intrusive rocks in the Permian Oslo Rift, SE Norway. *Norsk Geologisk Tidsskrift* 73(4): 250–266.

Andersen T, Erambert M, Larsen AO, et al. (2010) Petrology of nepheline syenite pegmatites in the Oslo Rift, Norway: Zirconium silicate mineral assemblages as indicators of alkalinity and volatile fugacity in mildly agpaitic magma. *Journal of Petrology* 51(11): 2303–2325.

Andersen T, Elburg M and Erambert M (2016) The miaskitic-to-agpaitic transition in peralkaline nepheline syenite (white foyaite) from the Pilanesberg Complex, South Africa. *Chemical Geology*.

Appelo C. A. and Postma D (2005) Geochemisty, Groudwater and Pollution.: 647.

Asadzadeh S and de Souza Filho CR (2016) A review on spectral processing methods for geological remote sensing. *International Journal of Applied Earth Observation and Geoinformation* 47: 69–90.

Aster Gdem Validation Team (2009) ASTER Global DEM Validation. *lpdaac usgs gov4 accessed 28 July 2009* (June 2009): 28.

Azizi H, Tarverdi MA and Akbarpour A (2010) Extraction of hydrothermal alterations from ASTER SWIR data from east Zanjan, northern Iran. *Advances in Space Research* 46(1): 99–109.

Baah OTP (2018) *Suitability of novel rock-based K-fertilizers for crop production*. Newcastle University.

Badura J and Przybylski B (2005) Application of digital elevation models to geological and geomorphological studies–some examples. *Przeglad Geologiczny* 53(10): 977–983.

Bakken AK, Gautneb H and Myhr K (1997) Plant available potassium in rocks and mine tailings with biotite, nepheline and K-feldspar as K-bearing minerals. *Acta Agriculturae Scandinavica Section B: Soil and Plant Science* 47(3): 129–134.

Bakken AK, Gautneb H, Sveistrup T, et al. (2000) Crushed rocks and mine tailings applied as K fertilizers on grassland. *Nutrient Cycling in Agroecosystems* 56(1): 53–57.

Ballantine JAC, Okin GS, Prentiss DE, et al. (2005) Mapping North African landforms using continental scale unmixing of MODIS imagery. *Remote Sensing of Environment* 97(4): 470–483.

Barnes G and Lumley J (2011) Processing gravity gradient data. *Geophysics* 76(2): I33–I47.

Bates M and Mechenneff F (2013a) *Data Acquisition Report (for) High Resolution Airborne Magnetic and Gravity Survey: The Comprehensive Countrywide Airborne Geophysical Survey*. Toronto, Canada: Sanders Geophysics Limited.

Bates M and Mechenneff F (2013b) *Data Acquisition Report (for) High Resolution Airborne Magnetic and Gravity Survey: The Comprehensive Countrywide Airborne Geophysical Survey*. Toronto, Canada: Sanders Geophysics Limited.

Beamish D (2013) Peat mapping associations of airborne radiometric survey data. *Remote Sensing* 6(1): 521–539.

Beccaluva L, Barbieri M, Born H, et al. (1992) Fractional crystallization and liquid immiscibility processes in the alkaline-carbonatite complex of juquiá (São Paulo, Brazil). *Journal of Petrology* 33(6): 1371–1404.

Belgiu M, Drăguţ L and Strobl J (2014) Quantitative evaluation of variations in rule-based classifications of land cover in urban neighbourhoods using WorldView-2 imagery. *ISPRS Journal of Photogrammetry and Remote Sensing* 87: 205–215.

Bell K and Doyle RJ (1971) K-Rb relationships in some continental alkalic rocks associated with the East African Rift Valley System. *Geochimica et Cosmochimica Acta* 35(9): 903–915.

Bell K and Powell L (1970) Strontium Isotopic Studies of Alkalic Rocks: The Alkalic Complexes of Eastern Uganda. (November): 3481–3490.

Ben-Dor E, Chabrillat S, Demattê JAM, et al. (2009) Using Imaging Spectroscopy to study soil properties. *Remote Sensing of Environment* 113(SUPPL. 1). Elsevier Inc.: S38–S55.

Benediktsson JA, Pesaresi M and Arnason K (2003) Classification and feature extraction for remote sensing images from urban areas based on morphological transformations. *IEEE Transactions on Geoscience and Remote Sensing* 41(9 PART I): 1940–1949.

Benjala MJ, Maida JHA, Lowole MW, et al. (2015) Liming and fertiliser P interaction effects on some indices of fertility of selected Malawi acidic soils. 6(9): 249–259.

Bennett V (2014) ASTER mineral index processing using ERDAS Imagine , ER Mapper , PCI Geomatica and Exelis ENVI. (December 1999): 1999.

Berger M, Moreno J, Johannessen JA, et al. (2012) ESA's sentinel missions in support of Earth system science. *Remote Sensing of Environment* 120: 84–90.

Best MG (2003) *Igneous and Metamorphic Petrology Second Edition. Blackwell Publishing*.

BGS (2009) *Mineral potential of Malawi*. Nottingham, UK: Ministry of Energy and Mines of Malawi and the British Geological Survey.

Bhadra BK, Pathak S, Karunakar G, et al. (2013) ASTER Data Analysis for Mineral Potential Mapping Around Sawar-Malpura Area, Central Rajasthan. *Journal of the Indian Society of Remote Sensing* 41(2): 391–404.

Bierwirth P (1996) Investigation of Airborne Gamma-Ray Images as a Rapid Mapping Tool for Soil and Land Degradation - Wagga Wagga, NSW (AGSO Record 1996/22).

Bishop C, Rivard B, de Souza Filho C, et al. (2018) Geological remote sensing. *International Journal of Applied Earth Observation and Geoinformation* 64(March 2017): 267–274.

Bloomfield K (1965) The Geology of the Zomba Area. *Malawi Ministry of Natural Resources: Geological Survey Department* (16).

Bowden P (1985) The geochemistry and mineralization of alkaline ring complexes in Africa (a review). *Journal of African Earth Sciences* 3(1–2): 17–39.

Breunig FM, Galvão LS, Formaggio AR, et al. (2009) The combined use of reflectance, emissivity and elevation Aster/Terra data for tropical soil studies. *Revista Brasileira de Ciência do Solo* 33(6): 1785–1794.

Broom-Fendley S, Styles MT, Appleton JD, et al. (2016) Evidence for dissolution-reprecipitation of apatite and preferential LREE mobility in carbonatite-derived late-stage hydrothermal processes. *American Mineralogist* 101(3): 596–611.

Broom-Fendley S, Brady AE, Horstwood MSA, et al. (2017) Geology, geochemistry and geochronology of the Songwe Hill carbonatite, Malawi. *Journal of African Earth Sciences* 134: 10–23.

BS7755 BS (1996) Soil quality - determination of the potential cation exchange capacity and exchangeable cations using barium chloride solution buffered at pH = 8.1.

Burke K, Ashwal LD and Webb SJ (2003) New way to map old sutures using deformed alkaline rocks and carbonatites. *Geology* 31(5): 391–394.

Cantisano A (n.d.) Know Your Soil a Handbook for Organic Growers and Gardeners in Temperate and Sub-Tropical Regions.

Carrino TA, Crósta AP, Toledo CLB, et al. (2015) Geology and hydrothermal alteration of the Chapi Chiara prospect and nearby targets, Southern Peru, using ASTER data and reflectance spectroscopy. *Economic Geology* 110(1): 73–90.

Carter AJ (2008) Quantitative Thermal Infrared Analyses of Volcanic Processes and Products: Application To Bezymianny Volcano, Russia.

Carter GS and Bennet JD (1973) *The Geology and Mineral Resources of Malawi: Malawi Survey Dept. Bulletin 6 . Zomba: Govt. Printer. Geological*. Zomba: Malawi Geological Survey Department/Govt. Printer.

Castaldi F, Casa R, Pascucci S, et al. (2012) Estimation of soil textural properties at the field scale from airborne and satellite hyperspectral remote sensing. 14(May 2014): 11646.

Chilimba ADC and Liwimbi L (2008) MW MZ ZnKS.pdf. In: *Annual Report of the Soil and Agricultural Engineering Commodity Group*. Mangochi: Department of Agricultural Research Annual Planning Meeting, pp. 63–75.

Chilimba ADC, Mughogho SK and Wendt J (1999) Mehlich 3 or Modified Olsen for soil testing in Malawi. *Communications in Soil Science and Plant Analysis* 30(7–8): 1231–1250.

Chirwa E and Dorward A (2014) Agricultural Input Subsidies: The Recent Malawi Experience. *Agricultural input subsidies: changing theory and practice*.

Chorowicz J (2005) The East African rift system. *Journal of African Earth Sciences* 43(1–3): 379–410.

Ciceri D, Manning DAC and Allanore A (2015) Historical and technical developments of potassium resources. *Science of the Total Environment* 502. Elsevier B.V.: 590–601.

Clark RN (1999) Chapter 1: Spectroscopy of Rocks and Minerals, and Principles of Spectroscopy. *Manual of Remote Sensing, Volume 3* 3: 3–58.

Clark RN (2004) *Spectroscopy of Rocks and Minerals, and Principles of Spectroscopy*.

Meteoritics & Planetary Science.

Clark RN, Swayze GA, Wise R, et al. (2007) USGS digital spectral library splib06a: U.S. Geological Survey, Digital Data Series 231.

Corrie RK, Ninomiya Y and Aitchison JC (2010) Applying Advanced Spaceborne Thermal Emission and Reflection Radiometer (ASTER) spectral indices for geological mapping and mineral identification on the Tibetan Plateau. *International Archives of the Photogrammetry, Remote Sensing and Spatial Information Sciences - ISPRS Archives* 38(June 2016): 464–469.

Croll R, Swinden S, Hall M, et al. (2014) Mkango Resources Limited Songwe REE Project Malawi. (06 November 2014): 402.

Curtis CD (1976) Stability of minerals in surface weathering reactions: A general thermochemical approach. *Earth Surface Processes* 1(1): 63–70.

Danner M, Locherer M, Hank T, et al. (2015) Spectral Sampling with the ASD FIELDSPEC 4. *EnMAP Consortium - GFZ Data Services*.

Danov M (2007) Measuring the spectral emissivity of rocks and the minerals that form them. *SPIE Newsroom* (January 2007): 10–12.

De la Roche H., Leterrier J, Grandclaude P, et al. (1980) A classification of volcanic and plutonic rocks using R1R2-diagram and major-element analyses — Its relationships with current nomenclature. *Chemical Geology* 29(1–4). Elsevier: 183–210.

De la Roche H, Leterrier J, Granclaude P, et al. (1980) The wide chemical , mineralogical and textural variety of igneous rocks re- quires a classification scheme which can systematise the data on both volcanic and plutonic rocks , and can help to reveal relationships among the different rock types and their p. 29.

Deer WA, Howie RA and Zussman J (1982) *Rock Forming Minerals, Volume 1A. The Geological Society*.

Del Giovine L and Fabietti F (2005) Copper chlorophyll in olive oils: Identification and determination by LIF capillary electrophoresis. *Food Control* 16(3): 267–272.

Demšar U, Harris P, Brunsdon C, et al. (2013) Principal Component Analysis on Spatial Data: An Overview. *Annals of the Association of American Geographers* 103(1): 106–128.

Di Tommaso I and Rubinstein N (2007) Hydrothermal alteration mapping using ASTER data in the Infiernillo porphyry deposit, Argentina. *Ore Geology Reviews* 32(1–2): 275–290.

Dickson BL (2004) Recent advances in aerial gamma-ray surveying. *Journal of Environmental Radioactivity* 76(1–2): 225–236.

Dickson BL and Scott KM (1997) Interpretation of aerial gamma-ray surveys - adding the geochemical factors. *AGSO Journal of Australian Geology and Geophysics* 17(2): 187–

200.

Dickson BL, Fraser SJ and Kinsey-Henderson A (1996) Interpreting aerial gamma-ray surveys utilising geomorphological and weathering models. *Journal of Geochemical Exploration* 57(1–3): 75–88.

Ding C, Li X, Liu X, et al. (2015) Quartzose-mafic spectral feature space model: A methodology for extracting felsic rocks with ASTER thermal infrared radiance data. *Ore Geology Reviews* 66. Elsevier B.V.: 283–292.

Dragut L, Csillik O, Eisank C, et al. (2014) Automated parameterisation for multi-scale image segmentation on multiple layers. *ISPRS Journal of Photogrammetry and Remote Sensing* 88: 119–127.

Eberle D, Hutchins D, Das S, et al. (2015) Automated pattern recognition to support geological mapping and exploration target generation - A case study from southern Namibia. *Journal of African Earth Sciences* 106. Elsevier Ltd: 60–74.

Eby GN (2004) Petrology, Geochronology, Mineralogy, and Geochemistry of the Beemerville Alkaline Complex, Northern New Jersey. *Neoproterozoic, Paleozoic, and Mesozoic Intrusive Rocks of Northern New Jersey and Southeastern New York. Twenty-First Annual Meeting Geological Association of New Jersey, Mahwah, NJ*: 52–68.

Eby GN, Woolley AR, Din V, et al. (1998) Geochemistry and Petrogenesis of Nepheline Syenites: Kasungu-Chipala, Ilomba, and Ulindi Nepheline Syenite Intrusions, North Nyasa Alkaline Province, Malawi. *Journal of Petrology* 39(8): 1405–1424.

Eismann MT (2012) *Hyperspectral Remote Sensing*. *SPIE Press*.

El-Sayed MM, Mohamed FH and Furnes H (2004) Petrological and geochemical constraints on the evolution of late Pan-African Bakriya posts-orogenic ring complex, Central Eastern Desert, Egypt. *Neues Jahrbuch Fur Mineralogie-Abhandlungen* 180(1): 1–32.

Elezaj Z (2016) Geophysical Airborne Survey and Mineral Resources Potential in Kosovo. *Journal of International Environmental Application and Science* 13(1): 146–154. (accessed 2 June 2018).

Elsaid M, Aboelkhair H, Dardier A, et al. (2014) Processing of Multispectral ASTER Data for Mapping Alteration Minerals Zones: As an Aid for Uranium Exploration in Elmissikat-Eleridiya Granites, Central Eastern Desert, Egypt. *The Open Geology Journal* 8(1): 5–69.

Enderle D and Weih R (2005) Integrating supervised and unsupervised classification methods to develop a more accurate land cover classification. *Journal of the ...* 59: 65–73.

Environmental Protection Agency (EPA) (2006) Standard Operating Procedures : Determination of Metals By Inductively Coupled Plasma (ICP). EPA/SW-846 Methods

3015/3050B/6010B.: 42.

EXELIS Visual Information Solutions (2014) ENVI Tutorial : Using ASTER Data with FLAASH.: 1–14.

Faber-Langendoen D, Keeler-Wolf T, Meidinger D, et al. (2014) EcoVeg: a new approach to vegetation description and classification. *Ecological Monographs* 84(4): 533–561.

Fan C, Hongjie X, Wu J, et al. (2012) Analysis of USGS spectral library of silicate minerals : Implication for remote sensing applications Analysis of United States Geological Survey spectral library of silicate minerals : implication for remote sensing applications. (September 2015).

Feizi F and Mansouri E (2014) Recognition of a porphyry system using ASTER data in Bideghan &ndash; Qom province (central of Iran). *Solid Earth Discussions* 6(2): 1765–1798.

Feizi F and Mansuri E (2013) Separation of Alteration Zones on ASTER Data and Integration with Drainage Geochemical Maps in Soltanieh, Northern Iran. *Open Journal of Geology* 03(02): 134–142.

Ferguson J and Currie KL (1971) Evidence of liquid immiscibility in alkaline ultrabasic dikes at callander bay, Ontario. *Journal of Petrology* 12(3): 561–585.

Ferrier G, Naden J, Ganas A, et al. (2016) Identification of Multi-Style Hydrothermal Alteration Using Integrated Compositional and Topographic Remote Sensing Datasets. *Geosciences* 6(3): 36.

Fitton J and Upton B (1987) Alkaline igneous rocks: a review symposium. *Journal of the Geological Society* 142(4): 697–708.

Fitton J and Upton B (2014) *Alkaline Igneous Rocks*. *Geological Society Special Publication No 30*.

Flohr MJK and Ross M (1990) Alkaline igneous rocks of Magnet Cove, Arkansas: Mineralogy and geochemistry of syenites. *Lithos* 26(1–2): 67–98.

Frost BR and Frost CD (2008) A geochemical classification for feldspathic igneous rocks. *Journal of Petrology* 49(11): 1955–1969.

Fuentes P (2013) Malawi Fertilizer Assessment. 1(1). IFDC, Alabama, USA: 1–60.

Gabr SS, Hassan SM and Sadek MF (2015) Prospecting for new gold-bearing alteration zones at El-Hoteib area, South Eastern Desert, Egypt, using remote sensing data analysis. *Ore Geology Reviews* 71. Elsevier B.V.: 1–13.

Gautneb H and Bakken AK (1995) Crushed rocks, minerals and mine tailings as sources of potassium in agriculture. *Norges Geologiske Undersøkelse* 427(1983): 119–122.

Gewali UB, Monteiro ST and Saber E (2018) Machine learning based hyperspectral image analysis: A survey.

Gill RC. (2010) *Igneous Rocks and Their Processes (A Practical Guide)*. 2nd Editio. London,Uk: Wiley Blackwell.

Gillespie AR, Rokugawa S, Hook SJ, et al. (1999) Temperature / emissivity separation algorithm theoretical basis document , Version 2 . 4.: 1–64.

Gillespie MR and Styles MT (1999) BGS Rock Classification Scheme Volume 1: Classification of igneous rocks. *British Geological Survey Research Report, (2nd edition), RR 99–06* 1: 1–52.

Goetz AFH and Rowan LC (2016) Geologic Remote Sensing Authors (s): Alexander F . H . Goetz and Lawrence C . Rowan Published by : American Association for the Advancement of Science Stable URL : http://www.jstor.org/stable/1686005 Accessed : 30-03-2016 09 : 05 UTC Your use of the JST. 211(4484): 781–791.

Goldschmidt VM (1922) Oversikgtskart over utbredelsen av de forskjellige kalimineraler I norsk fjeldgrund.: 268–269.

Gomez C, Delacourt C, Allemand P, et al. (2005) Using ASTER remote sensing data set for geological mapping, in Namibia. *Physics and Chemistry of the Earth, Parts A/B/C* 30(1–3): 97–108.

Goodarzi Mehr S, Ahadnejad V, Abbaspour RA, et al. (2013) Using the mixture-tuned matched filtering method for lithological mapping with Landsat TM5 images. *International Journal of Remote Sensing* 34(24). Taylor & Francis: 8803–8816.

Govil H, Gill N, Rajendran S, et al. (2018) Identification of new base metal mineralization in Kumaon Himalaya, India, using hyperspectral remote sensing and hydrothermal alteration. *Ore Geology Reviews* 92(September 2017). Elsevier: 271–283.

Gowela JP and Masamba CR (2000) *State of Forest and Tree Genetic Resources in Malawi. Prepared for the Second Regional Training Workshop on Forest Genetic Resources for Eastern and Southern African Countries*. Rome.

Gowela JP and Masamba CR (2002) State of Forest and Tree Genetic Resources in Malawi. Prepared for the Second Regional Training Workshop on Forest Genetic Resources for Eastern and Southern African Countries 6–10 December 1999, Nairobi, Kenya; and updated for the SADC Regional Workshop. In: *Forest Genetic Resources Working Papers, Working Paper FGRE*, 2002, p. 27.

Grasty RL and Minty BRS (1995) A Guide to the Technical Specifications for Airborne Gamma-Ray Surveys.: 89.

Grasty RL, Glynn JE and Grant JA (1985) The analysis of multichannel airborne gamma-ray spectra. *GEOPHYSICS* 50(12): 2611–2620.

Gregory PJ and George TS (2011) Feeding nine billion: The challenge to sustainable crop production. *Journal of Experimental Botany*.

Grotzinger J and Jordan TH (2010) *Understanding Earth*. *Earth*.

Grow R (2016) Imagine Exercise 12 : Supervised Classification in Erdas Instructions :: 3–7.

Gualtieri JA and Chettri S (2000) Support vector machines for classification of hyperspectral data. *Geoscience and Remote Sensing Symposium, 2000. Proceedings. IGARSS 2000. IEEE 2000 International* 2(5): 813–815.

Guha A and Vinod KK (2016) New ASTER derived thermal indices to delineate mineralogy of different granitoids of an Archaean Craton and analysis of their potentials with reference to Ninomiya's indices for delineating quartz and mafic minerals of granitoids-An analysis in Dharwar Cr. *Ore Geology Reviews* 74. Elsevier B.V.: 76–87.

Guha A, Singh VK, Parveen R, et al. (2012) Analysis of ASTER data for mapping bauxite rich pockets within high altitude lateritic bauxite, Jharkhand, India. *International Journal of Applied Earth Observation and Geoinformation* 21(1). Elsevier B.V.: 184–194.

Guha A, Ghosh B, Vinod KK, et al. (2015) Implementation of reflection spectroscopy based new ASTER indices and principal components to delineate chromitite and associated ultramafic-mafic complex in parts of Dharwar Craton, India. *Advances in Space Research* 56(7). COSPAR: 1453–1468.

Guillot L (2001) Extraction of full absorption peaks in airborne gamma-spectrometry by filtering techniques coupled with a study of the derivatives. Comparison with the window method. *Journal of Environmental Radioactivity* 53(3): 381–398.

Guimaraes SNP, Hamza VM and da Silva JJ (2013) Airborne geophysical surveys in the north-central region of Goias (Brazil): Implications for radiometric characterization of tropical soils. *Journal of Environmental Radioactivity* 116: 10–18.

Gunduz O and Kara GT (2015) Influence of DEM Resolution on GIS-Based Inundation Analysis. (JUNE).

Gupta AK (2015) *Origin of Potassium-Rich Silica-Deficient Igneous Rocks*. *Origin of Potassium-Rich Silica-Deficient Igneous Rocks*.

Guth PL (2010) Geomorphometric Comparison of Aster Gdem and Srtm. *A special joint symposium of ISPRS Technical Commission IV & AutoCarto - ASPRS/CaGIS 2010 Fall Specialty Conference*: 10.

Haaker RF and Ewing RC (1981) Naturally Occurring Crystalline Phases: Analogues for Radioactive Waste Forms. *Pacific Northwest Laboratory*: 1–263.

Hancock S, Gaulton R and Danson FM (2017) Angular Reflectance of Leaves with a Dual-Wavelength Terrestrial Lidar and Its Implications for Leaf-Bark Separation and Leaf

Moisture Estimation. *IEEE Transactions on Geoscience and Remote Sensing* 55(6): 3084–3090.

Harley AD and Gilkes RJ (2000) Factors influencing the release of plant nutrient elements from silicate rock powders: A geochemical overview. *Nutrient Cycling in Agroecosystems* 56(1): 11–36.

Harlov DE and Austrheim Håkon (2013) Metasomatism and the chemical transformation of rock: Rock-mineral-fluid interaction in terrestrial and extraterrestrial environments. In: *Lecture Notes in Earth System Sciences*, pp. 1–16.

Harlov DE and Austrheim Hakon (2013) *Metasomatism and the Chemical Transformation of Rock - The Role of Fluids in Terrestrial and Extraterrestrial Processes*. *Metasomatism and the Chemical Transformation of Rock SE - 8*.

Harris C and Grantham GH (1993) Geology and petrogenesis of the Straumsvola nepheline syenite complex, Dronning Maud Land, Antarctica.pdf. *Geological Magazine* 130(4): 531–532.

HARRIS Geospatial Solutions (2016) Empirical line atmospheric correction. *Harris geospatial solutions*: 1–7.

Harris NBW, Mohammed AERO and Shaddad MZ (1983) Geochemistry and petrogenesis of a nepheline syenite-carbonatite complex from the Sudan. *Geological Magazine* 120(2): 115–127.

Hauff P (1983) An overview of VIS-NIR-SWIR field spectroscopy as applied to precious metals exploration. *Arvada, Colorado: Spectral International Inc* 80001: 303–403.

Hecker C (2013) *Infrared Spectroscopy on Minerals and Rocks*.

Hecker C, der Meijde M van and van der Meer FD (2010) Thermal infrared spectroscopy on feldspars - Successes, limitations and their implications for remote sensing. *Earth-Science Reviews* 103(1–2). Elsevier B.V.: 60–70.

Hecker CA, Smith TEL, Ribeiro B, et al. (2013) Thermal Infrared Remote Sensing. 17.

Heier KS (1963) A Geochemical Comparison of the Blue Mountain (Ontario , Canada) and Stjernoy (Finnmark , North Norway).

Henderson CMB and Gibb FGF (1972) Plagioclase-Ca-rich-nepheline intergrowths in a syenite from the Marangudzi complex , Rhodesia. 38(June): 0–7.

Hoffbeck JP and Landgrebe DA (1996) Classification of remote sensing images having high spectral resolution. *Remote Sensing of Environment* 57(3): 119–126.

Hole G (2009) Research Skills, Graham Hole - February 2009 - T-tests. (February): 1–18.

Horneck DA, Sullivan DM, Owen JS, et al. (2011) Soil test interpretation guide. *Oregon State University Extension Service* (July): 1–12.

Hosseinjanizadeh M and Tangestani MH (2012) Sub-pixel mapping of the alteration minerals using aster data, a case study from the central part of Dehaj-Sarduiyeh copper belt, SE Kerman, Iran. In: *International Geoscience and Remote Sensing Symposium (IGARSS)*, 2012, pp. 1521–1524.

Hsu P-H (2007) Feature extraction of hyperspectral images using wavelet and matching pursuit. *ISPRS Journal of Photogrammetry and Remote Sensing* 62(2): 78–92.

Hubbard BE, Rowan LC, Dusel-bacon C, et al. (2007) Geologic Mapping and Mineral Resource Assessment of the Healy and Talkeetna Mountains Quadrangles, Alaska Using Minimal Cloud- and Snow-Cover ASTER Data. *Director*.

Hummel S, Hudak a T, Uebler EH, et al. (2011) A Comparison of Accuracy and Cost of LiDAR versus Stand Exam Data for Landscape Management on the Malheur National Forest. *Journal of Forestry* 109(August): 267–273.

Ibraheem I (2015) Comparative study of maximum likelihood and spectral angle mapper algorithms used for automated detection of melanoma. *Skin Research and Technology* 21(1): 84–89.

Ilbeyli N (2004) Field, petrographic and geochemical characteristics of the Hamit alkaline intrusion in the Central Anatolian Crystalline Complex, Turkey. *Turkish Journal of Earth Sciences* 13(3): 269–286.

Im J and Jensen JR (2005) A change detection model based on neighborhood correlation image analysis and decision tree classification. *Remote Sensing of Environment* 99(3): 326–340.

Inzana J, Kusky T, Higgs G, et al. (2003) Supervised classifications of Landsat TM band ratio images and Landsat TM band ratio image with radar for geological interpretations of central Madagascar. *Journal of African Earth Sciences* 37(1–2): 59–72.

Isioye OA and Jobin P (2012) An assessment of digital elevation models (DEMs) from different spatial data sources. *Asian Journal of Engineering, Sciences & Technology* 2(1): 1–17.

Izzuddin MA, Idris AS, Nisfariza MN, et al. (2017a) The development of spectral indices for early detection of *Ganoderma* disease in oil palm seedlings. *International Journal of Remote Sensing* 38(23). Taylor & Francis: 1–23.

Izzuddin MA, Idris AS, Nisfariza MN, et al. (2017b) The development of spectral indices for early detection of *Ganoderma* disease in oil palm seedlings. *International Journal of Remote Sensing* 00(00). Taylor & Francis: 1–23.

Jaireth S, Hoatson DM and Miezitis Y (2014) Geological setting and resources of the major rare-earth-element deposits in Australia. *Ore Geology Reviews*.

Jaques AL, Wellman P, Whitaker A, et al. (1997) High-resolution geophysics in modern geological mapping. *AGSO Journal of Australian Geology and Geophysics* 17(2): 159–173.

Jaremko D and Kalembasa D (2014) A comparison of methods for the determination of cation exchange capacity of soils. *Ecological Chemistry and Engineering S* 21(3): 487–498.

Jena SK, Dhawan N, Rao DS, et al. (2014) Studies on extraction of potassium values from nepheline syenite. *International Journal of Mineral Processing* 133: 13–22.

Jing C, Bokun Y, Runsheng W, et al. (2014) Regional-scale mineral mapping using ASTER VNIR/SWIR data and validation of reflectance and mineral map products using airborne hyperspectral CASI/SASI data. *International Journal of Applied Earth Observation and Geoinformation* 33(1).

JOGMEC (2017) *Annual Report*. Tokyo, Japan.

Johannsen A (1939) *A Quantitative Mineralogical Classification of Igneous Rocks*. *(5 volumes)*. Chicago: University of Chicago Press.

Kalinowski A, Oliver S, Aleks K, et al. (2004) {ASTER} {Mineral} {Index} {Processing} {Manual}. *Geoscience Australia* Remote Sen(October 2004): 1–37.

Kamanga BCG (2011) *Poor people and poor fields ?:Integrating legumes for smallholder soil fertility management in Chisepo, central Malawi.* Wageningen University, Wageningen, Netherlands.

Kamangadazi F, Mwabumba L, Missanjo E, et al. (2016) Selective Harvesting Impact on Natural Regeneration, Tree Species Richness and Diversity in Forest Co-management Block in Liwonde Forest Reserve, Malawi. *International Journal of Scientific Research in Environmental Sciences* 4(2): 47–54.

Kar S, Rathore VS, Champati ray PK, et al. (2016) Classification of river water pollution using Hyperion data. *Journal of Hydrology* 537. Elsevier B.V.: 221–233.

Kassou A, Essahlaoui A and Aissa M (2012) Extraction of Structural Lineaments from Satellite Images Landsat 7 ETM+ of Tighza Mining District (Central Morocco). *Research Journal of Earth Sciences* 4(2): 44–48.

Kechid S-A, Parodi GC, Pont S, et al. (2017) Davidsmithite, (Ca,□)2Na6Al8Si8O32: a new, Ca-bearing nepheline-group mineral from the Western Gneiss Region, Norway. (June): 1005–1013.

Keuchel J, Naumann S, Heiler M, et al. (2003) Automatic land cover analysis for Tenerife by supervised classification using remotely sensed data. *Remote Sensing of Environment* 86(4): 530–541.

Khorram S, Koch FH, van der Wiele CF, et al. (2012) *Remote Sensing*. *Remote sensing.*

King A. and Dawson A. (1976) The geology of the Mangochi-Makanjira area. *Malawi Ministry of Natural Resources: Geological Survey Department*. Bulletin 3. Zomba: Malawi Geological Survey Department/Govt. Printer.: 400.

King BC (1965) Petrogenesis of the alkaline igneous rock suites of the volcanic and intrusive centres of eastern uganda. *Journal of Petrology* 6(1): 67–100.

Kiss JJ, de Jong E and Bettany JR (1988) The distribution of natural radionuclides in native soils of southern Saskatchewan, Canada. *Journal of Environmental Quality* 17(3): 437–445.

Kletetschka G, Connerney JEP, Ness NF, et al. (2004) Pressure effects on martian crustal magnetization near large impact basins. *Meteoritics & Planetary Science* 39(11): 1839–1848.

Kovacevic M, Bajat B, Trivic B, et al. (2009) Geological Units Classification of Multispectral Images by Using Support Vector Machines. *2009 International Conference on Intelligent Networking and Collaborative Systems*: 267–272.

Krogh A (2008) What are artificial neural networks? *Nat Biotechnol* 26(2): 195–197.

Kröner A and Stern RJ (2005) AFRICA | Pan-African Orogeny. *Encyclopedia of Geology* 1(2004): 1–12.

Kruse FA (2012) Mapping surface mineralogy using imaging spectrometry. *Geomorphology* 137(1). Elsevier B.V.: 41–56.

Kruse FA and Perry SL (2007) Regional mineral mapping by extending hyperspectral signatures using multispectral data. *IEEE Aerospace Conference Proceedings*: 1–15.

Kumar C, Shetty A, Raval S, et al. (2015) Lithological Discrimination and Mapping using ASTER SWIR Data in the Udaipur area of Rajasthan, India. *Procedia Earth and Planetary Science* 11. Elsevier B.V.: 180–188.

Laboratories A & L Canada (2013) Understanding Soil Tests - Chemical.

Lakudzala DD (2013) Potassium Response in some Malawi Soils. *International Letters of Chemistry, Physics and Astronomy* 13: 175–181.

Langford RL (2015) Temporal merging of remote sensing data to enhance spectral regolith, lithological and alteration patterns for regional mineral exploration. *Ore Geology Reviews* 68.

Larson BA and Frisvold GB (1996) Fertilizers to support agricultural development in sub-Saharan Africa: What is needed and why. *Food Policy*.

Le Bas MJ, Le Maitre RW, Streckeisen A, et al. (1986) A chemical classification of volcanic rocks based on the total alkali silica diagram. *Journal of Petrology* 27(3): 745–750.

Le Bas MJ, Le Maitre RW and Woolley AR (1992) The construction of the Total Alkali-

Silica chemical classification of volcanic rocks. *Mineralogy and Petrology* 46(1): 1–22.

Le Maitre R., Streckeisen A, Zanettin B, et al. (2002) *Igneous Rocks: A Classification and Glossary of Terms (Recommendations of the IUGS Subcommission on the Systematics of Igneous Rocks). Cambridge University Press*.

Leenaars J, Kempen B, van Oostrum A, et al. (2014) Africa Soil Profiles database: A compilation of georeferenced and standardised legacy soil profile data for Sub-Saharan Africa. In: *GlobalSoilMap*, pp. 51–57.

Lein JK (2012) *Environmental Sensing: Analytical Techniques for Earth Observation*. *Environmental Sensing: Analytical Techniques for Earth Observation*.

Li M, Zang S, Zhang B, et al. (2014) A review of remote sensing image classification techniques: The role of Spatio-contextual information. *European Journal of Remote Sensing* 47(1): 389–411.

Lillesand R.W. TM and K (2015) *Remote Sensing and Image Interpretation*. *John Wiley and Sons, Inc., New York*.

Lillesand TM and Kiefer RW (1979) *Remote Sensing and Image Analysis*. *Geomorphology*.

Lillesand TM, Kiefer RW and Chipman JW (2008) *Remote Sensing and Image Interpretation*. *Lloydia Cincinnati*.

Lillesand TM, Kiefer RW and Chipman WJ (2015) Remote sensing and image interpretation. 7th edition. *Remote sensing and image interpretation.*

Lowell GR and Villas RN (2007) Petrology of nepheline syenite gneiss from Amazonian Brazil. *Geological Journal* 18(1): 53–75.

Lucas G (2013) Investigating the Potential of Landsat 8 OLI Satellite Imagery for Geological Mapping in Namibia.: 2005.

Ma D, Liu J, Huang J, et al. (2016) Spectral similarity assessment based on a spectrum reflectance-absorption index and simplified curve patterns for hyperspectral remote sensing. *Sensors (Switzerland)* 16(2).

Mac Arthur A (2007) Field Guide for ASD FieldSpec Pro- Radiance/Irradiance Measurements in raw DN mode.: 6.

Madi K, Nyabeze P, Gwavava O, et al. (2014) Uranium, thorium and potassium occurrences in the vicinity of hot springs in the northern neotectonic belt in the Eastern Cape Province, South Africa. *Journal of Radioanalytical and Nuclear Chemistry* 301(2): 351–363.

Maida JH. (2013) Phosphorus Status of Some Malawian Soils. *Soil Science* 102(5). Lilongwe, Malawi: 322–328.

Makungwa SD, Chittock A, Skole DL, et al. (2013) Allometry for biomass estimation in

Jatropha trees planted as boundary hedge in farmers' fields. *Forests* 4(2): 218–233.

Manap MA, Ramli MF and Redzwan G (2009) The application of digital elevation model for the interpretation of Klang Valley geological structure. *Disaster Prevention and Management: An International Journal* 18(5): 504–510.

Manchanda ML, Kudrat M and Tiwari AK (2002) Soil survey and mapping using remote sensing. *Tropical Ecology* 43(1): 61–74.

Manning DAC (2010) Mineral sources of potassium for plant nutrition . A review To cite this version : Mineral sources of potassium for plant nutrition . A review. 30: 281–294.

Manning DAC (2012) Minerals and soil development. Vaughan DJ and Wogelius RA (eds) *Environmental Mineralogy II*. Mineralogical Society of Great Britain and Ireland.

Manning DAC (2015) How will minerals feed the world in 2050? *Proceedings of the Geologists' Association* 126(1). The Geologists' Association.: 14–17.

Manning DAC (2017) Innovation in Resourcing Geological Materials as Crop Nutrients. *Natural Resources Research* 27(2). Springer US: 1–11.

Manning DAC, Baptista J, Sanchez Limon M, et al. (2017) Testing the ability of plants to access potassium from framework silicate minerals. *Science of the Total Environment* 574. Elsevier B.V.: 476–481.

Manzines M and Murthy R V. (1980) Mantle metasomatism as a precursor to the genesis of alkaline magmas - isotopic evidence. *American Journal of Science*.

Marks MAW and Markl G (2017) A global review on agpaitic rocks. *Earth-Science Reviews* 173(June). Elsevier: 229–258.

Marquis S, Genter T, Buet A, et al. (2013) International Fertiliser Society. *Conference International Fertiliser Society* 4(May): 1–33.

Mars JC and Rowan LC (2010) Spectral assessment of new ASTER SWIR surface reflectance data products for spectroscopic mapping of rocks and minerals. *Remote Sensing of Environment* 114(9). Elsevier B.V.: 2011–2025.

McKenzie HR (2003) Soil pH and Plant Nutrients. *Ag-Info Centre Fact Sheet* (May): 1–2.

Melendez-Pastor I, Navarro-Pedreño J, Gómez I, et al. (2008) Identifying optimal spectral bands to assess soil properties with VNIR radiometry in semi-arid soils. *Geoderma* 147(3–4): 126–132.

Methods A, Lecture RS, Indices S, et al. (n.d.) Advanced Methods in Remote Sensing Lecture 4: Spectral Indices and Spectral Separability Spectral Indices: An Introduction.: 1–12.

Meunier A, Caner L, Hubert F, et al. (2013) The weathering intensity scale (WIS): An alternative approach of the chemical index of alteration (CIA). *American Journal of Science* 313(2): 113–143.

Mezned N, Abdeljaoued S and Boussema MR (2010) A comparative study for unmixing based Landsat ETM+ and ASTER image fusion. *International Journal of Applied Earth Observation and Geoinformation* 12(SUPPL. 1): 131–137.

Miller RL, Escalante G, Reinemund JA, et al. (1995) Energy and Mineral Potential of the Central American-Caribbean Regions. *Circum-Pacific Council for Energy and Mineral Resources, Earth Science Series* 16.

Milton EJ (2003) Field Spectroscopy. *UNESCO-Encyclopedia of Life Support Systems (EOLSS)* I: 30.

Minty BRS (1998) Multichannel models for the estimation of radon background in airborne gamma-ray spectrometry. *GEOPHYSICS* 63(6): 1986–1996.

Mirzaie M, Darvishzadeh R, Shakiba A, et al. (2014) Comparative analysis of different uni- and multi-variate methods for estimation of vegetation water content using hyper-spectral measurements. *International Journal of Applied Earth Observation and Geoinformation* 26(1). Elsevier B.V.: 1–11.

Missanjo E and Kamanga-Thole G (2015) Estimation of Biomass and Carbon stock for Miombo Woodland in Dzalanyama Forest Reserve, Malawi. *Research Journal of Agriculture and Forestry Sciences* 3(3): 7–12.

Mitchell RH (2009) Peralkaline nephelinite-natrocarbonatite immiscibility and carbonatite assimilation at Oldoinyo Lengai, Tanzania. *Contributions to Mineralogy and Petrology* 158(5): 589–598.

Mitchell RH and Platt RG (1979) Nepheline - plagioclase intergrowths of metasomatic origin from the Coldwell Complex, Ontario. *Canadian Mineralogist* 17: 537–540.

Mohammed S., Brandt K, Gray ND, et al. (2014) Comparison of silicate minerals as sources of potassium for plant nutrition in sandy soil. *European Journal of Soil Science* 65(5): 653–662.

Mohammed S, K B, N.D G, et al. (2014) Comparison of silicate minerals as sources of potassium for plant nutrition in sandy soil . Comparison of silicate minerals as sources of K for plant nutrition in sandy soil. 65(September): 653–662.

Mohanty B, Gupta A and Das BS (2016) Estimation of weathering indices using spectral reflectance over visible to mid-infrared region. *Geoderma* 266(January): 111–119.

Moore G and Paine R (2014) Quantifying Urban-Rural Temperature Differences for Industrial Complexes Using Thermal Satellite Data.

Mountrakis G, Im J and Ogole C (2011) Support vector machines in remote sensing: A review. *ISPRS Journal of Photogrammetry and Remote Sensing*.

Mshali R (2009) Mineral resources of Malawi and mining potential. 62, 27-35. *Society of*

Malawi Journal, 62: 27–35.

Mulder VL, de Bruin S, Schaepman ME, et al. (2011) The use of remote sensing in soil and terrain mapping - A review. *Geoderma* 162(1–2). Elsevier B.V.: 1–19.

Munyati s C, Ratshibvumo T and Ogola J (2013) Landsat TM image segmentation for delineating geological zone correlated vegetation stratification in the Kruger National Park, South Africa. *Physics and Chemistry of the Earth* 55–57: 1–10.

Murrell TS (2013) Is Potassium Fertilizer Really Necessary ?: 9.

Mustard JF and Sunshine JM (1999) *Spectral Analysis for Earth Science: Investigations Using Remote Sensing Data*. *Remote Sensing for the Earth Sciences*.

Mwaniki MW (2010) Geology Mapping and Lineament Visualization using Image Enhancement Techniques: Comparison of Landsat 8 (OLI) and Landsat 7 (ETM+). *Remote Sensing* 8: 1–31.

Nabighian MN, Ander ME, Grauch VJS, et al. (2005) Historical development of the gravity method in exploration. *Geophysics* 70(6): 63ND.

Nair A and Mathew G (2012a) Lithological discrimination of the phenaimata felsic-mafic complex, Gujarat, India, using the advanced spaceborne thermal emission and reflection radiometer (ASTER). *International Journal of Remote Sensing* 33(1): 198–219.

Nair A and Mathew G (2012b) Lithological discrimination of the Phenaimata felsic – mafic complex , Gujarat , India , using the Advanced Spaceborne Thermal Emission and Reflection Radiometer (ASTER). *International Journal of Remote Sensing* 1161(October 2012): 37–41.

Neave DA, Black M, Riley TR, et al. (2016) On the feasibility of imaging carbonatite-hosted rare earth element deposits using remote sensing. *Economic Geology* 111(3): 641–665.

NERC Field Spectroscopy Facility (2010) Guidelines for importing and re-sampling spectra reflectance data for ENVI spectral libraries.

Ninomiya Y and Bihong F (2001) Spectral indices for lithologic mapping with ASTER thermal infrared data applying to a part of Beishan Mountains, Gansu, China. In: *Geoscience and Remote Sensing Symposium, 2001. IGARSS '01. IEEE 2001 International*, 2001, pp. 2988–2990 vol.7.

Ninomiya Y and Fu B (2016) Regional Lithological Mapping Using ASTER-TIR Data: Case Study for the Tibetan Plateau and the Surrounding Area. *Geosciences* 6(3).

Ninomiya Y, Fu B and Cudahy TJ (2005) Detecting lithology with Advanced Spaceborne Thermal Emission and Reflection Radiometer (ASTER) multispectral thermal infrared 'radiance-at-sensor' data. *Remote Sensing of Environment* 99(1–2): 127–139.

Nixon PH and Clark L (1967) The Alkaline Centre of Yelele and its Bearing on the

Petrogenesis of other Eastern Uganda Volcanoes. 104(5). Newcastle University.

Nordt LC and Driese SD (2010) New weathering index improves paleorainfall estimates from Vertisols. *Geology* 38(5): 407–410.

Nude PM, Shervais JW, Attoh K, et al. (2009) Petrology and geochemistry of nepheline syenite and related carbonate-rich rocks in the Pan-African Dahomeyide orogen, southeastern Ghana, West Africa. *Journal of African Earth Sciences* 55(3–4): 147–157.

Öborn I, Edwards AC and Hillier S (2010) Quantifying uptake rate of potassium from soil in a long-term grass rotation experiment. *Plant and Soil* 335(1): 3–19.

Onuma T, Takeda M, Kobayshi H, et al. (2013) *Final Report of the Project for Establishment of Integrated Geographic Information System (GIS) Database for Mineral Resources Abridgment*. Zomba,Malawi.

Ortiz JD (2011) Application of Visible/near Infrared derivative spectroscopy to Arctic paleoceanography. *IOP Conference Series: Earth and Environmental Science* 14(1): 012011.

Ott H (2012) Fertilizer markets and its interplay with commodity and food prices. *JRC Scientific and Policy Reports* (JRC73043).

Owen AJ (1995) Uses of Derivative Spectroscopy. *Spectroscopy*: 8.

Palandri JL and Kharaka YK (2004) A compilation of rate parameters of water-mineral interaction kinetics for application to geochemical modelinPalandri, J. L., & Kharaka, Y. K. (2004). A compilation of rate parameters of water-mineral interaction kinetics for application to geochemical mo. *USGS Open File Report* 2004–1068: 71.

Palluconi F, Hoover G and Alley R (1999) an Atmospheric Correction Method. (February): 0–27.

Paradella W, Bignelli PA, Veneziani P, et al. (1997) Airborne and spaceborne Synthethic Aperture Radar (SAR) integration with Landsat-TM and gamma ray spectrometry for geological mapping in a tropical rainforest environment, the Carajás Mineral Province, Brazil. *International Journal of Remote Sensing* , 18, i(February): 27–29.

Pasquarè G, Bistacchi A, Francalanci L, et al. (2008) Very long Pahoehoe inflated basaltic lava flows in the Payenia volcanic province (Mendoza and La Pampa, Argentina). *Revista de la Asociacion Geologica Argentina* 63(1): 131–149.

Patagonia N (2009) Mineral Exploration for Epithermal Gold in AND. (June 2016).

Pell J (1994) *Carbonatites, Nepheline Syenites.Kimberlites and Related Rocks in British Columbia (Bulletin: 88)*. Victoria, British Columbia, Canada: British Columbia. Ministry of Energy, Mines and Petroleum Resources.

Pereira AA, Pereira JMC, Libonati R, et al. (2017) Burned area mapping in the Brazilian

Savanna using a one-class support vector machine trained by active fires. *Remote Sensing* 9(11).

Pereira JM. (n.d.) Remote Sensing of fire. In: *dvanced trainng on Land Remote Rensing,* pp. 1–56. ESA Earth Online.

Pessoa RS, Silva CA, Moretti BS, et al. (2015) Solubilization of Potassium From Alternative Rocks By Humic and Citric Acids and Coffee Husk. *Ciência e Agrotecnologia* 39(6): 553–564.

Peters E. (1969) The geology of the Kasungu area. *Malawi Ministry of Natural Resources: Geological Survey Department*. Bulletin 2. Zomba: Malawi Geological Survey Department/Govt. Printer: 402.

Phiri AT, Njoloma JP, Kanyama-Phiri GY, et al. (2010) Maize yield response to the combined application of tundulu rock phosphate and pigeon pea residues in Kasungu, Central Malawi. *African Journal of Agricultural Research* 5(11): 1235–1242.

Potter NJ, Kamenetsky VS, Simonetti A, et al. (2017) Different types of liquid immiscibility in carbonatite magmas: A case study of the Oldoinyo Lengai 1993 lava and melt inclusions. *Chemical Geology* 455. Elsevier B.V.: 376–384.

Pour AB and Hashim M (2015) Hydrothermal alteration mapping from Landsat-8 data, Sar Cheshmeh copper mining district, south-eastern Islamic Republic of Iran. *Journal of Taibah University for Science* 9(2). Taibah University: 155–166.

Pour AB, Hashim M and Marghany M (2011) Using spectral mapping techniques on short wave infrared bands of ASTER remote sensing data for alteration mineral mapping in SE Iran. *International Journal of the Physical Sciences* 6(4): 917–929.

Pour BA and Hashim M (2014) ASTER, ALI and Hyperion sensors data for lithological mapping and ore minerals exploration. *SpringerPlus* 3(1): 130.

Pournamdari M, Hashim M and Pour AB (2014a) Application of ASTER and Landsat TM data for geological mapping of esfandagheh ophiolite complex, southern Iran. *Resource Geology* 64(3): 233–246.

Pournamdari M, Hashim M and Pour AB (2014b) Spectral transformation of ASTER and Landsat TM bands for lithological mapping of Soghan ophiolite complex, south Iran. *Advances in Space Research* 54(4): 694–709.

Prado B, Duwig C, Hidalgo C, et al. (2007) Characterization, functioning and classification of two volcanic soil profiles under different land uses in Central Mexico. *Geoderma* 139(3–4): 300–313.

Price JR and Velbel MA (2003) Chemical weathering indices applied to weathering profiles developed on heterogeneous felsic metamorphic parent rocks. *Chemical Geology* 202(3–

4): 397–416.

Priyono J and Gilkes RJ (2008) High-energy milling improves the effectiveness of silicate rock fertilizers: A glasshouse assessment. *Communications in Soil Science and Plant Analysis* 39(3–4): 358–369.

Process TB, Data SI, Spectra E, et al. (2013) ENVI Classic Tutorial : Target Finding with SAM and BandMax.: 1–16.

Qari MHT, Madani a a, Matsah MIM, et al. (2008) Utilization of Aster and Landsat Data in Geologic Mapping of Basement Rocks of Arafat Area , Saudi Arabia. *Science* 33(1): 99–116.

Qiu F, Abdelsalam M and Thakkar P (2006) Spectral analysis of ASTER data covering part of the Neoproterozoic Allaqi-Heiani suture, Southern Egypt. *Journal of African Earth Sciences* 44(2): 169–180.

Raghuwanshi SS (1992) Airborne gamma-ray spectrometry in uranium exploration. *Advances in Space Research* 12(7): 77–86.

Rajaraman HS, Nagendra Babu G, Chavan SJ, et al. (2013) Signature of potassium enrichment in granite of the Chitrial area, Nalgonda district, Andhra Pradesh: Inferences using its U, Th, K2O, Na 2O, Rb, Ba and Sr contents. *Journal of the Geological Society of India* 82(1): 53–58.

Rajendran S and Nasir S (2013) ASTER spectral analysis of ultramafic lamprophyres (carbonatites and aillikites) within the Batain Nappe, northeastern margin of Oman: a proposal developed for spectral absorption. *International Journal of Remote Sensing* 34(8): 2763–2795.

Rajendran S and Nasir S (2015) Mapping of high pressure metamorphics in the As Sifah region, NE Oman using ASTER data. *Advances in Space Research* 55(4). COSPAR: 1134–1157.

Rajesh H. (2004) Application of remote sensing and GIS in mineral resource mapping An overview. *Journal of Mineralogical and Petrological Sciences* 99: 83–103.

Ramakrishnan D and Bharti R (1996) Hyperspectral Remote Sensing and Applications. *Current Science* 108(v. 2821): 879–891.

Ramakrishnan D, Nithya M, Singh KD, et al. (2013) A field technique for rapid lithological discrimination and ore mineral identification: Results from Mamandur Polymetal Deposit, India. *Journal of Earth System Science* 122(1): 93–106.

Ravelo AC and Abril EG (2010) Remote sensing. *Applied Agrometeorology* (March): 1013–1024.

Reeves C V. and Zeil PW (1990) Airborne geophysics and remote sensing: some common ground in presentation techniques and interpretation. In: *Remote Sensing: An Operational Technology for the Mining and Petroleum Industries*. Springer, Dordrecht, pp. 75–88.

Reganold JP and Harsh JB (1985) Expressing cation exchange capacity in milliequivalents per 100 grams and in SI units. *Journal of Agronomic Education* 14(2): 84–90.

Research Systems (2000) ENVI Tutorials. *ENVI Tutorials*.

Robb L (2005) *Introduction To Ore-Forming Processes,. Blackwell Publishing*. Blackwell.

Roberts S and Vilakazi T (2014) Regulation and rivalry in transport and fertilizer supply in Malawi, Tanzania and Zambia. (2010): 1–31.

Robinson I and MacArthur A (2011) The Field Spectroscopy Facility Post Processing Toolbox User Guide. *Post processing spectral data in MATLAB*.

Roos S De and Jong SM De (2017) Spectral analysis of rock samples from East Suriname using the Spectral Evolution PSR +. (November).

Rossi G, Oberti R and Smith DC (1989) The crystal structure of a potassium-poor calcium-rich silicate with the nepheline framework, and crystal-chemical relationships in the compositional space (K,Na,Ca)8(Al,Si)16O32. *Eur. J. Mineral.* 1(1): 59–70.

Rowan LC, Simpson CJ and Mars JC (2004) Hyperspectral analysis of the ultramafic complex and adjacent lithologies at Mordor, NT, Australia. *Remote Sensing of Environment* 91(3–4): 419–431.

Ruzickova K (2012) Digital Surface Models for the Geosciences. *Transactions in GIS*.

Ruzickova K, Ruzicka J and Kukuliac P (2013) Digital terrain model and landforms classification. In: *13th SGEM GeoConference on Informatics, Geoinformatics And Remote Sensing*, 2013, pp. 395–402.

Sabins FF (1999a) Remote sensing for mineral exploration. *Ore Geology Reviews* 14(3–4). Elsevier B.V.: 157–183.

Sabins FF (1999b) Remote sensing for mineral exploration. *Ore Geology Reviews* 14(3–4): 157–183.

Salles R dos R, de Souza Filho CR, Cudahy T, et al. (2017) Hyperspectral remote sensing applied to uranium exploration: A case study at the Mary Kathleen metamorphic-hydrothermal U-REE deposit, NW, Queensland, Australia. *Journal of Geochemical Exploration* 179: 36–50.

Sanz-Scovino JI, Weil S and Jones AA (1992) The mineralogy and potassium reserves of a soil from Carimagua, Colombia. *Geoderma* 52(3–4): 291–302.

Sanz Scovino JI and Rowell DL (1988) The use of feldspars as potassium fertilizers in the savannah of Colombia. *Fertilizer Research* 17(1): 71–83.

Schetselaar E and Kemp E De (2000) Image Classification From Landsat Tm , Airborne Magnetics and Dem Data for Mapping Paleoproterozoic Bedrock Units , Baffin Island ,. *International Archives of Photogammetry and Remote Sensing* XXXIII(B7): 1325–1332.

Schorscher HD and Shea ME (1992) The regional geology of the Poços de Caldas alkaline complex: mineralogy and geochemistry of selected nepheline syenites and phonolites. *Journal of Geochemical Exploration* 45(1–3): 25–51.

Schumann A (1993) Changes in mineralogy and geochemistry of a nepheline syenite with increasing bauxitization, Poços de caldas, Brazil. *Chemical Geology* 107(3–4): 327–331.

Sekisova VS, Sharygin V V., Zaitsev AN, et al. (2015) Liquid immiscibility during crystallization of forsterite-phlogopite ijolites at Oldoinyo Lengai Volcano, Tanzania: Study of melt inclusions. *Russian Geology and Geophysics* 56(12). Elsevier B.V.: 1717–1737.

Sgavetti M, Pompilio L and Meli S (2006) Reflectance spectroscopy (0.3-2.5 μm) at various scales for bulk-rock identification. *Geosphere* 2(3): 142–160.

Shea ME (1992) Isotopic geochemical characterization of selected nepheline syenites and phonolites from the Poços de Caldas alkaline complex, Minas Gerais, Brazil. *Journal of Geochemical Exploration* 45(1–3): 173–214.

Sheldrick W., Syers JK and Lingard J (2002) A conceptual model for conducting nutrient audits at national, regional, and global scales. Nutr. Cycl. Agroecosys. 62(1958): 61–72.

Sheldrick WF and Lingard J (2004) The use of nutrient audits to determine nutrient balances in Africa. *Food Policy* 29(1): 61–98.

Shives RBK, Charbonneau BW, Ford KL, et al. (2000) The detection of potassic alteration by gamma-ray spectrometry—Recognition of alteration related to mineralization. *GEOPHYSICS* 65(6): 2001–2011.

Simakin AG, Salova TP and Eremyashev VE (2010) Mechanism of water solubility in silicate melts of the albite-nepheline system. *Mineralogy and Petrology* 99(3–4): 279–285.

Skirrow RG, Huston DL, Mernagh TP, et al. (2013) *Critical Commodities for a High-Tech World: Australia's Potential to Supply Global Demand*.

Smethurst MA, Strand T, Sundal AV, et al. (2008) Large-scale radon hazard evaluation in the Oslofjord region of Norway utilizing indoor radon concentrations, airborne gamma ray spectrometry and geological mapping. *Science of the Total Environment* 407(1): 379–393.

Smith RB (2003) Computing the Planck Function. *Professional Paper, Yale University* 77(February): 1–3.

Smith RT (2006) Introduction to Remote Sensing of\nEnvironment (RSE) With TNTMips

TNTView.: 32.

Snapp SS (1998) Soil nutrient status of smallholder farms in Malawi. *Communications in Soil Science and Plant Analysis* 29(17–18): 2571–2588.

Snapp SS (2008) Soil nutrient status of smallholder farms in Malawi. *Communication in Soil Science and Plant Analysis* 29(October 2013): 2571–2588.

Sorensen H (1997) The agpaitic rocks: an overview. 61(98): 485–498.

Sørensen H (1974) *The Alkaline Rocks*. Sørensen H (ed.). London: John Wiley & Sons Ltd.

Sorzano COS, Vargas J and Montano a P (2014) A survey of dimensionality reduction techniques. *arXiv preprint arXiv:1403.2877*: 1–35.

Sowmya P and Giridhar MVS. (2017) Analysis of Continuum Removed Hyper Spectral Reflectance Data of Capsicum Annum of Ground Truth Data. 10(8): 2233–2241.

Spargo J, Allen T and Kariuki S (2013) Interpreting Your Soil Test Results.: 4.

Stare J, Meden A and Hadži D (2018) Structure Determination by Joint Effort of X-ray Powder Diffraction and Quantum Calculations: Crystal Structure and Short Hydrogen Bonding in Pentadecafluorooctanoic Acid Hydrate. *Croatica Chemica Acta* 91(2): 209–220.

Stoorvogel JJ, Smaling EMA and Janssen BH (1993) Calculating soil nutrient balances in Africa at different scales - I Supra-national scale. *Fertilizer Research*.

Straaten P van (2002) *Rocks for Crops - Agromineral of Sub-Saharan*.

Sutherland DS (1967) A note on the occurrence of potassium-rich trachytes in the Kaiserstuhl carbonatite complex, West Germany. *Mineral. Mag* 36: 334–341.

Swinden S and Hall M (2012) *Technical Report and Mineral Resource Estimate for the Songwe Hill Rare Earth Element (REE) Project, Phalombe District, Republic of Malawi*. NI 43-101. Halifax, Canada: MSA Group/Mkango Resources.

Tanner AO (2014) *Feldspar and nepheline syenite*.

Tanner AO (2016) 2014 Minerals Yearbook: Germanium. *U.S. Geolocial Survey* (October).

Tavares L de F, de Carvalho AMX, Camargo LGB, et al. (2018) Nutrients release from powder phonolite mediated by bioweathering actions. *International Journal of Recycling of Organic Waste in Agriculture*.

Telford WM, Geldart LP and Sheriff RE (1990) *Applied Geophysics*. *Book*.

Terraplus (2016) RS-230 Super GAMMA-RAY SPECTROMETER with Memory. Ontario, Canada: Terraplus Inc.

Theodoro SH and Leonardos OH (2006) The use of rocks to improve family agriculture in Brazil. *Anais da Academia Brasileira de Ciencias*.

Thorup-Kristensen K (1994) An easy pot incubation method for measuring nitrogen mineralization from easily decomposable organic material under well defined conditions. *Fertilizer Research* 38(3): 239–247.

Torres CA (2007) Mineral Exploration Using GIS and Processed Aster Images. 6513(Spring).

Tourlière B, Perrin J, Le Berre P, et al. (2003) Use of airborne gamma-ray spectrometry for kaolin exploration. *Journal of Applied Geophysics* 53(2–3): 91–102.

Tsai F and Philpot W (1998) Derivative analysis of hyperspectral data. *Remote Sensing of Environment* 66(1): 41–51.

Tye AM, Milodowski AE and Smedley PL (2017) *Distribution of natural radioactivity in the environment*. Nottingham, UK.

USAID (2013) Climate Risk Profile - Brazil. (April).

USAID and IFDC (2015) Developing Competitive Fertilizer Markets in Africa : Policy Lessons from FTF Country Assessments. (November).

van der Meer F (1999) Can we map swelling clays with remote sensing? *International Journal of Applied Earth Observation and Geoinformation* 1(1): 27–35.

van der Meer FD, van der Werff HMA, van Ruitenbeek FJA, et al. (2012) Multi- and hyperspectral geologic remote sensing: A review. *International Journal of Applied Earth Observation and Geoinformation* 14(1). Elsevier B.V.: 112–128.

Van der Meer FD, van der Werff HMA and van Ruitenbeek FJA (2014) Potential of ESA's Sentinel-2 for geological applications. *Remote Sensing of Environment* 148. Elsevier Inc.: 124–133.

van Straaten P (2007) Farming with rocks and minerals: Challenges and opportunities. *Anais da Academia Brasileira de Ciencias* 78(4): 731–747.

Vaughan RG, Keszthelyi LP, Lowenstern JB, et al. (2012) Use of ASTER and MODIS thermal infrared data to quantify heat flow and hydrothermal change at Yellowstone National Park. *Journal of Volcanology and Geothermal Research* 233–234: 72–89.

Viana RR and Battilani GA (2014) Geochemistry and Petrography of Alkaline rocks from Monte Santo Alkaline Intrusive Suite , Western Araguaia Belt , Tocantins. *Techniques* (June): 72–79.

Vincent K, Dougill AJ, Mkwambisi DD, et al. (2014) Analysis of Existing Weather and Climate Information for Malawi. *University of Leeds* (April): 1–18.

Vinet L and Zhedanov A (2010) A 'missing' family of classical orthogonal polynomials. *Oxford University Press*: 87–165.

Walker P (2009) Guidlines fo Post Processing ASD FieldSpec Pro and FieldSpec 3 Spectral Data Files using the FSF MS Excel Template.: 18.

Wang G, Du W and Carranza EJM (2017) Remote sensing and GIS prospectivity mapping for magmatic-hydrothermal base- and precious-metal deposits in the Honghai district, China. *Journal of African Earth Sciences* 128. Elsevier Ltd: 97–115.

Warner TA, Campagna DJ, Evans CS, et al. (1991) Analyzing Remote-Sensing Geobotanical Trends in Quetico- Provincial-Park, Ontario, Canada, Using Digital Elevation Data. *Photogrammetric Engineering and Remote Sensing* 57(9): 1179–1183.

Warner TA, Levandowski DW, Bell R, et al. (1994) Rule-based geobotanical classification of topographic, aeromagnetic, and remotely sensed vegetation community data. *Remote Sensing of Environment* 50(1): 41–51.

Wedajo GK (2017) LiDAR DEM Data for Flood Mapping and Assessment ; Opportunities and Challenges : A Review. *Journal of Remote Sensing & GIS* 6(4): 2015–2018.

Wemegah DD, Preko K, Noye RM, et al. (2015) Geophysical Interpretation of Possible Gold Mineralization Zones in Kyerano , South-Western Ghana Using Aeromagnetic and Radiometric Datasets. *Journal of Geoscience and Envrionment Protection* 3(June): 67–82.

Werff H Van Der, Meer F Van Der and Jong S De (n.d.) Exercise: Continuum removal and spectral feature finding. *Continuum* (figure 3): 3–6.

Whitehead N (2014) Oasis Montaj 7.1 mapping and processing system. Ontario, Canada: Geosoft Inc., pp. 1–325.

Wiedenmann D, Keller J and Zaitsev AN (2010) Melilite-group minerals at Oldoinyo Lengai, Tanzania. *Lithos* 118(1–2): 112–118.

Wilford J (2012) A weathering intensity index for the Australian continent using airborne gamma-ray spectrometry and digital terrain analysis. *Geoderma* 183–184. Elsevier B.V.: 124–142.

Wilford J and Minty B (2006) Chapter 16 The Use of Airborne Gamma-ray Imagery for Mapping Soils and Understanding Landscape Processes. *Developments in Soil Science*.

Wilford JR (1992) Regolith Mapping Using Integrated Landsat TM Imagery and High Resolution Gamma-Ray Spectrometric Imagery - Cape York Peninsula (BMR Record 1992/78).

Winter JD (2014) *Principles of Igneous and Metamorphic Petrology*. 2nd editio. England: Pearson Education Limited.

Woolley A (2015) The peralkaline nepheline syenites intrusion , Chilwa province , of the The peralkaline nepheline syenites of the Junguni intrusion , Chilwa province , Malawi. 52(November): 425–433.

Woolley AR (1982) A Discussion of Carbonatite Evolution and Nomenclature, and the Generation of Sodic and Potassic Fenites. *Mineralogical Magazine* 46(338): 13–17.

Woolley AR (2001) *Alkaline Rocks and Carbonatites of the World. Part 3: Africa. Geological Magazine*. London, Bath: Geological Society of London.

Woolley AR and Kjarsgaard BA (2008) Carbonatite occurrences of the world: map and database. Geological Survey of Canada. Open File 5796.—2008.

Woolley AR, Williams CT, Wall F, et al. (1995) The Bingo carbonatite-ijolite-nepheline syenite complex, Zaire: geology, petrography, mineralogy and petrochemistry. *Journal of African Earth Sciences* 21(3): 329–348.

Worley BA and Cooper AF (1995) Mineralogy of the Dismal Nepheline Syenite, Southern Victoria Land, Antarctica. *Lithos* 35(1–2): 109–128.

Worley BA, Cooper AF and Hall CE (1995) Petrogenesis of carbonate-bearing nepheline syenites and carbonatites from Southern Victoria Land, Antarctica: origin of carbon and the effects of calcite-graphite equilibrium. *Lithos* 35(3–4): 183–199.

Xiaoye Liu (2008) Airborne LiDAR for DEM generation: some critical issues. *Progress in Physical Geography* 32(1): 31–49.

Yajima T (2014) ASTER Data Analysis Applied to Mineral Resource Exploration and Geological Mapping.: 69.

Yamaguchi Y and Naito C (2003) Spectral indices for lithologic discrimination and mapping by using the ASTER SWIR bands. *International Journal of Remote Sensing* 24(22): 4311–4323.

Ye X, Lin X, Dehmeshki J, et al. (2009) Shape-based computer-aided detection of lung nodules in thoracic CT images. *IEEE Transactions on Biomedical Engineering* 56(7): 1810–1820.

Youssef MAS and Elkhodary ST (2013) Utilization of airborne gamma ray spectrometric data for geological mapping, radioactive mineral exploration and environmental monitoring of southeastern Aswan city, South Eastern Desert, Egypt. *Geophysical Journal International* 195(3): 1689–1700.

Yu HJ and Li PJ (2010) Lithologic mapping using LANDSAT ETM plus and ASTER data. *Acta Petrologica Sinica* 26(1): 345–351.

Zhang X and Li P (2014) Lithological mapping from hyperspectral data by improved use of spectral angle mapper. *International Journal of Applied Earth Observation and Geoinformation* 31(1): 95–109.

Zhang X and Pazner M (2007) Comparison of Lithologic Mapping with ASTER, Hyperion, and ETM Data in the Southeastern Chocolate Mountains, USA. *Photogrammetric Engineering & Remote Sensing* 73(5): 555–561.

Zhang X, Pazner M and Duke N (2007) Lithologic and mineral information extraction for gold exploration using ASTER data in the south Chocolate Mountains (California). *ISPRS Journal of Photogrammetry and Remote Sensing* 62(4): 271–282.

Zhang Y-Z, Wu H, Jiang X-G, et al. (2017) Land Surface Temperature and Emissivity Retrieval from Field-Measured Hyperspectral Thermal Infrared Data Using Wavelet Transform. *Remote Sensing* 9(5): 454.

Zhang Y, Xiong S and Chen T (1998) Application of airborne gamma-ray spectrometry to geoscience in China. *Applied Radiation and Isotopes* 49(1–2): 139–146.

Zouzias D, Miliaresis GC and Seymour KS (2011) Interpretation of Nisyros volcanic terrain using land surface parameters generated from the ASTER Global Digital Elevation Model. *Journal of Volcanology and Geothermal Research* 200(3–4): 159–170.

Appendices

Appendix 1.1 The soil nutrients depletion status for African countries (Sheldrick and Lingard, 2004).

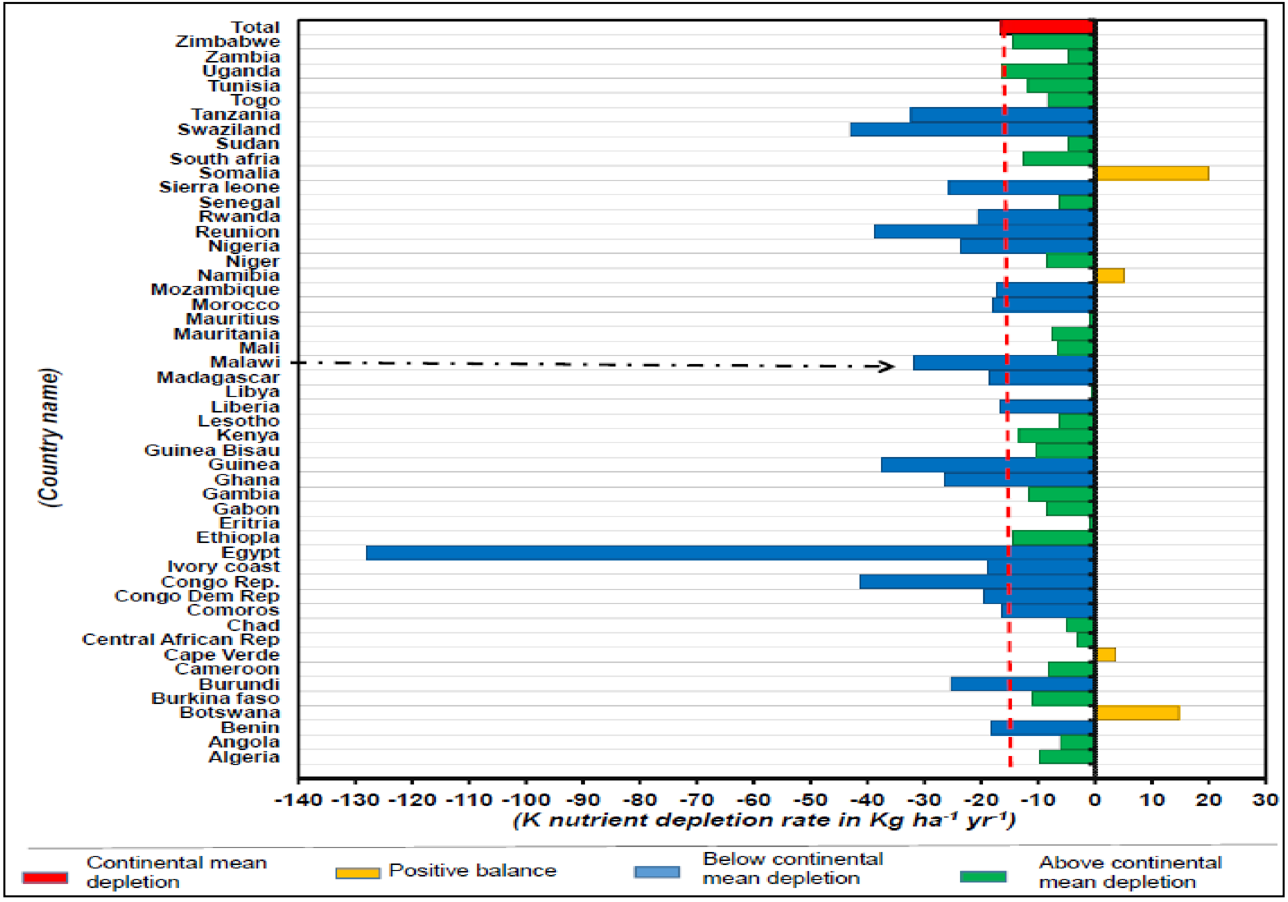

Appendix 5.1: Summary of radionuclide values for airborne and ground spectrometry for the areas sampled (X, Y coordinates in UTM WGS 84 zone 36S).

X	Y	Z (m)	AREA	ROCK NAME	K % (Ground)	U (ppm)	U Ground (ppm)	Th Air (ppm))	Th (Ground (ppm)	Th/U Air (ppm)	Th/U Ground (ppm)	K_2O Air (wt.%)	K_2O Ground (wt.%)	Vegetation (%)
550115	8558158	1172	Kasungu	Granite	3.1	6.57	3.7	23.19	19.9	3.53	5.38	2.58	3.13	30
550210	8558108	1172	Kasungu	Nepheline syenite	3.3	5.82	2.3	22.04	18.3	3.78	7.96	2.48	3.25	30
550258	8558140	1172	Kasungu	Nepheline syenite	3	5.48	3.4	21.46	20.6	3.91	6.06	2.51	3.62	30
550210	8558108	1203	Kasungu	Nepheline syenite	3	5.82	2.7	22.04	20.4	3.78	7.56	2.48	3.62	30
550105	8558063	1203	Kasungu	Nepheline syenite	2.7	6.39	4.1	23.58	17.9	3.69	4.37	2.48	3.62	30
550093	8557918	1201	Kasungu	Nepheline syenite	3.4	6.74	2.7	23.65	19.1	3.51	7.07	2.46	3.62	30
548934	8557263	1201	Kasungu	Nepheline syenite	2.6	5.55	4.1	19.52	20.9	3.52	5.1	2.45	3.62	40
548643	8557703	1204	Kasungu	Nepheline syenite	3.3	6.64	4.2	20.54	16.3	3.09	3.88	2.09	3.62	40
548795	8558382	1204	Kasungu	Nepheline syenite	3	8.27	4.7	23.5	19	2.84	4.04	2.16	3.62	40
549983	8558011	1204	Kasungu	Nepheline syenite	3	6.82	3	24.74	18.3	3.63	6.1	2.48	3.74	40
550263	8558134	1204	Kasungu	Nepheline syenite	3.3	5.48	3.1	21.44	16.4	3.91	5.29	2.51	3.74	40
549965	8557965	1237	Kasungu	Nepheline syenite	3.3	6.94	4.4	24.1	18.6	3.47	4.23	2.42	3.74	40
550258	8558140	1237	Kasungu	Nepheline syenite	3.1	5.48	4.8	21.46	13.9	3.91	2.9	2.51	3.98	40
549983	8558011	1259	Kasungu	Syenogranite	3.4	6.82	2	24.74	18	3.63	9	2.48	3.98	40

550105	8558063	1259	Kasungu	Syenogranite	3.1	6.39	3.6	23.58	19.4	3.69	5.39	2.48	3.98	40
550093	8557918	1098	Kasungu	Nepheline syenite	3.4	6.74	2.6	23.65	23.6	3.51	9.08	2.46	3.98	55
550115	8558158	1098	Kasungu	Nepheline syenite	3.7	6.57	2.9	23.19	14.6	3.53	5.03	2.58	4.1	55
549965	8557965	1113	Kasungu	Nepheline syenite	3	6.94	1.9	24.1	19.3	3.47	10.16	2.42	4.1	55
549099	8557083	1113	Kasungu	Nepheline syenite	3.4	4.37	3.1	17.5	16.4	4.01	5.29	2.37	4.1	55
548934	8557263	1113	Kasungu	Nepheline syenite	3.4	5.55	3.5	19.52	16	3.52	4.57	2.45	4.1	55
548934	8557263	1061	Kasungu	Nepheline syenite	3.9	5.55	0.9	19.52	27.5	3.52	30.56	2.45	4.1	55
548795	8558382	1061	Kasungu	Nepheline syenite	3.4	8.27	3.6	23.5	21.1	2.84	5.86	2.16	4.1	55
548643	8557703	1061	Kasungu	Nepheline syenite	3	6.64	4	20.54	20.8	3.09	5.2	2.09	4.22	55
548643	8557703	1080	Kasungu	Nepheline syenite	3.6	6.64	2	20.54	18.5	3.09	9.25	2.09	4.34	55
549099	8557083	1080	Kasungu	Nepheline syenite	3.5	4.37	2.5	17.5	18.5	4.01	7.4	2.37	4.46	55
548795	8558382	1080	Kasungu	Nepheline syenite	3	8.27	3.3	23.5	19.7	2.84	5.97	2.16	4.7	55
551346	8565068	1208	Chipala	Quartz-felds-biot gneiss	2.9	4.95	1	14.59	26.5	2.95	26.5	2.65	2.65	15
551379	8565075	1208	Chipala	Quartz-felds-biot gneiss	2.4	4.78	2.1	13.73	26.8	2.87	12.76	2.64	2.65	15
551379	8565075	1208	Chipala	Quartz-felds-biot gneiss	2.2	4.78	4.4	13.73	24.2	2.87	5.5	2.64	2.89	15
551346	8565068	1192	Chipala	Quartz-felds-biot gneiss	2.5	4.95	1	14.59	18.6	2.95	18.6	2.65	3.01	15
551346	8565068	1192	Chipala	Quartz-felds-biot gneiss	2.2	4.95	1.6	14.59	22.7	2.95	14.19	2.65	3.01	15
550950	8565104	1192	Chipala	Quartz-felds-biot gneiss	2.5	6.79	3.2	20.39	14.5	3	4.53	2.79	3.25	15
551156	8565032	1125	Chipala	Nepheline syenite	2.8	6.13	1	19.95	26.5	3.25	26.5	2.86	3.37	10
551193	8565153	1125	Chipala	Nepheline syenite	2.9	5.69	2.1	18.67	26.8	3.28	12.76	2.75	3.37	10
550947	8565272	1101	Chipala	Quartz-felds-biot gneiss	2.9	6.06	0.5	18.71	24.8	3.09	49.6	2.6	3.37	10
551156	8565032	1101	Chipala	Quartz-felds-biot gneiss	2.8	6.13	2.2	19.95	20.8	3.25	9.46	2.86	3.49	10
551379	8565075	1078	Chipala	Quartz-felds-biot gneiss	3.1	4.78	2.3	13.73	22.4	2.87	9.74	2.64	3.49	10
551193	8565153	1078	Chipala	Quartz-felds-biot gneiss	2.7	5.69	2.4	18.67	23.4	3.28	9.75	2.75	3.49	10
550797	8565076	1076	Chipala	Nepheline syenite	3.1	6.25	1.7	19.72	24	3.15	14.12	2.73	3.62	10
550950	8565104	1076	Chipala	Nepheline syenite	3.3	6.79	3.7	20.39	14.5	3	3.92	2.79	3.74	10
550891	8565109	1076	Chipala	Nepheline syenite	2.8	6.7	4.4	20.06	18.2	2.99	4.14	2.75	3.74	10
550947	8565272	1083	Chipala	Nepheline syenite	3.5	6.06	1.6	18.71	21.6	3.09	13.5	2.6	3.74	10
550891	8565109	1082	Chipala	Nepheline syenite	3.8	6.7	2.1	20.06	15.8	2.99	7.52	2.75	3.98	10
550797	8565076	1082	Chipala	Nepheline syenite	3.3	6.25	2.7	19.72	20.6	3.15	7.63	2.73	3.98	10
550947	8565272	1082	Chipala	Nepheline syenite	3.1	6.06	4.5	18.71	22.5	3.09	5	2.6	3.98	10
550891	8565074	1090	Chipala	Nepheline syenite	3	6.73	2.2	20.52	25.8	3.05	11.73	2.79	4.22	20
550891	8565109	1090	Chipala	Nepheline syenite	3.3	6.7	4.8	20.06	17.4	2.99	3.63	2.75	4.58	20
552602	8423000	1244	Dzalanyama	Alkali granite	2.7	6.08	0.5	26.27	23	4.32	46	2.54	3.13	20

553418	8417421	1244	Dzalanyama	Alkali granite	2.8	4.85	2.9	24.45	16.2	5.04	5.59	3.27	3.25	20
555358	8416020	1244	Dzalanyama	Alkali granite	2.7	3.56	3.1	17.92	20.1	5.04	6.48	3.09	3.25	20
555358	8416020	1266	Dzalanyama	Alkali granite	2.9	3.56	1.3	17.92	22.9	5.04	17.62	3.09	3.25	20
552602	8423000	1266	Dzalanyama	Alkali granite	3	6.08	1.8	26.27	19.9	4.32	11.06	2.54	3.37	20
555358	8416020	1266	Dzalanyama	Alkali granite	2.9	3.56	2.6	17.92	23.4	5.04	9	3.09	3.37	70
553554	8417563	1294	Dzalanyama	Alkali granite	2.7	5.12	1.1	23.51	25.3	4.6	23	3.86	3.49	70
553554	8417563	1294	Dzalanyama	Alkali granite	3	5.12	1.8	23.51	21.7	4.6	12.06	3.86	3.49	70
553418	8417421	1294	Dzalanyama	Alkali granite	3.2	4.85	3.8	24.45	17.5	5.04	4.61	3.27	3.62	70
553554	8417563	1265	Dzalanyama	Alkali granite	2.6	5.12	2.5	23.51	21.9	4.6	8.76	3.86	3.62	70
552602	8423000	1265	Dzalanyama	Alkali granite	2.8	6.08	3.2	26.27	19.5	4.32	6.09	2.54	3.62	70
553418	8417421	1265	Dzalanyama	Alkali granite	3	4.85	3.3	24.45	18.2	5.04	5.52	3.27	3.86	80
761171	8329281	980	Chaone	Nepheline syenite	5.1	2.53	1.2	12.38	6.7	4.89	5.58	3.65	6.15	80
760086	8327715	980	Chaone	Nepheline syenite	5.8	1.77	3.7	6.58	10.5	3.72	2.84	2.89	6.99	80
760086	8327715	1244	Chaone	Nepheline syenite	6.3	1.77	-	6.58	10.3	3.72	NaN	2.89	6.99	80
761171	8329281	1244	Chaone	Nepheline syenite	6.5	2.53	0.2	12.38	9.8	4.89	49	3.65	7.04	80
760086	8327715	1306	Chaone	Nepheline syenite	6.4	1.77	0.9	6.58	6.5	3.72	7.22	2.89	7.47	80
760216	8328402	1306	Chaone	Nepheline syenite	6.2	1.81	1.2	8.28	7.4	4.58	6.17	2.85	7.59	80
760086	8327715	1306	Chaone	Nepheline syenite	5.8	1.77	1.6	6.58	9.8	3.72	6.13	2.89	7.71	80
760216	8328402	1306	Chaone	Nepheline syenite	5.8	1.81	2.4	8.28	13	4.58	5.42	2.85	7.83	80
755920	8324150	669	Mongolowe	Nepheline syenite	4.7	NaN	2.2	NaN	12.9	NaN	5.86	5.04	4.94	70
756206	8322720	669	Mongolowe	Nepheline syenite	4.7	NaN	7.3	NaN	24	NaN	3.29	NaN	5.66	70
756206	8322720	742	Mongolowe	Nepheline syenite	4.1	NaN	-	NaN	4.7	NaN	-	NaN	5.66	5
754379	8324009	742	Mongolowe	Nepheline syenite	5.4	NaN	0.6	NaN	6.4	NaN	10.67	5.14	5.91	5
753795	8324893	742	Mongolowe	Nepheline syenite	5.6	NaN	1.4	NaN	6.3	NaN	4.5	5.35	5.91	5
753795	8324893	761	Mongolowe	Nepheline syenite	4.9	NaN	-	NaN	5.5	NaN	-	5.35	6.39	5
755920	8324149	761	Mongolowe	Nepheline syenite	6.3	NaN	0.3	NaN	9	NaN	30	5.04	6.51	30
754379	8324009	728	Mongolowe	Nepheline syenite	4.9	NaN	1.2	NaN	4.7	NaN	3.92	5.14	6.51	30
755920	8324149	728	Mongolowe	Nepheline syenite	5.4	NaN	2.1	NaN	8.7	NaN	4.14	5.04	6.75	55
753795	8324893	761	Mongolowe	Nepheline syenite	5.3	NaN	0.7	NaN	6.1	NaN	8.71	5.35	7.59	55
744341	8339639	502	Junguni	Nepheline syenite	4.1	NaN	7.5	NaN	47.2	NaN	6.29	3.61	4.94	55
745443	8339247	502	Junguni	Nepheline syenite	4.8	NaN	8.8	NaN	37.1	NaN	4.22	3.95	4.94	45
745443	8339247	502	Junguni	Nepheline syenite	4.2	NaN	11.5	NaN	57.3	NaN	4.98	3.95	5.06	45
742687	8338941	478	Junguni	Nepheline syenite	4.1	NaN	5	NaN	34.3	NaN	6.86	3.73	5.54	45
744341	8339639	478	Junguni	Nepheline syenite	8.9	NaN	7.6	NaN	25.6	NaN	3.37	3.61	5.66	45
745443	8339247	478	Junguni	Nepheline syenite	4.7	NaN	8.9	NaN	31.4	NaN	3.53	3.95	5.78	45
742687	8338941	492	Junguni	Nepheline syenite	5.4	NaN	7.6	NaN	10.8	NaN	1.42	3.73	5.91	45
742687	8338941	492	Junguni	Nepheline syenite	4.9	NaN	8.2	NaN	14.4	NaN	1.76	3.73	6.03	45
742513	8336698	492	Junguni	Nepheline syenite	4.6	NaN	9.7	NaN	19.1	NaN	1.97	4.74	6.39	15
742687	8338941	492	Junguni	Nepheline syenite	5	NaN	9.9	NaN	21.9	NaN	2.21	3.73	6.39	15

742687	8338941	492	Junguni	Nepheline syenite	5.3	NaN	11.4	NaN	13.4	NaN	1.18	3.73	6.51	15
742513	8336698	497	Junguni	Nepheline syenite	5.3	NaN	2.1	NaN	16.1	NaN	7.67	4.74	7.23	20
744341	8339639	497	Junguni	Nepheline syenite	6	NaN	2.5	NaN	13.9	NaN	5.56	3.61	10.7	20
727432	8403893	634	Mauni Hill	Quartz syenite	5.1	NaN	0.8	NaN	26.4	NaN	33	5.85	3.37	20
727432	8403893	634	Mauni Hill	Quartz syenite	4.8	NaN	1.4	NaN	14.2	NaN	10.14	5.85	3.49	20
727432	8403893	634	Mauni Hill	Quartz syenite	5.3	NaN	1.5	NaN	16.2	NaN	10.8	5.85	3.86	20
727433	8403504	634	Mauni Hill	Quartz syenite	5.5	1.64	1.6	15.07	11.1	9.16	6.94	5.39	5.78	20
727433	8403504	634	Mauni Hill	Quartz syenite	5.7	1.64	2.7	15.07	18.4	9.16	6.82	5.39	6.15	20
727433	8403504	634	Mauni Hill	Quartz syenite	5.6	1.64	3.9	15.07	16.8	9.16	4.31	5.39	6.39	20
727433	8403504	644	Mauni Hill	Quartz syenite	2.8	1.64	-	15.07	22.6	9.16	-	5.39	6.63	20
727433	8403504	644	Mauni Hill	Quartz syenite	2.9	1.64	1.2	15.07	20.5	9.16	17.1	5.39	6.75	45
727433	8403504	644	Mauni Hill	Quartz syenite	3.2	1.64	4.1	15.07	17.5	9.16	4.27	5.39	6.87	45
703158	8426619	556	Chantulo	Quartz syenite	3.9	1.07	-	6.14	13.9	5.72	-	3.17	4.7	45
703158	8426619	556	Chantulo	Quartz syenite	4.8	1.07	-	6.14	6.9	5.72	-	3.17	4.7	45
701435	8425307	556	Chantulo	Quartz syenite	3.9	1.48	0.9	5.59	2.8	3.79	3.11	5.12	5.54	45
701435	8425307	548	Chantulo	Quartz syenite	5.1	1.48	-	5.59	7.8	3.79	-	5.12	5.54	45
699725	8425417	548	Chantulo	Quartz syenite	4.6	1.41	0.1	8.92	4.9	6.35	49	4.79	5.66	45
703158	8426619	548	Chantulo	Quartz syenite	4.6	1.07	0.9	6.14	2.1	5.72	2.33	3.17	5.78	25
699725	8425417	539	Chantulo	Quartz syenite	5	1.41	-	8.92	6.7	6.35	-	4.79	6.03	25
699725	8425417	539	Chantulo	Quartz syenite	5	1.41	-	8.92	10.5	6.35	-	4.79	6.03	25
699725	8425417	539	Chantulo	Quartz syenite	5.1	1.41	-	8.92	9	6.35	-	4.79	6.15	15
701435	8425307	539	Chantulo	Quartz syenite	4.7	1.48	0.9	5.59	6.5	3.79	7.22	5.12	6.15	15
713512	8430260	506	Nkhuzi bay	Quartz syenite	6.9	1.23	-	6.18	4.5	5.01	-	4.65	7.23	15
712308	8432381	506	Nkhuzi bay	Quartz syenite	6	1.5	0.9	12	7.5	7.98	8.33	3.81	7.35	15
713512	8430260	506	Nkhuzi bay	Quartz syenite	6.1	1.23	1.3	6.18	8	5.01	6.15	4.65	7.35	15
712308	8432381	487	Nkhuzi bay	Quartz syenite	7.9	1.5	1.7	12	22.2	7.98	13.06	3.81	7.83	15
711706	8431263	487	Nkhuzi bay	Quartz syenite	6.5	1.94	3	12.91	17	6.67	5.67	4.63	7.95	15
711706	8431263	487	Nkhuzi bay	Quartz syenite	6.1	1.94	3.6	12.91	12.8	6.67	3.56	4.63	8.07	15
711706	8431263	487	Nkhuzi bay	Quartz syenite	6.7	1.94	-	12.91	12.5	6.67	-	4.63	8.32	15
713512	8430260	487	Nkhuzi bay	Quartz syenite	6.6	1.23	2	6.18	9.9	5.01	4.95	4.65	8.32	15
712308	8432381	487	Nkhuzi bay	Quartz syenite	6.9	1.5	2.2	12	12.5	7.98	5.68	3.81	9.52	40
776118	8404012	857	Mangochi	Syenite	3.1	NaN	0.6	NaN	17.9	NaN	29.83	5.9	3.13	40
776118	8404012	857	Mangochi	Syenite	2.8	NaN	2.3	NaN	19.2	NaN	8.35	5.9	3.13	40
776547	8402198	857	Mangochi	Syenite	2.9	NaN	2.5	NaN	14.4	NaN	5.76	4.54	3.25	40
776547	8402198	877	Mangochi	Syenite	3.1	NaN	0.5	NaN	17	NaN	34	4.54	3.37	40
776547	8402198	877	Mangochi	Syenite	2.8	NaN	1.8	NaN	15.1	NaN	8.39	4.54	3.37	40
776616	8401389	877	Mangochi	Syenite	2.8	NaN	2.2	NaN	19.9	NaN	9.05	5.42	3.37	40
776118	8404012	877	Mangochi	Syenite	2.7	NaN	2.4	NaN	14.5	NaN	6.04	5.9	3.49	40
776616	8401389	827	Mangochi	Syenite	2.6	NaN	2.2	NaN	18.7	NaN	8.5	5.42	3.49	40
776118	8404012	827	Mangochi	Syenite	2.9	NaN	2.6	NaN	15.3	NaN	5.89	5.9	3.62	50
776547	8402198	827	Mangochi	Syenite	2.6	NaN	3.7	NaN	16.5	NaN	4.46	4.54	3.74	50
776616	8401389	827	Mangochi	Syenite	3	NaN	14.7	NaN	14.7	NaN	1	5.42	3.74	50
801229	8279856	682	Tundulu	Carbonatite	3.8	NaN	3.2	NaN	21.4	NaN	6.69	NaN	2.89	50
801229	8279856	682	Tundulu	Carbonatite	2.8	NaN	4	NaN	15.8	NaN	3.95	NaN	2.89	50
801354	8280027	682	Tundulu	Carbonatite	3.7	NaN	6.3	NaN	20.2	NaN	3.21	NaN	2.89	50
801229	8279856	682	Tundulu	Carbonatite	3.3	NaN	18.5	NaN	18.5	NaN	1	NaN	3.01	50

801682	8280846	765	Tundulu	Nepheline syenite	3.5	NaN	0.8	NaN	21.1	NaN	26.38	NaN	3.37	50
801229	8279856	778	Tundulu	Carbonatite	2.4	NaN	0.9	NaN	40	NaN	44.44	NaN	3.86	50
801229	8279856	778	Tundulu	Carbonatite	3.4	NaN	2.4	NaN	44.8	NaN	18.67	NaN	3.86	50
801354	8280027	778	Tundulu	Carbonatite	3.3	NaN	2.5	NaN	32.8	NaN	13.12	NaN	3.98	50
801682	8280846	765	Tundulu	Carbonatite	2.5	NaN	1	NaN	47.2	NaN	47.2	NaN	3.98	20
801354	8280027	765	Tundulu	Nepheline syenite	3.2	NaN	1.6	NaN	19.8	NaN	12.38	NaN	4.1	20
801229	8279856	765	Tundulu	Carbonatite	4.7	NaN	2	NaN	29.9	NaN	14.95	NaN	4.22	20
801682	8280846	765	Tundulu	Nepheline syenite	3.2	NaN	2.5	NaN	18	NaN	7.2	NaN	4.46	20
801682	8280846	765	Tundulu	Carbonatite	2.4	NaN	3.4	NaN	53.2	NaN	15.65	NaN	4.58	20
801229	8279856	765	Tundulu	Carbonatite	2.4	NaN	4.7	NaN	40.3	NaN	8.57	NaN	5.66	20
792842	8274409	697	Nkalonje	Carbonatite	2.8	6.7	3	40.49	17.7	6.04	5.9	3.81	3.37	20
792842	8274409	697	Nkalonje	Carbonatite	2.9	6.7	3.5	40.49	18.8	6.04	5.37	3.81	3.49	20
792200	8273399	644	Nkalonje	Nepheline syenite	3.1	4.84	1.2	40.54	20.5	8.37	17.08	4.09	3.74	20
792200	8273399	644	Nkalonje	Nepheline syenite	3.2	4.84	3.2	40.54	17.6	8.37	5.5	4.09	3.86	20
801994	8263648	879	Songwe-Mauze	Nepheline syenite	3.4	NaN	1	NaN	23.7	NaN	23.7	NaN	3.25	20
801994	8263648	879	Songwe-Mauze	Nepheline syenite	3.5	NaN	1.3	NaN	19.5	NaN	15	NaN	3.49	20
801994	8263648	879	Songwe-Mauze	Nepheline syenite	3	NaN	3.9	NaN	17.3	NaN	4.44	NaN	3.49	20
802042	8263438	842	Songwe-Mauze	Fenites	2.9	NaN	1.2	NaN	55.7	NaN	46.42	NaN	3.49	20
801994	8263648	842	Songwe-Mauze	Fenites	3.1	NaN	1.4	NaN	52.7	NaN	37.64	NaN	3.62	20
802151	8263279	842	Songwe-Mauze	Fenites	3.9	NaN	4.1	NaN	32	NaN	7.81	NaN	3.62	20
802042	8263438	787	Songwe-Mauze	Nepheline syenite	2.9	NaN	0.4	NaN	18.5	NaN	46.25	NaN	3.74	20
802151	8263279	787	Songwe-Mauze	Nepheline syenite	2.7	NaN	2.6	NaN	21.3	NaN	8.19	NaN	4.1	20
802151	8263279	787	Songwe-Mauze	Nepheline syenite	2.9	NaN	2.9	NaN	11.7	NaN	4.03	NaN	4.22	20
802042	8263438	787	Songwe-Mauze	Nepheline syenite	3	NaN	4	NaN	15.8	NaN	3.95	NaN	4.7	20
801581	8263769	710	Songwe-Mauze	Carbonatite	4.8	NaN	2.8	NaN	37	NaN	13.21	NaN	5.18	20
801581	8263769	710	Songwe-Mauze	Carbonatite	4.3	NaN	4.3	NaN	36.4	NaN	8.47	NaN	5.78	20
748807	8299377	1421	Zomba Mt	Syenite	3.5	NaN	0.5	NaN	20.5	NaN	41	NaN	3.74	90
746874	8302650	1421	Zomba Mt	Syenite	3.8	1.67	2.3	7.61	15.5	4.55	6.74	0.92	3.86	90
746655	8305436	1421	Zomba Mt	Syenite	3.1	5.8	4.3	16.84	19.9	2.9	4.63	3.87	4.22	80
748807	8299377	1039	Zomba Mt	Syenite	3.5	NaN	1.9	NaN	18	NaN	9.47	NaN	4.22	75
747297	8299422	1295	Zomba Mt	Syenite	3.2	NaN	1.9	NaN	21	NaN	11.05	NaN	4.22	50
748807	8299377	1574	Zomba Mt	Quartzo-felds gneiss	3.9	NaN	1.2	NaN	22.1	NaN	18.42	NaN	4.58	50
746655	8305436	1574	Zomba Mt	Charnockitic-gneiss	3.5	5.8	3	16.84	17.9	2.9	5.97	3.87	4.7	50

Appendix 7.1: Technical specifications of the ASD Field Spec pro spectrometer (Danner et al., 2015).

Spectral range	350-2500 nm
Spectral resolution	3 nm @ 700 nm 10 nm @ 1400/2100 nm
Sampling Interval	1.4 nm @ 350-1050 nm 2 nm @ 1000-2500 nm
Scanning Time	100 milliseconds
Stray light specification	VNIR 0.02%, SWIR 1 & 2 0.01%
Wavelength reproducibility	0.1 nm
Wavelength accuracy	0.5 nm
Maximum radiance	VNIR 2X Solar, SWIR 10X Solar
Bands	2151

Detectors	VNIR detector (350-1000 nm): 512 element silicon array SWIR 1 detector (1000-1800 nm): Graded Index InGaAs Photodiode, TE Cooled SWIR 2 detector (1800-2500 nm): Graded Index InGaAs Photodiode, TE Cooled
Input	1.5 m fibre optic (25° field of view). Optional narrower field of view fibre optics available.
Noise equivalent radiance (NEdL)	VNIR 1.0 X10-9 W/cm2/nm/sr @700 nm SWIR 1 1.2 X10-9 W/cm2/nm/sr @ 1400 nm SWIR 2 1.9 X10-9 W/cm2/nm/sr @ 2100 nm
Weight	5.44 kg (12 lbs)
Calibrations	Wavelength, absolute reflectance, radiance*, irradiance*. All calibrations are NIST traceable. (*radiometric calibrations are optional)
Computer	Windows® 7 64-bit laptop (instrument controller)

Appendix 7.2: Steps for the SAM Target Finder with BandMax algorithms (Process et al., 2013).

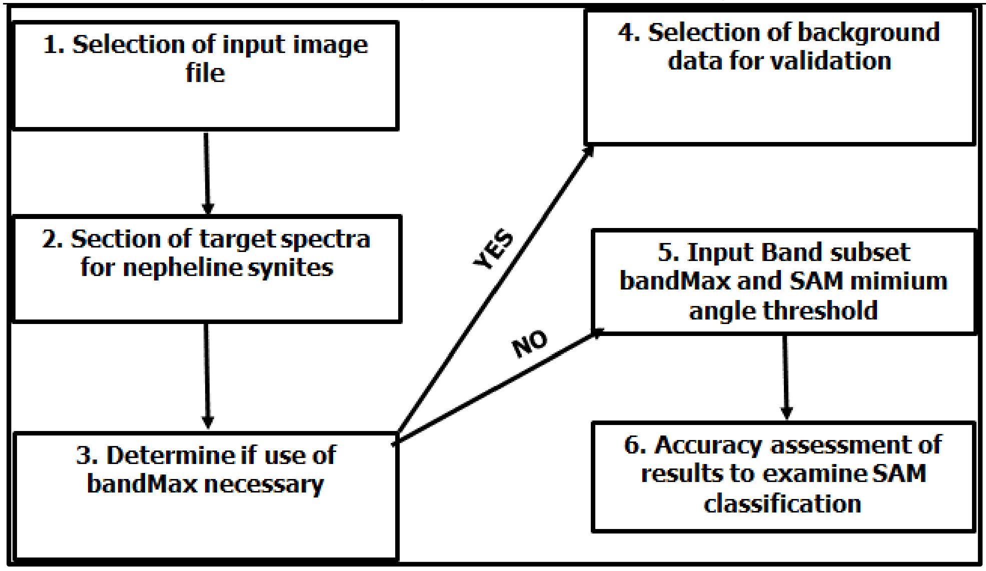

Appendix 7.3: A subset of field spectra for nepheline syenite (shown in unique colours) used as target spectra in the SAM Target Finder and BandMax algorithms' classification (A) shows the Target spectra on ASTER bands 1-9 and (B) for ASTER bands 5-9. The key absorption feature occurs in Band 6.

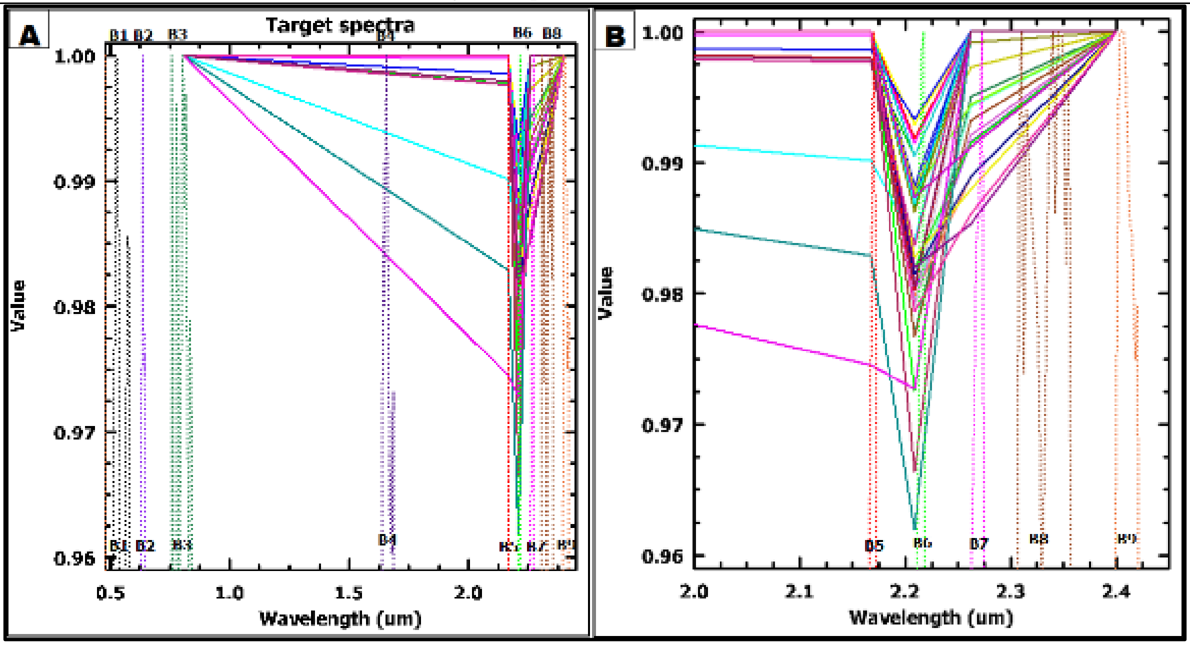

Appendix 7.4: Flow chart of procedure used to process and analyse the study's ASTER image data.

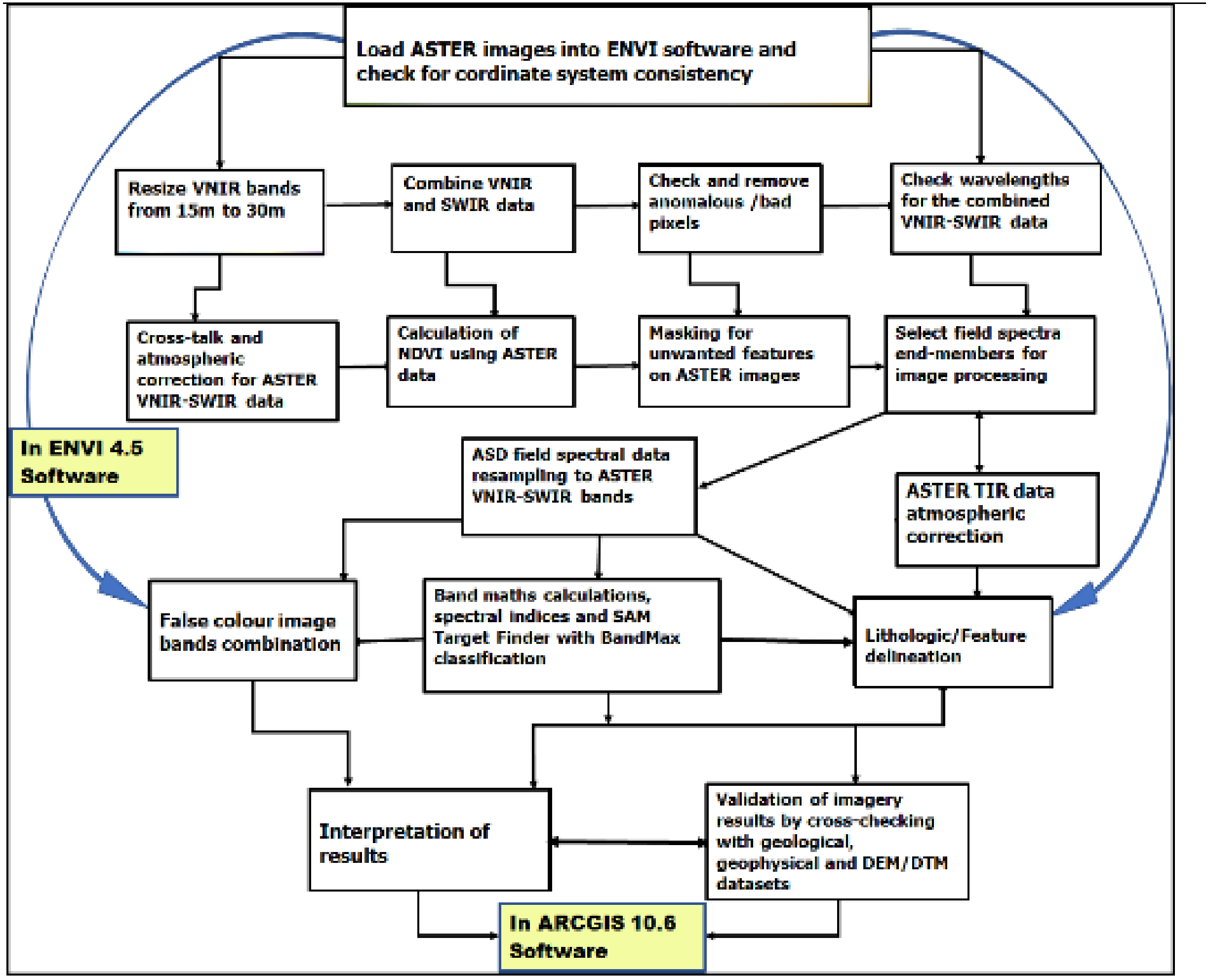

Appendix 7.5: Absolute reflectance for smoothed spectra of selected polished rock samples.

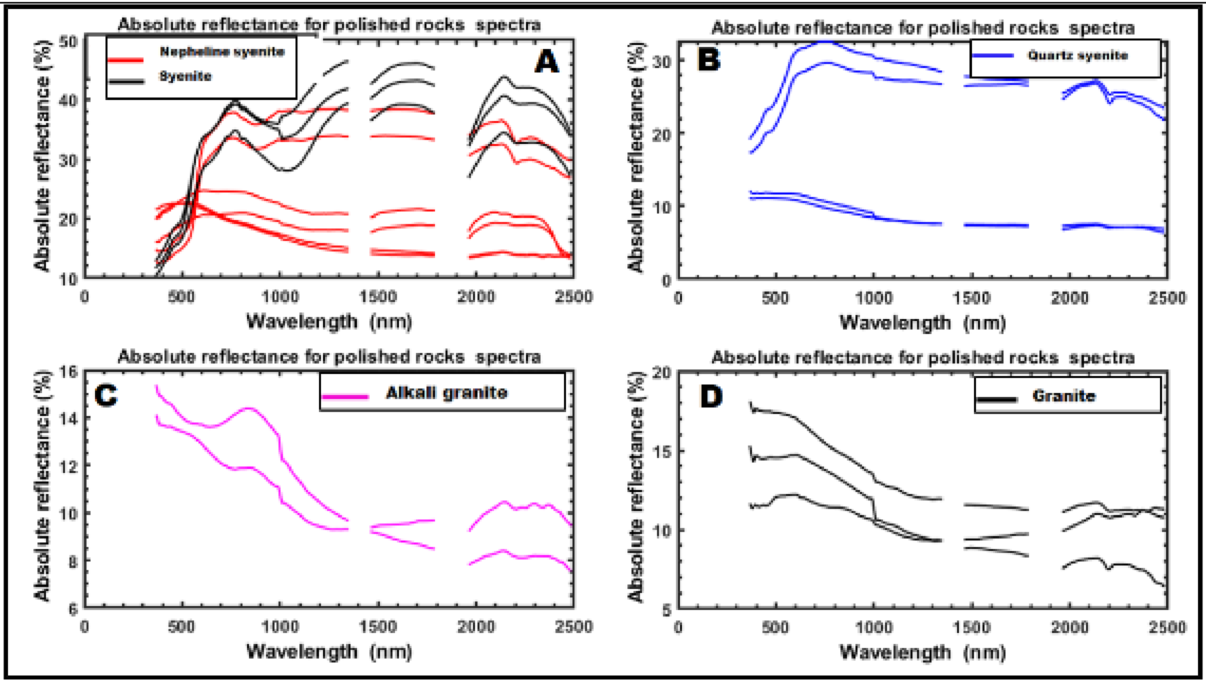

Appendix 7.6: First order derivatives of smoothed spectra of selected polished samples of (a) nepheline syenite and syenite (b) Quartz syenite (c) alkali granite (d) granite.

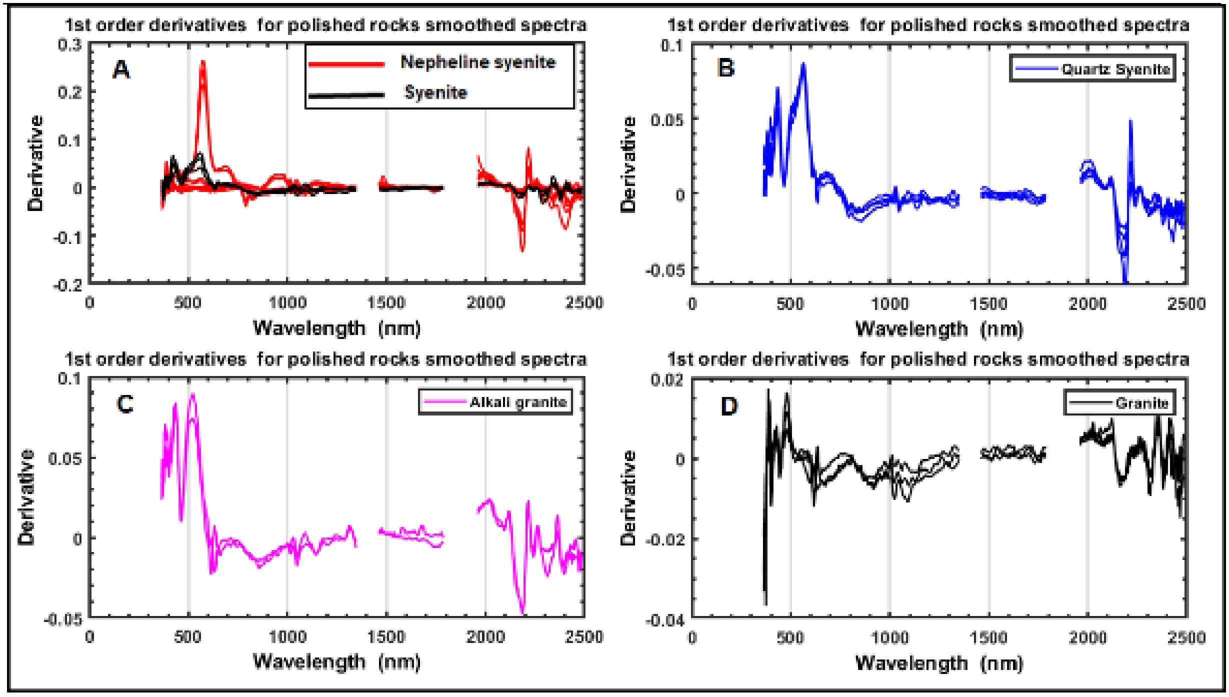

Appendix 7.7: Some wavelengths where different minerals and rocks were separable using 1st derivative data.

Sample Type	Sample name	Wavelength (nm)		Sample Type	Sample name	Wavelength (nm)
Mineral	Albite	1071		Mineral	Orthoclase	627
	Albite	2066			Orthoclase	939
	Albite	2067			Orthoclase	1688
	Albite	2068			Orthoclase	1690
	Albite	2069			Orthoclase	1691
	Albite	2072			Orthoclase	1693
	Albite	2073			Orthoclase	1964
	Albite	2074		Rock chip	Alkaline granite	1216
	Albite	2075			Alkaline granite	1234
Mineral	Calcite	995		Rock chip	Carbonatite	540
	Calcite	996			Carbonatite	1525
	Calcite	1001			Carbonatite	1582
	Calcite	1582			Carbonatite	1727
	Calcite	1633			Carbonatite	1733
	Calcite	1638			Carbonatite	1765
	Calcite	1690			Carbonatite	1771
	Calcite	2001			Carbonatite	1787
	Calcite	2010			Carbonatite	1852
	Calcite	2023			Carbonatite	1856
	Calcite	2029			Carbonatite	1960
	Calcite	2036			Carbonatite	2788
	Calcite	2040		Rock chip	Nepheline Syenite	1057
Mineral	Muscovite/biotite	933			Nepheline Syenite	1058
	Muscovite	991			Nepheline Syenite	1198
	Muscovite	993			Nepheline Syenite	1199
	Muscovite/biotite	1574			Nepheline Syenite	1174
	Muscovite	1575			Nepheline Syenite	1175
Mineral	Nepheline	1034			Nepheline Syenite	1176
	Nepheline	1035			Nepheline Syenite	1905
	Nepheline	1036			Nepheline Syenite	2047
	Nepheline	1037		Rock chip	Quartz Syenite	1198
	Nepheline	1074			Quartz Syenite	1199
	Nepheline	1147		Rock chip	Syenite	1905
	Nepheline	1964			Syenite	2047

Appendix 7.8: Some wavelengths where different minerals and rocks were separable using 2nd derivative data.

Sample type	Sample name	Wavelength (nm)		Sample type	Sample name	Wavelength (nm)
Rock chip	Alkaline granite	433		Rock chip	Syenite	388
	Alkaline granite	462			Syenite	420
	Alkaline granite	1897.5			Syenite	448
	Alkaline granite	2107			Syenite	1385
	Alkaline granite	2151			Syenite	1415
	Alkaline granite	2162			Syenite	1433
	Alkaline granite	2198			Syenite	2161
	Alkaline granite	2210			Syenite	2170
	Alkaline granite	2397			Syenite	2173
Rock chip	Carbonatite	409			Syenite	2385
	Carbonatite	540			Syenite	2400
	Carbonatite	705			Syenite	2415
	Carbonatite	735		Rock chip	Quartz syenites	382
Rock chip	Carbonatite	790			Quartz syenites	413
	Carbonatite	810			Quartz syenites	462
	Carbonatite	2115			Quartz syenites	530
	Carbonatite	2172			Quartz syenites	595
	Carbonatite	2230			Quartz syenites	1140
	Carbonatite	2413			Quartz syenites	1180
Rock chip	Granite	565			Quartz syenites	1290
	Granite	595			Quartz syenites	1365
	Granite	915			Quartz syenites	1395
	Granite	1900			Quartz syenites	1425
Rock chip	Nepheline syenite	445			Quartz syenites	1455
	Nepheline syenite	558			Quartz syenites	1890
	Nepheline syenite	600			Quartz syenites	1895
	Nepheline syenite	795			Quartz syenites	1899
	Nepheline syenite	1455			Quartz syenites	2115
	Nepheline syenite	1463			Quartz syenites	2120
	Nepheline syenite	2198			Quartz syenites	2125
	Nepheline syenite	2209			Quartz syenites	2422
	Nepheline syenite	2254			Quartz syenites	2447
	Nepheline syenite	2402			Quartz syenites	2450

Appendix 7.9: Selected spectra for (A) Nepheline syenite and (B) nepheline mineral overlaid on ASTER bands. Both nepheline and nepheline syenite show diagnostic absorption features in ASTER Band 6 and band 3. (Number 1-9 in Figure 7.14 A represents the ASTER band number).

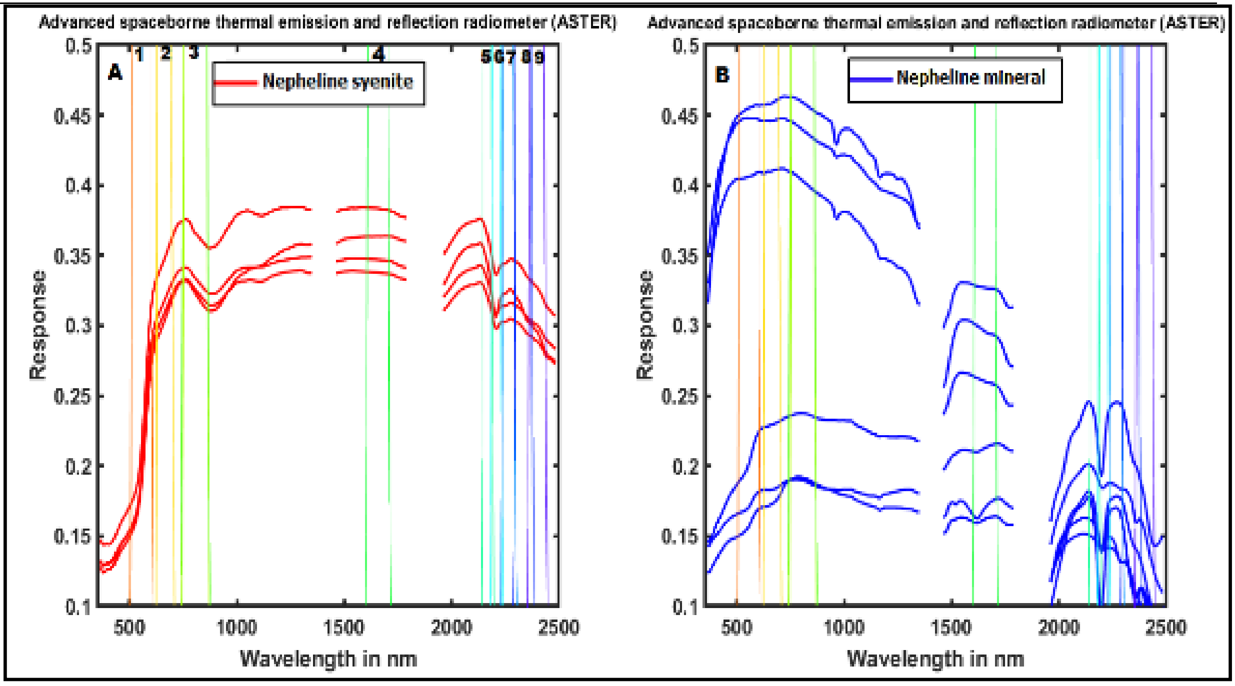

Appendix 7.10: ASTER 368 band composite images (A) for South Malawi nepheline syenites (B) for S.E Malawi quartz and fold syenites.

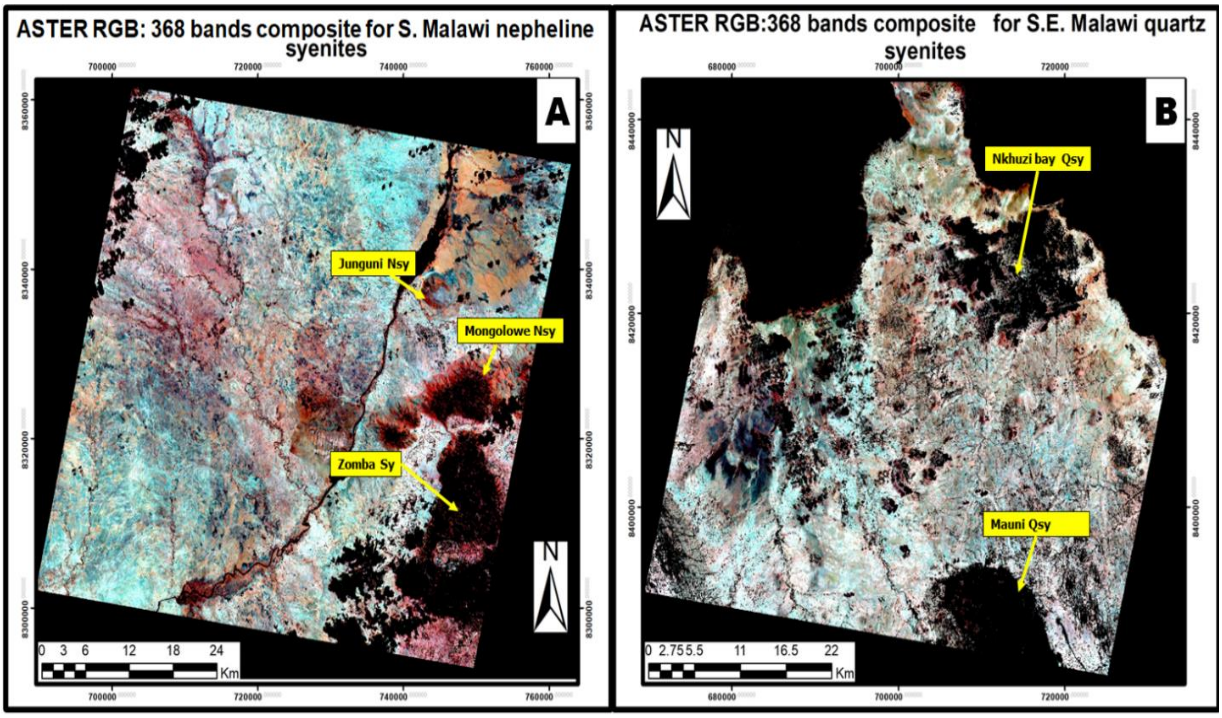

Appendix 7.11: The combined geology layers of the south east quartz syenites showing mismatching of adjoining official geological maps.

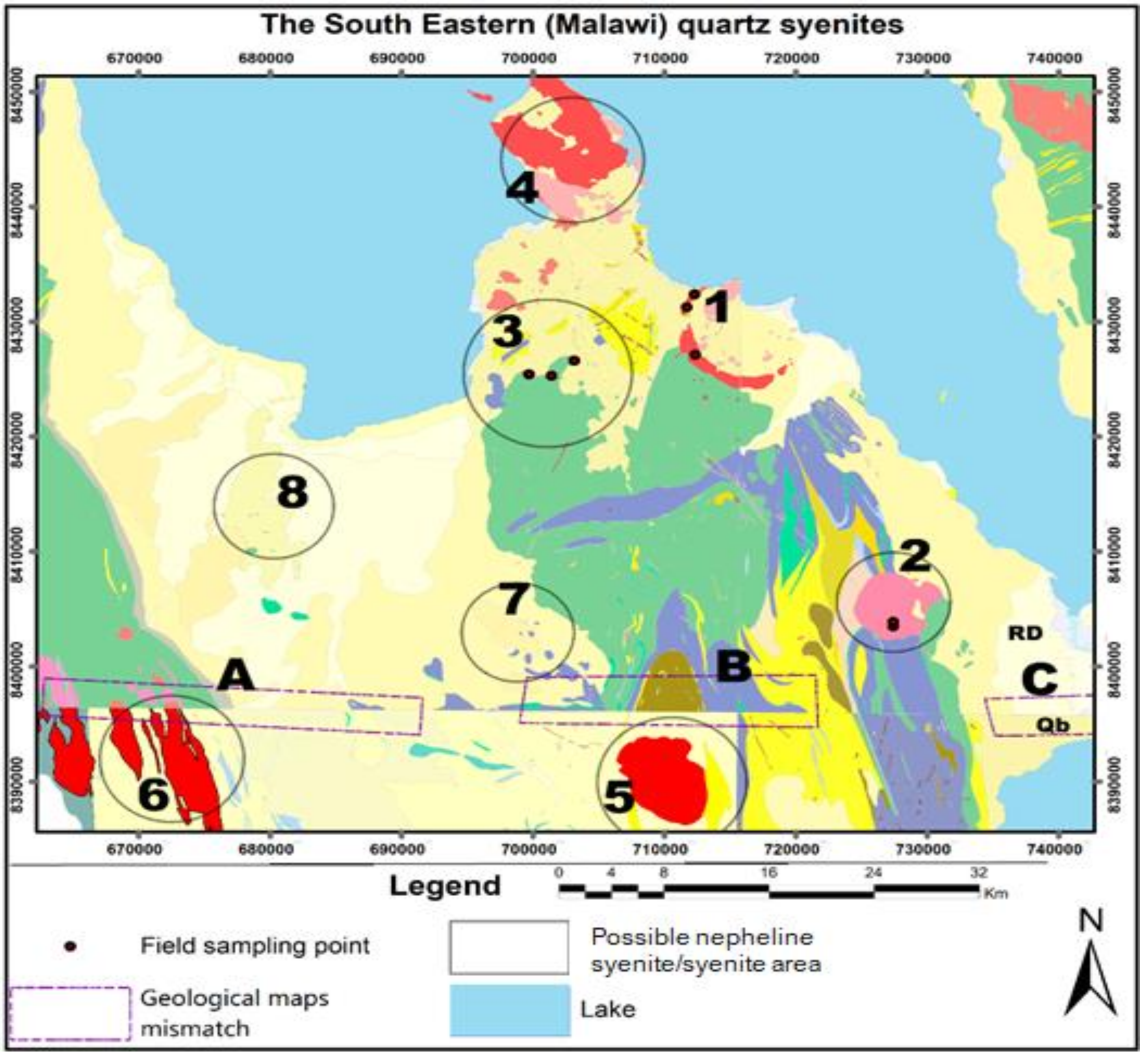

Appendix 8.1: Description of soil samples from Malawi and used in this study, Coordinates =WGS 84 Zone 36S

X	Y	Field Sample ID	Sampling Location name	Parent rock type	Soil field physical description
-	-	NJULI SS-01	Njuli quarry	Basalt	Fine-silty ground quarry dust
550258	8558140	KU SS-001	Kasungu mountain	Nepheline syenite	Fine-grained brown soils
549983	8558011	KU SS-002	Kasungu mountain	Nepheline syenite	Fine-silty brown soils
550263	8558134	KU SS-003	Kasungu mountain	Nepheline syenite	Fine-silty brown soils
549099	8557083	KU SS-009	Kasungu mountain	Nepheline syenite	Fine-silty brown soils
548934	8557263	KU SS-010	Kasungu mountain	Nepheline syenite	Fine-silty brown soils
548795	8558382	KU SS-012	Kasungu mountain	Nepheline syenite	Fine-silty brown soils
551346	8565068	KUCP SS-002	Kasungu Chipala	Nepheline syenite	Fine-silty pale grey soils
551193	8565153	KUCP SS-004	Kasungu Chipala	Nepheline syenite	Fine-silty pale grey soils
550891	8565109	KUCP SS-007	Kasungu Chipala	Nepheline syenite	Fine-silty pale grey soils
550947	8565272	KUCP SS-009	Kasungu Chipala	Nepheline syenite	Silty pale brown loamy soils
552156	8565033	KUCP SS-06	Kasungu Chipala	Alkaline granite	Silty dark brown loamy soils
553418	8417421	DZA SS-001	Dzalanyama	Alkaline granite	Silty dark brown sandy soils
553418	8417421	DZA SS-001A	Dzalanyama	Alkaline granite	Silty dark brown sandy soils
553554	8417563	DZA SS-002	Dzalanyama	Alkaline granite	Silty dark brown loamy soils
555358	8416020	DZA SS-004	Dzalanyama	Alkaline granite	Silty dark brown loamy soils
555083	8417818	DZA SS-005	Dzalanyama	Alkaline granite	Silty pale-yellowy loam soil
558237	8421921	DZA SS-06	Dzalanyama	Alkaline granite	Silty pale-yellowy loam soil
761171	8329281	CHA SS-002	Chaone	Nepheline syenite	Fine-silty brown soils
760086	8327715	CHA SS-003	Chaone	Nepheline syenite	Fine-silty brown soils
742513	8336698	JUN SS-002	Junguni	Nepheline syenite	Fine-silty dark grey soils
744341	8339639	JUN SS-004	Junguni	Nepheline syenite	Fine-silty dark grey soils
727433	8403504	MAU SS-002	Mauni	Quartz syenite	Fine-silty brown loamy soils
756206	8322720	MOG SS-001	Mongolowe	Nepheline syenite	Silty dark grey soils
755106	8323460	MOG SS-004	Mongolowe	Nepheline syenite	Fine-silty dark grey soils
711706	8431263	NKHU SS-001	Nkhuzi bay	Quartz syenite	Fine-silty brown loamy soils
711706	8431263	NKHU SS-003	Nkhuzi bay	Quartz syenite	Fine-silty brown loamy soils
776118	8404012	MANGO SS-001	Mangochi Hill Forest	Syenite	Silty-sandy dark greyish oils
801229	8279856	TUNDU SS-01	Tundulu complex	Nepheline syenite	Fine-silty yellowish grey soil

Appendix 8.2: Methodology for extraction and calculation for the different elements.

A. SOIL ANALYSIS - DETERMINATION OF pH-H2O

1) PRINCIPLE OF METHOD

5 mL soil is shaken with 25 mL water for 1 hour. The soil-water suspension is then left to equilibrate for between 1 and 3 hours. The pH-H2O of the suspension is measured using a pH electrode and meter, which have been calibrated using standard buffer solutions.

2) APPARATUS

Sample bottles must be rinsed several times with deionised water and dried, before use.

- ✓ 5 mL scoop
- ✓ Spatula
- ✓ 60 mL, wide mouth, polypropylene bottles
- ✓ 30 mL, bottle top dispenser, set to deliver 25 mL, BDH Pressette, serial no. E5179, fitted to 2500 mL capacity amber glass bottle, labelled, “Soil Analysis, Determination of pH – H2O, Deionised water”
- ✓ 2500 mL capacity amber glass bottle, labelled, “Soil Analysis, Determination of pH – H2O, Deionised water”
- ✓ Orbital shaker, Janke & Kunkel, IKA Labortechnik, KS 500, serial no. 487089
- ✓ pH meter, Hanna HI 83141, serial no. D0073280, VWR part number 662-4115
- ✓ Combination pH electrode, with BNC connector, VWR part number 662-1385
- ✓ ATC Temperature probe, Hanna HI 7669AW, VWR part number 662-4015.

3) REAGENTS

Deionised Water, 15MΩ.cm

4) SAMPLE PREPARATION

Use air-dried soil, crushed to pass through a 2 mm sieve.

5) QUALITY CONTROL

No Reference Material is currently available for this determination.

6) PROCEDURE

1) Fill the scoop with sample.
2) Remove excess sample by scraping the flat edge of the spatula across the top of the scoop.
3) Transfer the soil into a 60 mL bottle.
4) Fill the amber glass bottle with enough water for the number of analyses to be performed.
5) Place the bottle top dispenser on the bottle.
6) Using the dispenser, add 25 mL of deionised water to the 60 mL bottle.
7) Stopper the bottle.
8) Set the shaker speed at 275 ± 10 revs per minute.
9) Place the bottle in a horizontal position on the orbital shaker.
10) Start the shaker.
11) After 1 hour ± 10 minutes, stop the shaker.
12) Remove the bottle from the shaker.
13) Leave the solution to stand for at least 1 hour, but not longer than 3 hours, before measuring the pH-H2O.
14) Calibrate the pH meter and electrode as described in Method I002.
15) Shake the suspension thoroughly just before measurement of pH-H2O.
16) Measure the pH-H2O in the settling suspension.

NOTE: The reading can be considered to be stable when the pH measured over a period of 5 seconds does not vary by more than 0.02 pH units.

18) Record the value to two decimal places.
19) Check that the temperature of the buffer solutions and sample suspensions do not differ by more than 1□C.
20) Rinse the pH electrode and temperature probe thoroughly with deionised water.
21) Dry the pH electrode and temperature probe by wiping lightly with a tissue.
22) Check the calibration of the pH meter every 10 samples.

7) REPEATABILITY

The results of duplicate determinations should be within the limits stated below.

B. SOIL ANALYSIS - DETERMINATION OF SPECIFIC ELECTRICAL CONDUCTIVITY

1) PRINCIPLE

20 g of soil is shaken with 100 mL water at 20ºC for 30 minutes, and then filtered. The specific electrical conductivity of the filtrate is measured at 25ºC, using a conductivity meter and electrode.

2) APPARATUS

The polypropylene bottles and funnels must be cleaned using the Miele dishwasher, and then dried thoroughly in a drying cabinet.

2000 mL polyethylene bottle labelled “Method S008, Soil Analysis - Determination of Specific Electrical Conductivity, Water, 18MΩ.cm”
Balance readable to ± 0.001 g
250 mL wide mouth polypropylene bottles
100 mL pipette, Volac no. 18215
Shaking machine, IKA KS 500
Timer, calibrated, Fisherbrand serial no. 61573216
30 mL polypropylene Universal tubes,
Tube Rack
Filter papers, 150 mm, Whatman No 42
Funnels, polypropylene, 65 mm diameter
Water bath set at 25°C
Thermometer, number IL1, -5°C to 50°C, in 0.1°C divisions
Conductivity meter, Hanna HI9835, with Hanna HI 76309 electrical conductivity electrode, and temperature probe, calibrated as described in Method I005

3) REAGENTS

NOTE: Procedures for the preparation of reagents are given in the Method/Appendices indicated.
Water, 18MΩ.cm
Limit of Quantitation Verification Solution, Potassium chloride, 0.00017 mol/L, 25.0 µS/cm (Appendix B)

4) SAMPLE PREPARATION

Use air-dried soil, crushed to pass through a 2 mm sieve.

5) QUALITY CONTROL

Analyse a portion of Inorganic Laboratory Reference Soil No. 4.

6) PROCEDURE

At least 2 replicate determinations should be performed.
Carry out a blank determination.

NOTE: Between measurements, rinse the conductivity electrode thoroughly with deionised water. Shake off excess water and dry the probe with tissue.

NOTE: to measure the conductivity of a solution, dip the conductivity electrode into the solution. Stir the solution using the electrode. Tap the electrode gently to remove any trapped air bubbles. Wait a few seconds to allow the electrode to equilibrate with the solution before recording the reading.

1) Add sufficient water to perform the required number of samples, to the 2000 mL polyethylene bottle.
2) Allow to stand for a minimum of 1 hour to reach room temperature.
3) Weigh 20.00 g ± 0.01 g of soil into a 250 mL wide mouth polypropylene bottle.
4) Record the weight.
5) Record the sample i.d. and bottle number.
6) Add 100 mL water to the bottle.
7) Stopper the bottle.
8) Place the bottle in a horizontal position on the orbital shaker.
9) Set the shaker speed at 180 ± 10 revs per minute.
10) Start the shaker.
11) Shake the bottle for 30 minutes.
12) Remove the bottle from the shaker.
13) Filter the suspension through a No 42 filter paper into a Universal tube.
14) Collect approximately 10 mL of filtrate.
15) Place the Universal tube on the tube rack.
16) Transfer approximately 10 mL of Limit of Quantitation Verification Solution, to a Universal tube.
17) Place the Universal tube on the tube rack.
18) Place the tube rack in the water bath.
19) Leave the bottles to stand for a minimum of 1 hour, to allow the solution to reach 25□C.
20) Calibrate the conductivity meter as described in Method I005, using Electrical Conductivity Calibration Solution, 0.010 mol/L potassium chloride, 1413 µS/cm.

NOTE: if the conductivity of any of the sample solutions is less than 84□s/cm, re-calibrate the conductivity meter using electrical conductivity calibration solution, 0.000542 mol/l potassium chloride, 84.0 µs/cm. check the calibration by measuring the conductivity of the limit of quantitation verification solution.

21) Measure the conductivity of the blank solution.
22) Record the conductivity meter reading, □S/cm.

NOTE: the value of the blank solution should not be greater than 10 µs/cm. If the value of the blank solution exceeds 10 µs/cm, repeat the extractions.

23) Measure the conductivity of the Reference Sample solution.
24) Record the conductivity meter reading, µS/cm or mS/cm.

25) Check that the value is within the limits stated for the Reference Sample.
26) Measure the conductivity of the sample solution.
27) Record the conductivity meter reading, µS/cm or mS/cm.
28) Check the calibration of the conductivity meter every 10 samples.

NOTE: if the conductivity of the sample is greater than that of the calibration solution, re-calibrate the conductivity meter using a calibration solution with a higher conductivity than that of the sample, and re-measure the sample conductivity.

7) CALCULATION
The specific electrical conductivity is calculated as follows:

$$\text{Specific Electrical Conductivity, mS/m} = \frac{E_s - E_{bl}}{10}$$

where
Es is the measured Conductivity of the sample, µS/cm
Es is the measured Conductivity of the blank, µS/cm
Report results less than 2.5 mS/m as "< 2.5 mS/m"

8) REPEATABILITY
The results of duplicate determinations should be within the limits stated below.

CONDUCTIVITY mS/m	ACCEPTABLE VARIATION
0 – 50 >50 – 200 >200	5 mS/m 20 mS/m 10%

9) DISPOSAL
1) Place the filter papers into a yellow bag for disposal by incineration.
2) Autoclave the polypropylene bottles and funnels.
3) Rinse the autoclaved filtrate to waste, diluting greatly with running water.
4) Rinse the soil from the bottles, into a 5000 mL conical flask.
5) Allow the soil to settle to the bottom of the flask overnight.
6) Decant the supernatant solution through a Whatman, No.1, 27 cm, filter paper.
7) Transfer the soil and remaining solution onto the filter paper.
8) Empty the filtrate to drain diluting greatly with running water.
9) Transfer the filter paper and soil to a yellow bag for disposal by incineration.

PREPARATION OF STOCK POTASSIUM CHLORIDE SOLUTION, 0.017 mol/L

1) APPARATUS
Weighing bottle
Laboratory Oven set at 105°C
Thermometer, number IL2, -10°C to 110°C
Desiccator, containing silica gel drying agent
Balance, readable to ± 0.1 mg
50 mL beaker
Stirring rod
Funnel, diameter 65 mm
100 mL volumetric flask
125 mL polyethylene bottle labelled "Method S008, Limit of Quantification, Stock Potassium chloride solution, 0.017 mol/L"

2) REAGENTS
Water, 18MΩ.cm
Potassium chloride
3) PROCEDURE
1) Weigh approximately 1g potassium chloride into a weighing bottle.
2) Place the weighing bottle in an oven at 105□C □ 5□C, for 24 hours.
3) Remove the weighing bottle from the oven.
4) Immediately place the weighing bottle in the desiccator.
5) Allow the weighing bottle to cool for a minimum of 45 minutes.
6) Weigh 0.1267 g of the dried potassium chloride into a 50 mL beaker.
7) Add approximately 30 mL water.
8) Stir to dissolve.
9) Transfer the solution, quantitatively, to a 100 mL volumetric flask.
10) Dilute to 100 mL with water.
11) Transfer to the 125 mL polyethylene bottle for storage.

PREPARATION OF LIMIT OF QUANTITATION VERIFICATION SOLUTION, POTASSIUM CHLORIDE, 0.00017 mol/L, 25.0 µS/cm

1) APPARATUS
5 mL pipette, no. I2067, E-mil
500 mL volumetric flask
500 mL polyethylene bottle labelled "Method S008, Limit of Quantification Verification solution, Potassium chloride solution, 0.00017 mol/L, 25.0 µS/cm"

2) REAGENTS
Water, 18MΩ.cm
Potassium chloride solution, 0.017 mol/L, (Appendix A)
3 PROCEDURE
1) Pipette 5 mL potassium chloride solution, 0.017 mol/L, into a 500 mL volumetric flask.
2) Dilute to 500 mL with water.
3) Transfer to the 500 mL polyethylene bottle for storage.

C. SOIL ANALYSIS - DETERMINATION OF POTENTIAL CATION EXCHANGE CAPACITY AND EXCHANGEABLE CATIONS USING BARIUM CHLORIDE SOLUTION BUFFERED AT pH = 8.1

1) PRINCIPLE OF METHOD
Air-dried soil, < 2 mm is shaken with buffered barium chloride solution three times to saturate the exchange sites with barium ion. Excess barium chloride solution is removed by washing the soil with water. An excess of 0.020 mol/L magnesium sulphate solution is then added, which precipitates all the barium present as highly insoluble barium sulphate, and the exchange sites are readily occupied by magnesium ion. The CEC is determined by measuring the excess magnesium concentration using Atomic Absorption Spectrometry.
Exchangeable calcium, magnesium, potassium and sodium are determined by analysis of the barium chloride extract using Atomic Absorption Spectrometry.

2) PROCEDURE
PART 1 – EXTRACTION PROCEDURE
1) APPARATUS
Centrifuge tubes and screw caps, polypropylene, nominal capacity 50 mL, labelled 1, 2, 3… Nalgene, part no. 3119-0050
Centrifuge tube rack, polypropylene, Nalgene, part no. 5930-0030
Balance, readable to ± 0.1 mg
Weighing boats, 30 mL, diamond shaped
Bottle top dispenser, Jencons Zipette, serial no. X5413, capacity 30 mL, set to deliver 30 mL, fitted to 5 litre polyethylene bottles, containing Extraction solution (Refer to Appendix D)
Orbital shaker, IKA KS 500
Centrifuge, Sorvall RC5Bplus, fitted with SS34 fixed angle rotor
Funnels, polypropylene, 65 mm diameter
Volumetric flask, 100 mL labelled "Solution A, 1, 2. . .
Wash bottle containing Extraction solution labelled "BaCl2/Triethanolamine Extraction solution"
Dropping pipette, polyethylene
Filter papers, Whatman, No.2, 125 mm
Polyethylene bottles, 125 mL capacity labelled "Method S017, Solution A, CEC, 1, 2. . .. . BaCl2"
Measuring cylinder, 50 mL
Container, 25 litres, labelled "Waste Barium Chloride solution"
Pipette, 30 mL
Funnels, polypropylene, 47 mm diameter
Filter papers, Whatman, No.2, 90mm
Polyethylene bottles, 60 mL capacity labelled "Method S017, Solution B, CEC, 1, 2… Mg2SO4"

2) REAGENTS
NOTE: Procedures for the preparation of reagents are given in the Appendices indicated.
Extraction solution (Appendix D)
Magnesium sulphate solution, 0.020 mol/L (Appendix E)
3) SAMPLE PREPARATION
Use air-dried soil, crushed to pass through a 2 mm sieve.
4) QUALITY CONTROL
No Reference Material is currently available for this determination.

5) PROCEDURE
REFER TO COSHH RISK ASSESSMENT S017
Carry out a blank determination.
Record all data on the "METHOD S017, DETERMINATION OF CEC – BaCL2" data sheet.
1) Record the sample identification.
2) Record the centrifuge tube number.
3) Place a centrifuge tube plus cap on the balance.
4) Record the weight of centrifuge tube plus cap (m1) to the nearest 1 mg.
5) Remove the cap from the centrifuge tube.
6) Place the centrifuge tube on the tube rack.

NOTE: To avoid weighing errors, it is important to ensure that a tube is kept with the same cap, throughout the procedure.
7) Place a 30 mL weighing boat on the balance.
8) Press the tare button to set the balance reading to zero.
9) Weigh between 2.5 g and 10.0 g of soil into the weighing boat.

NOTE: Use 2.5g to 5 g of soil with a high clay content or 10 g of soil with a high sand content or low content of humus.

10) Carefully, transfer the soil to the centrifuge tube.
11) Place the cap on the centrifuge tube.
12) Place the centrifuge tube plus cap plus soil on the balance.
13) Record the weight of tube plus cap plus soil, (m2) to the nearest 0.1 mg.
14) Remove the cap from the centrifuge tube.
15) Using the bottle top dispenser, add 30 mL extraction solution to the centrifuge tube.
16) Place the cap on the centrifuge tube.
17) Place the centrifuge tube, in a horizontal position, on the orbital shaker.
18) Start the shaker.
19) Set the shaker speed to 275 revs per minute.
20) After 1 hour stop the shaker.
21) Remove the centrifuge tube from the shaker.
23) Install the SS34 rotor in the centrifuge.
24) Place the centrifuge tube in the centrifuge rotor.
25) Set the centrifuge speed to 6000 rpm.
26) Set the centrifuge timer to 10 minutes.
27) Start the centrifuge.
28) When the centrifuge has stopped, carefully remove the tube from the centrifuge, avoiding disturbing the soil cake.
29) Place the centrifuge tube on the tube rack.
30) Remove the cap from the centrifuge tube.
31) Taking care not to lose any soil material, decant the supernatant solution, from the centrifuge tube, through a 65 mm diameter funnel, into a 100 mL volumetric flask.
32) Repeat steps 15 to 31, twice more.
33) Dilute the solution in the 100 mL volumetric flask to just below the 100 mL mark with extraction solution.
34) Using a dropping pipette, dilute the solution to exactly 100 mL with extraction solution.
35) Place the stopper firmly in the flask.
36) Shake the flask vigorously to thoroughly mix the solution.
37) Remove the stopper from the flask.
38) Filter the solution through a 125 mm, No.2 filter paper, in a 65 mm diameter funnel, into a 125 mL capacity polyethylene bottle labelled “S017, Solution A, CEC, 1, 2. . . BaCl2”.
39) Retain this solution, “Solution A” for the determination of exchangeable cations, Part 3, Determination of Exchangeable Sodium, Part 4, Determination of Exchangeable Potassium, Part 5, Determination of Exchangeable Calcium and Magnesium.
40) Add 30 mL water to a 50 mL measuring cylinder.
41) Transfer the water to the centrifuge tube.
42) Place the cap on the centrifuge tube.
43) Use the vortex mixer to break up the soil cake.
44) Place the centrifuge tube, in a horizontal position, on the orbital shaker.
45) Start the shaker.
46) Set the shaker speed to 275 revs per minute.
47) After 2 minutes stop the shaker.
48) Remove the centrifuge tube from the shaker.
49) Place the centrifuge tube on the tube rack.
50) Install the SS34 rotor in the centrifuge.
51) Place the centrifuge tube in the centrifuge rotor.
52) Set the centrifuge speed to 6000 rpm.
53) Set the centrifuge timer to 10 minutes.
54) Start the centrifuge.
55) When the centrifuge has stopped, carefully remove the tube from the centrifuge, avoiding disturbing the soil cake.
56) Place the centrifuge tube on the tube rack.
57) Remove the cap from the centrifuge tube.
58) Taking care not to lose any soil material, decant the supernatant solution into the container labelled “Waste Barium Chloride solution”.
59) Place the cap on the centrifuge tube.
60) Place the centrifuge tube plus cap plus soil plus residual water on the balance.
61) Record the weight of the centrifuge tube plus cap plus soil plus, water, (m3) to the nearest 0.1 mg.
62) Remove the cap from the centrifuge tube.
63) Using a pipette, add 30 mL magnesium sulphate solution, 0.020 mol/L, to the centrifuge tube.
64) Place the cap on the centrifuge tube.
65) Use the vortex mixer to break up the soil cake.
66) Place the centrifuge tube, in a horizontal position, on the orbital shaker.
67) Start the shaker.
68) Set the shaker speed to 275 revs per minute.
69) After 16 to 24 hours stop the shaker.
70) Remove the centrifuge tube from the shaker.
71) Place the centrifuge tube on the tube rack.
72) Install the SS34 rotor in the centrifuge.
73) Place the centrifuge tube in the centrifuge rotor.
74) Set the centrifuge speed to 6000 rpm.
75) Set the centrifuge timer to 10 minutes.
76) Start the centrifuge.
77) When the centrifuge has stopped, carefully remove the tube from the centrifuge, avoiding disturbing the soil cake.
78) Place the centrifuge tube on the tube rack.
79) Remove the cap from the centrifuge tube.
80) Decant the supernatant solution through a No.2 filter paper in a 47 mm diameter funnel, into a 60 mL polyethylene bottle labelled “S017, Solution B, CEC, 1, 2… Mg2SO4”
81) Retain this solution, “Solution B” for the determination of cation exchange capacity, Part 2.

D. DETERMINATION OF CATION EXCHANGE CAPACITY

1) APPARATUS

Pipettor, 1mL variable capacity
Volumetric flask, 100 mL
Atomic Absorption Spectrometer (AAS), Varian Spectraa 400
Dropping pipette, polyethylene

2) REAGENTS

NOTE: Procedures for the preparation of reagents are given in the Appendices indicated.

Lanthanum chloride solution, 10 % m/V La
CEC Standard solutions, 0 – 0.050 mmol/L Mg.

3) **PROCEDURE**

Record all data on the “DETERMINATION OF CEC – BaCL2” data sheet.

1) Pipette 0.2 mL of “Solution B” into a 100 mL volumetric flask.
2) Pipette 1.0 mL lanthanum chloride solution, 10% m/V La, into the 100 mL volumetric flask.
3) Dilute the solution in the 100 mL volumetric flask to just below the 100 mL mark with water.
4) Using a dropping pipette, dilute the solution to exactly 100 mL with water.
5) Place the stopper firmly in the flask.
6) Shake the flask vigorously to thoroughly mix the solution.
7) Set up the atomic absorption spectrometer (AAS) as described in the operating manual.
8) Set the wavelength to 285.2 nm.
9) Use an air/acetylene flame.
10) Calibrate the atomic absorption spectrometer (AAS) using the CEC standard solutions.
11) Measure the magnesium concentrations of the diluted solution B.
12) Recheck the instrument calibration by measuring the 0.00 mmol/L and 0.05 mmol/L Mg, CEC standard solutions, after every 5 samples.

4) CALCULATION

The cation exchange capacity is calculated as follows;

The magnesium concentration, C, measured in solution B, is corrected for dilution by the liquid retained in the centrifuged soil after being treated with water using the formula:

$$\mathrm{Cc} = \frac{C(30 + m_3 - m_2)}{30}$$

where

C is the magnesium concentration measured in the diluted solution B, mmol/L.

Cc is the corrected magnesium concentration in the diluted solution B, mmol/L.

m2 is the weight of centrifuge tube plus stopper plus soil, g

m3 is the weight of centrifuge tube plus stopper plus soil plus water, g

The cation exchange capacity is calculated using the formula:

$$\text{CEC, cmol+/kg} = \frac{3000(C_{bl} - C_c)}{(m_2 - m_1)D}$$

where

Cbl is the magnesium concentration in the diluted blank solution, mol/L. m1 is the weight of tube plus stopper, g

D is the dry matter factor determined as described in Method S002

PART 3: DETERMINATION OF EXCHANGEABLE SODIUM

1) APPARATUS

Pipettor, 1mL capacity
Pipettor, 5mL capacity
Universal container, 30 mL, disposable

Atomic Absorption Spectrometer (AAS) , Varian Spectraa 400, set in emission mode.

2) REAGENTS

REFER TO COSHH RISK ASSESSMENT S017/3

NOTE: Procedures for the preparation of reagents are given in the Appendices indicated.

Extraction solution (Appendix D)

Hydrochloric acid solution, 1.0 mol/L. Exchangeable Cation Standard solutions, 0 -10 mg/L Na; 0 -10 mg/L K.

3) PROCEDURE

Record all data on the “DETERMINATION OF EXCHANGEABLE SODIUM” data sheet.

1) Pipette 0.2 mL of “Solution A” into a universal container.
2) Record the volume (v) of Solution A.
3) Add 1.8 mL extraction solution to the container.
4) Pipette 1.0 mL hydrochloric acid solution, 1.0 mol/L in to the container.
5) Pipe
6) Place the cap on the container.
7) Shake the container vigorously to thoroughly mix the solution.
8) Set up the atomic absorption spectrometer (AAS), in emission mode, as described in the operating manual.
9) Set the wavelength to 589.0 nm for determination of sodium.
10) Use an air/acetylene flame.
11) Calibrate the atomic absorption spectrometer (AAS) using the Exchangeable Cation standard solutions.
12) Measure the sodium concentrations of the diluted solution A.
13) Recheck the instrument calibration by measuring the 0.0 mg/L and 10.0 mg/L Na, Exchangeable Cation Standard solutions, after every 5 samples.
14) If the sodium concentration of any of the measured solutions is higher than that of the highest concentration standard solution, re-dilute solution A, using a smaller volume, as described below.
15) Pipette the required volume of “Solution A” into a universal container.
16) Record the volume (v) of Solution A.
17) Add enough extraction solution to make the total volume up to 2.0 mL.
18) Continue as described from step 3.

CALCULATION

The exchangeable sodium is calculated as follows;

Exchangeable Na, cmol+/kg = $\dfrac{(Cs - Cbl)4.3498}{v(m_2 - m_1)D}$

where

Cs is the sodium concentration in solution A, mg/L
Cbl is the sodium concentration in the blank solution, mg/L
m1 is the weight of tube plus stopper, g
m2 is the weight of tube plus stopper plus soil, g
v is the volume of solution A used for dilution, mL
D is the dry matter factor determined as described in Method S002

E. DETERMINATION OF EXCHANGEABLE POTASSIUM

1) Pipettor, 1mL capacity
Pipettor, 5mL capacity
Universal container, 30 mL, disposable
Atomic Absorption Spectrometer (AAS) , Varian Spectraa 400, set in emission mode

2) REAGENTS

REFER TO COSHH RISK ASSESSMENT S017/4

NOTE: Procedures for the preparation of reagents are given in the Appendices indicated.

Extraction solution (Appendix D)

Hydrochloric acid solution, 1.0 mol/L (Appendix I)

Exchangeable Cation Standard solutions, 0 - 10 mg/L Na; 0- 10 mg/L K,

3) PROCEDURE

Record all data on the “DETERMINATION OF EXCHANGEABLE POTASSIUM” data sheet.

1) Pipette 2.0 mL of “Solution A” into a universal container.
2) Record the volume (v) , mL, of Solution A.
3) Pipette 1.0 mL hydrochloric acid solution, 1.0 mol/L in to the container.
4) Pipette 7.0 mL of water in to the container.
5) Place the cap on the container.
6) Shake the container vigorously to thoroughly mix the solution.
7) Set up the atomic absorption spectrometer (AAS), in emission mode, as described in the operating manual.
8) Set the wavelength to 766.5 nm for determination of potassium.
9) Use an air/acetylene flame.
10) Calibrate the atomic absorption spectrometer (AAS) using the Exchangeable Cation standard solutions.
11) Measure the potassium concentrations of the diluted solution A.
12) Recheck the instrument calibration by measuring the 0.0 mg/L and 10.0 mg/L K, Exchangeable Cation Standard solutions, after every 5 samples.
13) If the potassium concentration of any of the measured solutions is higher than that of the highest concentration standard solution, re-dilute solution A, using a smaller volume, as described below.
14) Pipette the required volume of “Solution A” into a universal container.
15) Record the volume (v) of Solution A.
16) Add sufficient extraction solution to make the total volume up to 2.0 mL.
17) Continue as described from step 3.

4) CALCULATION

The exchangeable potassium is calculated as follows;

Exchangeable K, cmol+/kg = $\dfrac{(Cs - Cbl)2.5576}{v(m_2 - m_1)D}$

where

Cs is the potassium concentration in solution A, mg/L
Cbl is the potassium concentration in the blank solution, mg/L
m1 is the weight of tube plus stopper, g
m2 is the weight of tube plus stopper plus soil, g
v is the volume of solution A used for dilution, mL
D is the dry matter factor determined as described in Method S002

F. DETERMINATION OF EXCHANGEABLE CALCIUM AND MAGNESIUM

1) APPARATUS

Pipettor, 1mL capacity
Pipettor, 5mL capacity
Universal container, 30 mL, disposable
Atomic Absorption Spectrometer (AAS) , Varian Spectraa 400

2) REAGENTS

REFER TO COSHH RISK ASSESSMENT S017/5

NOTE: Procedures for the preparation of reagents are given in the Appendices indicated.

Extraction solution (Appendix D)

Hydrochloric acid solution, 1.0 mol/L (Appendix I)

Exchangeable Cation standard solutions, 0 - 10 mg/L Ca; 0 – 1.0 mg/L Mg, (Appendix J)

3) PROCEDURE

Record all data on the “DETERMINATION OF EXCHANGEABLE CALCIUM AND MAGNESIUM” data sheet.

CALCULATION

The exchangeable calcium and magnesium are calculated as follows;

Exchangeable Ca, cmol+/kg = $\dfrac{(Cs - Cbl)4.9903}{v.(m_2 - m_1).D}$

Exchangeable Mg, cmol+/kg = $\dfrac{(Cs - Cbl)8.2288}{v.(m_2 - m_1).D}$

where

Cs is the calcium/magnesium concentration in solution A, mg/L
Cbl is the calcium/magnesium concentration in the blank solution, mg/L
m1 is the weight of tube plus stopper, g
m2 is the weight of tube plus stopper plus soil, g
v is the volume of solution A used for dilution, mL
D is the dry matter factor determined as described in Method S002

PREPARATION OF BARIUM CHLORIDE SOLUTION, 1.0 mol/L

1) APPARATUS

Balance readable to ± 1 mg
Beaker, 2000 mL
Stirring rod
Glass funnel, diameter 100 mm
Volumetric flask, 2000 mL
Dropping pipette, polyethylene

2) REAGENTS

REFER TO COSHH RISK ASSESSMENT S017A

NOTE: Procedures for the preparation of reagents are given in the Appendices indicated.
Barium chloride dehydrate

3) PROCEDURE
WARNING: REFER TO COSHH RISK ASSESSMENT S017
A THIS PROCEDURE MUST BE PERFORMED
IN A FUME CUPBOARD.
1) Weigh 488.54 g barium chloride dihydrate into a 2000 mL beaker.
2) Add approximately 1000 mL water.
3) Using a stirring rod, stir the solution to dissolve the barium Chloride dihydrate.
4) Rinse the solution through the funnel, into a 2000 mL Volumetric flask.
NOTE: If necessary, to completely dissolve all the barium chloride Add more water to the beaker, stir and rinse into the flask.
5) Dilute the solution to just below the 2000 mL mark with water.
6) Using a dropping pipette, dilute the solution to exactly 2000 mL with water.
7) Place the stopper firmly in the flask.
8) Shake the flask vigorously to thoroughly mix the solution.
NOTE: Prepare this solution on the day of use.
PREPARATION OF HYDROCHLORIC ACID SOLUTION, 2.0 mol/L
1) APPARATUS
Measuring cylinder, 250 mL
Volumetric flask, 1000 mL
Polyethylene bottle, 1000 mL, labelled “Soil Analysis, Method S017, Determination of Cation Exchange Capacity, Hydrochloric acid solution, 2.0 mol/L”
Dropping pipette, polyethylene 2)
REAGENTS
REFER TO MATERIAL SAFETY DATASHEETS.
REFER TO COSHH RISK ASSESSMENT S017B
Hydrochloric acid, S.G.1.18, 35%

3) PROCEDURE
WARNING: Safety glasses and rubber gloves must be worn at all times.
This Procedure must be performed in a fume cupboard.
1) Add approximately 500 ml water to the 1000 ml volumetric Flask.
2) Cautiously, add 175 mL hydrochloric acid, S.G.1.18, 35%, to the measuring cylinder.
3) Transfer the hydrochloric acid to the 1000 mL volumetric flask.
4) Dilute the solution to just below the 1000 mL mark with water.
5) Using a dropping pipette, dilute the solution to exactly 1000 mL with water.
6) Place the stopper firmly in the flask.
7) Shake the flask vigorously to thoroughly mix the solution.
8) Transfer to the labelled 1000 mL polyethylene bottle for storage.

PREPARATION OF TRIETHANOLAMINE SOLUTION, pH 8.1

1) APPARATUS
Volumetric flask, 2000 mL
100 mL measuring cylinder
250 mL measuring cylinder
Magnetic stirrer, Bibby HB502
Stirring bar
Dropping pipette, polyethylene
Triethanolamine
Hydrochloric acid solution, 2.0 mol/L.
3) PROCEDURE

1) Add approximately 1000 mL water to the 2000 mL volumetric flask.
2) Measure 90 mL triethanolamine into a 100 mL measuring cylinder.
3) Transfer the triethanolamine to the volumetric flask.
4) Add a magnetic stirring bar to the volumetric flask.
5) Place the flask onto the magnetic stirrer.
6) Start the stirrer.
7) Calibrate the pH meter using the pH 7.0 and 10.0 buffer solutions as described in Method I003.
8) Place the pH electrode and temperature probe in the triethanolamine solution.
9) Add 140 mL hydrochloric acid solution, 2.0 mol/L to a 250 mL measuring cylinder.
10) Transfer the hydrochloric acid solution, 2.0 mol/L to the volumetric flask.
11) Adjust the pH of the solution to 8.10 ± 0.02 with further dropwise addition of hydrochloric acid solution, 2.0 mol/L.
12) Using the magnetic rod, remove the magnetic stirring bar from the flask, while rinsing with water.
13) Dilute the solution to just below the 2000 mL mark with water.
14) Using a dropping pipette, dilute the solution to exactly 2000 mL with water.
15) Place the stopper firmly in the flask.
16) Shake the flask vigorously to thoroughly mix the solution.

NOTE: Prepare this solution on the day of use.

G.PREPARATION OF BARIUM CHLORIDE/TRIETHANOLAMINE EXTRACTION SOLUTION

1) APPARATUS
5000 mL polyethylene bottle labelled “Soil Analysis, Method S017, Determination of Cation Exchange Capacity, Extraction Solution”
Bottle top dispenser, Jencons Zipette, serial no. X5413, capacity 50 mL, set to deliver 30 mL
Wash bottle, 500 mL capacity, labelled “BaCl2/Triethanolamine Extraction Solution”

2) REAGENTS

REFER TO COSHH RISK ASSESSMENT S017D
Barium chloride solution, 1.0 mol/L, (Appendix A)
Triethanolamine solution. pH 8.1, (Appendix C)
3). PROCEDURE
REFER TO COSHH RISK ASSESSMENT S017D
1 Pour 2000 mL triethanolamine solution. pH 8.1, into a 5000 mL polyethylene bottle.
2 Add 2000 mL barium chloride solution, 1.0 mol/L to the polyethylene bottle.
3 Fit the bottle top dispenser onto the polyethylene bottle.
4 Shake well to mix the solution.
5 Transfer extraction solution to the wash bottle as required.
NOTE: Prepare this solution on the day of use.

PREPARATION OF MAGNESIUM SULPHATE SOLUTION, 0.020 mol/L
Balance readable to ± 0.1 mg
Beaker, 250 mL
Glass funnel, diameter 100 mm
Stirring rod
Volumetric flask, 2000 mL
Dropping pipette
Polyethylene bottle, 2000 mL labelled “Soil Analysis, Method S017, Determination of Cation Exchange Capacity, Magnesium Sulphate solution, 0.020 mol/L”

REFER TO COSHH RISK ASSESSMENT S017E
NOTE: Procedures for the preparation of reagents are given in the Appendices indicated.
Magnesium sulphate, heptahydrate
NOTE: Magnesium sulphate heptahydrate may lose water of crystallisation on standing. The reagent should be stored in a sealed polythene bag at 4ºC in a refrigerator.

3) CALCULATION

REFER TO COSHH RISK ASSESSMENT S017E
The organic carbon content is calculated as follows:
Organic Carbon, % = Cs - Cbl
where
Cs is the measured carbon percentage of the sample
Cbl is the measured carbon percentage of the blank

To calculate the organic carbon content to an oven dry basis:
Organic Carbon, % =
where
D is the dry matter factor, determined as described in Method S002.

PROCEDURE
1) Weigh 9.8588 g magnesium sulphate, heptahydrate into a 250 mL beaker.
2) Add approximately 100 mL water.
3) Stir to dissolve.
4) Transfer the solution, quantitatively, to a 2000 mL volumetric flask.
5) Dilute the solution to just below the 2000 mL mark with water.
6) Using a dropping pipette, dilute the solution to exactly 2000 mL with water.
7) Place the stopper firmly in the flask.
8) Shake the flask vigorously to thoroughly mix the solution.
9) Transfer to the labelled 2000 mL polyethylene bottle for storage.

H. PREPARATION OF CATION EXCHANGE CAPACITY STANDARD SOLUTIONS

1) APPARATUS

1 mL pipettor
5 mL pipettor
Volumetric flasks, 100 mL
Dropping pipettes
Polyethylene bottles, 125 mL, labelled “Soil Analysis, Method S017, Determination of Cation Exchange Capacity, Cation Exchange Capacity Standard Solutions”

2) REAGENTS

REFER TO COSHH RISK ASSESSMENT S017F
NOTE: Procedures for the preparation of reagents are given in the Appendices indicated.
Magnesium sulphate solution, 0.0010 mol/L
Lanthanum chloride solution, `SpectrosoL` grade, 10% m/V lanthanum

3) PROCEDURE

REFER TO COSHH RISK ASSESSMENT S017F
1) Pipette 0.00 mL, 1.00 mL, 2.00 mL, 3.00 mL, 4.00 mL, 5.00 Ml magnesium sulphate standard solution, 0.0010 mol/L, into 100mL volumetric flasks.
2) Pipette 1.0 mL Lanthanum chloride solution, 10% m/V Lanthanum in to the 100 mL volumetric flasks.
3) Dilute the solutions to just below 100 mL mark with water.
4) Using a dropping pipette, dilute the solutions too exactly 100 mL with water.
5) Place the stoppers firmly in the flasks.
6) Shake the flasks vigorously to thoroughly mix the solution.
7) Transfer to the labelled 125 mL polyethylene bottles for storage.
6) These solutions have magnesium concentrations of 0.0 mmol/L, mmol/L, 0.02 mmol/L, 0.03 mmol/L, 0.04 mmol/L, 0.05 mmol/L.

I. PREPARATION OF MAGNESIUM STANDARD SOLUTION, 0.001 mol/L

1) APPARATUS

50 mL pipette, Volac, class A, serial no. 3C4634
Pipette filler
Volumetric flask, 1000 mL, Volac, class A, serial no. B390
Dropping pipettes
Polyethylene bottle, 1000 mL labelled “Soil Analysis, Method S017, Determination of Cation Exchange Capacity, Magnesium Sulphate solution, 0.001 mol/L”

2) **REAGENTS**

Magnesium sulphate solution, 0.020 mol/L, (Appendix E)

3) PROCEDURE

REFER TO COSHH RISK ASSESSMENT S017G
1) Pipette 50 mL of 0.020 mol/L magnesium sulphate solution into a 1000 mL volumetric flask.
2) Dilute the solution to just below the 1000 mL mark with water.
3) Using a dropping pipette, dilute the solution to exactly 1000 mL with water.
4) Place the stopper firmly in the flask.
5) Shake the flask vigorously to thoroughly mix the solution.
6) Transfer the solution to the labelled 1000 mL polyethylene bottles for storage.

J. PREPARATION OF EXCHANGEABLE POTASSIUM AND SODIUM STANDARD SOLUTIONS

1) APPARATUS

Pipettor 1 mL
Measuring cylinder, 25 mL
Measuring cylinder, 10 mL
Dropping pipette
Volumetric flasks, 100mL
Polyethylene bottles, 125 mL labelled “Soil Analysis, Method S017, Determination of Cation Exchange Capacity, Exchangeable Potassium and Sodium Standard Solutions”

2) REAGENTS

REFER TO COSHH RISK ASSESSMENT S017H
NOTE: Procedures for the preparation of reagents are given in the Appendices indicated.
Potassium stock standard solution, `SpectrosoL` grade, 1000 mg/L potassium
Sodium stock standard solution, `SpectrosoL` grade, 1000 mg/L sodium
Hydrochloric acid solution 1.0 mol/L,
Extraction solution.

3) PROCEDURE

REFER TO COSHH RISK ASSESSMENT S017H

1) Pipette 0.00 mL, 0.20 mL, 0.40 mL, 0.60 mL, 0.80 mL, 1.0mL of potassium stock standard solution, 1000 mg/L, 2.0into 100mL volumetric flasks.
2) Pipette 0.00 mL, 0.20 mL, 0.40 mL, 0.60 mL, 0.80 mL, 1.0mL of sodium stock standard solution, 1000 mg/L, into the same 100mL volumetric flasks.
3) Add 20 mL extraction solution to the 25 mL measuring cylinder.
4) Transfer the extraction solution to each of the volumetric flasks.
5) Add 10 mL of hydrochloric acid solution, 1.0 mol/L to the 10 mL measuring cylinder.
6) Transfer the hydrochloric acid solution, 1.0 mol/L to each of the volumetric flasks.
7) Dilute the solutions to just below the 100 mL mark with water.
8) Using a dropping pipette, dilute the solution to exactly 100 Ml with water.
9) Place the stopper firmly in the flask.
10) Shake the flasks vigorously to thoroughly mix the solution.
11) Transfer to the labelled 125 mL polyethylene bottles for storage.
12) These solutions contain 0.0 mg/L, 2.0 mg/L, 4.0 mg/L, 6.0 mg/L, 8.0 mg/L and 10.0 mg/L of potassium and sodium.

PREPARATION OF 1.0 mol/L HYDROCHLORIC ACID SOLUTION

1) APPARATUS

Volumetric flask, 1000 mL
Measuring cylinder, 100 mL
Dropping pipette, polyethylene
Polyethylene bottle, 1000 mL, labelled “Soil Analysis, Method S017, Determination of Cation Exchange Capacity, Hydrochloric acid solution, 1.0 mol/L”

2) REAGENTS

REFER TO COSHH RISK ASSESSMENT S017I
NOTE: Procedures for the preparation of reagents are given in the Appendices indicated.
Hydrochloric acid, S.G.1.18, 35%

3) PROCEDURE

REFER TO COSHH RISK ASSESSMENT S017I
1) Add approximately 800 mL water to the 1000 mL volumetric flask.
2) Measure 90 mL hydrochloric acid, S.G.1.18, 35%, into a 100 Ml measuring cylinder.
3) Add the hydrochloric acid, S.G.1.18, 35%, to the volumetric flask.
4) Dilute the solution to just below the 1000 mL mark with water.
5) Using a dropping pipette, dilute the solution to exactly 1000 mL with water.
6) Place the stopper firmly in the flask.
7) Shake the flask vigorously to thoroughly mix the solution.
8) Transfer to the labelled 1000 mL polyethylene bottle for storage.

K. PREPARATION OF EXCHANGEABLE CALCIUM AND MAGNESIUM STANDARD SOLUTIONS

1) APPARATUS

1 mL pipettor
Measuring cylinder, 10 mL (x2)
Dropping pipette
Volumetric flasks, 100mL
Polyethylene bottles, 125 mL labelled “Soil Analysis, Method S017, Determination of Cation Exchange Capacity, Exchangeable Calcium and Magnesium Standard Solutions”

2) REAGENTS

REFER TO COSHH RISK ASSESSMENT S017J
NOTE: Procedures for the preparation of reagents are given in the Appendices indicated.
Calcium stock standard solution, `SpectrosoL` grade, 1000 mg/L calcium
Magnesium stock standard solution, 100 mg/L magnesium
Hydrochloric acid solution 1.0 mol/L
Extraction solution.

3) PROCEDURE

REFER TO COSHH RISK ASSESSMENT S017J

PREPARATION OF MAGNESIUM STOCK STANDARD SOLUTION, 100 mg/L

1) APPARATUS

5 mL pipettor
Dropping pipette
Volumetric flask, 50mL

Polyethylene bottle, 60 mL, labelled “Soil Analysis, Method S017, Determination of Cation Exchange Capacity, Exchangeable Magnesium Stock Standard Solutions, 50 mg/L”

2) REAGENTS

REFER TO COSHH RISK ASSESSMENT S017K
NOTE: Procedures for the preparation of reagents are given in the Appendices indicated.
Magnesium stock standard solution, `SpectrosoL` grade, 1000 mg/L magnesium.

3) PROCEDURE

REFER TO COSHH RISK ASSESSMENT S017K

1) Pipette 5.00 mL magnesium stock standard solution, ` SpectrosoL` grade, 1000 mg/L magnesium, into a 50 mL volumetric flask.
2) Dilute the solution to just below the 50 mL mark with water.
3) Using a dropping pipette, dilute the solution to exactly 50 mL with water.
4) Place the stopper firmly in the flask.
5) Shake the flask vigorously to thoroughly mix the solution.
6) Transfer to the labelled 60 mL polyethylene bottle for storage.

L. SOIL ANALYSIS - DECARBONISATION OF SOIL FOR DETERMINATION OF ORGANIC CARBON

1) PRINCIPLE OF METHOD

Approximately 0.1 g of sample, in a porous crucible, is treated with sufficient hydrochloric acid, 4 mol/L, to remove carbonates. After the acid has drained from the crucible, the crucible and sample are dried overnight at 65°C. The organic carbon is determined as described in Method I004

2) APPARATUS

Filtering/porous crucibles, Leco part no. 528-028
Crucible tray(s)
Crucible tongs
Balance, readable to ± 0.1 mg
Pipette, 10 mL graduated in 0.1 mL divisions

Laboratory Oven No. 2, set at 65°C ± 5°C
Aluminium foil

3) REAGENTS

WARNING: REFER TO COSHH RISK ASSESSMENT S003
NOTE: Procedures for the preparation of reagents are given in the Appendices indicated.
Hydrochloric acid, 4.0 mol/L (Appendix A)

4) SAMPLE PREPARATION

Take a sub-sample of approximately 20 g of air-dried soil, previously crushed to pass a 2 mm sieve, and grind using a ball mill until the whole sub-sample passes through a 250µm sieve. Use a portion of this sub-sample to determine the dry matter factor as described in Method S002.

5) QUALITY CONTROL

Analyse a portion of Inorganic Laboratory Reference Soil No. S003. Use approximately 0.1 g for analysis

6) PROCEDURE

WARNING: REFER TO COSHH RISK ASSESSMENT S003
WARNING: Safety glasses and rubber gloves must be worn at all times while using hydrochloric acid. All procedures using hydrochloric acid solutions must be performed in a fume cupboard.
NOTE: To minimise the risk of contamination, always use tongs when handling crucibles, and do not make identification marks on the crucibles.
NOTE: To minimise the risk of contamination, cover the crucibles and crucible tray with aluminium foil.
Carry out a method blank determination.
1) Place a crucible on the balance pan.
2) Press the tare button to set the scale to zero.
3) Weigh approximately 0.1 g of sample into the crucible.
4) Record the weight of sample, in g, to the nearest 0.1 mg.
5) Place the crucible on the crucible tray.
6) Record the position number, of the crucible, on the tray.
7) Repeat steps 1 to 6 for each sample.
8) For the Method Blank determination, place an empty crucible on the crucible tray.
9) Record the position number, of the crucible, on the tray.
10) Record the weight of “Method Blank” as 0.1000 g.
NOTE:
To minimise the risk of contamination, cover the crucibles and crucible
Tray with aluminium foil.
11) Remove the crucibles from the tray and place in the well of the fume cupboard.

NOTE: Place the crucibles in the fume
Cupboard in the same relative
Positions as the positions on the tray.
12) Cautiously, add 1.0 mL of hydrochloric acid 4.0 mol/L, to each crucible.
CAUTION:To avoid sample loss, add the acid
To the sample, a drop at a time, initially, as vigorous effervescence
Will occur, due to the production of carbon dioxide, if carbonates are present. The acid may have to be added in several
Aliquots to avoid loss of the sample.
13) Allow the acid to drain from the crucible for 4 hours.
14) Place the crucibles on the crucible tray, making sure that they are in their original positions.
15) Place the crucible tray in the oven at 60 to 70□C.
16) Leave the crucible tray in the oven for 16 to 24 hours.
17) Remove the crucible tray from the oven.
WARNING: The crucible tray will be hot.
Wear heat resistant gloves.
18) Allow the crucibles to cool.
19) To prevent contamination or loss of sample, cover the crucible tray with aluminium foil until the samples are analysed.
20) Calibrate the Leco CS230 Carbon/Sulphur Analyser, as described in Method I003, using a minimum of 5 standards.
21) Measure the organic carbon content of Reference Soil
No. S003, as described in Method I004.
22) Record the organic carbon content, %, of Reference
Soil No.S003.
23) Measure the organic carbon content of the method blank, as described in Method I004.
24) Record the organic carbon content, %, of the method blank.
25) Check that the organic carbon value of Reference Soil No.S003 is within the limits stated.
2 Measure the organic carbon content of the samples, as described in Method I004.
27) Record the organic carbon content, %, of the samples.

CALCULATION

The organic carbon content is calculated as follows:

Organic Carbon, % = Cs - Cbl
where
Cs is the measured carbon percentage of the sample
Cbl is the measured carbon percentage of the blank
To calculate the organic carbon content to an oven dry basis:

$$\text{Organic Carbon, \%} = \frac{C_s - C_{bl}}{D}$$

where
D is the dry matter factor, determined as described in Method S002.

8) REPEATABILITY

The results of duplicate determinations should be within the limits stated below.

PREPARATION OF HYDROCHLORIC ACID SOLUTION, 4.0 mol/L

2) REAGENTS

REFER TO MATERIAL SAFETY DATA SHEETS.
WARNING: REFER TO COSHH RISK ASSESSMENT S003A
NOTE: Procedures for the preparation of reagents are given in the Appendices indicated.
Hydrochloric acid, S.G.1.18, 35%

3) PROCEDURE

WARNING: Safety glasses and rubber gloves must be worn at all times. This procedure must be performed in a fume cupboard.
1) Add 325 mL deionised water to the 500 mL measuring cylinder.
2) Cautiously, add 175 mL hydrochloric acid, S.G.1.18, 35%, to the measuring cylinder.
3) Transfer the solution to the 500 mL amber glass bottle.
4) Stopper the bottle securely.
5) Invert the bottle several times to thoroughly mix the solution.
6) Store the bottle in a ‘Safepak’ container in a storage cabinet.

Appendix 8.3: XRD profile for additional key minerals in the soils namely, biotite, muscovite kaolinite and analcime at 2θ (degrees) with position of peaks for nepheline and quartz from crystal diffract software's library.

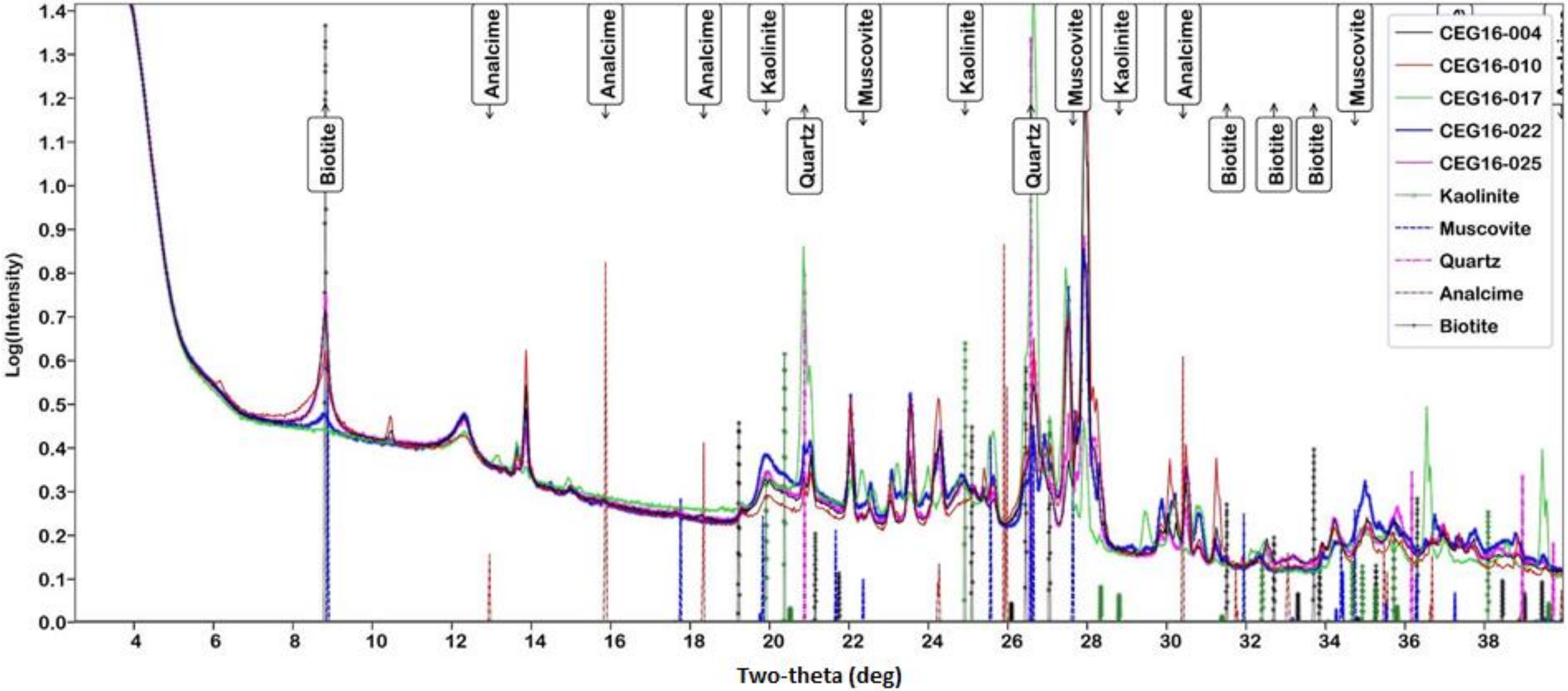

Appendix 8.4: XRD profile for additional key minerals in the soils namely, biotite, muscovite kaolinite and analcime at higher 2θ (degrees) with position of peaks for nepheline and quartz from crystal diffract software's library.

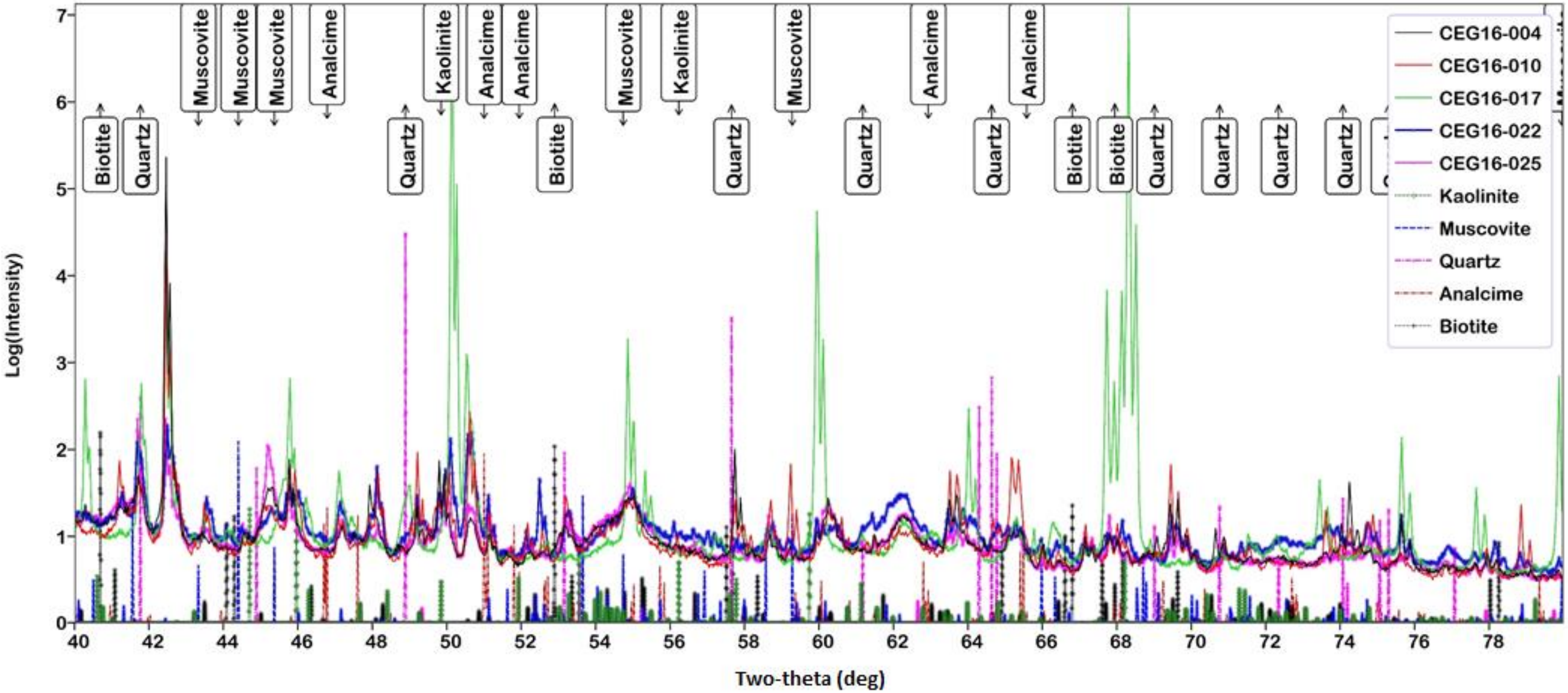

Appendix 8.5: Standard deviation for concentration of nutrients in soil in response to different K fertiliser treatments for (A) K (B) Mg (C) Ca (D) Na and (E) P using application rates of 0 (mg K/kg soil) , 100 (mg K/kg soil) , 330 (mg K/kg soil) , 660 (mg K/kg soil) , 860 (mg K/kg soil) and 1250 (mg K/kg soil) and a control, using data from Baah (2018) .

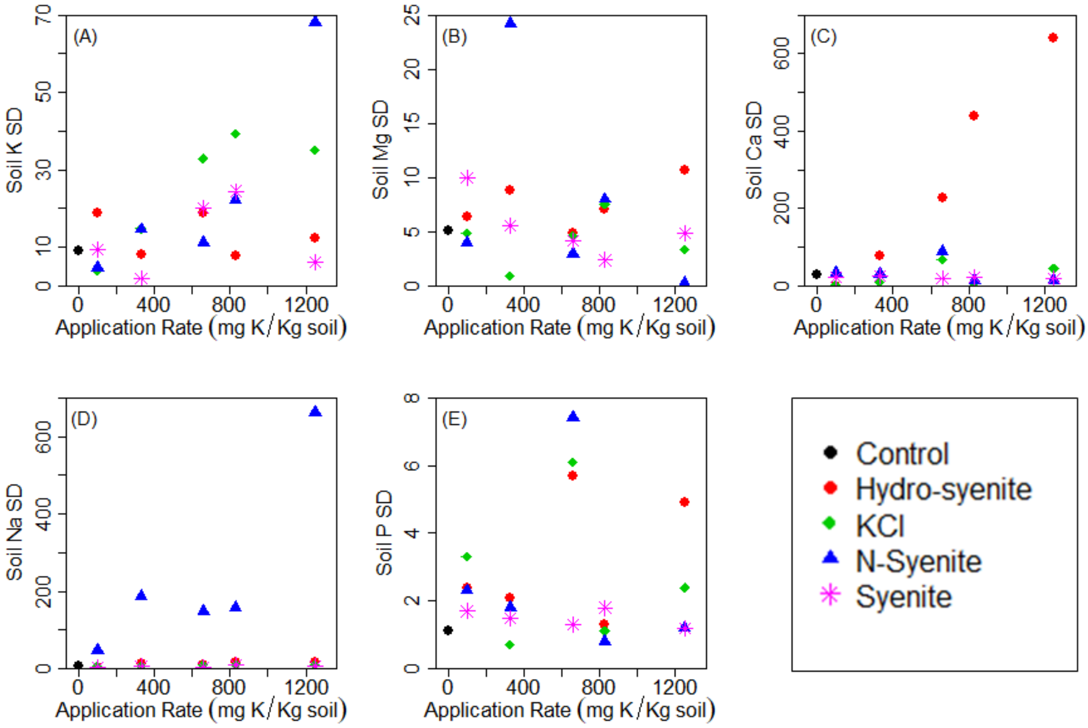

Appendix 8.6: Standard deviation for plants' height in response to K treatments of the different fertilisers at (A) 7 days (B) 14 days (C) 28 days (D) 42 days (E) 63 days and (F) 70 days after transplanting using application rates of 100 (mg K/kg soil) , 330 (mg K/kg soil) , 660 (mg K/kg soil) , 860 (mg K/kg soil) and 1250 (mg K/kg soil) and a control using data from Baah (2018) .

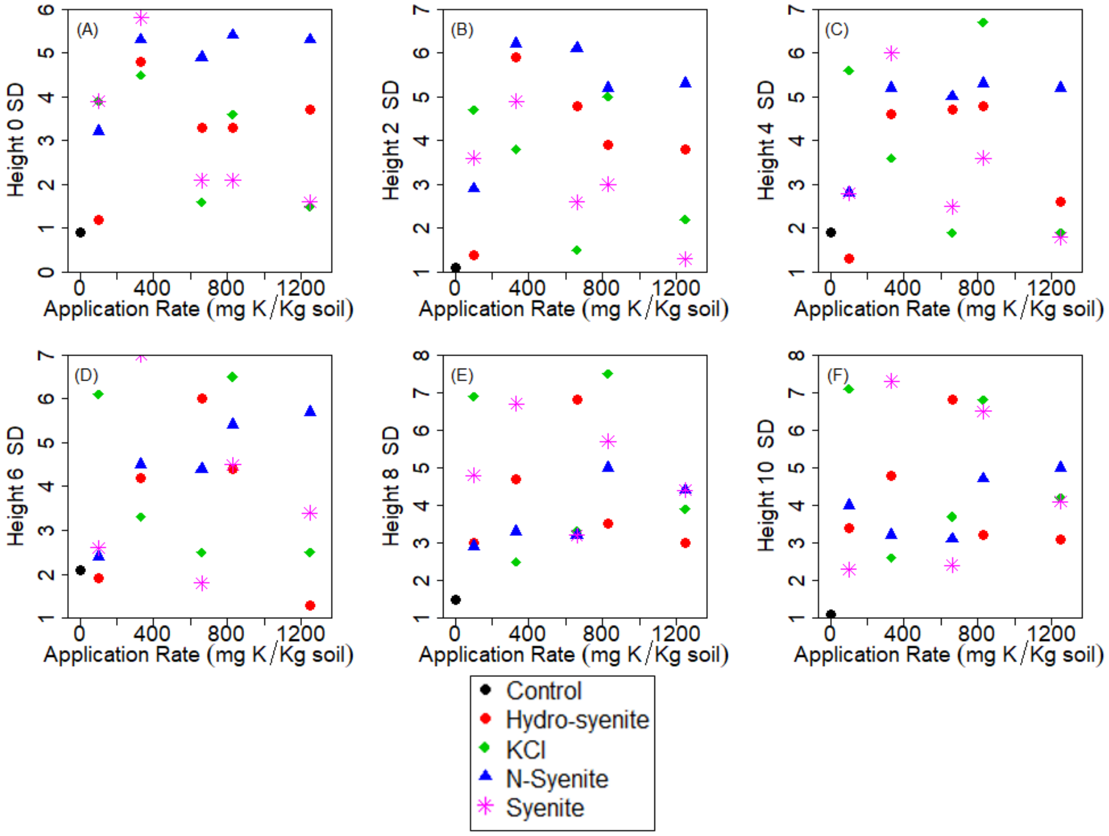

Appendix 8.7: Standard deviation for plants' dry matter content of (A) K, (B) Mg (C) Ca and (D) Na in response to K treatments of different fertilisers after 70 days after transplanting using application rates of 100 (mg K/kg soil) , 330 (mg K/kg soil) , 660 (mg K/kg soil) , 860 (mg K/kg soil) and 1250 (mg K/kg soil) and a control, using data from Baah (2018) .

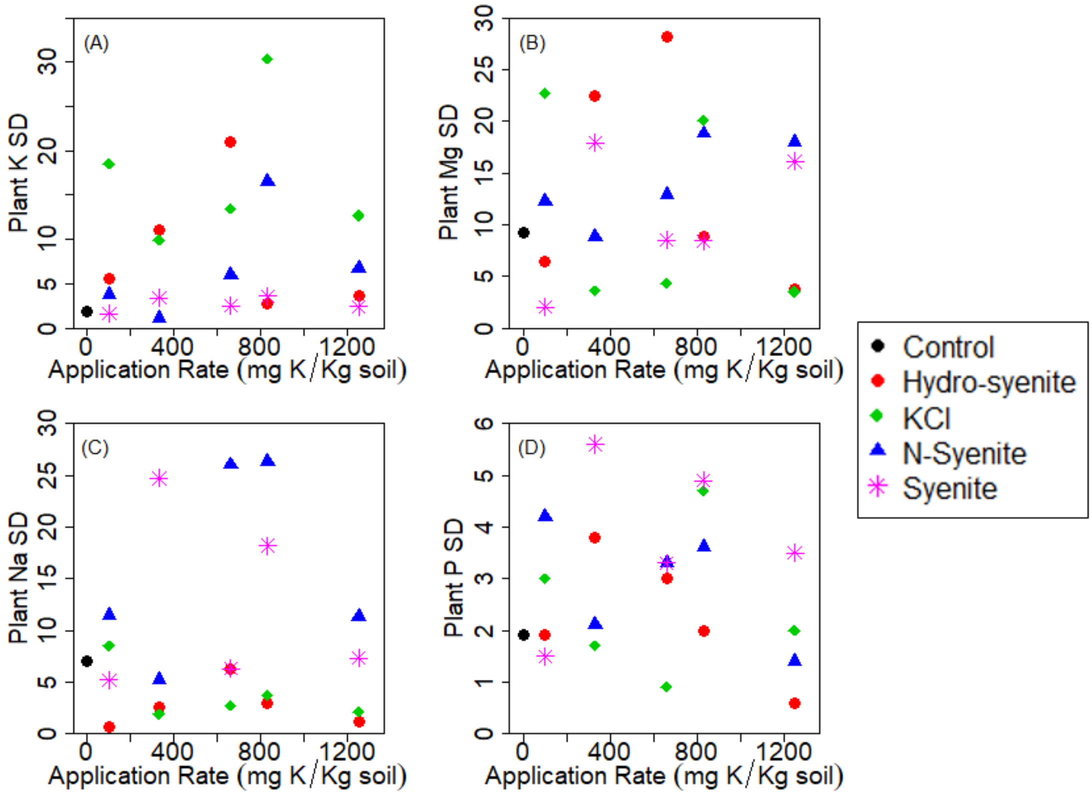

Appendix 8.8: Standard deviation for fruits' dry matter content of (A) K, (B) Mg (C) Ca and (D) Na in response to K treatments of different fertilisers after 70 days after transplanting using application rates of 100 (mg K/kg soil) , 330 (mg K/kg soil) , 660 (mg K/kg soil) , 860 (mg K/kg soil) and 1250 (mg K/kg soil) and a control, using data from Baah (2018) .